Analyse et diagnostique de l'air exhalé par spectroscopie photoacoustique (QEPAS).: Application aux maladies cardiovasculaires.

Diba Ayache

THÈSE POUR OBTENIR LE GRADE DE DOCTEUR DE L'UNIVERSITÉ DE MONTPELLIER

En Electronique

École doctorale : Information, Structures, Systèmes

Unité de recherche : Institut d'Electronique et des Systèmes

Analyse et diagnostic de l'air exhalé par spectroscopie photoacoustique (QEPAS). Application aux maladies cardiovasculaires.

~

Breath analysis and diagnosis by Quartz Enhanced Photoacoustic Spectroscopy (QEPAS). Application to cardiovascular diseases.

Présentée par Diba AYACHE

Le 11 Décembre 2023

Sous la direction de Aurore VICET

Devant le jury composé de

Ulrike WILLER, Associate professor, Clausthal University of Technology	Rapporteur
Virginie ZENINARI, Professeur, Université de Reims	Rapporteur
Emmanuel LE CLEZIO, Professeur, Université de Montpellier	Président de jury
Fares GOUZI, Maître de conférences des universités praticien hospitalier, Université de Montpellier	Examinateur
Weidong CHEN, Professeur, Université Côte d'Opale	Examinateur
Aurore VICET, Maître de conférences, Université de Montpellier	Directrice de thèse
Eric ROSENKRANTZ, Maître de conférences, Université de Montpellier	Invité
Michael BAHRIZ, Maître de conférences, Université de Montpellier	Invité

UNIVERSITÉ DE MONTPELLIER

"I have seen nothing but beauty…"

Acknowledgments

This work was conducted at the Institute of Electronics and Systems (Montpellier) in the Nanomir group. I would like to use these few lines to express my gratitude to the different structures and persons that have helped me, in any ways, to achieve this work.

I have to start by thanking Aurore Vicet, my director, for trusting me with this project and integrating me into her team. I have met Aurore during my first college year in electronics, and I am very proud that was able to grow as a scientist under her supervision. So, thank you for your advices, for guiding me through these three years and for being so encouraging. I must also thank you for being humanly present and making this workplace a comfortable place.

I also want to thank Fares Gouzi, who was my unofficial co-director. I really had a lot of fun learning all about the medical aspects. It was a pleasure working with someone that is so passionate.

To my jury, Ulrike Willer, Virginie Zéninari and Weidong Chen thank you for taking the time, for reviewing my thesis and for the interesting discussions.

To the president of the jury, Emmanuel Le Clezio… "la boucle est bouclée". I will never annoy you, as a student, anymore.

Of course, thank you Mike for always taking the time and for your jokes. It was a pleasure for me to work with you. I hope that you will be ready for this 20 km hike before I leave (hehe).

Many (many many) thanks to Eric Rosenkrantz for helping me with the acoustics aspects. Thank you for the many hours spent with us figuring out (with humour) the secrets of acoustic cavities.

I would also like to thank Vincent Bosch from the MGC Diagnostics company, for facilitating this collaboration and Nicolas Molinari and his two students Célia Vidal and Christelle Fernandez for managing the data processing.

A special thanks to my colleague Roman Rousseau with whom I have worked at the beginning of my thesis. Thank you for making QEPAS and research in general look so easy (now I know it was a trap). "We are researchers, our job is to make things evolve not make them look perfect" I remembered before using huge amount of glue to fix basically everything.

To the gas sensor team: Nico, Wioletta, Julien, Meriem, Tarek, Fanny and also Julie (even if you hate me). Thank you for your help, for making our offices and salle de manip happy places, for understanding my frustrations, for the gossip and for the 3 hours meeting.

To the people without whom this thesis would probably have taken three more years to be completed: Jean-Marc, Fabrice, Said, Vincent and Messir Boris… THANK YOU.

And of course, what would this thank-you-section look like if I didn't mention the Nanomir team? You ALL have been a little family to me during these three years. I am physically leaving but the echo of my voice, that I know you all appreciated when you were trying to be focused, will be there forever. One thing that we shared perfectly was our love for the food at any time. So, thank you for the sweet coffee breaks and especially the non-sense jokes.
Thank you LolOOO and JB for providing me both depression and therapy sessions. I hope you will not forget about me when you will be the heads of the "Gros Lolo & Falafel" company. Thank you to Daniel and Zayneb, I have no doubt that we will stay in touch in the future.

To the ones with who I have started this journey, we have struggled together but we made it through, alive (and doctors), you will always be my favourite colleagues: Pierro, Jul, Davide, Mikki, Andres (Papi).

Now allow me to be more emotional.

Thank you, mum. You told me so many times how proud, you are, of me, but you can also, and especially, be proud of yourself for raising the first doctor of the family. Thank you for giving so much importance to my education, I know the sacrifices that you had to make. Thank you for your unconditional support and for managing my stress so well (and for preparing me food).

To my cousin Dib, and my family, you have been the best (and craziest) support. Thank you for making me feel loved. (You were wondering what I was doing for three years? …You have these 200 pages to figure out, have fun.)

To my friends, Elissa, Abir, Kays, Eva, Sofian, Lynn, Sarah, Zahra(s) who have supported me through the highs and the many lows, thank you, I love you all.

Contents

Introduction

The investigation of the body fluids is not a recent concept. Hippocrates, a Greek physician, also known as the "Father of Medicine", has contributed significantly to today's medicine. He believed in a rational and scientific approach of the medicine and documented over his clinical observations, associating symptoms to pathological conditions. His theories were based on the analysis of the body fluids as well, notably the urine, which sweetish taste referred to diabetes. More than two thousand years later, an English physician named John Rollo, has described the smell of a decaying apple in the breath of a diabetic patient [1]. This reference to sweetness relates in reality of the excess of acetone produced by this illness conditions and eliminated through the urine and the breath. In contemporary medical practice, different methodologies exist to quantify and identify what are commonly referred to as biomarkers. Biomarkers have been defined by the Food and Drug Administration (FDA) as "characteristics that are objectively measured as indicators of health, disease, or a response to an exposure or intervention, including therapeutic interventions" [2]. In the early 1970s, Paulin et al [3] have published the first study revealing the presence of about 250 volatiles organic compounds (VOCs) in the exhaled breath of humans. Amongst these compounds, some are metabolically produced by the body, participate in exchanges between the blood and the lungs and are evacuated through the respiration. If it is possible to correlate these exhaled gases to a specific medical condition, accurately identify and quantify them, then it is possible to have an early and non-invasive access to the body metabolism.

The World Health Organisation (WHO) has identified cardiovascular disease as the leading cause of death worldwide [4]. However, it is still diagnosed very late because of the invasive nature of the procedures for the patients. The initial step involves a comprehensive family tree analysis to ascertain potential hereditary risk factors. Subsequently, a range of blood and radiological examinations may be prescribed. Lastly, one of the most invasive procedures is the cardiac catheterization, wherein a catheter is inserted through a peripheral artery to trace the circulatory path back to the heart, aiming to identify any obstructions or constrictions. Recently, numerous studies have shown a direct or indirect link between certain gases measurable in exhaled breath and cardiovascular diseases (CVD), opening up the possibility of rapid, non-invasive and inexpensive diagnosis. However, the definition of new biomarkers requires the support of rigorously standardised studies leading to the clear definition of a pathological threshold.

The SENSIR project represents a collaboration between the Department of Clinical Physiology at the University Hospital of Montpellier, involved in research related to

respiratory diseases (with PhyMedExp laboratory) and the Institute of Electronic and Systems (IES), in charge of the development of gas sensors using photoacoustic spectroscopy. This project, funded by the University of Montpellier (MUSE), aims to implement a sensor capable of detecting gases in exhaled air in order to help in the diagnosis of CVD.

Four different gases have been identified within the scope of this project: nitric oxide (NO) [5], carbon monoxide (CO) [6], isoprene [7] and acetone [8]. The link between these gases and their concentration with cardiovascular pathologies is established in the Chapter 1 of this manuscript. The respiratory system and the various physiological, pathological and external factors that are involved in the modification of gas concentrations in exhaled air are presented showing the importance of conducting measurements in standardized procedures. The description of the respiratory system and its different compartments allows us to define a crucial measurement criterion, which is real-time monitoring, enabling the reconstruction of the complete expirogram for each molecule, i.e., tracing its concentration in each compartment of the respiratory system.

In Chapter 2, the detection technique used to develop the gas measurements presented in this manuscript is described. This technique is Quartz Enhanced Photoacoustic Spectroscopy (QEPAS), which relies on photoacoustic principles applied in the infrared (IR) domain where various, numerous and intense absorption gas lines are present. As its name suggests, this technique is based on the conversion of an electromagnetic wave into an acoustic wave, which is measured using a piezoelectric transducer known as the Quartz Tuning Fork (QTF). The use of tunable lasers with smaller spectral width than the absorption lines improves the selectivity of the technique. This criterion is essential for applications such as exhaled air analysis, where gas matrices are complex and may exhibit spectrally close absorptions. Finally, the sensor that has been developed consists of lasers and transducers that can be combined in different configurations to optimize the sensor's sensitivity.

In Chapter 3, a literature review is presented, referencing the various spectrophone configurations (transducer + acoustic cavity) implemented by different research teams since the introduction of QEPAS in 2002 [9]. The off-beam configuration used in the experimental setup, allows the laser to be aligned within a T-shaped acoustic cavity. This configuration helps to minimize the photothermal perturbations generated when the laser passes directly between the prongs of the tuning fork (on-beam or bare configuration). This configuration is studied through a numerical model constructed using the Acoustic Pressure (ACPR) module of COMSOL Multiphysics and compared to an analytical model based on the definition of acoustic impedances inside the T-shaped cavity. In order to understand the coupling between the two elements composing the spectrophone, the last part of this chapter is focused on a Multiphysics study designed to observe the effect of the QTF position on the frequency of the acoustic wave exiting the cavity.

The Chapter 4 presents the experimental work conducted at the IES on the implementation of the QEPAS detection module for each of the four gases as well as the adaptation of this technique to the exhaled breath application. The first part of this chapter relies on the implementation of breath sampling system and the management of the high amount of humidity present in the breath and playing an important role on the stability of the resonance frequency of the QTF. The second part of this chapter presents the development and the performances of each QEPAS devices. Finally, the last part of this chapter describes the combination of the QEPAS sensor with the Medisoft apparatus used at Montpellier hospital in pulmonary tests. This configuration will be used in a future clinical study conducted at the hospital involving CHF (chronic heart failure) patients and healthy volunteers. This study aims to reconstruct the expirogram of each molecule in order to understand their production in each respiratory compartment. QEPAS measurements combined with the flow rate and the capnography proposed by the Medisoft sensor will be used to provide information on the airways management.

References

[1] J. Rollo, *An account of two cases of the diabetes mellitus, etc. Cases of the diabetes mellitus; with the results of the trials of certain acids, and other substances, in the cure of the lues venerea... with large additions*. C. Dilly, 1798.

[2] "'FDA on biomarkers. Website accessed on 09-24-2023 : https://www.fda.gov/drugs/biomarker-qualification-program/about-biomarkers-and-qualification.'" .

[3] L. Pauling, A. B. Robinson, R. Teranishi, and P. Cary, "Quantitative analysis of urine vapor and breath by gas-liquid partition chromatography.," *Proc. Natl. Acad. Sci. U. S. A.*, vol. 68, no. 10, pp. 2374–2376, 1971, doi: 10.1073/pnas.68.10.2374.

[4] "'WHO on cardiovascular diseases. Website accessed on 09-24-2023: https://www.who.int/news-room/fact-sheets/detail/cardiovascular-diseases-(cvds)'.pdf." .

[5] D. S. Winlaw, G. A. Smythe, A. M. Keogh, C. G. Schyvens, P. M. Spratt, and P. S. Macdonald, "Increased nitric oxide failure production," 1994.

[6] B. Tun, R. Ehrbar, M. Short, S. Cheng, R. S. Vasan, and V. Xanthakis, "Association of exhaled carbon monoxide with ideal cardiovascular health, circulating biomarkers, and incidence of heart failure in the framingham offspring study," *J. Am. Heart Assoc.*, vol. 9, no. 21, 2020, doi: 10.1161/JAHA.120.016762.

[7] S. Mendis, P. A. Sobotka, and D. E. Euler, "Expired hydrocarbons in patients with acute myocardial infarction," *Free Radic. Res.*, vol. 23, no. 2, pp. 117–122, 1995, doi: 10.3109/10715769509064026.

[8] J. C. Anderson, "Measuring breath acetone for monitoring fat loss: Review," *Obesity*, vol. 23, no. 12, pp. 2327–2334, 2015, doi: 10.1002/oby.21242.

[9] A. A. Kosterev, Y. A. Bakhirkin, R. F. Curl, and F. K. Tittel, "Quartz-enhanced photoacoustic spectroscopy," *Opt. Lett.*, vol. 27, no. 21, 2002, doi: 10.3969/j.issn.1001-0548.2015.06.025.

Chapter 1
Physiological factors influencing exhaled breath composition

The lungs or respiratory system is the site of gaseous exchange between the internal environment of the body and the external environment, in favour of the supply of molecules that are used for the body metabolism (such as oxygen (O_2)) and the removal of molecules that are produced by the body metabolism (such as carbon dioxide (CO_2)). Respiration is defined as the cellular reactions of oxidation of energy substrates leading to energy production. Therefore, although the lungs are known as the "respiratory system", they are not strictly involved in the respiration. The lungs constitute the first step leading to the O_2 supply and CO_2 removal to the human internal environment. The renewal of the lung gases from the external environment is called "ventilation". The oxygen supply to, and CO_2 removal from, the bloodstream (and thus the internal environment) is called "haematosis". The lungs, which occupy most of the thoracic cage, are the main site of all involved mechanisms. Both of these mechanisms, which appears to be automatic, are controlled by different reactions, physics laws and mechanisms that govern the concentration of a gaseous molecule (O_2, CO_2 or any other molecule of the body or external environment) in the lungs during the ventilation, and thus, in the exhaled air. For a better understanding of the application targeted by this project, the following sections provide a simple description of the different respiratory compartments and the gas exchanges that take place within them.

1- The human respiratory system: structure and functions

The respiratory system is made up of several organs and tissues that work together in a very elegant way. The external environment of the lung is the ambient air, which is composed of a mixture of different gases (N_2: 78%, O_2: 21%, CO_2: 0.04% and others). Yet, at the end of the respiratory system (the alveoli), the gas composition is different (N_2: 78%, O_2: 16%, CO_2: 4% and others), and reflects the mechanisms involved in the lung ventilation and haematosis in the different lung structures.

The respiratory system can be divided into two main parts: the upper airways and the lower airways (Figure 1).

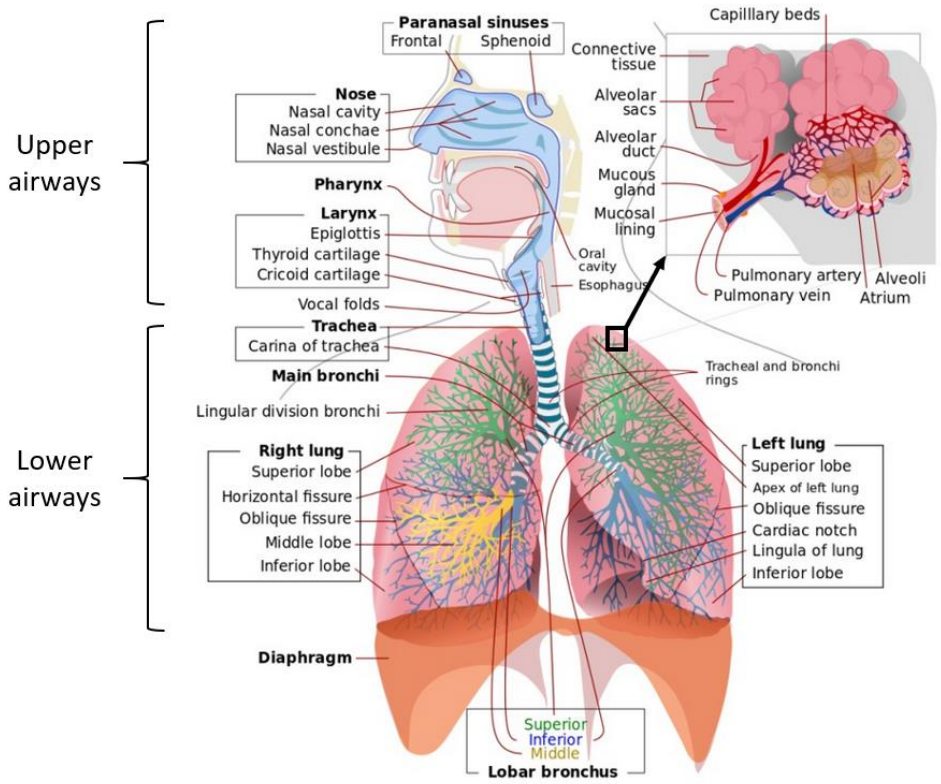

Figure 1: The anatomy of the respiratory system [1]

The upper part consists of:

- The nose and the mouth,
- The pharynx: carries out food and air and is divided in two parts leading to the respiratory or digestive system,
- The larynx: contains the vocal chords involved in phonation.

At this first stage, the air is humidified, warmed up and cleaned before contacting the lower part's delicate tissues, which modifies the composition of the gas in the airways.

The lower part of the respiratory system consists of:

- The trachea: this canal is 10-12 cm long and about 2 cm wide, and its horseshoe-shaped walls also help to clean the air and prevent particles from entering the lungs,
- The bronchi, divided into an inverted Y,
- The lungs.

The lungs supply oxygen to the internal milieu of the human body and allow waste gases such as CO_2 to be removed. The human body has two lungs, each weighing about 1 kg.

In the lungs, the bronchi divide into what is known as the bronchial tree (Figure 2). This irregular separation of the main bronchi into several generation of daughters, of different sizes and diameters, leads to the formation of the alveoli. The pulmonary vascular system

follows a similar pattern, starting with the main pulmonary artery and rapidly branching into several small arteries and capillaries.

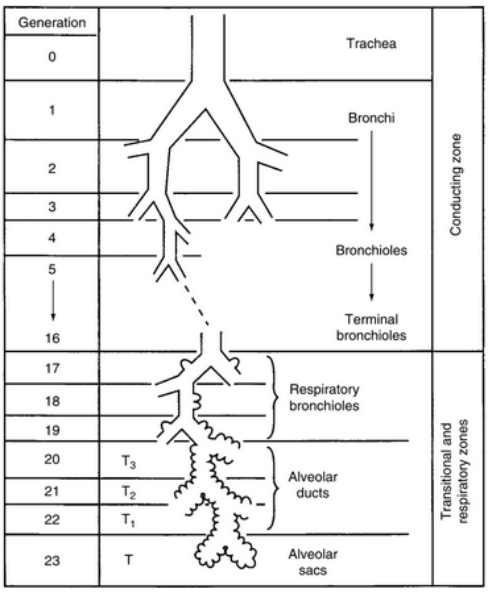

Figure 2: Branching of the conducting and terminal airways [2]

In the division of the bronchi, three zones can be identified: one purely air-conducting zone [3], one purely gas-exchange zone and a transitional zone that separates the two zones mentioned above (Figure 2) [4]. The different functions of the lungs emerge as we move deeper into the respiratory system. The conducting zone, as its name suggests, is only involved in the transport of the inhaled gases to the respiratory zone where occurs all the gaseous exchanges between the respiratory compartments and the internal environment (bloodstream).

The gas exchange region is composed of tissues, blood and air. The tissues constitute a stable support for the blood and air compartments. In these compartments, gases diffuse from the air into the blood, and vice versa, over a large surface area of 140 square metres [5]. Gas exchanges take place through a thin wall, of about 1 μm thick [6], separating the alveoli from the blood capillaries. An adult human has about 480 million alveoli, each around 250-300 μm in diameter, which walls are lined up with small blood vessels. Altogether, this immense surface area facilitates the transport of gases between the blood and air compartments. In the alveoli, the composition of the gas is modified through its diffusion in the lung capillaries. The different mechanisms involved in this transport will be described in the section 2 of this chapter.

Last, the respiratory system is constituted of the thoracic rib cage, the respiratory muscles (intercostal muscles and the diaphragm [2]) and the nervous system structures (phrenic nerves that controls the diaphragm and bulbar respiratory centres in the brainstem). They are involved in the control and cyclic movement of the respiratory system that actions the respiratory system as a "pump" leading to successive phases of inspiration and expiration,

that constitutes the ventilation. The composition of the gas that circulates within the respiratory system depends on:

- The external environment: the changes in the ambient air or the inhalation of external gases or molecules modifies the concentrations of the gas in the lungs.
- The internal environment: which is dependent on the endogenous production of molecules by the human body.
- The structures and function of the respiratory system, including:
  - The mechanics of the ventilation
  - The respiratory compartments (airways and alveoli)
  - The gas exchanges occurring between the alveoli and the capillaries, which is dependent of the alveolo-capillary diffusion of the gas and molecules
  - the repartition of the air inhaled from the external environment.
  - the pulmonary vascular system, and the repartition of the lung perfusion of the alveoli.

While the composition of the exhaled breath is determined by the environment and endogenous production in healthy condition, the ventilatory mechanisms in respiratory or cardiovascular diseases can also affect the exhaled gas matrix. In other words, **what** we exhale can also be affected by **how** we breath.

Altogether, it is logical that the measurement of concentration of gaseous molecules in the exhaled air has emerged as a potential diagnosis tool in 3 different contexts:

- Environmental toxic exposure
- Systemic diseases, leading to circulating biomarker
- Respiratory or cardiovascular diseases

A molecule like the exhaled CO has been validated as a tool to assess the external exposure to "toxic" partial combustion of organic materials (like tobacco-smoke). Yet, it has recently emerged as a potential disease biomarker, given its ability to reflect the excessive internal environment concentration in different diseases, like chronic heart failure.

Last, diseases of the lung, and airways in particular can impact the concentration of a gaseous molecule in the respiratory system. In the context of asthma, the concentration of NO, which is mainly produced in the airways can increase in the exhaled air. Other molecules, that are the consequence of their diffusion from the internal environment in the alveoli, can also be altered in the context of pulmonary or cardiovascular diseases, that impact the diffusion and lung alveolar ventilation or perfusion.

2- The mechanics of ventilation and lung volumes

During the breathing process, the muscles in the abdomen and chest contract and relax, causing the lungs to expand and contract. A normal breathing process is a cyclic phenomenon composed of what is commonly known as the inspiration and the expiration. These two phenomena can be defined as the ventilation. During the inspiration, the contraction of the muscles involved in the ventilation process causes the pressure inside the alveoli to fall under the atmospheric pressure. Therefore, an airflow is directed into the lungs, causing the lung volume to increase. Conversely, during the expiration, the pressure in the alveoli is higher than the atmospheric pressure. Thus, the airflow is directed in the opposite direction. The ventilatory cycle is characterized by an opposite trend between the alveolar pressure and the pulmonary volumes (Figure 3).

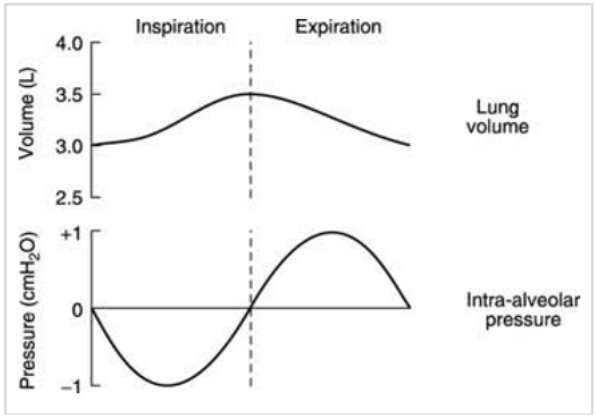

Figure 3: Variation of the lungs volume and alveolar pressure during a normal breathing cycle.

During each breath, about 500 mL of air moves in and out of the lungs: it is the tidal volume V_T. For a normal adult, the respiratory rate (RR) ranges between 10 – 12/ minutes. The minute ventilation V'_T is defined as the product of the V_T and RR and designates the flow of air (in litre) mobilized per minute.

While the cyclic succession of inspiration and expiration during the ventilation occurs unconsciously, the inspiration constitutes an active process which means that the involved muscles of the thoracic cage receive a nervous order to contract. This cyclic activity (RR) and pattern of the V_T is dependent on the brainstem command and regulatory mechanisms. Conversely, the expiration is a passive process occurring as a consequence of the lung expansion. It takes place in the same way an "elastic" compartment would go back to its resting configuration when the constraint is no longer applied.

- **The static properties of the thoracic- pulmonary system: study of the lung elasticity.**

Boyle's law links the volume and the pressure exerted by a certain mass at an unchanged temperature as:

$$PV = cste \tag{1.1}$$

With P the alveolar pressure and V the lung volume. This law describes the phenomenon of ventilation previously explained. The difference of pressure and volume observed during each inspiration and expiration are related to the compliance and elastic properties of the lung as:

$$C = \frac{1}{E} = \frac{\Delta V}{\Delta P} \tag{1.2}$$

With C the compliance of the lungs equal to the inverse of its elasticity E.

Thus, the lung volume (maximal lung volume and resting lung volume (P=0)) depend on the thoracic compliance.

- **Assessment of the lung volumes: spirometry**

The respiratory capacity can be investigated by the mean of a spirometer (Figure 4) during a totally non-invasive ventilatory manoeuvres. Basically, the air flows correspond to variations of the lung volumes. By connecting a spirometer to the mouth of the patient, it is possible to deduce the variation of volumes over a period of time. During a spirometry [7] [8] these volumes can be estimated to investigate the lungs function.

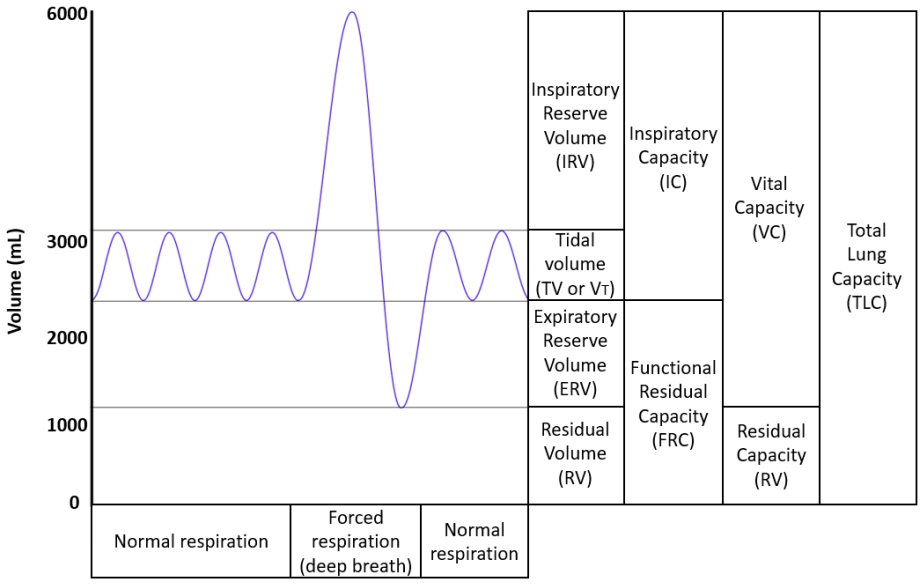

Figure 4: Respiratory volumes and capacities of a normal adult.

Figure 4 presents the different lung volumes during a breathing procedure:

- The tidal volume (V_T) ≈ 500 mL: volume of air that moves in and out of the lung during normal breathing cycle. At the end of the expiration, the lung volume reaches its resting lung volume, which is the volume when the pressure in the system is equal to zero (no contraction of the respiratory muscles). Thus, this volume depends on the compliance of the thoraco-pulmonary system.
- Inspiratory reserve volume (IRV) ≈ 2100-3200 mL: amount of air that can be inhaled by forcing the inspiration. It is directly dependent on the contractile activity of the respiratory muscles.
- Expiratory reserve volume (ERV) ≈ 1200 mL: amount of air that can be exhaled by forcing the expiration. The expiration becomes an active process during this procedure as the thoracic muscles contract to push the air outside the body.
- The vital capacity (VC) = V_T + IRV + ERC

Considering what has been previously described, any change in the lung compliance, in the respiratory muscle function or ventilatory brainstem command ("restrictive functional deficit" on a spirometry [9]) will modify the lung volumes and ventilation and thus, the composition of gaseous molecules in the lung and exhaled air. For instance, any voluntary change in the ventilation pattern (V'_T= RR* V_T) impacts the concentration of the gaseous molecules in the lung.

During a voluntary apnea (V'_T=0) or a hypoventilation (decrease V'_T), there is no (or a little) renewal of the gas in the lung, and thus, the concentrations of the gas tend to reach the concentrations in the internal milieu (alveolar parts). During a voluntary hyperventilation (increase in V_T and/or RR), the renewal of the lung gas from the external environment is increased, and thus, the concentrations of the gas tend to reach the concentrations in the external environment.

To illustrate this, the exhaled concentration of CO_2 is measured and the variation during hypoventilation and hyperventilation are presented in Figure 5. The measurement of the exhaled CO_2 over a period of time is called a capnograph and will be detailed section 3.2 of this mauscript.

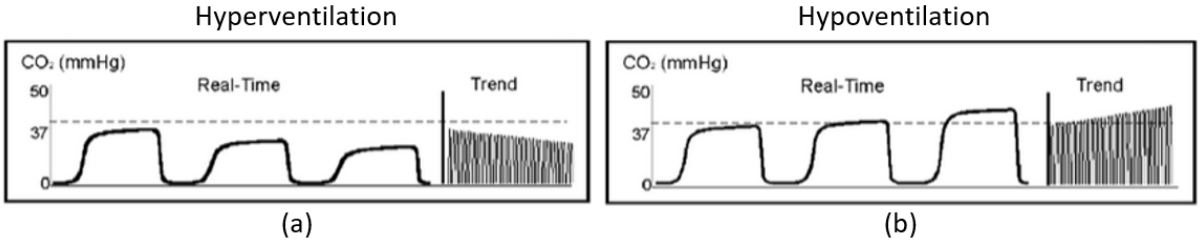

Figure 5: Typical capnogram obtained during (a) hyperventilation, (b) hypoventilation.

During hyperventilation the measured concentration of CO_2 tend to decrease and get closer to the poor inhaled concentration of CO_2 compared to the hypoventilation where the

concentration of CO_2 tends to increase and get closer to the high concentration of CO_2 released during the respiration.

If the ventilation process tends to modify the concentration of the gases present in the exhaled breath, it is necessary to use standardized procedures, for the flow related to the volume, between the different study investigating the exhaled breath composition as well as between the different subjects participating in these studies in order to minimize the biases.

3- Gas exchanges

3.1- Alveolar ventilation: V'$_A$ and dead space

As the ventilation is a cyclic process, not all of the air volume that enters the lungs is involved into gas exchanges occurring in the respiratory part. A portion of the inhaled air remains in what is called the "dead space". The alveolar volume V_A (mL) can be expressed as:

$$V_A = (V_T - V_D) = 350 \quad (1.3)$$

With V_D the dead space volume approximately equal to 150 mL for a healthy adult. The composition of the alveolar air is different from the composition of the inspired air. Before reaching the alveolar part, the air is subject to different modifications, starting from the upper airways part, where the air is humidified. Additionally, a part of the alveolar volume is replaced at each cycle with a part of the tidal volume (V_T) (Figure 6). Finally, the alveolar air composition is dependent of the gaseous exchanges.

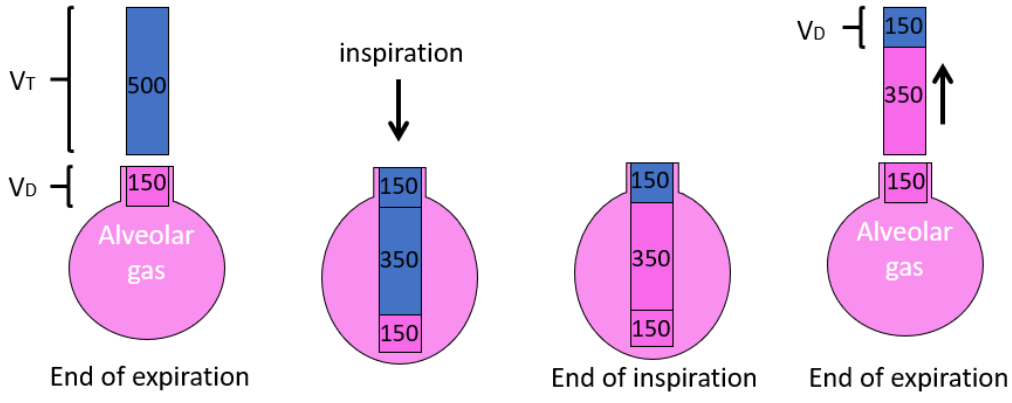

Figure 6: Repartition of the tidal volume V_T, in the dead space and alveolar compartments.

Figure 6 shows how the alveolar air is mixed, at each breath, with the tidal air volume. At the end of the expiration, the composition of the dead space is a representation of the alveolar air. In the dead space, this volume does not undergo any gas exchanges: it remains unchanged. At each inspiration, 500 mL of "fresh" air in introduced inside the lung. The

air contained in the dead space (150 mL) is introduced inside the alveolar part, with a part of the inspired air. At the end of the inspiration, the dead space is representative of the inspired air and the alveolar part is a mixture of the dead space air (composed of the alveolar air at the previous expiration) and a part of the inspired air.

$$V_T' = V_T \cdot RR = 500 \cdot 12 = 6000 \ \frac{mL}{min} \tag{1.4}$$

By using Equation (1.3), the alveolar ventilation V_A' can be calculated as:

$$V_A' = V_A \cdot RR = 4200 \ \frac{mL}{min} \tag{1.5}$$

3.2- Distribution of the alveolar ventilation and airways flows

All the alveoli are not equally ventilated which means that the alveoli do not receive the same amount of air. Based on that, the ventilation of the airways is totally inhomogeneous. In addition, the distribution of the ventilation is dependent on the airway resistances. The Hagen-Poiseuille law can be successfully applied to air flowing in the airways. For an incompressible and Newtonian fluid (here inhaled air) flowing through a pipe (here the airways), this law links the difference of pressure in two points of the pipe to its resistance and the air flow going through it:

$$\Delta P = RV' \tag{1.6}$$

With R the resistance of the pipe and V' the flow.

If the turbulences caused by the separation of the branches leading to the alveoli are neglected, the resistance can be calculated by considering the laminar flow of the air through the branch:

$$R = \frac{8\mu l}{\pi r^4} \tag{1.7}$$

With l and r respectively the length and radius of the considered branch and μ the dynamics viscosity of the fluid (air). The resistance exerted on the fluid strongly depends on the radius of the branch in which the fluid is flowing: the bigger the radius, the smaller the friction, the smaller the resistance. The resistance of the airways affects the air flow inside the lungs. The resistance can be increased in some diseases. In that case, the flow is modified and the maximal flow values measured by a spirometer during a forced expiration are decreased ("obstructive functional deficit") and reflects an obstructive disease of the airways [10].

Altogether, the regional distribution of the ventilation is measured by the inhalation of a radioactive gas (Xenon 133 (^{133}Xe)). The images obtained from this kind of test show, indeed, an important heterogeneity in the regional ventilation of the lungs but also inform

on the better ventilation of the inferior part of the lung. The augmentation of the ventilation from the bottom to the upper part of the lung is represented in Figure 7.

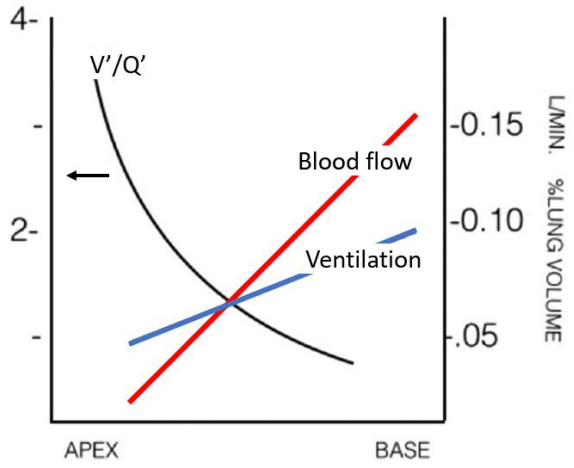

Figure 7: Ventilation (V') (blue curve) and blood flow (Q') (red curve) from the apex to the base of the lung and the V'/Q' ratio (black curve). The ventilation is described section 3.1 of this chapter. The blood flow is related to the perfusion describe in section 3.3. The ratio V'/Q' is described section 3.4.

- **Assessment of the ventilation inhomogeneity and lung compartments: N_2 washout method**

During this procedure, the subject is asked to breath normally before inhaling (in a close circuit) 100 % of O_2 and exhaling slowly and continuously until reaching the residual volume. During the expiration, the N_2 is measured continuously with a gas analyser and plotted as function of the expired volume (mL).

During the inspiration, the air goes to the bases of the lungs that are more ventilated and containing more alveoli. Therefore, when the oxygen is inhaled, it moves towards the bases of the lungs. The concentration of N_2 present at the base of the lung is diluted in this region. The clinician obtains a graph that is representative of heterogeneity in the distribution of the inhaled gas. This graph is composed of 4 phases that are described in (Figure 8).

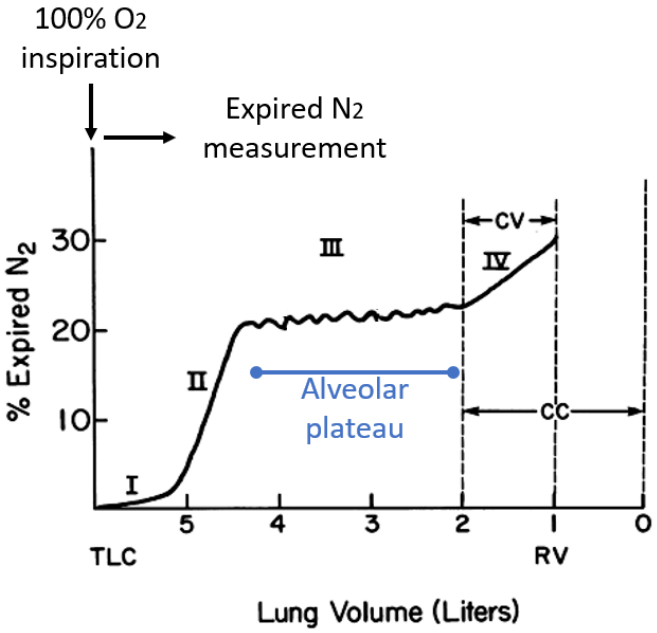

Figure 8: Representation of the 4 stages of the expired % of N_2 function of the total lung volume during a washout N_2 procedure. TLC: total lung capacity. CC: closing capacity. RV: residual volume. CV: vital capacity.

The first phase corresponds to the void of N_2 since it represents the composition of the upper airways from the end of the prior inhalation. The second phase is a mixture between the middle airways and the alveoli. As long as the person exhales the lung volume decreases which leads to narrowing the small airways. Therefore, the stage 3 is a mixture between the apexes (upper part of the lung), the middle and base of the lung. This phase is often referred to as the alveolar plateau. At the end of the expiratory manoeuvre, the smaller airways in the inferior part of the lungs are closed, the contribution of the alveoli to the N_2 concentration is considerably decreased, the concentration of N_2 comes from the apex region where the N_2 is less diluted. The 4^{th} phase is representative of the closing volume, it occurs after the small airways closes. This volume is normally equal to 10 % of the vital capacity for a healthy adult. Changes of this value can be attributed to small airways diseases, aging, premature closure of the airways, smoking, etc. The slope of the phase 3 is generally representative of these variations (Figure 9).

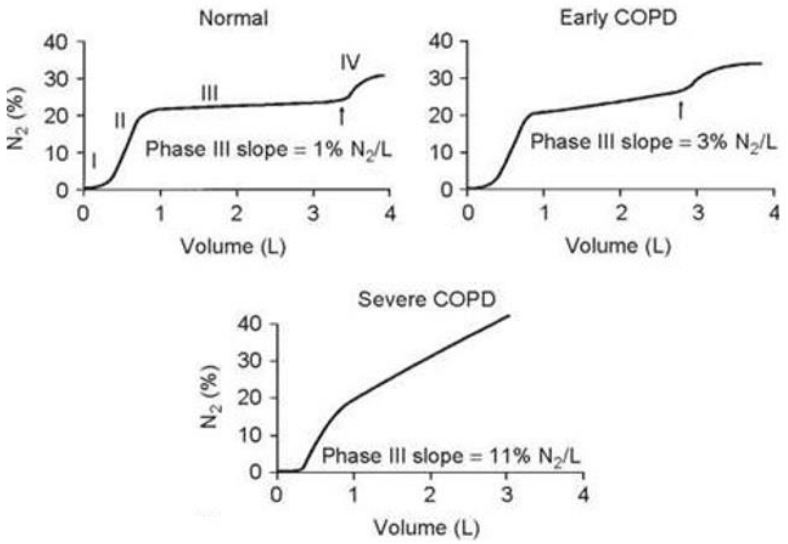

Figure 9: N_2 concentration in the expired air measured during a N_2 washout procedure in a healthy (normal) person and patients with an early and severe lung obstructive disease (COPD).

- **Assessment of the ventilation inhomogeneity and lung compartments: Capnography**

The capnography is the measurement of the partial pressure of CO_2 during inspiration and expiration. The measurement of CO_2 informs on the airway management and is often used in emergency departments at the hospital [11][12], during anaesthesia [13] or for the placement of endotracheal tubes [14]. The maximum of partial pressure of CO_2 is obtained at the end of the exhalation which corresponds to the end tidal CO_2 (P_{ETCO2}). This value is often compared to the partial pressure of alveolar CO_2 (P_{aCO2}≈ 40 mmHg) for clinical interpretation.

The exhaled CO_2 curve over the ventilation time is represented on Figure 10.

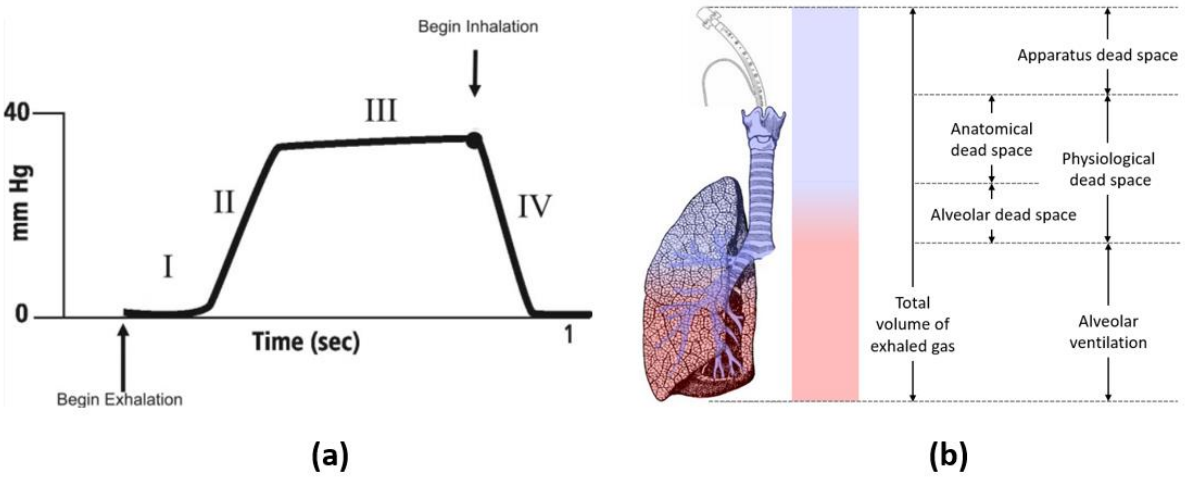

Figure 10: (a) Shape of a normal capnogram. [15] (b) Airways stages including the apparatus and physiological dead space containing air that will not operate in gas exchanges and alveolar ventilation where blood and air exchanges occur

Similarly, the capnogram reflects the lung compartments and the heterogeneity of the distribution of the alveolar ventilation, different phases are described (Figure 10a):

- Phase I: at the beginning of the exhalation the CO_2 is approximately equal to the atmospheric concentration of CO_2 (≈ 340 ppmv). This value is also related to the anatomical and apparatus dead space (Figure 10b).
- Phase II: synchronous release of atmospheric air mixed with alveolar air.
- Phase III: stabilization of CO_2: alveolar plateau.
- Phase IV: end of exhalation and return to "zero" baseline.

The CO_2 can also be measured over the expired air volume but requires more elaborated equipment [16] (Figure 11).

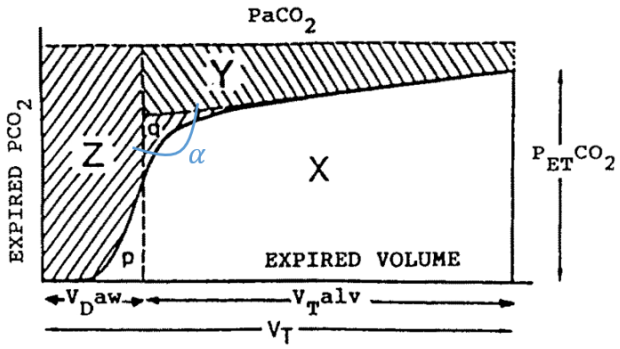

Figure 11: Normal capnogram function of the expired volume. [16]

Crucial information can be interpreted from this capnograph:

- Z and Y are respectively the anatomical and alveolar dead space (Z+Y= physiological dead space).
- X corresponds to the effective tidal volume ($V_T$alv) and determines the volume of CO_2 in the breath.
- $V_D$aw corresponds to the airways dead space.
- V_T is the tidal volume = $V_D$aw + $V_T$alv.
- In this graph the component "p" and "q" are equal. "p" represents the effective ventilation component of phase II and "q" its dead space component.
- The α angle is usually ranging between 100° and 110° for a normal person and increases with the phase III slope. Therefore, α value is a good representative of the airway obstruction (Figure 12).

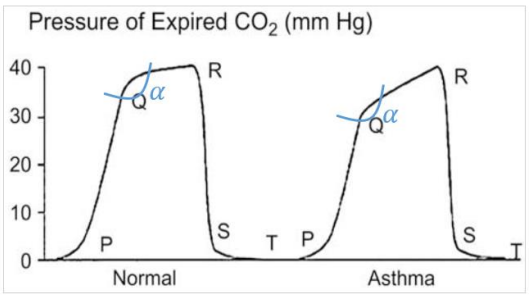

Figure 12: Capnogram of a normal and asthmatic subject showing different shapes and value of alpha angle. [17]

The measurement of the exhaled CO_2 is a good indicator of the obstruction as Figure 12 shows. For an asthmatic person, the normally ventilated alveoli will release the CO_2 faster while the obstructed alveoli, that are poorly ventilated will release a higher concentration of CO_2 later during the expiration [17].

Finally, CO_2 curves and N_2 expired concentrations constitute interesting tools for the assessment of the respiratory function. This non-invasive measurement provides important information on the heterogeneity of the ventilation, the exchanges between the different compartments as well as the degree of lung obstruction. Moreover, a full expiration obtained in real time associates a concentration of CO_2 to its origin in the airways. Therefore, and as it has been presented in Figure 10 and Figure 11, the CO_2 expirogram is a valuable tool in the identification and management of the airways.

3.3- Lungs perfusion: Q'

The pulmonary circulation is composed of veins, arteries and capillaries similarly to the systemic circulation. Two main differences exist between the two circulations:

- The first one is directly related to the lungs function: the blood that arrives to the lung tissues is charged with CO_2 and leaves the lungs charged with O_2.
- The pressure in the pulmonary circulation is much lower than the pressure of the systemic circulation. This leads to high blood flow that are close to the cardiac flow rate.

The pulmonary circulation is organized in a tree structure ending with the capillaries that cover the surface of the alveoli. Their very thin walls facilitate the gas exchanges between the blood and the airways. The distribution of the lung perfusion (vascularisation) is, just like the ventilation distribution, very heterogenous and higher at the base of the lung (Figure 7).

Different factors can influence the size and the resistance of the pulmonary blood vessels:

- The pulmonary volume,
- Gravity: the length of the lung of a person that is standing up ranges between 20-30 cm. The blood distribution undergoes gravity, the pressure in the blood vessels is higher in the inferior part of the lung and blood flow is unequally distributed along the lung. The effect of gravity on the blood vessels and the perfusion is minimized in a layed down position.
- The physical exercises,
- Hypoxia (O_2 deficiency) condition due to vasoconstriction: causes variations in the regional distribution of the perfusion. In small region suffering from hypoxia the blood vessels constrict and the perfusion is redistributed to other healthy regions.

The inhomogeneous perfusion of the lung plays an important role on the composition of the expired air. The capnography presented in section 3.2 shows that the CO_2 in the lower and better perfused part of the lung (alveolar plateau) is higher than the concentration in the upper part of the lung where the perfusion is smaller. Other gases that are coming from the systemic circulation and evacuated throughout the respiration will logically diffuse from the pulmonary circulation (capillaries) to the alveoli located at the base of the lungs similarly to CO_2. The gas exchanges occurring between the blood and the airways take place in the better perfused regions (base). The position of the subject undergoing expired air composition investigation as well as its physical movement that both tend to modify the perfusion of the lungs should be standardized.

3.4- Alveolar-capillary diffusion

Two main mechanisms are involved in the transportation of gases in the lungs: convection and diffusion [18]. The former is characterised by mass flow and is responsible for the movement of air between the environment and the respiratory compartments while the latter is responsible for gas exchange between blood and air. The diffusion process is described by a partial pressure difference between two different compartments. This phenomenon is directly related to the gas concentration, regardless of the other gases. Therefore, whenever a difference of pressure exists between a gas (gaseous phase) and a dissolved one (liquid phase), a gradient of diffusion is established from the compartment containing the highest concentration of gas to the lowest one. The equilibrium between the liquid phase (blood) and the gaseous phase (alveolar air) is described by Henry's law stating that the amount of dissolved gas in liquid is directly proportional to its partial pressure above the liquid.

For O_2 passing from the airways to the blood, the volume and flow rate of the diffusion between the two compartments can be described by Fick's law:

$$V'_{O_2} = \frac{\alpha}{\sqrt{M_{O_2}}} \cdot \frac{S}{e} \cdot \left(P_{alvO_2} - P_{capO_2}\right) \quad (1.8)$$

With V'_{O_2} the flow rate in L/min, α the solubility of the O_2 in the membrane separating the two compartments, M_{O_2} the O_2 molar mass, S the surface of the membrane where the exchange is taking place and e its thickness and $P_{alvO_2} - P_{capO_2}$ the difference of partial pressure of O_2 between the alveoli and capillaries.

In an ideal case, the O_2 would diffuse from the air to the capillaries and the equilibrium in partial pressure between the alveolar and blood compartments would be maintained as long as the O_2 is not involved in other exchanges (occurring with the tissues). In reality, different factors contribute to the inhomogeneity of the O_2 in the overall circulation: the alveolar dead space, the anatomic shunt and the difference between the perfusion and ventilation of the lungs (Figure 13).

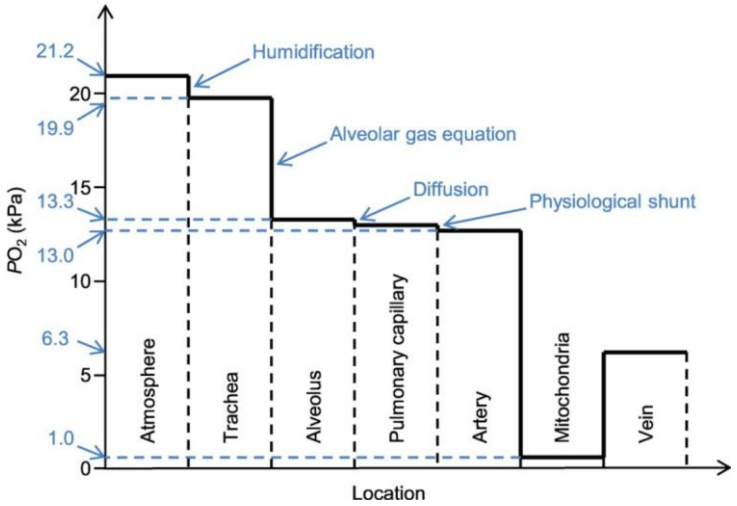

Figure 13: O_2 cascade: from the atmosphere to the mitochondria (small cells that generate most of the energy inside the body)

- **The anatomic shunt**

In addition to the pulmonary circulation that is described above, the lung also receives blood from the systemic circulation. This blood that comes from the tissues contains a high amount of CO_2 but does not take part in the gaseous exchanges. Instead, this blood shunts the ventilated part of the lung and directly joins the pulmonary arteries transporting O_2 to the tissues without being re-oxygenated. The consequence of this shunt is a decrease of the partial pressure of O_2 in the capillaries.

- **The ventilation and perfusion ratio**

The global ratio of perfusion and ventilation rate is equal to 1 at rest as both V' and Q' are close to 5 L/min in healthy and resting conditions. However, the ventilation and the perfusion are regionally heterogenous. The V'_A increases slowly from the apex to the base

of the lung while the Q' increases rapidly between these two regions. This heterogeneity is observed with the V'_A/Q' ratio (Figure 7):

- The V'_A/Q' ratio is equal to 1, in the middle of the lungs.
- The V'_A/Q' ratio increases towards the apex of the lungs as this region is better ventilated than perfused.
- The V'_A/Q' ratio decreases towards the base of the lungs as this region is better perfused than ventilated.

Therefore, a physiological shunt is created, the blood that will not be re-oxygenated will contribute, just like the anatomic shunt to the decrease of the partial pressure of O_2 in the blood. This effect can be intensified with pathologies affecting the airways or the blood vessels.

- **The alveolar dead space:**

In the case where the alveoli are not perfused at all, the alveolar air is close to the inspired air which means that it is composed of a high amount of O_2 and small amount of CO_2. The consequence of the non-perfusion would be an V'_A/Q' ratio $\rightarrow \infty$ that corresponds to the alveolar dead space. Similarly, to the anatomical dead space, gas exchanges do not occur in these regions. The physiological dead space is defined as the addition of the alveolar and anatomical dead space (Figure 10b).

Finally, the efficiency of the diffusion and gas exchanges is governed by the regional ventilation and perfusion ratio, the shunt effect (partially anatomic), the alveolar dead space as well as the exchange surface and its thickness that can be modified in some pathological conditions. A better diffusion will obviously facilitate the transport of the O_2 from the airways to the blood but also the CO_2 and other gases from the blood to the airways making the alveolar air composition a mirror of the body metabolism.

All in all, the composition of the alveolar air depends on:

- The alveolar ventilation V'_A, and its inhomogeneous distribution is the lung
- The lung perfusion, and its inhomogeneous distribution is the lung
- The air diffusion in the alveolo-capillary barrier

4- Endogenous production of CO, NO, isoprene and acetone

In the following section, the endogenous production of CO, NO, acetone and isoprene as well as their link with the cardiovascular system and diseases is explained.

4.1- Endogenous production of CO

Inside the body the main production source of CO is related to the catabolism of heme proteins. Heme proteins have multiple biological functions including the transport of oxygen or electrons in the body. The degradation of the heme proteins in the body is induced by the heme oxygenase (HO). This enzyme acts as a defence mechanism against oxidative stress [19]. The form of HO that is involved in the degradation of heme proteins and production of CO is the HO-1. The chemical reaction leads to the formation of CO, ferrous ion and biliverdin. The ferrous ion is stored as iron, the biliverdin is reduced into bilirubin that has anti- proliferative, oxidant and inflammatory functions inside the body (Figure 14).

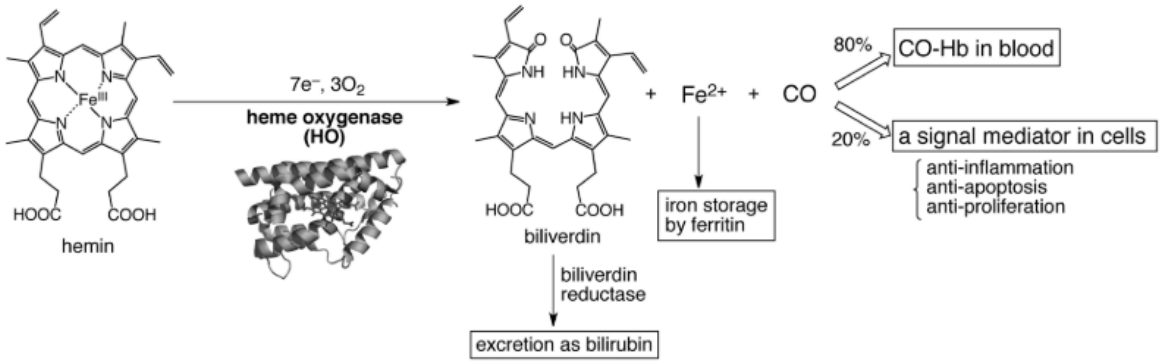

Figure 14: Heme degradation and production of carbon monoxide in Mammalians. [20]

The endogenously produced CO has a vasodilatation function [21]. Higher concentration of CO has been found in chronic cardio vascular diseases [22] and inflammatory diseases [23] [24] and its action has been proven in the prevention of endothelial cell apoptosis (programmed cell death) [25].

Different studies have shown a good correlation between HbCO and exhaled CO meaning that exhaled breath tests, that are completely non-invasive could be used as a good indicator of the body metabolisms [26][27]. In healthy, non-smokers, the end tidal concentration of CO ranges between 1 and 3 ppmv [28]. However, multiple external sources are often contributing to the increase of the exhaled CO concentrations. The main sources of CO are related to pollution, exposure to combustion in enclosed environments and active and passive consumption of cigarettes [29].

The production of CO is predominantly systemic. The CO follows the blood pathway and participates into gas exchanges between the capillaries and the alveoli. Therefore, CO is removed from the body after crossing the alveolar-capillary membrane [30]. Consequently, the upper airways present smaller CO concentration than the alveolar part. The expirogram of CO follows the same trend as the CO_2's (Figure 15). Different studies presenting real-time complete expirograms confirms these trends [31].

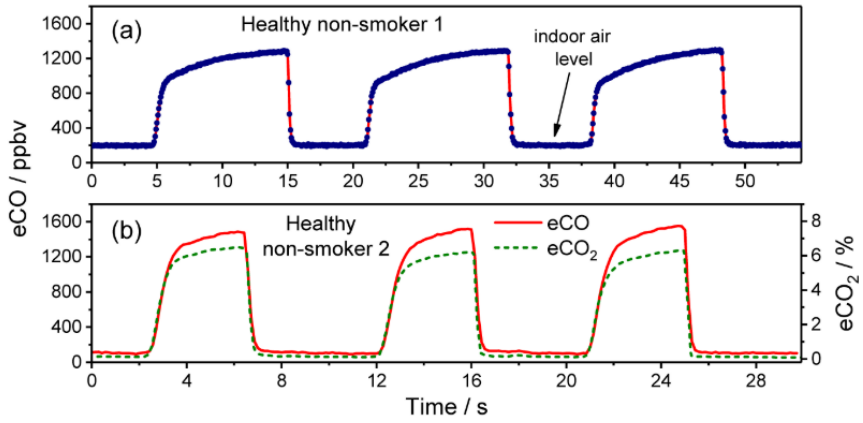

Figure 15: Real-time expirogram of CO combined with the expirogram of CO_2 obtained for healthy non-smoker subjects. [31]

4.2- Endogenous production of NO

Conversely to CO, the production of NO is mainly located in the airways [30] which is consistent with the results presented in some studies where the exhaled NO did not match the systemic concentration of NO [32][33]. Endogenously, NO is produced from the conversion of L-arginine by a nitric oxide synthases (NOS) (Figure 16a). The NOS are enzymes that are present in endothelial (inner layer of blood cells) or neuronal cells. They are differentiated in three types that are involved in the synthetization of NO and L-citrulline from L-arginine. L-arginine and L-citrulline are both amino acids that are used in the production of proteins or removal of waste product during exercises [34]. Even if the main source of NO is found in the airways, the different types of NOS are expressed in different tissues including the heart, and the systemic circulations [35] [36] (Figure 16b).

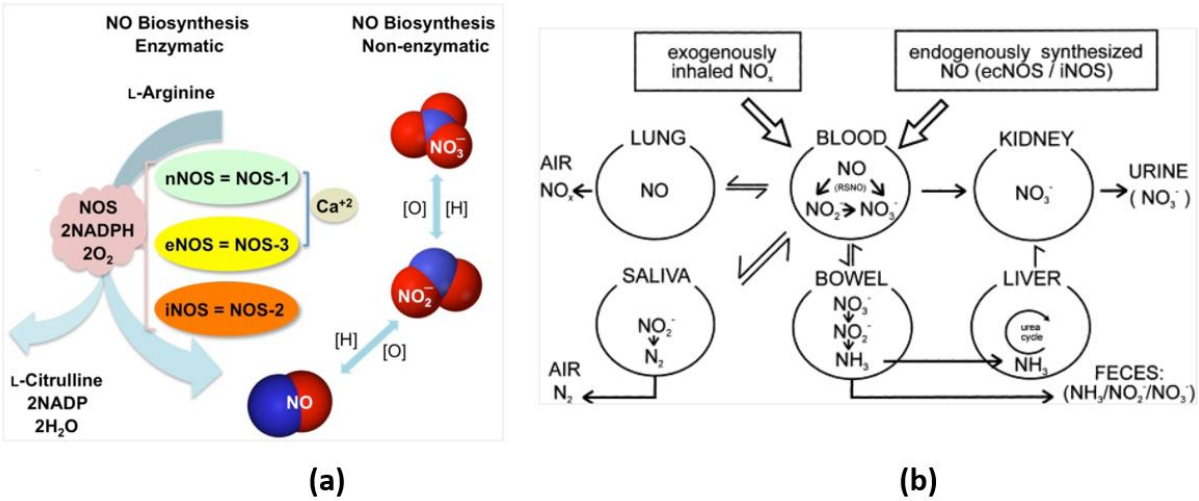

Figure 16: (a) Biosynthesis of NO. [37] (b) Biotransformation of NO in mammals. [35]

A correlation has been found between exhaled NO levels and patients with asthma [38]. Higher concentrations of NO were observed in patients presenting asthmatic conditions

and these levels were decreased in response to corticosteroids treatments (anti-inflammatory) [37]. These observations led to the adoption of exhaled NO in the diagnosis and monitoring of asthma. Moreover, NO is involved in different physiologic processes including vasorelaxation [37]. In heart failure, characterized by vasoconstrictive forces, NO is known to counter these forces and the overall NO levels are increased in a case of heart failure or cardiomyopathy [39][40][41].

The first exhaled breath measurement of NO was presented in the 1990s and was performed with a chemiluminescence-based analyser [42]. The concentration of NO was evaluated in the part per billions range. Today, the assessment of the fraction of exhaled NO (FENO) in the diagnosis of inflammatory diseases has been approved by the Food and Drug Administration (FDA). The measurements are standardized and the limitations are well-known [43]. The complete expirogram of NO has been presented in [44]. By associating the NO concentration to capnography measurements, it results that the concentration of NO is higher in the upper airways part (Figure 17). NO has also been found in higher concentration when measured directly from the nose where concentration levels can reach the ppmv range [45][46].

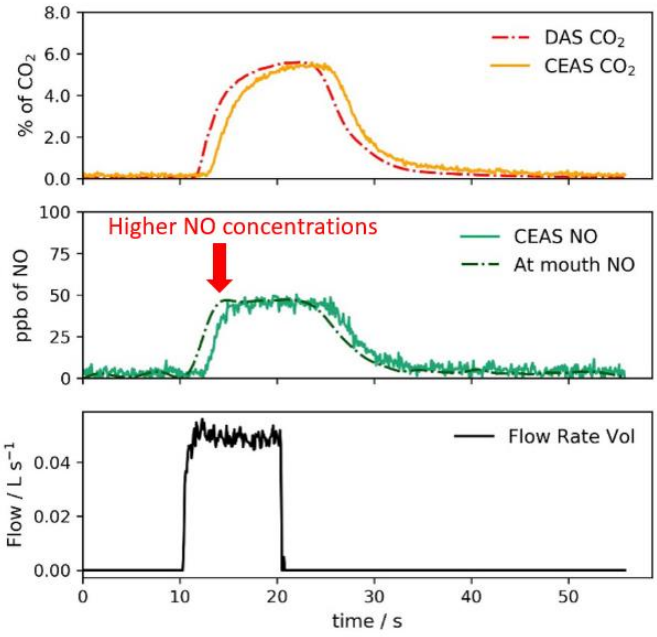

Figure 17: NO expirogram associated with capnography and flow measurements. To measure this expirogram, two techniques are compared: Cavity enhanced absorption spectroscopy (CEAS) [47] and Direct absorption spectroscopy (DAS) (described in the section 1.4-4 of the Chapter 2 of this manuscript).

Similarly, to CO, the endogenous production of NO can be affected by external sources. NO is commonly known as an environmental pollutant found in vehicles exhaust [52][53]

and different studies have found a decreases of NO concentrations in cigarette smokers [50][51].

4.3- Endogenous production of isoprene

Isoprene has been discovered in 1860 during a process involving the thermal decomposition of natural rubber [52]. As a matter of fact, isoprene is produced in the manufacturing of synthetic rubber. Isoprene is also known as a pollutant as it participates in the generation of secondary organic aerosol (SOA) in the atmosphere [53]. The exposition and inhalation of isoprene is regulated as it is suspected to cause lung cancers. On a completely different level, the natural production of isoprene has been observed in trees as a protection mechanism to exposure to high heat [54].

The origins and the physiological behaviour of isoprene in the body are to date not fully understood [55]. However, this hydrocarbon that is the main endogenous hydrocarbon found in the exhaled breath has raised the interest of many research teams [56]. Isoprene can be found in the blood, in the urine but also in the exhaled breath. Due to its very poor solubility in water, the elimination of this gas through the urinary path is minor compared to the exhalation path. This also significates that isoprene is not (or very poorly) re-absorbed by the mucus layer in the upper airways part, and that its exhaled concentration is a good representative of its alveolar levels.

First, the main endogenous production of the isoprene was attributed to the biosynthesis of cholesterol [57][58]. Later, many studies have shown that the main site of isoprene production is the muscle tissues [59][60]. This last observation stands as a solid argument in the investigation of the origin of this hydrocarbon. Indeed, different studies measuring the concentration of isoprene in the exhaled breath have proved a rapid and intense increase of its concentration few minutes after the beginning of the physical exercise going from a baseline at rest around 100 ppbv to about 800 ppbv [61] (Figure 18). At the beginning of an exercise the blood flows significantly through the muscles and washes out the isoprene that is transported in the systemic circulation until being evacuated from the body.

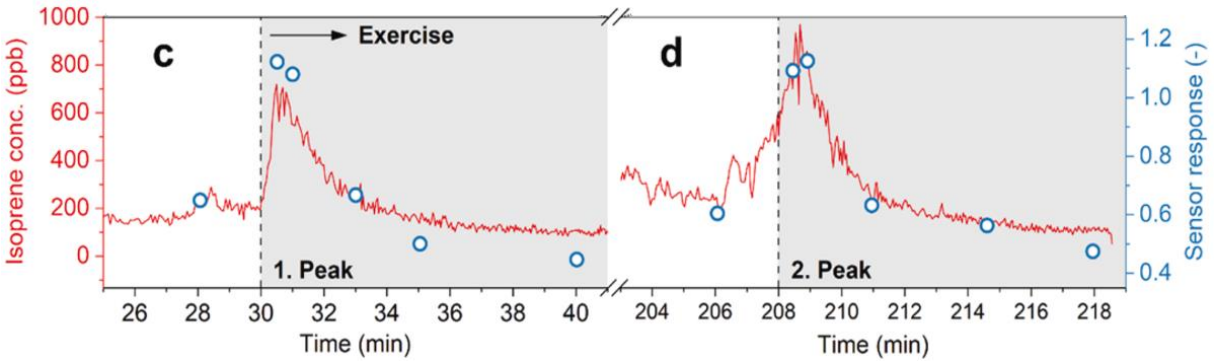

Figure 18: Evaluation of exhaled isoprene concentration before, during and after a physical exercise. [61]

The misunderstanding of the exact production pathway of the isoprene inside the body as well as its high dependence on age, gender and physical activities do not encourage its adoption in clinical procedures neither help towards standardizations of its measurement [66][67]. Nevertheless, isoprene has been investigated in different conditions. Compared to controls, higher concentrations of isoprene have been found in patients with chronic kidney diseases, with an increase before and after haemodialysis [68][69], lung cancers [66] and also chronic liver diseases [67]. No correlation was found between the exhaled isoprene values and the cholesterol level in the blood [68]. In cardiovascular-related studies, the augmentation of the isoprene concentrations has been observed in acute myocardial infarction [69] while one study has shown a decrease of this gas level in chronic heart failure [70].

4.4- Endogenous production of acetone

Acetone (C_3H_6O) is a ketone body mainly (but not solely) produced in the liver and released during the fatty acid metabolism. Fatty acids are transformed by the liver into Acetyl-CoA. In certain conditions, it happens that the body uses fat instead of glucose for energy production. Therefore, depending on the glucose concentration, Acetyl-CoA can be transformed into acetoacetate. The latter undergoes different decarboxylation and produces two different ketone body, including acetone (Figure 19).

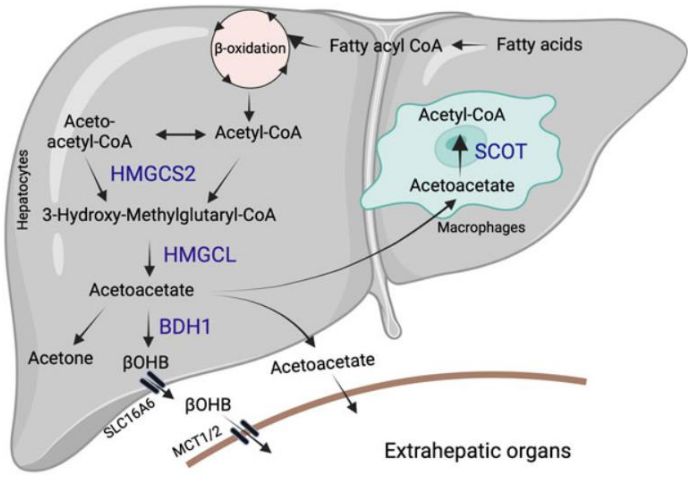

Figure 19: Hepatic generation of acetone. [71]

Acetone, as well as the other produced ketone bodies, enter the bloodstream circulation. Due to its small size, acetone diffuses into the airways and can be measured in the exhaled breath. At high plasma acetone concentrations, approximately 80% of the acetone production rate was attributed to exhaled breath. Thus, in diabetic patients, the exhaled breath was positively correlated with the plasma acetone concentrations during ketoacidosis. In addition, exercise, sleep and diet also alter exhaled acetone concentrations. In particular, fasting increased breath acetone while high carbohydrate feeding decreased or maintained breath acetone at low concentration. Different studies have observed the effect of fasting onto the exhaled breath concentrations. Thus, the diet should be controlled by standardizing the meals or the fasting duration before the measurement, in order to reduce the acetone variability [72]. Acetone has been defined as a biomarker for diabetes [73] where a significant difference of concentration between patients and controls was found with concentrations higher than 0.8 ppmv in the first group [74][75]. Many studies have been investigating the exhaled acetone concentration as biomarker of heart failure/ cardiovascular diseases. A systematic review and meta-analysis published by our team demonstrates that acetone concentrations were higher is patients than in controls even though the results were lacking standardisation to conclude on a pathological threshold [72].

The expirogram of acetone has been established in different studies. As for CO and CO_2 that are mainly circulating in the bloodstream and diffuse into the airways, the concentration of acetone at the beginning of the exhalation is low and the maximum is reached from the alveolar volume (Figure 20) [78][79].

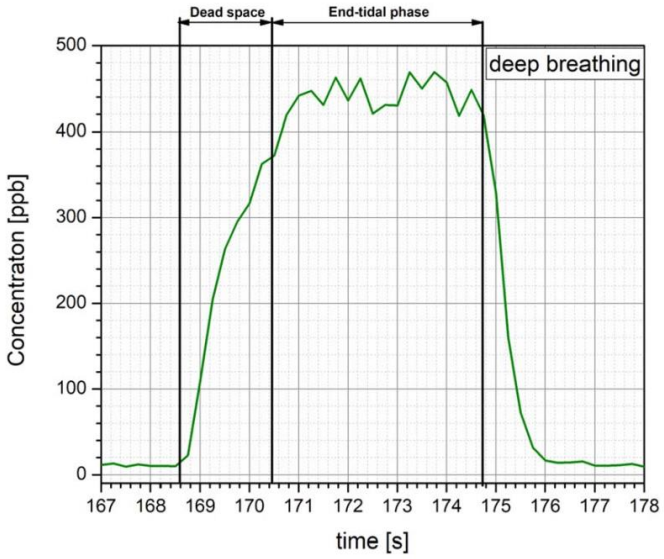

Figure 20: Complete expirogram of acetone.[77]

During the breathing process, gases from the environment enter the body through the nose and reach the bloodstream and organs through the exchanges that take place between the alveoli and the blood capillaries in the last part of the respiratory system. These gases include CO_2 and oxygen, which are necessary for the proper functioning of physiological metabolisms. Endogenously, the body produces a range of gases that are derived from or necessary for some internal processes. These gases can also access the bloodstream and can be removed from the body during respiration if they are able to pass through the alveolocapillary membranes. Therefore, just as CO_2 informs us of certain physiological or pathological states in the body, these gases, if they can be measured, can also provide useful clinical information in the diagnosis or monitoring of some pathologies.

In the previous section, we introduced capnography as a tool to associate the exhaled CO_2 concentration over time with a specific area of the respiratory system. Most studies that focus on analysing gases exhaled by the body tend to disregard the initial portion corresponding to the dead space and only analyse the alveolar volume. However, crucial information can be obtained from gas concentrations originating in these zones. This is particularly the case for exhaled NO, which concentration appears to be higher in the upper part of the respiratory compartments.

In this project, we have chosen to associate the measurement of gases identified for our application with a simultaneously measured capnography curve. As a result, it is possible to track how the concentration of this gas evolves during a complete exhalation, associate this concentration with a CO_2 concentration, and thus with a respiratory compartment, obtain the alveolar concentration originating from the blood. These measurements will be further discussed in the Chapter 4 of this manuscript.

Many factors are involved in the identification and definition of a biomarker. Ideally, our study is based on measuring a range of gases in the exhaled breath to diagnose cardiovascular diseases. The first thing to note is that we are not able to measure a single gas and relate it directly to the heart function. One valid reason for this is that the evolution of these gases may follow the same trend in different physiological or pathological processes. Another reason is the variability linked to external parameters. Therefore, for a gas with relatively high concentrations, a small variation linked to the pathology being studied will not necessarily be distinguished. In addition, in order to accurately define a biomarker, we need to be able to define a discriminating threshold for separating patients from a control group, as well as the tolerance range for this value. At the beginning of this project, we were interested in acetone concentrations in the exhaled breath, with the aim of finding a threshold that would allow us to separate people with heart failure from healthy people. The next part describes the different stages of this work.

5- How to: write a literature review and meta-analysis

Despite the positive results observed in many clinical studies, the measurement of the exhaled breath acetone has still not been approved for clinical practice. Different hypothesis suggests the high variability of the acetone with external parameters, the lack of reference values, the lack of large multicentric studies in heart failure or even the insufficient standardization in the procedures involving different detection techniques and breath sampling.

Performing a systematic review is a relevant approach to establish whether findings are consistent and can be generalized [78]. It allows the identification of factors of variability as well as normal values of a biomarker [79][80][81]. However, previous systematic reviews in exhaled acetone did not include HF patient studies, and did not perform a quantitative meta-analysis of the data [82][73]. Therefore, we aimed to systematically review the exhaled acetone concentrations from studies in healthy controls and heart failure (HF) patients and to meta-analyse them in order: (a) to quantify the heterogeneity of the breath acetone between published studies and to determine its normal range; (b) to identify factors of variability and relations with HF diagnosis and prognostic factors (New York Heart Association (NYHA) dyspnea, left ventricular ejection fraction (LVEF) and plasma BNP); (c) to provide pooled estimate of its diagnosis accuracy and prognosis performance. The prognosis of a disease is a parameter that helps understand the behaviour and predict its development, expectancy of improvement or regression in the medical condition: NYHA classifies the patients in four categories according to the extent of the heart failure, LVEF is the ability of the heart to pump blood to the rest of the body, the value is > 50% in a healthy heart and plasma BNP is measured from the blood, it is a hormone produced by the heart muscle, its value increases in case of heart failure.

5.1- Protocol and registration

Different guidelines have to be followed when reporting a systematic review and meta-analysis. Our review was performed following the 2020 Preferred Reporting Items for Systematic Reviews and Meta-analysis (PRISMA) statement and the protocol of our study was registered in the International Prospective Register of Systematic Reviews (PROSPERO ID: CRD42020192672). The review work team was composed of a cardiologist, a physiologist, a methodologist/statistician and two persons working on the development of a gas detection module.

5.2- Literature research

The literature research was conducted in English on PubMed and Web of Science to include papers published between 1991 and 2020. The collection work took place in May 2020. Additional published studies were added after analysis of reviews on the topic and on the basis of references in the articles we initially retrieved. Unpublished sources were not included. Medline Subject Headings (MeSH) database of Medline was used to define the exact keywords. A combination of the following MeSH terms was used:

'Acetone ***AND*** (Breath **OR** Exhaled **OR** Air **OR** Exhaled breath **OR** Airway) ***AND*** (Adults **OR** Patients **OR** Healthy volunteers **OR** Control groups)'.

To minimize information bias, the first step consists in screening the study titles and abstracts. Then, the full texts of the potentially eligible studies were retrieved to obtain the complete details for inclusion. Study selection was on the basis of agreement of the authors and, in cases of disagreement, the consensus of the authors was sought.

5.3- Study selection

Studies were included in the systematic review and meta-analysis if they met the PICOS inclusion criteria (Appendix A). We included every type of study reporting a measured concentration of acetone in the exhaled breath of subjects defined as adult HF patients or adult healthy subjects. The study type had to be clinical. Thus, a minimum of 15 subjects should be included in order to exclude laboratory validation studies. The design had to be comparative with acetone concentrations compared between healthy subjects and patients. Every type of analytic method was included in the study and the methodology had to be detailed. HF patients were defined according to the conclusion of a medical examination and echocardiography (showing LVEF < 50%) performed by a medical doctor. If information regarding the inclusion criteria were lacking in the study full text, the authors were contacted. If no answer was obtained the study was excluded. Duplicates were identified and removed from the analysis. In addition, we further identified studies eligible for the diagnostic and prognostic accuracy assessment, by adding the following criteria: (a)

an original comparative study including well defined populations of HF patients and healthy control and (b) providing receiver operating characteristic (ROC) curve analysis parameters (for a diagnostic marker) or providing survival analysis parameters (for a prognostic marker).

5.4- Data extraction

Studies providing charts only for acetone concentrations were included in the qualitative synthesis but not in the meta-analysis. If the breath sampling occurred in different conditions (sitting or lying down, during a workout, etc), only concentrations assessed at baseline was extracted. Data were extracted blindly and independently by the authors using a standardized form (Appendix B). When discrepancy occurred, the final data record was based on consensus. From the eligible articles, we extracted the acetone concentrations in volumic part per billion (ppbv) and the standard deviation (SD). To standardize the unit, acetone concentrations in $mol.L^{-1}$ or $g.L^{-1}$, were converted in ppbv, using the acetone molar volume and molecular molar mass (24.79 $L.mol^{-1}$ and 58 $g.mol^{-1}$ at $P = 1$ bar, $T = 25$ °C, respectively) and the following simple calculations:

$$[Acetone]\ (ppbv) = \left([Acetone](g.L^{-1}) \times \frac{24.79}{58}\right) \times 10^9 \quad (1.9)$$

$$[Acetone]\ (ppbv) = ([Acetone](mol.L^{-1}) \times 24.79) \times 10^9 \quad (1.10)$$

We also extracted age, sex ratio, body mass index, disease status, NYHA symptom classification of dyspnea, clinical state (stable/acute HF), LVEF (%), measurement method, sampling method, fasting state, smoking status and ventilatory procedure (breath-hold, control of expiratory flow, alveolar washout) because all these factors have been shown to modify the exhaled acetone concentration. When acetone concentrations showed discrepancies, authors were contacted by email to confirm the data. If no answer was obtained, the study was excluded from the meta-analysis.

5.5- Study quality assessment

As the selected studies were mostly observational with a cross-sectional design, the study quality was assessed using the journal's impact factor and discipline, the study's aim (clinical/sensor development), the 'selection' items of the Newcastle Ottawa Scale [83], the procedure of volunteer selection (medical examination), the inclusion/exclusion criteria, the description of the study's population (HF ethology, medications, and other characteristics). Finally, the risk of bias (selective reporting, etc) was assessed.

5.6- Statistical analysis

Quantitative data are presented as means ± standard deviation (SD) and means [95% confidence interval]. Median, min–max, SEM and interquartile range were converted according to Shoman et al [80]. If there were subgroups with different sample size (n_1, n_2, etc), data were pooled into a single group (sample size: n_{tot}) and the SD was calculated according to the following formula:

$$SD = \sqrt{\left(\left(\frac{n_1}{n_{tot}}\right)^2 \times SD_1^2\right) + \left(\left(\frac{n_2}{n_{tot}}\right)^2 \times SD_2^2\right) + \cdots} \quad (1.11)$$

Forest plots were used to graphically evaluate both the variability (i.e. SD) of the data and the weight of each study, according to its population size and variability. Statistical tests were performed by a statistician using R 4.0.3 software. The details of the different tests can be found in [72].

5.7- Results and discussion

The search equation performed in PubMed and Web of Science retrieved 375 and 907 articles, respectively. Figure 21 details the flow of studies included in the review. First, the study eligibility evaluation was performed on these 971 papers according to the title and abstract. The details of the reason of exclusion are given in the Appendix C. Thirty-nine studies were included for the qualitative synthesis and a final library of 18 studies (13 in healthy subjects and seven in HF patients) were included in the meta-analysis. Two studies have directly compared HF patients to healthy control and were included in the diagnostic and prognostic accuracy analysis [84][85]. Seven studies have compared exhaled acetone concentration in heathy controls to other patients (diabetes [74], [86], cancer patients [87], [88], respiratory [89], [90], or liver disease [91]). Nine studies were not comparative [92]–[99]. These studies involved 1842 subjects (883 healthy subjects and 1009 HF patients). The age, the sex, the origin as well as the smoking habits of the included subjects are given in [72].

To sum up, the concentration of acetone was compared between healthy subjects and heart failure patients. The results showed that the exhaled acetone was 1.89 higher in the patients' group. The effect of different parameters on the acetone concentration was assessed. However, no correlation between the smoking habits, the age or the gender was found with the exhaled acetone concentration. It is also important to note that our study showed an important heterogeneity between the results. Indeed, many detection techniques were used, some studies only analysed the end tidal air volume and some used on-line measurements while other performed off-line measurements. Heterogeneity is still observed between clinical studies while exhaled breath investigators are encouraged to used standardized procedures. It is not pertinent to develop this part in this manuscript, but an interesting

discussion about the diagnosis and prognosis potential of breath acetone has been proposed by the medical doctors working on this review [72].

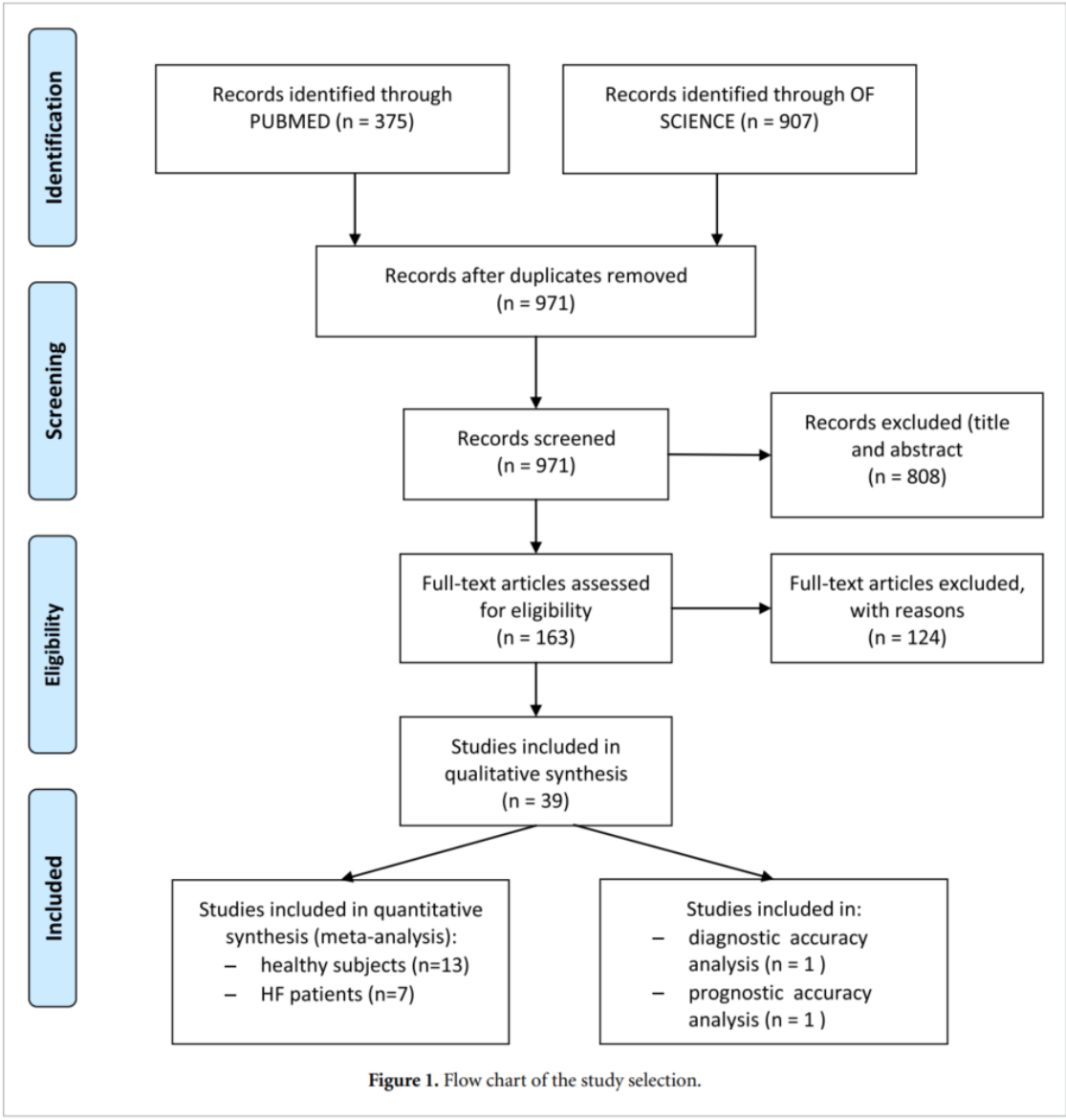

Figure 21: flow chart of the study selection. [72]

6- Exhaled breath values

For the four different gases, identified in this project and presenting a link with cardiovascular diseases, exhaled concentrations reported in the literature for patients and healthy control are presented in the Table 1. The objective of this table is to define different ranges of concentration that needs to be targeted in the development of a gas detection module. No study presenting exhaled NO concentration in patients has been found.

Table 1: Concentration of acetone, isoprene, CO and NO found in the litterature for healthy subjects and patients with cardiovascular diseases.

Ref	Gas	Study	Healthy concentration	Patients concentrations
[72]	Acetone	Systematic review and meta-analysis: breath acetone in heart failure vs healthy controls	412 (347-478) ppbv	1.89 times higher than healthy controls
[84]	Acetone	Exhaled acetone as biomarker of heart failure severity	< 496 ppbv	> 496 ppbv
[69]	Isoprene	Acute myocardial infraction	177.5 ± 25 ppbv (mean±SEM)	285 ± 30 ppbv
[100]	Isoprene	Healthy subjects	22 - 234 ppbv	
[26][101][28]	CO	Healthy smokers and non-smokers	1 – 3 ppmv > 6ppmv	
[102]	CO	Increased risk of cardiovascular disease		> 4 ppmv
[103][104][105]	NO	General review	0 – 25 ppbv	

7- Modelling the gas exchanges in the lung

A gradient of concentration is established between the species that are endogenously produced by the body and the airways encouraging the diffusion in the direction of the alveolar air. It is estimated that the composition of the alveolar air, thus the expired air, reflects the body metabolism and can be investigated in clinical practice, then, understanding the pattern followed by the gases diffusing between these two compartments is crucial.

Farhi [106] has proposed a first model depending on the blood/gas partition coefficient, the V'_A and the cardiac flow rate Q'_C. In this model, the lung is considered as one alveolus in contact with one capillary. The model predicted that the blood concentration of an inert gas is equal to its alveolar concentration assessed at the end of the exhalation. This model only considers gases coming from the circulation and taking part into the capillary/alveolar diffusion. Gases, such as it was presented for NO in section 4.2, that are produced in the airways are not included. Different teams have challenged Farhi's model by proposing a

representation of the total airways compartment. These models take into account the contribution of the airways to gas exchanges which is a more accurate representation of the reality. On one hand, King's model for exhaled isoprene represents the body in three different homogenous structures representing the alveolar compartment, a richly perfused compartment representing the tissue and peripheral tissue compartment accounting the storage of the isoprene (muscles). The perfusion and ventilation are described at rest for a healthy adult. This model is consistent with the experimental values of expired isoprene [59]. On the other hand, Ghorbani et al. have proposed a trumpet shape representation of the lung considering the conducting airways and the respiratory part including the respiratory bronchioles and the alveoli. This model proposed for exhaled CO has shown consistent results compared to real time assessment of CO concentration during one exhalation [107].

In this project, deep-learning techniques and the development of an AI are used to predict the evolution of a specific gas during a complete exhalation. This part is conducted in collaboration with the IDESP laboratory in Montpellier.

Conclusion

The composition of the exhaled breath depends on different factors that can be physiological, anatomical or pathological. The environment in which a subject is breathing also plays an important role on its expired air composition. The European Respiration Society (ERS) has published recommendations regarding the biomarkers of the lung diseases. These recommendations are relevant to any investigation of the exhaled breath. The lack of standardized procedures governing studies of the exhaled breath composition explains that some gases, presenting a strong correlation with physiological or pathological processes, cannot be assessed in clinical routine. In this chapter, the respiratory system was presented and the different factors involved in the modification of the expired air are identified. With this in mind, it is essential to correctly control these parameters by:

- Knowing the environment in which the subject is breathing: it helps defining a background in the assessment of the exhaled breath. This includes measurement of the humidity level, the smoke exposure and habits, the CO_2 concentration but also understanding the effect of the food consumption and beverage onto the expired air.
- Regulating the flow, the condition of the test (at rest or during a physical exercise) and the position of the subject (standing up, sitting, laying down) which constitute modifications factors of the perfusion and ventilation of the lungs, thus a modification of the expired air.

- Additional recommendation of the ERS prone the regulation of the sampling of the breath (on-line, off-line) and its storage but also the gas detection apparatus that sometimes tend to under- or overestimate the concentrations.

Over the years, teams working on gas detection have presented different types of sensors whose performances makes them suitable for use in a variety of applications such as environmental, industries or medical. What is expected in terms of performance? Depending on the application, good performances are achieved when the sensor is able to measure the lowest concentration of the gas of interest (sensitivity). A very important characteristic is also its selectivity: is this sensor able to detect one gas of interest, even if it is presented in a complex gas matrix? Finally, and if it is necessary, the sensor needs to be able to perform real time measurements, be compact in order to be transported on field and present an attractive price. Some sensors do indeed meet these criteria and are available on the today's market. In the next chapter, we will discuss the different sensors most commonly found on the market and their different characteristics.

References

[1] M. Ball, M. Hossain, and D. Padalia, "Anatomy, Airway.," Treasure Island (FL), 2023.

[2] R. M. Kacmarek and C. W. Mack, *Essentials of Respiratory Care*. Elsevier Health Sciences, 2005.

[3] H. T. Robertson, "Dead space: The physiology of wasted ventilation," *Eur. Respir. J.*, vol. 45, no. 6, pp. 1704–1716, 2015, doi: 10.1183/09031936.00137614.

[4] A. A. Siebens *et al.*, "Human Respiratory System," *Encyclopedia Britannica, https://www.britannica.com/science/human-respiratory-system.* .

[5] P. Gehr, M. Bachofen, and E. R. Weibel, "The normal human lung: ultrastructure and morphometric estimation of diffusion capacity," *Respir. Physiol.*, vol. 32, no. 2, pp. 121–140, 1978, doi: https://doi.org/10.1016/0034-5687(78)90104-4.

[6] E. R. Weibel *et al.*, "Morphometric model for pulmonary diffusing capacity. I. Membrane diffusing capacity.," *Respir. Physiol.*, vol. 93, no. 2, pp. 125–149, Aug. 1993, doi: 10.1016/0034-5687(93)90001-q.

[7] M. C. Ponce, A. Sankari, and S. Sharma, "Pulmonary Function Tests.," Treasure Island (FL), 2023.

[8] B. J. Delgado and T. Bajaj, "Physiology, Lung Capacity.," Treasure Island (FL), 2023.

[9] H. C. Robinson, "Respiratory Conditions Update: Restrictive Lung Disease.," *FP Essent.*, vol. 448, pp. 29–34, Sep. 2016.

[10] D. Singh *et al.*, "Global strategy for the diagnosis, management, and prevention of chronic obstructive lung disease: The GOLD science committee report 2019," *European Respiratory Journal*, vol. 53, no. 5. 2019, doi: 10.1183/13993003.00164-2019.

[11] J. Nagler and B. Krauss, "Capnography: A Valuable Tool for Airway Management," *Emerg. Med. Clin. North Am.*, vol. 26, no. 4, pp. 881–897, 2008, doi: 10.1016/j.emc.2008.08.005.

[12] L. J. Santos, J. Varon, L. Pic-Aluas, and A. H. Combs, "Practical uses of end-tidal carbon dioxide monitoring in the emergency department," *J. Emerg. Med.*, vol. 12, no. 5, pp. 633–644, 1994, doi: 10.1016/0736-4679(94)90416-2.

[13] K. Bhavani-shankar, H. Moseley, and Y. Delph, "Capnometry and anaesthesia," *Can. J. Anaesth.*, vol. 39, no. 6, pp. 617–632, 1992.

[14] R. E. O'Connor and R. A. Swor, "Verification of endotracheal tube placement following intubation," *Prehospital Emergency Care*, vol. 3, no. 3. pp. 248–250, 1999, doi: 10.1080/10903129908958945.

[15] B. Krauss and D. R. Hess, "Capnography for Procedural Sedation and Analgesia in the Emergency Department," vol. 50, no. 2, pp. 172–181, 2007, doi: 10.1016/j.annemergmed.2006.10.016.

[16] K. Bhavani-Shankar, A. Y. Kumar, H. S. L. Moseley, and R. Ahyee-Hallsworth, "Terminology and the current limitations of time capnography: A brief review," *Journal of Clinical Monitoring*, vol. 11, no. 3. pp. 175–182, 1995, doi: 10.1007/BF01617719.

[17] M. Yaron, P. Padyk, M. Hutsinpiller, and C. B. Cairns, "Utility of the expiratory capnogram in the assessment of bronchospasm," *Ann. Emerg. Med.*, vol. 28, no. 4,

pp. 403–407, 1996, doi: 10.1016/S0196-0644(96)70005-7.
[18] H. K. Chang, "Convection, diffusion and their interaction in the bronchial tree.," *Adv. Exp. Med. Biol.*, vol. 227, pp. 39–52, 1988, doi: 10.1007/978-1-4684-5481-9_4.
[19] E. O. Owens, "Endogenous carbon monoxide production in disease," *Clinical Biochemistry*, vol. 43, no. 15. Elsevier B.V., pp. 1183–1188, 2010, doi: 10.1016/j.clinbiochem.2010.07.011.
[20] H. Kitagishi and S. Minegishi, "Iron(II)porphyrin-cyclodextrin supramolecular complex as a carbon monoxide-depleting agent in living organisms," *Chemical and Pharmaceutical Bulletin*, vol. 65, no. 4. pp. 336–340, 2017, doi: 10.1248/cpb.c16-00767.
[21] R. Wang, Z. Wang, and L. Wu, "Carbon monoxide-induced vasorelaxation and the underlying mechanisms," in *Carbon Monoxide and Cardiovascular Functions*, Bristish Journal of Pharmacology, 1997.
[22] F. S. Cikach Jr. and R. A. Dweick, "Cardiovascular Biomarkers in Exhaled Breath," *Prog. Cardiovasc. Dis.*, vol. 55, no. 1, pp. 34–43, 2012, [Online]. Available: https://www.ncbi.nlm.nih.gov/pmc/articles/PMC3624763/pdf/nihms412728.pdf.
[23] P. Montuschi, S. A. Kharitonov, and P. J. Barnes, "Exhaled carbon monoxide and nitric oxide in COPD," *Chest*, vol. 120, no. 2, pp. 496–501, 2001, doi: 10.1378/chest.120.2.496.
[24] K. Zayasu, K. Sekizawa, S. Okinaga, M. Yamaya, T. Ohrui, and H. Sasaki, "Increased carbon monoxide in exhaled air of asthmatic patients," *Pneumologie*, vol. 52, no. 1, p. 33, 1998.
[25] B. S. Brouard *et al.*, "Carbon Monoxide Generated by Heme Oxygenase 1 Suppresses Endothelial Cell Apoptosis," vol. 192, no. 7, 2000.
[26] N. Maurin *et al.*, "First clinical evaluation of a quartz enhanced photo-acoustic CO sensor for human breath analysis," *Sensors Actuators, B Chem.*, vol. 319, no. April, p. 128247, 2020, doi: 10.1016/j.snb.2020.128247.
[27] M. F. Andersson and A. M. Møller, "Assessment of carbon monoxide values in smokers: A comparison of carbon monoxide in expired air and carboxyhaemoglobin in arterial blood," *Eur. J. Anaesthesiol.*, vol. 27, no. 9, pp. 812–818, 2010, doi: 10.1097/EJA.0b013e32833a55ea.
[28] S. W. Ryter and A. M. K. Choi, "Carbon monoxide in exhaled breath testing and therapeutics," *J. Breath Res.*, vol. 7, no. 1, 2013, doi: 10.1088/1752-7155/7/1/017111.
[29] A. Veronesi *et al.*, "Use of carboxyhemoglobin as a biomarker of environmental CO exposure: critical evaluation of the literature," *Environmental Science and Pollution Research*, vol. 24, no. 33. Environmental Science and Pollution Research, pp. 25798–25809, 2017, doi: 10.1007/s11356-017-0270-1.
[30] S. A. Kharitonov and P. J. Barnes, "Exhaled Markers of Pulmonary Disease," *Am. J. Respir. Crit. Care Med.*, vol. 163, no. 1, pp. 1693–1722, 2001.
[31] R. Ghorbani and F. M. Schmidt, "ICL-based TDLAS sensor for real-time breath gas analysis of carbon monoxide isotopes," *Opt. Express*, vol. 25, no. 11, p. 12743, 2017, doi: 10.1364/oe.25.012743.
[32] P. Biban, T. Zangardi, E. Baraldi, N. Dussini, L. Chiandetti, and F. Zacchello, "Mixed exhaled nitric oxide and plasma nitrites and nitrates in newborn infants," *Life Sci.*, vol. 68, no. 25, pp. 2789–2797, 2001, doi: 10.1016/S0024-3205(01)01086-4.

[33] C. M. St. Croix, T. J. Wetter, D. F. Pegelow, K. C. Meyer, and J. A. Dempsey, "Assessment of nitric oxide formation during exercise," *Am. J. Respir. Crit. Care Med.*, vol. 159, no. 4 I, pp. 1125–1133, 1999, doi: 10.1164/ajrccm.159.4.9806144.
[34] H. Y. Park *et al.*, "Dietary Arginine and Citrulline Supplements for Cardiovascular Health and Athletic Performance: A Narrative Review," *Nutrients*, vol. 15, no. 5, 2023, doi: 10.3390/nu15051268.
[35] M. Kelm, "Nitric oxide metabolism and breakdown," *Biochim. Biophys. Acta - Bioenerg.*, vol. 1411, no. 2–3, pp. 273–289, 1999, doi: 10.1016/S0005-2728(99)00020-1.
[36] F. T. Kaneko *et al.*, "Biochemical reaction products of nitric oxide as quantitative markers of primary pulmonary hypertension," *Am. J. Respir. Crit. Care Med.*, vol. 158, no. 3, pp. 917–923, 1998, doi: 10.1164/ajrccm.158.3.9802066.
[37] K. M. Dillon, R. J. Carrazzone, J. B. Matson, and K. Kashfi, "The evolving landscape for cellular nitric oxide and hydrogen sulfide delivery systems: A new era of customized medications.," *Biochem. Pharmacol.*, 2020.
[38] S. A. Kharitonov, D. Yates, R. A. Robbins, R. Logan-Sinclair, E. A. Shinebourne, and P. J. Barnes, "Increased nitric oxide in exhaled air of asthmatic patients," *Lancet*, vol. 343, no. 8890, pp. 133–135, 1994, doi: 10.1016/S0140-6736(94)90931-8.
[39] R. Zelis, S. H. Nellis, J. Longhurst, G. Lee, and D. T. Mason, "Abnormalities in the regional circulations accompanying congestive heart failure," *Prog. Cardiovasc. Dis.*, vol. 18, no. 3, pp. 181–199, 1975, doi: 10.1016/0033-0620(75)90010-9.
[40] D. S. Winlaw, G. A. Smythe, A. M. Keogh, C. G. Schyvens, P. M. Spratt, and P. S. Macdonald, "Increased nitric oxide failure production," 1994.
[41] N. Seshadri *et al.*, "Dysregulation of endogenous carbon monoxide and nitric oxide production in patients with advanced ischemic or nonischemic cardiomyopathy," *Am. J. Cardiol.*, vol. 92, no. 7, pp. 820–823, 2003, doi: 10.1016/S0002-9149(03)00890-7.
[42] L. E. Gustafsson, A. M. Leone, M. G. Persson, N. P. Wiklund, and S. Moncada, "Endogenous nitric oxide is present in the exhaled air of rabbits, guinea pigs and humans," *Biochem. Biophys. Res. Commun.*, vol. 181, no. 2, pp. 852–857, 1991, doi: 10.1016/0006-291X(91)91268-H.
[43] N. M. Grob and R. A. Dweik, "Exhaled nitric oxide in asthma. From diagnosis, to monitoring, to screening: are we there yet?," *Chest*, vol. 133, no. 4. United States, pp. 837–839, Apr. 2008, doi: 10.1378/chest.07-2743.
[44] L. S. Petralia *et al.*, "Accurate real-time F E NO expirograms using complementary optical sensors," *J. Breath Res.*, 2020, doi: 10.1088/1752-7163/ab9c31.
[45] L. A. Rolim *et al.*, "Nitric oxide in upper airways inflammatory diseases," *Nature*, vol. 388. pp. 539–547, 2020.
[46] E. Weitzberg and J. O. N. Lundberg, "Humming greatly increases nasal nitric oxide," *Am. J. Respir. Crit. Care Med.*, vol. 166, no. 2, pp. 144–145, 2002, doi: 10.1164/rccm.200202-138BC.
[47] D. Romanini, I. Ventrillard, G. Méjean, J. Morville, and E. Kerstel, "Introduction to Cavity Enhanced Absorption Spectroscopy," in *Cavity-Enhanced Spectroscopy and Sensing*, G. Gagliardi and H.-P. Loock, Eds. Berlin, Heidelberg: Springer Berlin Heidelberg, 2014, pp. 1–60.
[48] G. D. Thurston, "Outdoor Air Pollution: Sources, Atmospheric Transport, and Human Health Effects," *Int. Encycl. Public Heal.*, no. 2002, pp. 367–377, 2016, doi:

10.1016/B978-0-12-803678-5.00320-9.
[49] C. Y. Lin, L. W. Chen, and L. T. Wang, "Correlation of black smoke and nitrogen oxides emissions through field testing of in-use diesel vehicles," *Environ. Monit. Assess.*, vol. 116, no. 1–3, pp. 291–305, 2006, doi: 10.1007/s10661-006-7402-2.
[50] K. Torén, N. Murgia, L. Schiöler, B. Bake, and A. C. Olin, "Reference values of fractional excretion of exhaled nitric oxide among non-smokers and current smokers," *BMC Pulm. Med.*, vol. 17, no. 1, pp. 1–7, 2017, doi: 10.1186/s12890-017-0456-9.
[51] D. C. Chambers, W. S. Tunnicliffe, and J. G. Ayres, "Acute inhalation of cigarette smoke increases lower respiratory tract nitric oxide concentrations," *Thorax*, vol. 53, no. 8, pp. 677–679, 1998, doi: 10.1136/thx.53.8.677.
[52] C. G. H. Williams, "IV. On isoprene and caoutchine," 1860.
[53] M. Arashiro *et al.*, "Effect of secondary organic aerosol from isoprene-derived hydroxyhydroperoxides on the expression of oxidative stress response genes in human bronchial epithelial cells," *Environmental Science: Processes and Impacts*, vol. 20, no. 2. pp. 332–339, 2018, doi: 10.1039/c7em00439g.
[54] T. D. Sharkey, E. L. Singsaas, P. J. Vanderveer, and C. Geron, "Field measurements of isoprene emission from trees in response to temperature and light," *Tree Physiol.*, vol. 16, no. 7, pp. 649–654, 1996, doi: 10.1093/treephys/16.7.649.
[55] P. Mochalski, J. King, C. A. Mayhew, and K. Unterkofler, "A review on isoprene in human breath," *Journal of Breath Research*, vol. 17, no. 3. p. 037101, Jul. 01, 2023, doi: 10.1088/1752-7163/acc964.
[56] D. Gelmont, R. A. Stein, and J. F. Mead, "Isoprene - The main hydrocarbon in human breath," *Biochem. Biophys. Res. Commun.*, vol. 99, no. 4, pp. 1456–1460, 1981, doi: 10.1016/0006-291X(81)90782-8.
[57] K. V Krishnaiah, V. C. Joshi, and T. Ramasarma, "Effect of Dietary Cholesterol and Ubiquinone on lsoprene Synthesis in Rat Liver," *Arch. Biochem. Biophys.*, 1967.
[58] T. Karl *et al.*, "Human breath isoprene and its relation to blood cholesterol levels: New measurements and modeling," *J. Appl. Physiol.*, vol. 91, no. 2, pp. 762–770, 2001, doi: 10.1152/jappl.2001.91.2.762.
[59] J. King *et al.*, "Physiological modeling of isoprene dynamics in exhaled breath," *J. Theor. Biol.*, vol. 267, no. 4, pp. 626–637, 2010, doi: 10.1016/j.jtbi.2010.09.028.
[60] J. King *et al.*, "Isoprene and acetone concentration profiles during exercise on an ergometer," *J. Breath Res.*, vol. 3, no. 2, 2009, doi: 10.1088/1752-7155/3/2/027006.
[61] J. van den Broek *et al.*, "Selective monitoring of breath isoprene by a portable detector during exercise and at rest," *Sensors Actuators B Chem.*, vol. 357, Apr. 2022, doi: 10.1016/j.snb.2022.131444.
[62] W. Lindinger, A. Hansel, and A. Jordan, "On-line monitoring of volatile organic compounds at pptv levels by means of Proton-Transfer-Reaction Mass Spectrometry (PTR-MS) Medical applications, food control and environmental research," *Int. J. Mass Spectrom. Ion Process.*, vol. 173, no. 3, pp. 191–241, 1998, doi: 10.1016/s0168-1176(97)00281-4.
[63] D. Smith, P. Španěl, B. Enderby, W. Lenney, C. Turner, and S. J. Davies, "Isoprene levels in the exhaled breath of 200 healthy pupils within the age range 7-18 years studied using SIFT-MS," *J. Breath Res.*, vol. 4, no. 1, 2010, doi: 10.1088/1752-7155/4/1/017101.
[64] E. Capodicasa *et al.*, "Volatile alkanes and increased concentrations of isoprene in

exhaled air during hemodialysis," *Nephron*, vol. 82, no. 4, pp. 331–337, 1999, doi: 10.1159/000045448.
[65] S. Davies, P. Španel, and D. Smith, "A new 'online' method to measure increased exhaled isoprene in end-stage renal failure," *Nephrol. Dial. Transplant.*, vol. 16, no. 4, pp. 836–839, 2001, doi: 10.1093/ndt/16.4.836.
[66] A. Bajtarevic *et al.*, "Noninvasive detection of lung cancer by analysis of exhaled breath," *BMC Cancer*, vol. 9, p. 348, 2009, doi: 10.1186/1471-2407-9-348.
[67] S. S. Sehnert, L. Jiang, J. F. Burdick, and T. H. Risby, "Breath biomarkers for detection of human liver diseases: Preliminary study," *Biomarkers*, vol. 7, no. 2, pp. 174–187, 2002, doi: 10.1080/13547500110118184.
[68] I. Kushch *et al.*, "Breath isoprene - Aspects of normal physiology related to age, gender and cholesterol profile as determined in a proton transfer reaction mass spectrometry study," *Clin. Chem. Lab. Med.*, vol. 46, no. 7, pp. 1011–1018, 2008, doi: 10.1515/CCLM.2008.181.
[69] S. Mendis, P. A. Sobotka, and D. E. Euler, "Expired hydrocarbons in patients with acute myocardial infarction," *Free Radic. Res.*, vol. 23, no. 2, pp. 117–122, 1995, doi: 10.3109/10715769509064026.
[70] L. T. McGrath, P. Patrick, and B. Silke, "Breath isoprene in patients with heart failure," *Eur. J. Heart Fail.*, vol. 3, no. 4, pp. 423–427, 2001, doi: 10.1016/S1388-9842(01)00128-3.
[71] R. G. R. Mooli and S. K. Ramakrishnan, "Emerging Role of Hepatic Ketogenesis in Fatty Liver Disease," *Front. Physiol.*, vol. 13, no. July, pp. 1–14, 2022, doi: 10.3389/fphys.2022.946474.
[72] F. Gouzi, D. Ayache, C. Hédon, N. Molinari, and A. Vicet, "Breath acetone concentration: Too heterogeneous to constitute a diagnosis or prognosis biomarker in heart failure? A systematic review and meta-analysis," *J. Breath Res.*, vol. 16, no. 1, p. 16001, 2022, doi: 10.1088/1752-7163/ac356d.
[73] V. Saasa, T. Malwela, M. Beukes, M. Mokgotho, C. P. Liu, and B. Mwakikunga, "Sensing technologies for detection of acetone in human breath for diabetes diagnosis and monitoring," *Diagnostics*, vol. 8, no. 1, pp. 1–17, 2018, doi: 10.3390/diagnostics8020012.
[74] W. Li *et al.*, "A cross-sectional study of breath acetone based on diabetic metabolic disorders," *J. Breath Res.*, vol. 9, no. 1, p. 16005, 2015, doi: 10.1088/1752-7155/9/1/016005.
[75] V. Saasa, M. Beukes, Y. Lemmer, and B. Mwakikunga, "Blood ketone bodies and breath acetone analysis and their correlations in type 2 diabetes mellitus," *Diagnostics*, vol. 9, no. 4, 2019, doi: 10.3390/diagnostics9040224.
[76] M. E. O'Hara, S. O'Hehir, S. Green, and C. A. Mayhew, "Development of a protocol to measure volatile organic compounds in human breath: A comparison of rebreathing and on-line single exhalations using proton transfer reaction mass spectrometry," *Physiol. Meas.*, vol. 29, no. 3, pp. 309–330, 2008, doi: 10.1088/0967-3334/29/3/003.
[77] P. Mochalski *et al.*, "Non-contact breath sampling for sensor-based breath analysis," *J. Breath Res.*, vol. 13, no. 3, p. 36001, 2019, doi: 10.1088/1752-7163/ab0b8d.
[78] M. M. G. Leeflang, "Systematic reviews and meta-analyses of diagnostic test accuracy," *Clin. Microbiol. Infect.*, vol. 20, no. 2, pp. 105–113, 2014, doi: 10.1111/1469-0691.12474.

[79] L. Siegel, M. H. Murad, and H. Chu, "Estimating the reference range from a meta-analysis," *Res. Synth. Methods*, vol. 12, no. 2, pp. 148–160, 2021, doi: 10.1002/jrsm.1442.
[80] Y. Shoman *et al.*, "Reference ranges of 8-isoprostane concentrations in exhaled breath condensate (Ebc): A systematic review and meta-analysis," *Int. J. Mol. Sci.*, vol. 21, no. 11, 2020, doi: 10.3390/ijms21113822.
[81] F. Gouzi *et al.*, "Reference values for vastus lateralis fiber size and type in healthy subjects over 40 years old: A systematic review and metaanalysis," *J. Appl. Physiol.*, vol. 115, no. 3, pp. 346–354, 2013, doi: 10.1152/japplphysiol.01352.2012.
[82] J. C. Anderson, "Measuring breath acetone for monitoring fat loss: Review," *Obesity*, vol. 23, no. 12, pp. 2327–2334, 2015, doi: 10.1002/oby.21242.
[83] C. Luchini, B. Stubbs, M. Solmi, and N. Veronese, "Assessing the quality of studies in meta-analyses: Advantages and limitations of the Newcastle Ottawa Scale," *World J. Meta-Analysis*, vol. 5, no. 4, p. 80, 2017, doi: 10.13105/wjma.v5.i4.80.
[84] F. G. Marcondes-Braga *et al.*, "Exhaled acetone as a new biomarker of heart failure severity," *Chest*, vol. 142, no. 2, pp. 457–466, 2012, doi: 10.1378/chest.11-2892.
[85] M. Kupari, J. Lommi, M. Ventilä, and U. Karjalainen, "Breath acetone in congestive heart failure," *Am. J. Cardiol.*, vol. 76, no. 14, pp. 1076–1078, 1995, doi: 10.1016/S0002-9149(99)80304-X.
[86] M. G. Zhou *et al.*, "Investigation and identification of breath acetone as a potential biomarker for type 2 diabetes diagnosis," *Chinese Sci. Bull.*, vol. 59, no. 17, pp. 1992–1998, 2014, doi: 10.1007/s11434-014-0244-3.
[87] H. Ma *et al.*, "Analysis of human breath samples of lung cancer patients and healthy controls with solid-phase microextraction (SPME) and flow-modulated comprehensive two-dimensional gas chromatography (GC × GC)," *Anal. Methods*, vol. 6, no. 17, pp. 6841–6849, 2014, doi: 10.1039/c4ay01220h.
[88] A. Ulanowska, T. Kowalkowski, E. Trawińska, and B. Buszewski, "The application of statistical methods using VOCs to identify patients with lung cancer," *J. Breath Res.*, vol. 5, no. 4, 2011, doi: 10.1088/1752-7155/5/4/046008.
[89] M. Barker *et al.*, "Volatile organic compounds in the exhaled breath of young patients with cystic fibrosis," *Eur. Respir. J.*, vol. 27, no. 5, pp. 929–936, 2006, doi: 10.1183/09031936.06.00085105.
[90] M. E. Dolch *et al.*, "Quantification of propionaldehyde in breath of patients after lung transplantation," *Free Radic. Biol. Med.*, vol. 85, pp. 157–164, 2015, doi: 10.1016/j.freeradbiomed.2015.04.003.
[91] S. Van den Velde, F. Nevens, P. Van hee, D. van Steenberghe, and M. Quirynen, "GC-MS analysis of breath odor compounds in liver patients," *J. Chromatogr. B Anal. Technol. Biomed. Life Sci.*, vol. 875, no. 2, pp. 344–348, 2008, doi: 10.1016/j.jchromb.2008.08.031.
[92] T. Yokokawa *et al.*, "Exhaled acetone concentration is related to hemodynamic severity in patients with non-ischemic chronic heart failure," *Circ. J.*, vol. 80, no. 5, pp. 1178–1186, 2016, doi: 10.1253/circj.CJ-16-0011.
[93] D. Biagini *et al.*, "Determination of volatile organic compounds in exhaled breath of heart failure patients by needle trap micro-extraction coupled with gas chromatography-tandem mass spectrometry," *J. Breath Res.*, vol. 11, no. 4, 2017, doi: 10.1088/1752-7163/aa94e7.
[94] G. Wang, G. Maranelli, L. Perbellini, E. Raineri, and F. Brugnone, "Blood acetone

concentration in 'normal people' and in exposed workers 16 h after the end of the workshift," *Int. Arch. Occup. Environ. Health*, vol. 65, no. 5, pp. 285–289, 1994, doi: 10.1007/BF00405690.

[95] D. E. Euler, S. J. Davé, and H. Guo, "Effect of cigarette smoking on pentane excretion in alveolar breath," *Clin. Chem.*, vol. 42, no. 2, pp. 303–308, 1996, doi: 10.1093/clinchem/42.2.303.

[96] C. Turner, P. Španěl, and D. Smith, "A longitudinal study of ammonia, acetone and propanol in the exhaled breath of 30 subjects using selected ion flow tube mass spectrometry, SIFT-MS," *Physiol. Meas.*, vol. 27, no. 4, pp. 321–337, 2006, doi: 10.1088/0967-3334/27/4/001.

[97] K. Schwarz *et al.*, "Breath acetone - Aspects of normal physiology related to age and gender as determined in a PTR-MS study," *J. Breath Res.*, vol. 3, no. 2, 2009, doi: 10.1088/1752-7155/3/2/027003.

[98] F. G. Marcondes-Braga *et al.*, "Exhaled breath acetone for predicting cardiac and overall mortality in chronic heart failure patients," *ESC Hear. Fail.*, vol. 7, no. 4, pp. 1744–1752, 2020, doi: 10.1002/ehf2.12736.

[99] M. A. Samara *et al.*, "Single exhaled breath metabolomic analysis identifies unique breathprint in patients with acute decompensated heart failure," *J. Am. Coll. Cardiol.*, vol. 61, no. 13, pp. 1463–1464, 2013, doi: 10.1016/j.jacc.2012.12.033.

[100] P. Španěl, S. Davies, and D. Smith, "Quantification of breath isoprene using the selected ion flow tube mass spectrometric analytical method," *Rapid Commun. Mass Spectrom.*, vol. 13, no. 17, pp. 1733–1738, 1999, doi: 10.1002/(SICI)1097-0231(19990915)13:17<1733::AID-RCM707>3.0.CO;2-S.

[101] M. Underner and G. Peiffer, "[Interpretation of exhaled CO levels in studies on smoking].," *Rev. Mal. Respir.*, vol. 27, no. 4, pp. 293–300, Apr. 2010, doi: 10.1016/j.rmr.2009.09.004.

[102] S. Cheng *et al.*, "Association of exhaled carbon monoxide with subclinical cardiovascular disease and their conjoint impact on the incidence of cardiovascular outcomes," *Eur. Heart J.*, vol. 35, no. 42, pp. 2980–2987, 2014, doi: 10.1093/eurheartj/ehu052.

[103] S. Duong-Quy, N. N. Le-Dong, T. Hua-Huy, and A. T. Dinh-Xuan, "Measurement of exhaled nitric oxide (NO) as a marker of airway inflammation," *J. Funct. Vent. Pulmonol.*, vol. 4, no. 11, pp. 16–22, 2013, doi: 10.12699/jfvp.4.11.2013.16.

[104] P. Ma *et al.*, "Non-invasive exhaled breath diagnostic and monitoring technologies," *Microw. Opt. Technol. Lett.*, vol. 65, no. 5, SI, pp. 1475–1488, 2023, doi: 10.1002/mop.33133.

[105] I. van der Lee, J. M. M. van den Bosch, and P. Zanen, "Reduction of variability of exhaled nitric oxide in healthy volunteers," *Respir. Med.*, vol. 96, no. 12, pp. 1014–1020, 2002, doi: 10.1053/rmed.2002.1390.

[106] L. E. Farhi, "Elimination of inert gas by the lung.," *Respir. Physiol.*, vol. 3, no. 1, pp. 1–11, Aug. 1967, doi: 10.1016/0034-5687(67)90018-7.

[107] R. Ghorbani and F. M. Schmidt, "Fitting of single-exhalation profiles using a pulmonary gas exchange model - Application to carbon monoxide," *J. Breath Res.*, vol. 13, no. 2, 2019, doi: 10.1088/1752-7163/aafc91.

Chapter 2
Gas sensors for breath analysis

Different gas detection techniques and their features are presented. This involves electrochemical, metal oxide semiconductors (MOS) and non-dispersive infrared (NDIR) sensors that are widely present on the market and used for breath analysis. A focus is made on the infrared domain (IR) and photoacoustic based techniques used to perform gas detection and breath investigation demonstrated in this manuscript.

The performance of a gas sensor can be defined according to the application for which it is intended. For example, a sensor may be suitable for detecting high concentrations of gas in the environment and be characterised as a "good" sensor, while the same characteristics may not be sufficient for breath analysis applications. Then, what is expected in terms of performance for this medical application? In the Chapter 1, the composition of exhaled air was presented as a complex matrix of gases that varies according to intrinsic parameters, such as the anatomy, the physiology or the metabolism of a subject, or extrinsic parameters, such as the environment in which a subject is evolving. In addition, the four different exhaled biomarkers defined for the diagnosis of cardiovascular disease (CVD) are present in very low concentration ranging from the part per million (ppmv) to the part per billion (ppbv). Consequently, the sensor dedicated to the detection of these species needs to be **selective** in order to separate them from other species of the exhaled breath. The sensor must also be **sensitive** enough to detect the lowest concentration of the gas of interest. Finally, the sensor has to perform **real-time** measurements as one of the objectives of this project is to propose a complete expirogram for each species.

1- Gas detection techniques

1.1- Mass spectrometry-based sensors

Gas chromatography combined with mass spectrometry (GC-MS) is a technique that was invented in the 1950s, mostly used in chemistry for the identification and the quantification of gaseous compounds [1]. As suggested by its name, two main features compose the detection block: a gas chromatography (GC), that separates the gases composing the mixture according to their affinity with a stationary phase, and a mass spectrometer (MS) that separates the different analytes into ions and enables their identification using their mass-to-charge ratio. These two combined processes result into extremely good limit of detections, in the part per trillion (pptv) range and a highly selective detection technique even if this parameter can be affected by relatively close compounds or isomers leading to

false positive or negatives. For these reasons, GC-MS has been defined as the gold standard in terms of gas detections and analysis. Nevertheless, one of the main drawbacks of this technique is the preconcentration step that is necessary when working with complex gas matrixes [2]. Thus, this step is added to enhance the selectivity of the technique. It consists of using different procedures in order to separate the gas of interest from its environment. In complex gas mixtures such as the expired air, added such a step makes the on-line and real-time measurement not practicable.

According to what has been defined in the previous paragraph, GC-MS technique could match the expectancy in terms of sensitivity for the breath analysis but the real-time and on-line characteristics remain hard to achieve, therefore reconstructing the complete expirogram of one exhaled gas using GC-MS is practically impossible.

Three group of sensors dominate the market according to Yole group's (Figure 1): Electrochemical, MOS and NDIR. In the next sections, the different types of sensors as well as their characteristics and limitations are described.

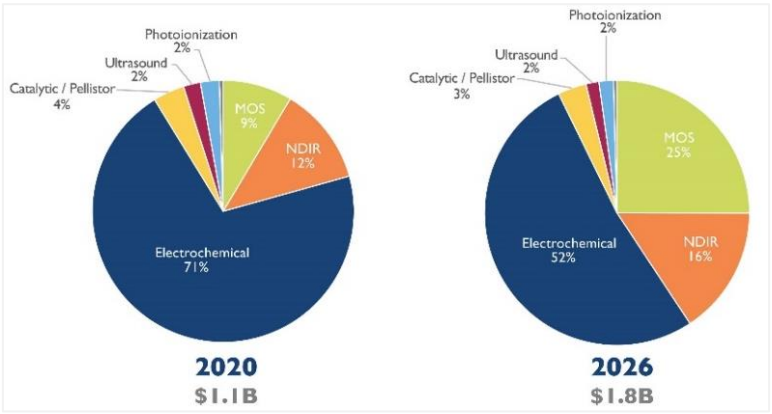

Figure 1: Market of gas sensors [3]

1.2- Electrochemical sensors

The working principle of these sensors is simple (Figure 2): a chemical reaction is converted into an electrical signal. The chemical compounds (gases in this case) enter the sensor through a capillary barrier and a hydrophobic membrane. These two elements prevent dust from entering the sensor and trap the water outside while keeping the electrolyte inside the sensor. When contacting the sensing electrode, the gas is reduced or oxidized. This reaction produces charges that are transmitted through the electrodes to an amplification system and further analysed [4].

Generally, the life expectancy for electrochemical sensors lies between one to three years depending on the consumption of the electrode and the environment conditions in which the sensor is operating. Indeed, these types of sensors are somehow sensitive to difference

of temperature and are unable to operate in severe conditions that happen to affect their response time. For most commercially available models, the minimum operating temperature ranges close to -10°C. Besides this, electrochemical devices benefit from a low power consumption, high potential of miniaturisation and a wireless design. Without being extremely sophisticated they also offer a great reliability, linearity (displays real-zero when no target gas is present) and selectivity in the measurement. The selectivity of these sensors is defined by the sensing electrode that is especially chosen for one species. However, other gases causing the same reactions could lead to interference in the measurement. Low detection limits in the part per billion range were demonstrated with electrochemical sensor targeting isoprene in the exhaled breath [5] but also in environmental applications [6]. The response time of electrochemical sensors is around few seconds which make them unsuitable for real time measurements.

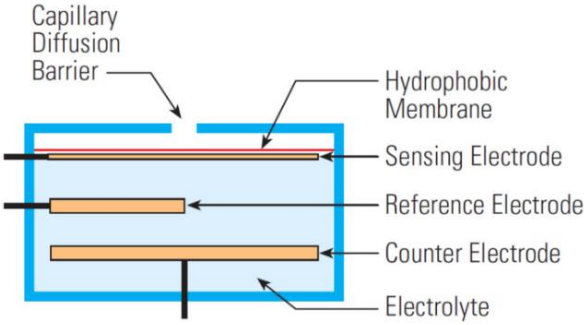

Figure 2: typical –amperometric– electrochemical sensor: composed of a sensing electrode reacting with the gas of interest, a reference electrode, that impose a minimum voltage to the sensing electrode and a counter electrode, that balances the sensing electrode's reactions, all separated with an electrolyte [7].

1.3- MOS sensors

The working principle of these sensors is based on a reversible adsorption of the target gas on the surface of the heated metal oxide. The reaction of the chemical compound (gases in this case) is usually an oxidation that results in a change of the resistance of the oxide surface (Figure 3). The variation of the resistance is measured by the mean of simple electronic circuits and is related to the concentration of deposited gases [4].

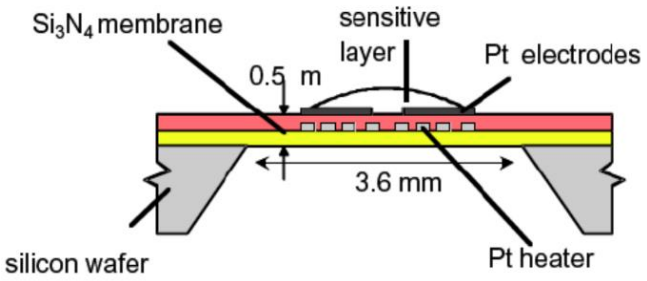

Figure 3: Metal oxide semiconductor sensor with a sensitive layer deposited on a silicon wafer. [8]

Compared to electrochemical sensors, the main advantages of MOS sensors are [9]:

- Their sensitivity,
- The high life expectancy, integration and low cost.

The main issue is related to the poor selectivity when in presence of interferents. In addition, the sensing element must be heated to operating temperatures ranging between 100 and 500°C. The cost of operating in this range of temperature is the power consumption that is relatively high: generally, approximately 1 W is specified for commercial products.

Many studies have reported the assessment of breath analysis in diabetes and lung cancers with MOS sensors presenting detection limits in the ppbv range [10], [11]. However, the slow response and recovery time makes these sensors impossible to use in real-time application or during rapid changes of concentrations.

1.4- NDIR sensors

The working principle of these sensors is completely different from the previously presented ones. Basically, it is based on the absorption of light by molecules present in the medium and as their name suggests, this phenomenon is applied to the IR domain. Before presenting NDIR sensors, the IR domain characterized by a large range of molecules absorbing at specific wavelength, has to be described.

1.4-1. The infrared domain

The light spectrum has been divided in different regions: the visible domain, typically between 380 and 780 nm, is surrounded by the Ultra-Violet (UV) at smaller wavelength and the infrared (IR) at higher wavelength. The infrared region is defined by three sub-regions (Figure 4):

- SWIR: Short Wave InfraRed, between 0.8 and 3 µm,
- MWIR: Medium Wave InfraRed, between 3 and 5 µm,
- LWIR: Long Wave InfraRed, between 8 and 14 µm,

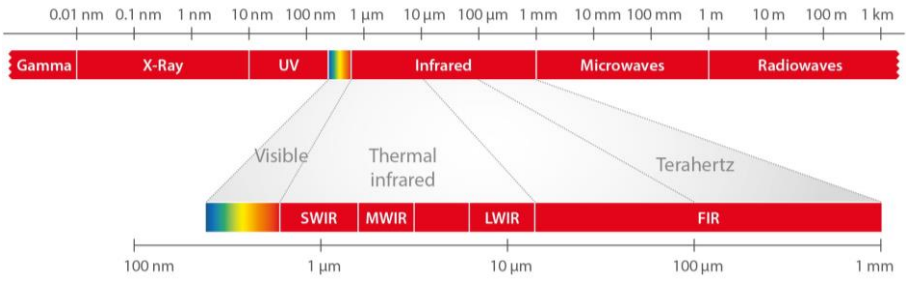

Figure 4: Ranges within the electromagnetic spectrum. [12]

The IR is characterized by multiple and intense gas absorption lines interesting for industrial, medical and environmental applications (Figure 5). The energy accumulated from the absorption of light is returned to the medium through a non-radiative process [13]. These absorption shapes and wavelengths are very specific to each species, they are usually defined as the fingerprint of the molecules. The IR region also contains different atmospheric transmission windows that are attractive for applications such as free-space communications [14].

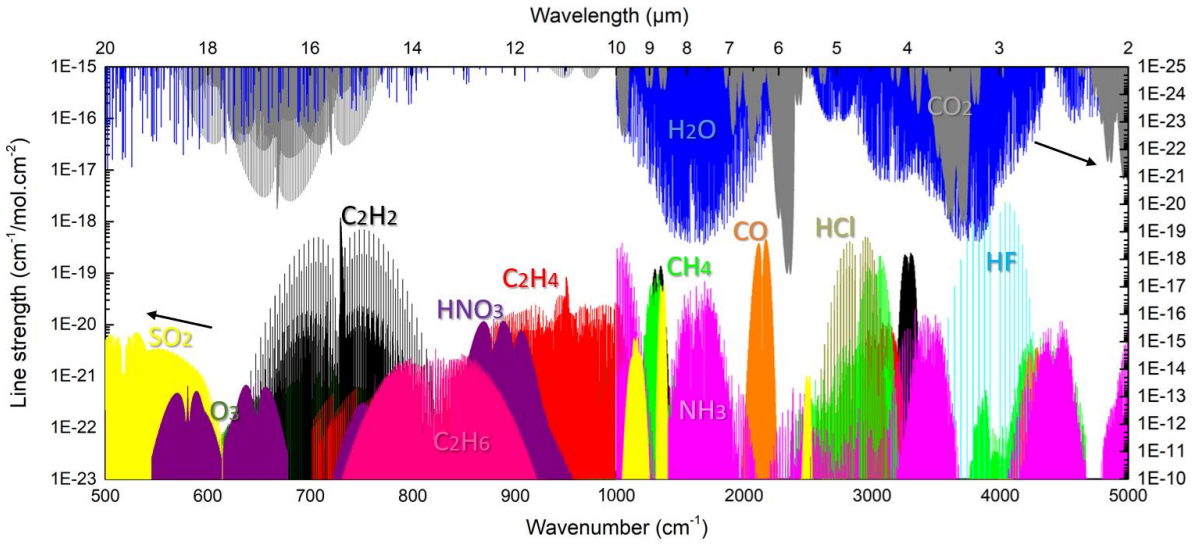

Figure 5: Various gas absorption lines between 2 and 20 µm. [15]

1.4-2. Line broadening

The shape of the absorption lines is modelled by different effects [16]:

- The natural broadening: this effect is always present and is related to the lifetime of excited states. It is described as homogenous as it has the same effect on all molecules and results in a Lorentzian profile. The natural broadening is observed for electronic transitions thus, it is never observed for vibrational-rotational transitions occurring in the IR. In this domain, the broadening is mainly due to the phenomena described below.
- The Doppler broadening: its effect on the line shape is dominant at low pressure (< 10 Torr). The Doppler broadening is related to the motion of the molecule caused by thermal excitations (Brownian motion). It results in a random shift of the frequency and is described as a Gaussian:

$$f_G(\sigma - \sigma_{ij}, p, T) = \frac{1}{\gamma_G(p,T)}\sqrt{\frac{\ln(2)}{\pi}}\, e^{\left(-\ln(2)\left(\frac{\sigma-\sigma_{ij}}{\gamma_G(p,T)}\right)^2\right)}. \qquad (2.1)$$

Where, f_G is the line shape function depending on p, the pressure and T, the temperature. $\sigma = \frac{1}{\lambda}$ (cm^{-1}) is the wavenumber, ij designates an energy transition from the state i to j and γ_G is the linewidth of the Doppler broadening given by:

$$\gamma_G = \frac{\sigma_{ij}}{c}\left(2\ln(2)\frac{kT}{m}\right)^{\frac{1}{2}}. \tag{2.2}$$

Where c is the light speed $(m.s^{-1})$, m is the mass of the target species (kg) and k is the Boltzmann constant.

- The collisional broadening: in atmospheric conditions of temperature and pressure in the IR, this effect is dominant and can be described as a Lorentzian profile:

$$f_L(\sigma - \sigma_{ij}, p, T) = \frac{1}{\pi}\frac{\gamma_L(p,T)}{\gamma_L^2(p,T) + (\sigma - \sigma_{ij})^2}. \tag{2.3}$$

Where, γ_L is the linewidth of the Lorentzian line shape calculated by considering each s species present in the gas sample:

$$\gamma_L(p,T) = \sum_s \gamma_{L,s}^0 \frac{p_s}{p_0}\left(\frac{T_0}{T}\right)^{n_s}. \tag{2.4}$$

With $\gamma_{L,s}^0$ the broadening due to the specie s at p_0 and T_0, p_s the partial pressure of the specie and n_s a temperature dependant coefficient, close to 0.5.

The convolution of the Gaussian and Lorentzian profile results in the Voigt profile, even if at ambient temperature and pressure, the Lorentzian shape is a sufficient approximation of the absorption broadening.

1.4-3. Molecular absorption spectra

It is relatively straightforward to have access to a wide range of absorption lines defined for various molecules. For example, HITRAN database covers the whole IR domain (and UV parts) and reconstructs the absorption spectra for a large range of molecules such as water, carbon dioxide, carbon monoxide, ethylene, methane, etc [15]. Cross-sections, measured experimentally, are also available for more complex molecules such as acetone or BTEXs (benzene, toluene, ethylbenzene and xylene) [15]. However, not all molecules, including homo-nuclear molecules as N_2, absorb in the infrared.

Typically, using HITRAN it is possible to modelise the absorption or the transmission (in %) of a chosen molecule. The transmittance is described by the Beer-Lambert law as:

$$T(\sigma) = \frac{I_t(\sigma)}{I_0(\sigma)} = e^{-\alpha(\sigma)L}. \tag{2.5}$$

With I_0 the emitted intensity of a monochromatic light source and I_t the intensity of light transmitted after passing through an absorbing gas sample, α is the absorption coefficient and L the length of the absorbing path (m).

In the case where $\alpha L \ll 1$, Equation (2.5) can be linearized as:

$$T(\sigma) = 1 - \alpha(\sigma)L = 1 - A(\sigma). \tag{2.6}$$

And knowing that:

$$\alpha(\sigma) = N \cdot k_v(\sigma) \tag{2.7}$$

with N, the number density in $molecule/cm^3$ and k_v the absorption cross section in $cm^2/molecule$ defined for a molecular transition ij as:

$$k_{v,ij}(\sigma, p, T) = S_{ij}(T) f\big(\sigma - \sigma_{ij}, p, T\big). \tag{2.8}$$

With S_{ij} is the line strength in $\frac{cm^{-1}}{molecule \cdot cm^{-2}}$, f is the line shape described in section 1.4-2.

In a gas matrix composed of multiple gases, the mixture ratio of the specie involved in the light absorption process is calculated as:

$$C = \frac{N}{N_0} \tag{2.9}$$

With N_0 the total number of molecules in the mixture in $molecule/cm^3$ defined for a certain temperature T and pressure p as:

$$N_0(p, T) = \frac{p}{p_0}\frac{T_0}{T}\frac{N_A}{V_0} \tag{2.10}$$

Where p_0 and T_0 are the standard pressure and temperature, V_0 is the molar volume of an ideal gas and N_A is the Avogadro constant.

For an easier reading, the mixture ratio is called "concentration" in the rest of the manuscript.

In the previous parts of this manuscript, the ppmv and ppbv units were used to quantify the concentration of a target gas. From Equation (2.9), the concentration in ppmv or ppbv can be expressed as:

$$C_{ppmv} = \frac{N}{N_0} 10^6 \tag{2.11}$$

And,

$$C_{ppbv} = \frac{N}{N_0} 10^9 \tag{2.12}$$

1.4-4. NDIR sensors

The simplest detection technique based on the molecular absorption is the direct absorption. This technique is easily described by the Beer-Lambert law (Equation (8)). A light source characterized by its incident intensity I_0 passing through a gas will be absorbed at the wavelength corresponding to the absorption wavelength of the target gas. The intensity of the absorption, quantified by the transmitted light intensity I_t, is measured with an optical detector and depends on the concentration of gas in the medium. I_0 and I_t are compared to quantitatively and qualitatively identify the target gas.

NDIR sensors are based on this principle. They have been demonstrated for the first time in 1953 by Luft [17], [18]. These sensors are composed of simple elements including (Figure 6):

- light source, usually broadband,
- filtered optical detectors.

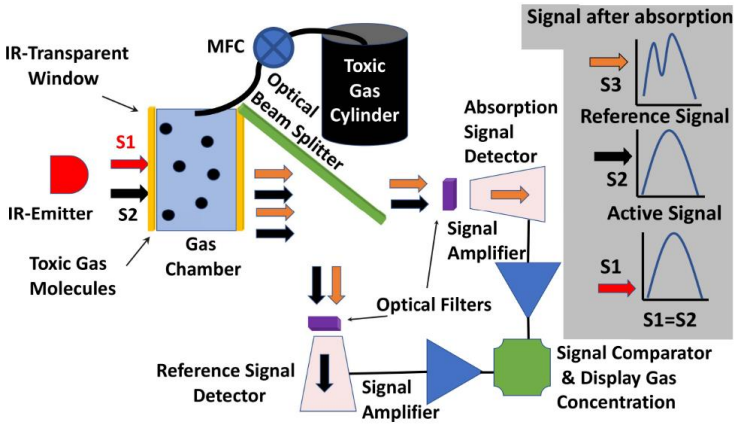

Figure 6: Typical NDIR sensor. [18]

Figure 6 presents the operation principle of NDIR sensors: the light is propagated through the absorption medium, one part is optically filtered over the absorption band of the target gas and the other part is narrowly filtered far from this region (reference signal). The reference region is usually chosen to be far from the target gas but also from any other interferent such as water, which is not always comfortable to achieve in the IR region. Then, the signal after absorption (S3) is compared to the reference signal (S2 or S1).

NDIR sensors can be very compact (Figure 7b). They are also very simple to assemble and low cost and that is probably how they earned their success. Nevertheless, the performances achieved with these cheap elements are somehow limited. Indeed, classical IR microbulbs used for NDIR provide high power and cost less than 2$ but they also operate at low frequencies (tenth of Hz). It is as well the case of thermopile detector, for example, that are known to be optimized at 1-2 Hz, where the 1/f noise is dominant. Better performances can be achieved with longer pathlength or detectors or light sources that are more sophisticated.

NDIR sensors dedicated to environmental investigation have demonstrated limits of detection in the ppb range with a pathlength of 12.5 cm (Li-Cor CO_2/H_2O sensor) [19] (Figure 7a). Different models, that are more compact, are used in breath analysers, for the detection of CO (Table 1) or CO_2 (Figure 7b) for example, with response time < 1 second, which make them suitable for real time investigations. Unfortunately, the scope of application of these sensors is limited by the bandwidth of the employed optical filters.

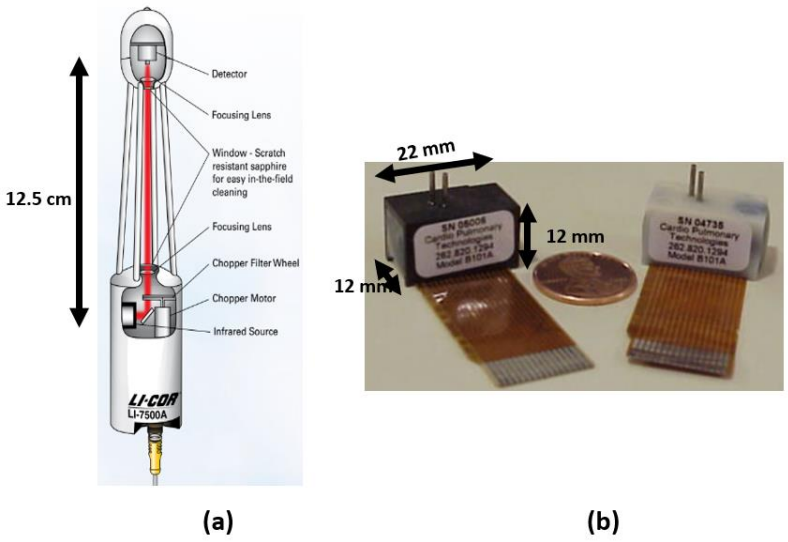

Figure 7: Commercial NDIR sensors. (a) Li-Cor sensor for CO_2 and H_2O in the atmosphere. (b) COMET II and COMET I sensor for CO_2 used in breath analyser with limits of detection ranging between 0 and 13 % and typical response time of 28 ms. [20]

1.4-5. Commercial sensors in clinical practice

Among the four gases that were identified for investigation in the exhaled breath, only CO and NO are approved in clinical practice. Different companies have introduced the sensors presented in Table 1. Generally, NO is dedicated for asthma diagnosis and CO for measuring the diffusion capacity of the lungs (DLCO). This test is realized by comparing an inhaled concentration of CO with the concentration after expiration. The name, the detected gas, the type of sensor, its size and weight are reported. In addition, technical specifications such as the detection range and accuracy on the measured value as well as the time response important for real time measurement are presented.

This non-exhaustive list of breath analysers used at the hospital or by clinicians shows that most sensor targeting NO in the exhaled breath are electrochemical. However, even if on-line measurements are performed, the main drawback of these sensors, in the point of view of our application, is the response time that is far from 1 second. Performing real-time measurements being impossible, it is also impossible to record a complete expirogram of for NO using these detection modules. Chemiluminescence is the reference method for on-line NO measurements. Its clinical use has been approved and matches the European Respiratory Society (ERS) and the American Thoracic Society (ATS) recommendations

[21]. Chemiluminescence sensors are based on the chemical reaction of NO with ozone (O_3) that emits light which intensity is proportional to the concentration of the gas. This sensor provides real-time measurements and is adapted for the reconstitution of NO expirograms.

The CO is mostly detected in DLCO tests [22] or for CO intoxication but not as biomarker used in diagnosis. The infrared sensors seem to be well adapted for the measurement. They present response time lower than 1 second and detection ranges that exceed the requirements for exhaled CO concentrations.

Table 1: Non-exhaustive comparison of sensors used by medical doctors or at hospital in the detection of exhaled NO and CO.

Ref.	Sensor	Gas	Detection technique	Detection range (ppbv)	Time response (sec)	Accuracy (ppbv)	Size: HxWxD (cm) / Weight (kg)
[23]	NIOX® FeNO	NO	Electrochemical	5-300	60	± 5 under 50	14.5x18.5x4 / 1
[24]	NObreath®	NO	Electrochemical	5-300	< 10	± 5 under 50	152x87x47 / 0.4
[25]	Medisoft FeNO+	NO	Electrochemical	1-200	25	2.5	14x21x33 / 10
[26]	Ecomedics Analyzer CLD 88	NO	Chemiluminescence	0.1-5000	< 0.1	NF	13.5x50x54 / 24
[27]	Cubic Gasboard-2050	CO	NDIR	0-3500ppmv	<0.3	± 1% full scale	18.3x6.56x ?
[28]	EasyOne Pro	CO	NDIR	0-3500ppmv	NF	±0.003%	27x33.5x27 / 8
[29]	Medisoft Hyp air	CO	Chemical Fuel cell	0-3500ppmv	20	± 0.1%	14x40x33 / 12
[29]	Medisoft Hyp air	CO	IR spectrometer	0-3500ppmv	<0.1	± 0.1%	

The infrared region witnesses the development of various gas sensors dedicated to different applications. Other types of sensors also based on the same working principle as NDIR devices exist. They are more sophisticated, which means that they are more complex to assemble and more expensive. However, they present interesting characteristics, including extremely low detection limits, high selectivity and real-time responses that are mandatory in applications such as medical diagnosis. Laser modulation spectroscopy is the heart of these techniques. It is performed by the mean of tunable laser sources whose emission wavelength is scanned across one gas absorption line.

1.4-6. Infrared laser sources

With the development of semiconductors, typical microbulbs used in NDIR sensors were replaced by Light Emitting Diodes (LED) introduced in 1962. These broadband light sources can be operated at higher modulation frequencies which allows to decrease the 1/f noise. In the early 1960s, different families of semiconductor materials presenting direct bandgaps permitted the development of lasers sources [30].

Focusing on technologies using quantum wells (QWs) in their active region, three main groups are known: interband diodes, interband cascade lasers (ICLs), quantum cascade lasers (QCLs). The light emission of the first two groups is obtained from transitions between conduction and valence bands while the third one's relies on transitions between intersubbands, usually, conduction band. Altogether, these lasers sources based on antimonide material family, cover the whole IR spectrum and present interesting features for gas sensing application from 2-20 μm (Figure 8).

For widespread sensors, mid-IR diode lasers are more attractive than QCLs as they are cost-effective and less complex to produce. Diode laser and ICLs, are more developed between 2 and 3 μm, they exhibit around tenth of milliwatts (mW) output power and are characterized by low power consumption and low threshold current (Figure 8). In most photoacoustic based techniques, the output signal is proportional to the power of the light source. Even if QCLs are known to be power consuming with threshold currents relatively high, their high output power defines them as good candidates in such applications when it comes to achieving better performances.

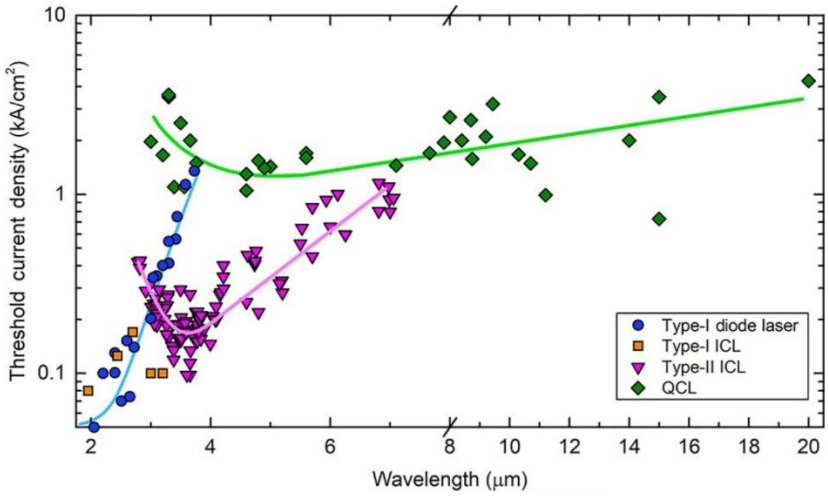

Figure 8: Threshold current density function of the wavelength for type I diode laser and ICL, usually using GaInAsSb in their active region, type II ICL, which active region is made of GaInAs/GaAsSb and QCLs (InAs/AlSb). [31]

Laser based spectroscopy techniques earn their selectivity from the fact that they employ single mode laser sources. Therefore, the emission of the laser is centred across a single (in an ideal case, free of interferents) absorption line. Compared to LEDs that are characterized by a broad wavelength emission (Figure 9a), lasers present thicker bandwidth and can be multi-mode (Fabry Perot lasers) or single mode (DFB-lasers) (Figure 9b).

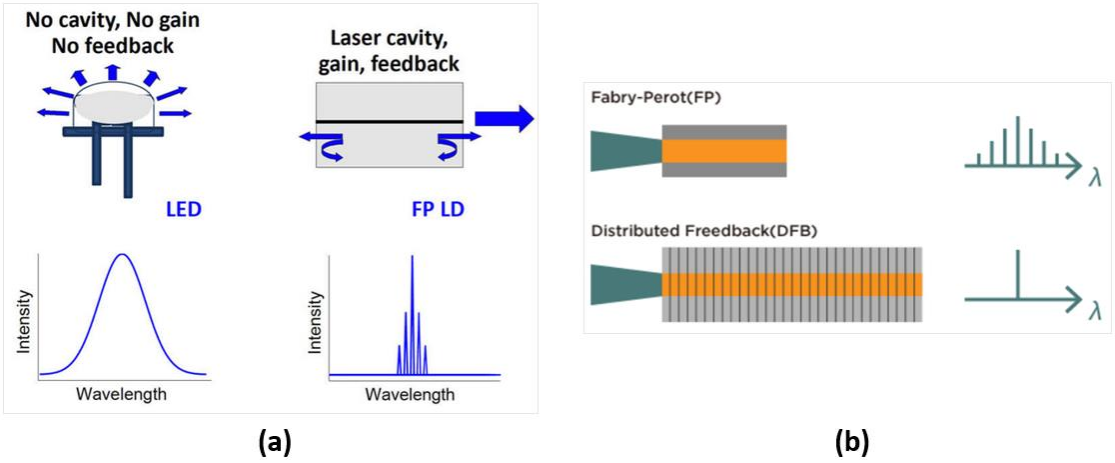

Figure 9: (a) comparison of LEDs and Fabry Perot Laser Diodes spectrum. (b) Comparison between a multimode FP spectrum and a single mode DFB spectrum. Figures adapted from [32], [33].

Single mode laser sources present a spectral linewidth in the MHz range while classical absorption lines range in the GHz at atmospheric pressure. The spectral response of the laser being thinner that the absorption lines, the detection becomes extremely selective as it allows the investigation of a single absorption line (thus, gas) at the time. Semiconductor lasers' wavelength is related to the injected current or temperature. Therefore, if the injecting current is modulated, the wavelength is modulated as well: this property is the tunability of the laser expressed in nm/mA or nm/°C.

In WMS, the injecting current of the laser can be swept between the laser's minimum and maximum specified limits. This first component can be seen as a sawtooth with a slow frequency (tenth of Hz) and a high amplitude. Then, a sinewave, with a small amplitude and a high frequency (ranging between the kHz and the MHz) is added by the mean of a function generator and used as a reference for the lock-in amplifier (LIA) for example. This high frequency sinewave is used to modulate the laser but also to perform the demodulation of the signal transmitted to the photodiode (detector) (Figure 10). The shape of WMS signal will be detailed in section 2.3.

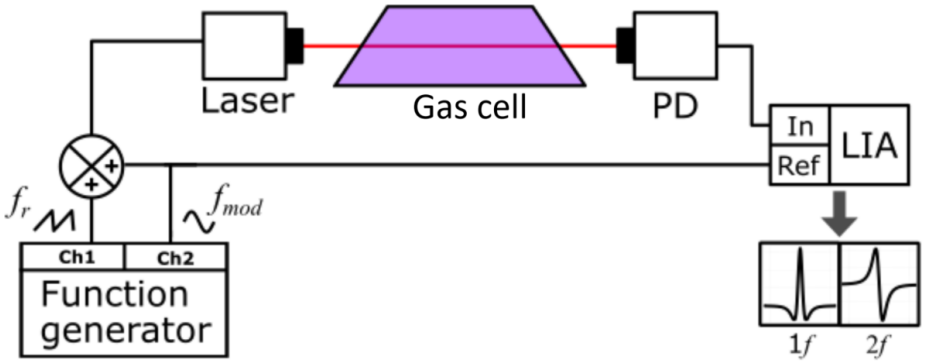

Figure 10: Typical WMS experimental setup. [16]

Even if this technique provides a better selectivity and helps getting rid of the 1/f noise dominant at low frequencies, its sensitivity remains dependent of the propagation pathlength. Different designs including the use of multipass cells have been introduced in order to achieve longer pathlength. However, the proposed setups that are far from compact become also difficult to align and expensive.

Different alternatives that are based on photoacoustics principles bypass the long pathlength problem and offer a high potential of miniaturization. As its name implies, this phenomenon describes the conversion of an optical energy to an acoustic energy that can be further detected with cheap and widely available detectors such as microphones: this technique is the classical photoacoustic spectroscopy (PAS).

2- Photoacoustic spectroscopy (PAS)

Photoacoustics can be briefly explained as follows (Figure 11):

- The modulated light of the laser passes through the medium containing the gas of interest,
- If the wavelength of the laser λ_{laser} matches the absorption wavelength of the gas, the light is absorbed.

- As the laser is modulated (at a frequency = f_0), a phenomenon of modulated absorption (excitation) and relaxation is witnessed in the medium.
- In the IR domain, the relaxation is non-radiative. The energy is dissipated in form of collisions between the molecules (and the gas cell walls) creating a modulated heat source.
- This rapid variation of temperature leads to a variation of the pressure, hence to the generation of an acoustic wave that will further be detected.

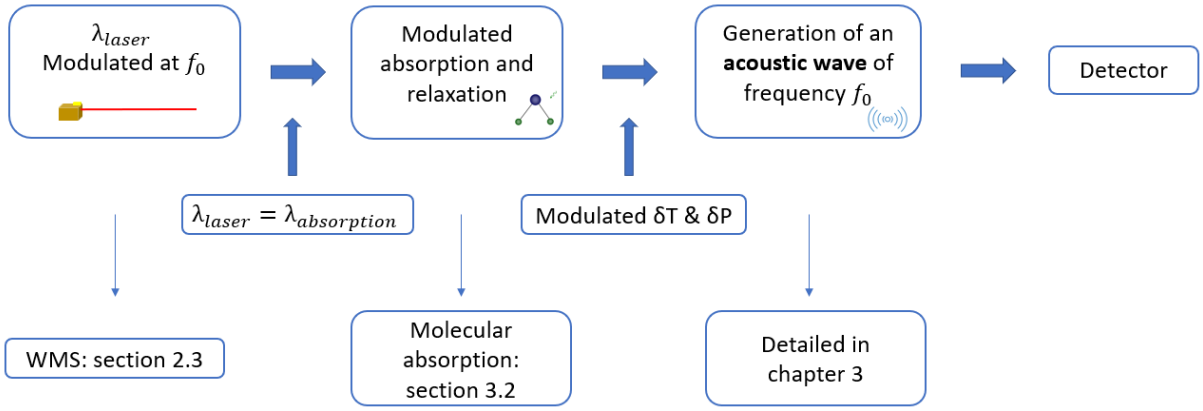

Figure 11: Photoacoustics working principle.

The photoacoustic effect has been observed in solids for the first time in 1880 by Bell [34]. This effect in liquids and gas phases has been rapidly characterized after that but, the lack of adapted light sources as well as detectors has led to its late exploitation. Unlike WMS that depends on the absorption pathlength the photoacoustic signal is proportional to the power of the employed laser (W) and the absorption coefficient of the target gas (cm^{-1}). With the development of sophisticated laser sources and microphones, trace gases detection has been demonstrated [35].

In conventional PAS, the detector is a microphone. Always in the pursuit of miniaturization, microelectromechanical system (MEMS) microphone have been developed. They present interesting characteristics, notably their potential of integration, small size, low power consumption and cost. Most commonly used microphones are based on a capacitive measurement of the acoustic waves. They are composed of a movable and a fixed plate, composing altogether a capacitor. The acoustic waves, directed to the microphone, cause the mechanical movement of the mobile face which induce a change in the capacitance. Thus, charges, proportional to the amplitude of the acoustic wave are generated. These microphones are usually employed in audio systems and present a resonance peak above 20 kHz. In Figure 12, the response of a typical microphone [36] used in PAS is presented [37]–[40].

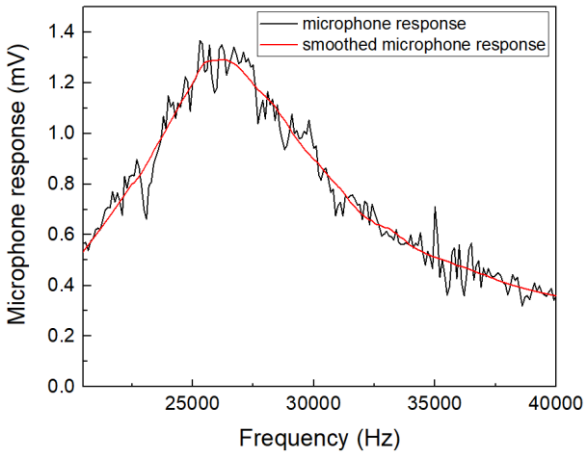

Figure 12: SPU0410LR5H-QB response between 20 and 40 kHz. The generation of the acoustic wave leading to this response is obtained by exciting ambient water molecules at 2.3 μm with a DFB diode laser.

Working at the 10th of kHz helps enhancing the Signal to Noise Ratio (SNR) obtained in PAS measurement as the noise is generally inversely proportional to the modulation frequency [41]. However, the poor quality factor of the microphone makes this technique highly sensitive to background noises and vibrations. In order to enhance the SNR, different geometries of resonators have been developed (Figure 13)[42]. When the generated acoustic wave is confined between the boundaries of the resonator, its amplitude is amplified due to the generation of constructive interferences. Naturally, the microphone is placed at the antinode of the standing acoustic wave, where the amplitude is at an optimum.

2.1- Gas cells as non-passive elements

Just like optical cavities made of mirrors, acoustic cavities can be built in order to spatially confine and amplify the acoustic wave that is initially generated at a very small amplitude.

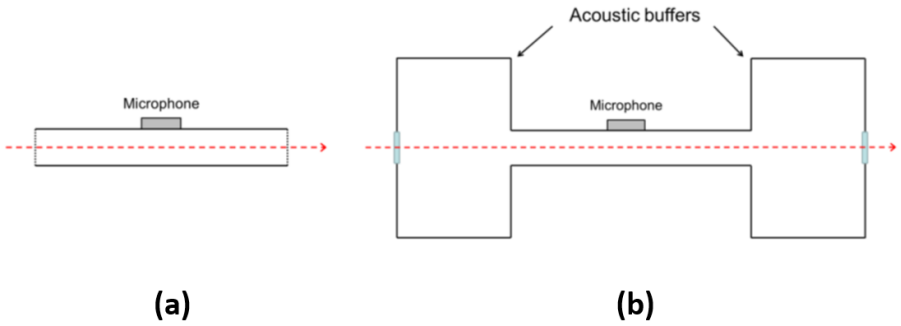

Figure 13: Schematic of a (a) simple pipe (b) pipe with buffer volume used in PAS. [43]

Acoustic resonators should be correctly designed in order to have a significant impact on the acoustic wave amplification. In order to target low frequencies, suitable for photoacoustic signal generation in slow relaxing molecules, the first order of the

longitudinal mode of the acoustic wave is usually exploited. Simple pipes (Figure 13a) are designed for this purpose with their lengths greater than their radius (L >> R). The laser passes through the acoustic cavity (along its axis) containing the target gas. The microphone is positioned where the maximum of the acoustic wave occurs. Most of the time, buffer volumes are added at each side of the pipe in order to attenuate the background noise generated by the absorption of the light on the windows or cell walls (Figure 13b) [42].

Another option is the implementation of differential resonant cells.

They consist in two air buffers separated by capillary tubes. The system can be assimilated to a mechanical oscillator composed of a mass and a spring with the mass being the air buffers and the spring being air volume in the capillaries. The pressure oscillates from one buffer to the other and the amplification depends on the thermal and viscous losses of the cells. In the design of the well-known Helmholtz resonator (Figure 14) [44], two microphones are placed in each buffer volume measuring the noisy photoacoustic signal. The differential measurement helps reducing this background noise. The gas in/outlet can be placed along the capillaries, at the nodes, to reduce the noise generated by the circulating gas.

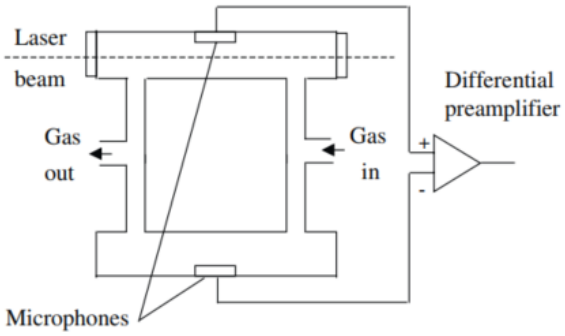

Figure 14: Schematic of a typical differential Helmholtz resonator. [44]

To conclude, PAS benefits from the great selectivity offered by optical techniques but can be more compact, as its sensitivity does not depend on the optical pathlength. Microphones used as detectors, are cheap and widely available conversely to the photodiodes used in WMS that are expensive and do not cover the whole IR spectrum. However, even if some designs allow the reduction of the background noise, the system is limited by the noise of the microphone. Different techniques based on photoacoustic principles and matching the performances of the classical PAS have been introduced. They differ by the way the acoustic wave is measured and quantified.

2.2- Resonant transducers

Different types of transducers have been implemented with photoacoustic measurements. The mechanisms leading to the generation of the acoustic wave remain similar to classical photoacoustics. However, the detector and read-out system are different.

- CEPAS has been introduced in 2003 [45] and stands for Cantilever Enhanced Photoacoustic Spectroscopy. Cantilevers can be designed on Silicon wafers, offering the possibility to be integrated. Their geometry can be adapted in order to match with a special resonance frequency and maximize the displacement of the cantilever beam caused by the acoustic wave. Cantilevers do not necessarily operate at their resonance frequencies as good sensitivity can be achieved as long as the displacement is optimized, i.e. at low frequencies. The displacements are most generally measured optically with an interferometer which makes the final sensor quite bulky.

- QEPAS, introduced in 2002 [46] uses a highly resonant quartz tuning fork and a piezoelectric transduction for the detection of the acoustic wave. This technique is employed for the gas detection presented in this manuscript and will be detailed in the next sections.

-MEMSPAS (introduced in 2018) relies on the microelectromechanical system especially designed for photoacoustics [47]. It is based on a capacitive transduction and the frequency of the MEMS can be adapted during the design process in order to match the relaxation time of each detected molecule [48]. This newly introduced technique has proven its efficiency with performances reaching the state of the art for PA sensors [49].

2.3- Study of WMS signals

2.3-1. Working principle

In direct absorption techniques, the shape of the transmitted signal is the same as the shape of the absorption lines. In WMS, a modulated signal is recorded from the photodiode and the demodulation is generally operated at the 1^{st} or 2^{nd} harmonic of the signal which amplitude and maximum, respectively, are proportional to the concentration of target gas. Usually, the 2^{nd} harmonic is preferred, because it is offset free, even if the 1^{st} harmonic present a higher amplitude. At small modulation frequencies, the 1^{st} and 2^{nd} harmonics are directly equal to the 1^{st} and 2^{nd} derivative of the absorption lines.

The theoretical description of the detected WMS signal was initiated by Arndt (1965) [50]. But the model was proposed only for pure frequency modulation (FM). Later on, Kluczynski et al [51][52] have given a generalized description of the signal detected through intensity and frequency modulation (IM-FM) using Fourier decomposition. The effect of

large frequency modulation on the laser as well as the residual background are considered in their model. Schilt [53][54] has used a comparable formalism to describe IM-FM modulation in photoacoustics undergoing a phase shift. Different parameters induced by the IM modulation creating a distortion of the detected signal are introduced and investigated. This model has been widely studied in [16].

In this section, WMS will be described exclusively but it is relevant to note the existence of a Frequency Modulation Spectroscopy (FMS). These two techniques differ by the order of magnitude of the modulation frequency. While the latter uses a frequency with the same order of magnitude as the absorption linewidths ($f_m > \Delta\sigma_{line}(Ghz)$), the former's frequency is considerably smaller than the absorption linewidths ($f_m \ll \Delta\sigma_{line}$).

For this study, the idea is not to redesign a model for WMS signals or study the above-mentioned models. The following description, using simple Fourier series serves as a support to understand the shape of the signal observed experimentally. This model does not take into consideration the variation of the laser's power induced by the large wavelength variation.

The modulation of the laser is described as an AC component $\lambda(t)$ defined with a sinewave of amplitude $\Delta\lambda_{amp}$ to which is added a DC component λ_c. Gas absorption profiles are often described as an absorption function of the wavenumber or the wavelength $g(\lambda)$. Therefore, we can write:

$$f(t) = g\ o\ \lambda(t) = g\big(\lambda(t)\big) \tag{2.13}$$

as a pseudo-periodic function, of period T, that can be developed with Fourier series.

The development of $f(t)$ in Fourier series, gives:

$$f(t) = a_0 + \sum_{n=1}^{\infty} a_n \cos\left(\frac{2\pi nt}{T}\right) + \sum_{n=1}^{\infty} b_n \sin\left(\frac{2\pi nt}{T}\right). \tag{2.14}$$

Where a_0 is directly related to $f(t)$ and a_n represents the nth harmonics of the photoacoustic signal calculated over one period T with:

$$a_0 = \frac{1}{T}\int_{-\frac{T}{2}}^{\frac{T}{2}} f(t)dt \tag{2.15}$$

$$a_n = \frac{2}{T}\int_{-\frac{T}{2}}^{\frac{T}{2}} f(t)\cos\left(\frac{2\pi nt}{T}\right)dt \tag{2.16}$$

$f(t)$ is an even function, therefore the b_n are equal to zero.

2.3-2. Example of a Lorentzian line shape: carbon monoxide at 4.6 µm

In this example, the absorption line of carbon monoxide around 4.6 µm, with a pathlength of 1 cm and a concentration of 1 ppmv is extracted from HITRAN database and defined as $g(\lambda)$. It is presented as a Lorentzian line shape measured in atmospheric pressure conditions and ambient temperature. The 1st and 2nd harmonics of the signal are calculated in Figure 15.

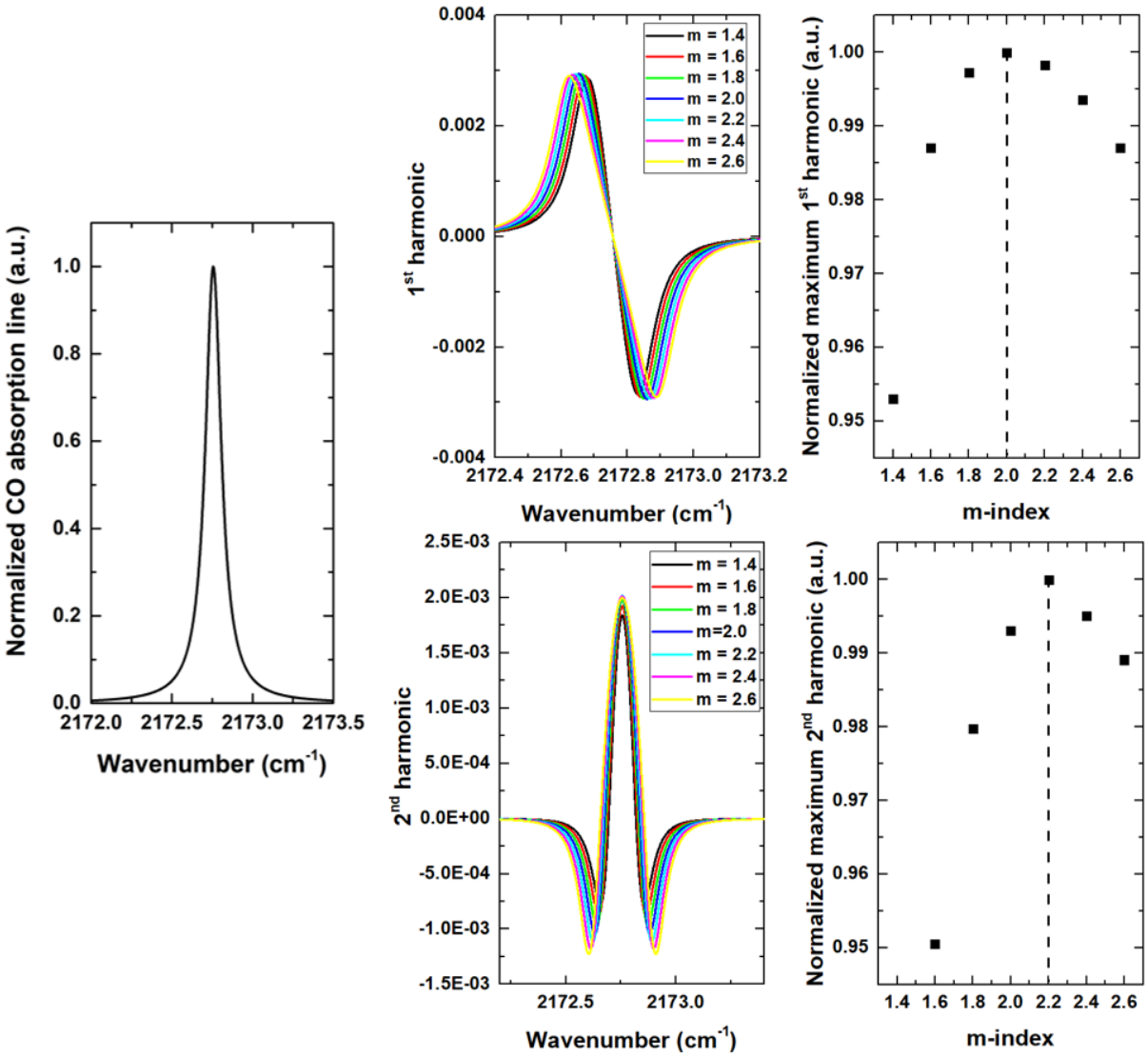

Figure 15: 1st and 2nd harmonics obtained for WMS simulations for a carbon monoxide absorption line at 4.6 µm.

In this example, the modulation index m is introduced. It is calculated with experimental parameters related to the laser. Indeed, let Δi_{exp} be the experimental modulation amplitude related to a certain wavelength variation $\Delta\lambda_{amp}$ and $\frac{\Delta\lambda_{amp}}{\Delta i}$, the current tunability of the laser, the variation of wavelength induced on the laser are defined as:

$$\Delta\lambda_{laser} = \Delta i_{exp} \frac{\Delta\lambda_{\mathrm{amp}}}{\Delta i} \tag{2.17}$$

For different modulation amplitude, m can be calculated by:

$$m = \frac{\Delta\lambda_{laser}}{\Delta\lambda_{line}} \tag{2.18}$$

$\Delta\lambda_{line}$ being the half width at half maximum of the considered absorption line.

This modulation index has been studied by Schilt [53] and the optimum for the 1st and 2nd harmonics of the signal are found respectively for $m = 2$ and $m = 2.2$.

The optimization and the effect of the modulation play an important role on the amplitude and the shape of the experimental signal. In fact, for higher modulation amplitudes, after the optimum obtained for the index m, a distortion can be observed as the secondary lobes become larger and higher in amplitude. In our model, this effect is not observed. Simultaneously, the amplitude of the 2nd harmonics (resp., the maximum for the 1st harmonics) starts to decrease.

In reality, a factor of 2 can be observed between the calculated optimum and the one obtained experimentally. This effect occurs mostly because the tunability of the laser is measured statically, i.e. at fixed current and temperature, while the experimental signal is often observed during what we called "dynamic conditions" where the injected current is tuned with a high frequency sinewave. The latter indeed induce a mismatch if the temperature, that also plays a role on the actual laser wavelength, is not completely stabilized at each current step [55].

3- Quartz enhanced photoacoustic spectroscopy

Quartz enhanced photoacoustic spectroscopy was introduced in 2002 by Kosterev et al [46]. This technique, based on photoacoustic principles, presents challenging performances to PAS while having the merit of being immune to background noise. Indeed, the QEPAS uses a commercial Quartz Tuning Fork (QTF), with a high quality factor (around 8000 in atmospheric condition of pressure), as a transducer. Conversely to the microphone used in PAS, that is positioned at the output of the gas cell, the QTF is located inside the cell. Indeed, added to the fact that the QTF is tiny (around 3 mm large and 8 mm long), the detected phenomenon, i.e. the acoustic wave, is localized at its neighbourhood which opens opportunities for miniaturization. By the mean of an external modulation, the light source is modulated at a frequency f_0 chosen to be equal to the resonance frequency of the QTF $f_{QTF} = 32.756\ kHz$. The modulated absorption and relaxation lead to the generation of an acoustic wave at this same frequency which will induce the actuation of the QTF. By piezoelectric effect, the movement of the QTF generates electrical charges that are proportional to the photoacoustic wave intensity and to the concentration of the target gas

(Figure 16). Afterwards, these charges are converted into a voltage and amplified by a transimpedance amplifier (TA).

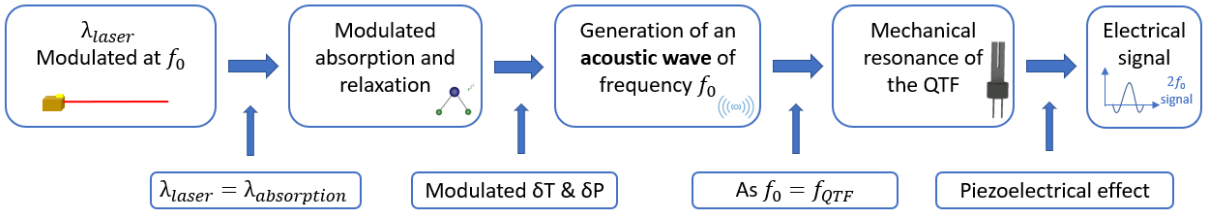

Figure 16: QEPAS working principle.

The experimental setup is presented in Figure 17. The laser is focused inside the gas cell containing the gas of interest by the mean of a focusing lens. The configuration presented in Figure 17 is called the off-beam configuration. This configuration has been used in the entire measurements conducted in this manuscript. Basically, the laser is not focused between the prongs of the QTF as it could have been the case in a bare or on-beam configuration (Figure 18a and b) but inside a designed acoustic cavity. Compared to these two configurations and given the fact that the space between the two prongs of the QTF is very small (≈ 0.3 µm), the off-beam configuration makes the alignment with the laser easier. This also tends to the minimize the photothermal noise generated when the laser hits the QTF prongs. In addition, compared to the bare configuration, the acoustic cavity leads to an enhancement of the photoacoustic signal by a factor 30 [56][57]. A study of the acoustic cavity in off-beam configuration is proposed in the Chapter 3 of the manuscript.

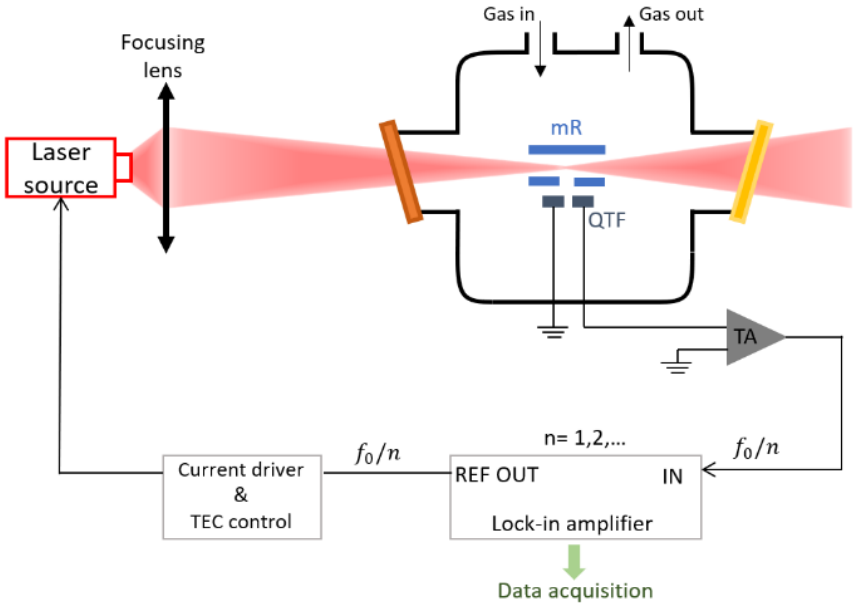

Figure 17: QEPAS experimental setup.

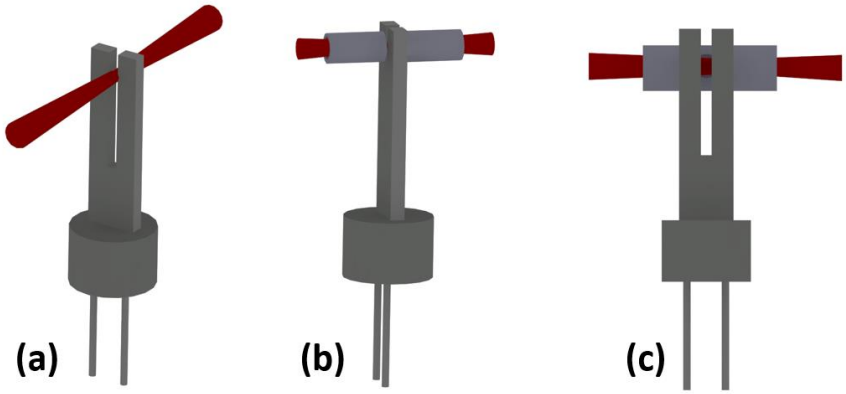

Figure 18: Different spectrophone configurations (a) bare, (b) on-beam and (c) off beam.

By focusing the laser inside the acoustic cavity, one needs to make sure that the maximum power of the laser is collected at the output of the cavity. Lasers used during this project were mainly QCLs, the beam of these light sources is studied and described by Gaussian optics principles as the beam is considered as Gaussian shaped. Figure 20 describes the geometrical parameters to consider when focusing this type of sources.

3.1- Gaussian beams

For this example, we consider a DFB QCL designed and manufactured at the IES. Dr Daniel Andres Diaz Thomas was working as a post-doc researcher on this project. His work aimed to develop different lasers targeting the different gases identified for the SENSIR project.

The laser considered in this example is emitting around $\lambda = 11\ \mu m$ targeting an isoprene absorption line in this region. The active region (where the light exits from the optical cavity of the laser) is rectangular, leading to an elliptical optical beam. The width s of the ridge is equal to 8 µm and the thickness t of the active zone is equal to 4.6 µm (Figure 19).

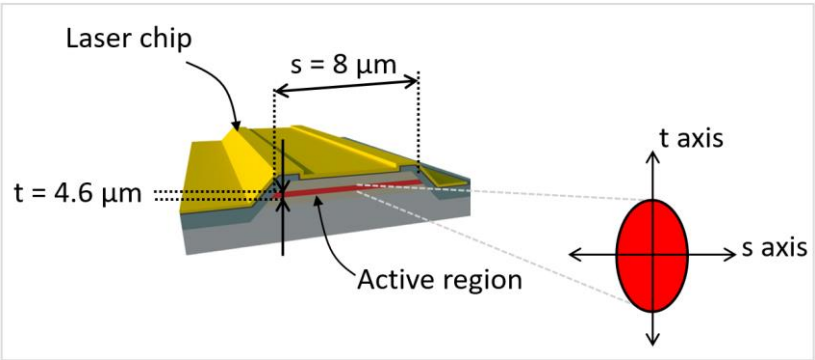

Figure 19: Description and dimensions of the active region. [58]

Let's define $w_{0,t}$ as the waist radius of the laser light in the t direction, equal to half the thickness of the active zone and $w_{0,s}$ the waist radius of the laser light in the s direction, equal to half the width of the active zone. Finally, $w_{0,t} = 2.3\ \mu m$ and $w_{0,s} = 4\ \mu m$.

The light is collected with a focusing lens of focal $f = 5.95\ mm$ and the laser is positioned at around 6.15 mm.

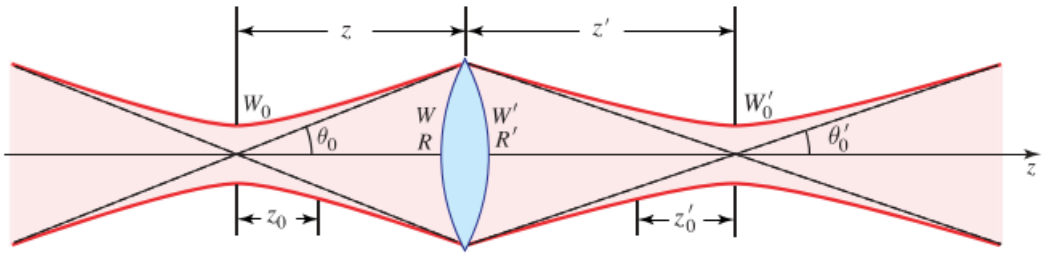

Figure 20: Focusing a gaussian beam. [59]

Let w_0' be the waist of the focused light, after the lens. w_0' can be calculated as:

$$w'_{0,s,t} = \alpha w_{0,s,t}. \tag{2.19}$$

With

$$\alpha = \frac{f}{\sqrt{(|z| - f)^2 + z_0^2}}, \tag{2.20}$$

where z is the distance from the lens and z_0 is Rayleigh range defined as follows:

$$z_0 = \frac{\pi w_{0,s,t}^2}{\lambda} \tag{2.21}$$

Therefore, the focused light is calculated in the s and t directions. $w'_{0,s} = 119\ \mu m$ and $w'_{0,t} = 68.4\ \mu m$.

The distance $z'$is calculated:

$$z' = f + \alpha^2(|z| - f) = 18.3\ cm. \tag{2.22}$$

The acoustic cavity is positioned where the waist of the laser is the smallest, i.e. at $z' = 18.3\ cm$. Therefore, the waist radius of the laser at the entrance of the acoustic cavity should be smaller than its radius in order to collect the maximum of the emitted intensity. The waist of the laser at the distance $z' - \frac{L}{2}$ is calculated. L being the length of the acoustic cavity equal to 6 mm.

$$w_{0,s,t}\left(z' - \frac{L}{2}\right) = \frac{w_{0,s,t}}{z_0}\left(f^2 - 2(|z| - f)\left(z' - \frac{L}{2} - f\right) + \left(\frac{z' - \frac{L}{2} - f}{\alpha}\right)^2\right) \tag{2.23}$$

At the distance $z' - \frac{L}{2} = 18\ cm$, $w_{0,s}\left(z' - \frac{L}{2}\right) \approx 239\ \mu m$ and $w_{0,t}\left(z' - \frac{L}{2}\right) \approx 138\ \mu m$ which remains inferior than the radius of the acoustic cavity that is equal to 360 µm.

To conclude, if the light of the laser is focused at approximately 18.3 cm from the lens, the beam is not affected by the small radius of the acoustic cavity.

3.2- Molecular absorption in the infrared

In the description of photoacoustic based techniques, two phenomena were mentioned: the absorption of photon by the molecules and their non-radiative relaxation. The absorption is characterized by vibrational and rotational transitions that will be described in the first part of this section in order to understand how is composed the absorption spectrum of a molecule. As for the relaxation, it is made of collisions between the molecules or between the molecules and the medium walls and translations. This phenomenon generates a heat wave that is directly involved in the generation of the acoustic wave. The relaxation time, i.e. the time needed to return to a zero-energy level depends on the collision partners and the experimental conditions. This part will be described in the second part of this section.

3.2-1. Vibrational-Rotational transitions

Different types of interactions between light and matter exist. The absorption of light by molecules remains the most important in the IR domain (compared to Raman diffusion or fluorescence). A molecule is described by its energy levels and separated in two main groups. Diatomic molecules that are composed of two atoms (thus, two nucleus) and polyatomic molecules that are a combination of more than two atoms. The total energy of one molecule is the contribution of its electronic, vibrational and rotational energy. Electronical transitions occur at smaller wavelength, namely UV or visible. Therefore, in spectroscopy, when using IR lasers, the energy emitted by the light source and absorbed by the molecules will mainly generate vibrational and rotational transitions. Schilt [53] gave a complete description of the vibrational and rotational spectrum for diatomic and polyatomic molecules. The spectrum of polyatomic molecules is more complex and will not be detailed in this manuscript.

Separately, the pure rotational (resp. vibrational) spectrum is obtained by considering only the rotation (resp. only the vibration) of the molecules. The vibrational-rotational (V-R) spectrum is obtained by considering every degree of freedom of the molecule. While the pure rotational spectrum is located at higher wavelengths in the LWIR and microwaves, the pure vibrational spectrum is located in the NWIR and MWIR.

The pure vibrational spectrum is constituted of different states of energy which intensity decreases rapidly over the frequency (Figure 21). The vibration transitions can be described

as harmonic transitions as each level of energy is approximately proportional to the fundamental's frequency.

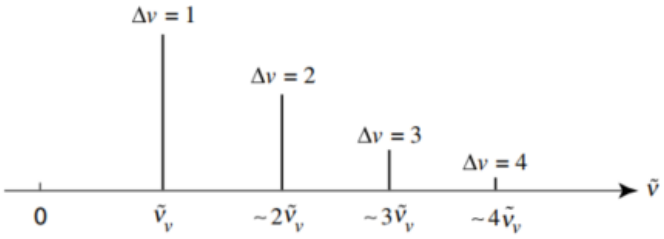

Figure 21: Pure vibrational spectrum of a diatomic molecule. Δv being the difference between a superior state of energy and an inferior one. If the vibrational spectrum was purely harmonic it would have been composed of only one absorption line $\tilde{\nu_v}$. [53]

The pure rotational spectrum is instead separated by equidistant transitions with a shape that is broadened by temperature increase. The V-R spectrum takes its shape from the rotational spectrum. Indeed, the group originating from the vibrational and rotational combination is located in a frequency region established by the vibrational spectrum. The V-R spectrum is constituted by two series of rotational transitions located on one side and the other of the vibrational state that is absent from the spectrum. The branch P is located at the left side of the vibrational state frequency, while the R branch is on the right side, at higher frequencies. The V-R spectrum draws two transitions groups at each side of the vibrational state with an intensity and a frequency spreading according to the temperature and pressure conditions (Figure 22).

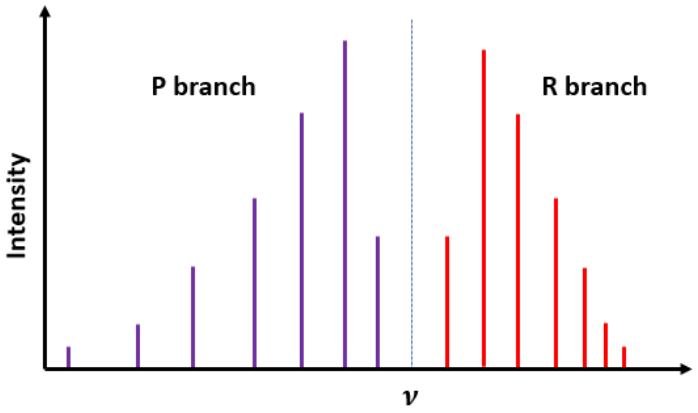

Figure 22: Schematic representation of a Vibrational-Rotational spectrum of a diatomic molecule.

3.2-2. Example of a diatomic molecule: carbon monoxide (CO)

The spectrum of CO in the IR domain is shown in Figure 23.

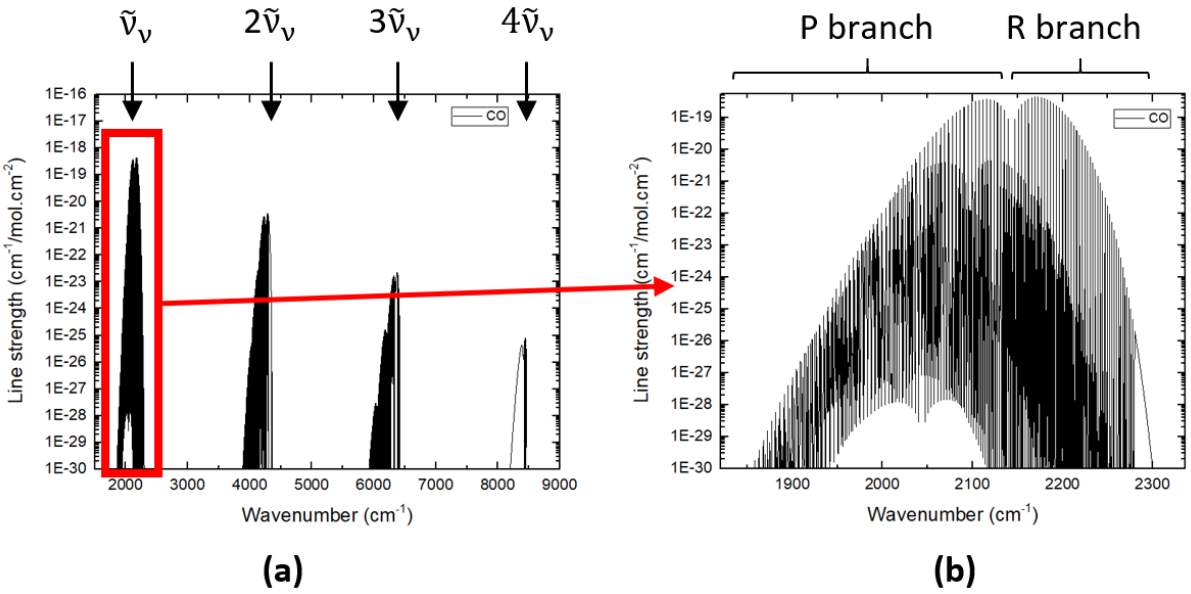

Figure 23: Carbon monoxide spectrum, with the different isotopes, in the IR domain depicting the different vibrational-rotational absorptions. Spectrum extracted from HITRAN database.

On Figure 23a, it is possible to observe in the MWIR, the absorption features of CO separated in different harmonic groups around $\tilde{\nu}_\nu = 2143.2, 2\tilde{\nu}_\nu = 4259.6, 3\tilde{\nu}_\nu \approx 6430$ and $4\tilde{\nu}_\nu \approx 8570\ \mathrm{cm}^{-1}$. These groups distributed around the vibrational state decrease rapidly in intensity as presented in Figure 21. Figure 23b presents the typical branches, P and R, of the V-R transitions of CO and its isotopes.

3.2-3. Investigating water as collisional partner.

The investigation of the effect of the collisional partners cannot be neglected as it can result in an enhancement of the photoacoustic signal and the performances of the sensor. Water (H_2O) is now well-known to play in important role in the relaxation process of some molecules, such as CO_2 [60] or CO that will be discussed in this section. Helium (He) have also proved to have the same catalyst effect on CH_4 and O_2 [61][62].

In photoacoustic sensing techniques, the laser source is modulated and the detected signal is expected to be generated in one modulation period. This means that the energy absorbed by the molecules has to be released to the medium in less than a modulation period. In QEPAS, the modulation frequency is close to 32 kHz (for 1f detection or 16 kHz for 2f detection when using a commercial QTF) but some molecules relax at much lower frequencies. Therefore, the absorbed energy is not totally released within one half modulation period. This issue can be overcome by using transducers (QTFs) that present

a lower resonance frequency in order to match the relaxation frequencies of certain molecules. One other solution is to add water (or other catalysts) to the gas mixtures.

In addition, depending on the environment in which the sensor is going to operate, different humidity level can be encountered. It is notably the case for environmental applications where the humidity level depends on the weather or the investigation of the exhaled breath saturated in water vapor. Knowing the effect of this molecules on the photoacoustic signal, it is important to characterize and quantify its effect on the gases investigated in this project.

- **Carbon monoxide in water**

Vibrational, rotational and translational transitions of carbon monoxide have been investigated and the effect of different collisional partners (N_2 and H_2O) assessed [63]. The enhancement of the detected signal of CO is observed for concentration of water above 0.2 %v [63] The same effect has been observed with higher concentration of water by Maurin et al. [64]. In Figure 24a, the amplitude of signal detected for CO measurement is plotted for different levels of humidity, between 0 and 2.1 %v, and two different pressures, 800 mbar and 200 mbar. Figure 24b presents the relaxation path prevailed by carbon monoxide in presence of water. On this graph, different paths and interactions are presented. These dynamics are characterized by the rate of occurrence of the energy transfer. The bigger this rate is, the more this path is to be chosen by the molecule. Therefore, in presence of water, the relaxation of CO will occur through vibrational-vibrational energy transfer to water.

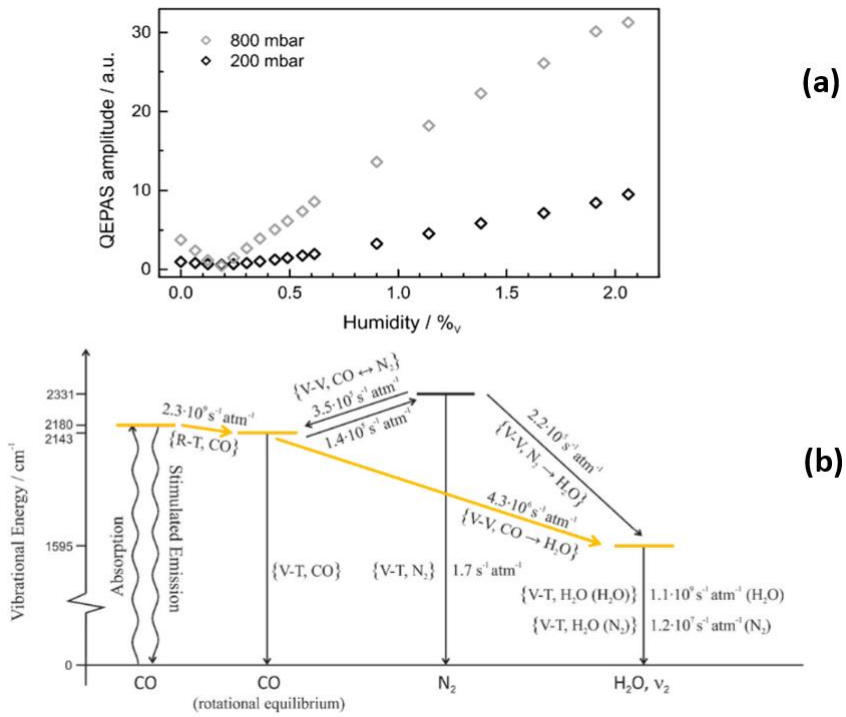

Figure 24: (a) Evolution of the normalized QEPAS signal obtained for the detection of carbon monoxide with different humidity levels. (b) is the relaxation path for carbon monoxide in presence of water or N_2. The privileged path in presence of water is described in yellow. [63]

To understand the effect of different humidity levels on the detected gases presented in the Chapter 4, these gases were humidified before entering the detection module. The humidification of the gas is done by the mean of a homemade bubble bath positioned in a water chiller. The chiller is controlled with an immersive thermostat: changing the temperature of the chiller leads to a change of the bubble bath temperature thus, a change of humidity. The experimental setup is presented in Figure 25.

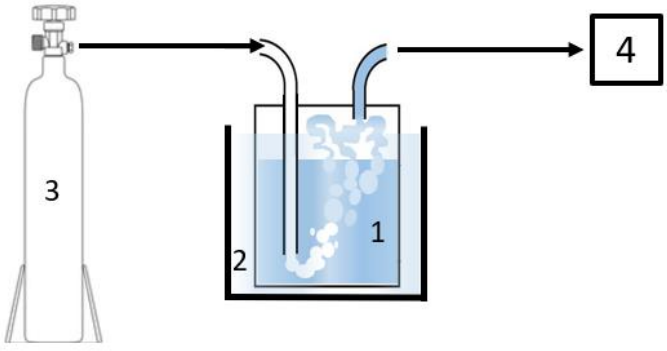

Figure 25: Experimental setup used to humidify a known concentration of a target gas. (1) is the bubble bath in which the gas is humidified. (2) is a water chiller used to control the temperature of the bubble bath. (3) is a gas cylinder containing a calibrated concentration of gas and (4) the gas cell, detection module.

In applications such as breath analysis, investigators have to deal with high levels of humidity that also tend to vary from one subject to another. Therefore, in order to get measurements that are the most reliable possible, the humidity can be fixed by the mean of a bubble bath that will maintain the breath humidity at a certain level depending on its temperature. The minimum temperature that can be reached with a water solution is 1 °C. The measurement presented in Figure 26 is started at 1 °C and the bubble bath is progressively heated until 20 °C. For each temperature step, the relative humidity (% RH) is measured inside the gas detection module. The CO amplitude increases considerably: an enhancement factor of about 10 is found between the QEPAS signal measured from dry CO (0 ppmv of humidity) and wet CO in 24000 ppmv of water.

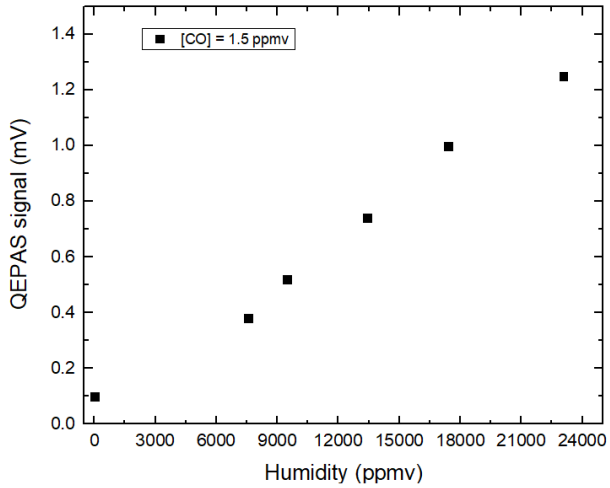

Figure 26: CO QEPAS signal obtained for different level of humidity with a DFB-QCL at 4.6 μm. The concentration of CO in this experiment was maintained at 1.5 ppmv.

- **Nitric oxide in water.**

The investigation of the effect of different humidity levels on the photoacoustic signal obtained for nitric oxide around 5.2 μm is performed with a DFB QCL targeting a NO absorption line. The experimental scheme has been presented in Figure 25. In the range of studied water concentrations, the signal is enhanced from 0.1 mV (with zero humidity level) to 0.8 mV where it is stabilized around 12000 ppmv of humidity (Figure 27). A similar dependence of the shape of the photoacoustic signal obtained for NO in water has been observed in [65] and [66]. H. Wu et al have presented a similar plateau reached after 12000 ppmv.

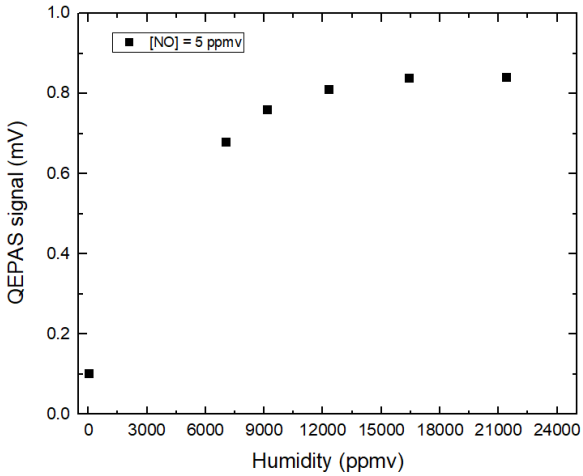

Figure 27: Photoacoustic signal obtained for nitric oxide in presence of different humidity levels. The concentration of NO in the experiment was maintained at 5 ppmv.

- **Isoprene in water**

The same study has been performed for isoprene, however, no significative effect of the level of humidity onto the photoacoustic signal has been observed (Figure 28). No qualitative or quantitative resource were found in the literature to confirm the effect of water as a collisional partner of isoprene.

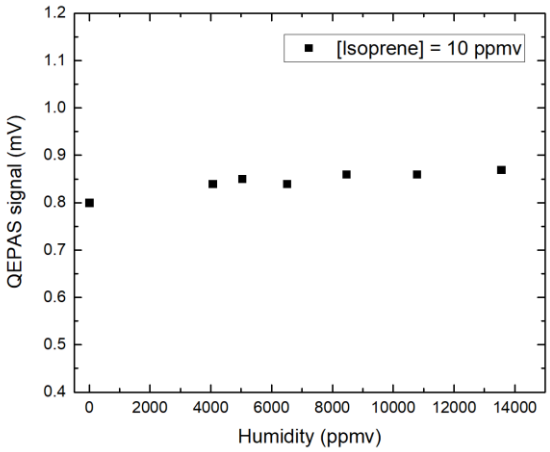

Figure 28: Photoacoustic signal obtained for isoprene in presence of different humidity levels

This measurement has not been performed on the acetone, no information has been found in the literature.

3.3- The quartz tuning fork

The QTF is a piezoelectric element originally designed for the watch industry as a clock oscillator of frequency 32768 Hz (2^{15}). Other applications have adapted the properties of this element to microscopy (AFM) [67] or even humidity sensors in which the QTF have

shown interesting and reliable measurements [68]. The consequence of its massive production is its very low cost and its availability. On a more "technical" aspect, the QTF response to an electrical excitation draws a sharp and intense Lorentzian shaped line around 32768 Hz underlining a very high quality factor. This Q-factor, around 8000 in atmospheric conditions of pressure and 100000 in vacuum, offers to QEPAS a strong immunity to background noises oppositely to the microphone that is characterized by a wide bandwidth (Figure 12).

The QTF is made of quartz: the piezoelectric properties of this material were discovered by Pierre and Jacques Curie in 1880. This reversible phenomenon can be seen as a coupling between the electrical and mechanical properties of the material. Succinctly, the mechanical deformation of the crystal causes the generation of electrical charges and conversely, the electrical excitation causes the deformation of the material. The QTF is etched along the z-axis of a quartz wafer with the two branches of the QTF (called prongs in this manuscript), perfectly symmetric, along the y-axis. Silver electrodes are deposited on each side of the prongs for charges collection. The orientation of the crystal and the deposition of the prongs define the possible vibrational modes [69].

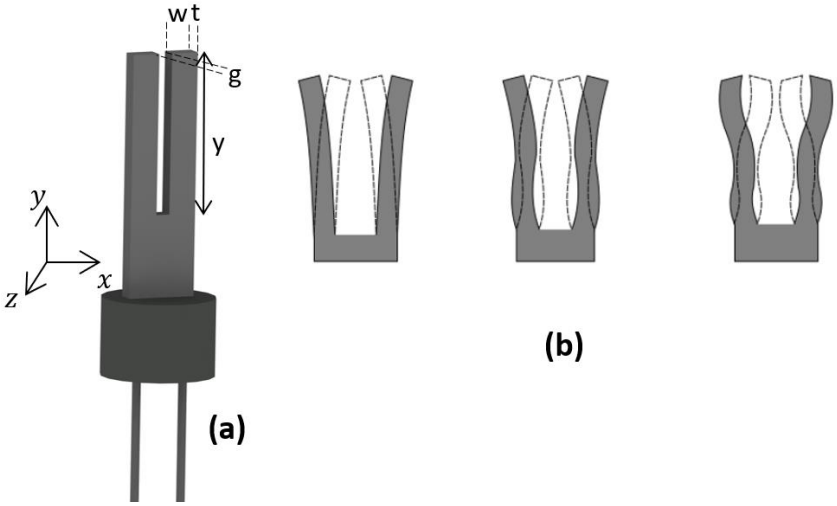

Figure 29: Scheme of (a) commercial quartz tuning fork with y= 4 mm, w= 0.6 mm, t= 0.33 mm and g= 0.3 mm. (b) presents the 1st ,2nd and 3rd in plane resonance of the QTF.

For a frequency of 32 kHz, exploited in QEPAS, the deformations are allowed in the plan axis of the QTF, oppositely and symmetrically to its centre of mass, that is kept unchanged. An approximation of Euler-Bernoulli beam theory can be used to describe the frequency of the vibrational modes. The vibrations are considered as very small displacements. Each prong is considered separately, one part of the prong is defined as clamped, i.e. motionless, and the other part is free [70].

$$EI\frac{\partial^4 y}{\partial x^4}(x,t) + \rho A\frac{\partial^4 y}{\partial t^4}(x,t) = 0 \qquad (2.24)$$

Where ρ is the density of quartz ($\rho = 2659\frac{kg}{m^3}$),
E is the Young's modulus of the quartz ($E = 7.87 \times 10^{10} N/m^2$)
I is the second moment of area in the z direction (m^2)
A prongs cross section m^2.

Resolving this equation gives the frequency of each flexural mode n [71]:

$$f_n = \frac{k_n^2 w}{2\pi y^2}\sqrt{\frac{E}{12\rho}} \tag{2.25}$$

Table 2: frequency of the three first resonance modes

n	k_n [71]	f_n (Hz)
1	1.875	32950
2	4.694	206500
3	7.855	578300

The electrical model of the QTF can be approximated by the Butterworth Von Dyke model as an RLC circuit in parallel with a capacitance representing a parasitic capacitance (Figure 30)

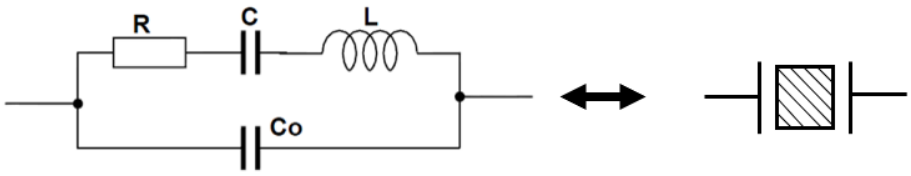

Figure 30: Electrical model of the QTF

The total impedance of the circuit can be written as:

$$\frac{1}{Z_{tot}} = \frac{1}{R + jL\omega + \frac{1}{jC\omega}} + jC_0\omega \tag{2.26}$$

For a lossless LC circuit, the angular frequency (ω_0) is introduced. This frequency is calculated at resonance, when the reactance equals zero and the inductance and capacitance are equal and behave synchronously and in phase. ω_0 can be defined as:

$$Z_L = Z_C \;\leftrightarrow\; \omega_0 L = \frac{1}{\omega_0 C} \;\leftrightarrow\; \omega_0 = \frac{1}{\sqrt{LC}} \tag{2.27}$$

Noting that

$$\omega_0 = 2\pi f_0 \tag{2.28}$$

The quality factor of a resonant circuit is defined as:

$$Q = \frac{\omega_0}{BW} = \frac{L}{R}\sqrt{\frac{L}{C}} = \frac{\omega_0 L}{R} = \frac{1}{\omega_0 RC} \tag{2.29}$$

The quality factor of a resonant circuit defines its ability to maintain its own energy when the exterior excitation is stopped.

By introducing Equation (2.28) and (2.29) into Equation (2.26), it is possible to rewrite Z_{tot} as:

$$\frac{1}{Z_{tot}} = \frac{\frac{1}{jL\omega}}{1 - \left(\frac{\omega_0}{\omega}\right)^2 - \frac{j\omega_0}{\omega Q}} + jC_0\omega \tag{2.30}$$

At resonance, the parasitic capacitance C_0 is considered very small. Therefore, the additional term $jC_0\omega$ can be neglected. Accordingly, the squared magnitude of the complex impedance can be written as in Equation (2.31) and describes a Lorentzian shaped function.

$$\left|\frac{1}{Z_{tot}}\right|^2 = \frac{1}{R^2}\frac{1}{1 + \left(\frac{2Q(\omega - \omega_0)}{\omega_0}\right)} \tag{2.31}$$

Using Proteus 8, the frequency response of the QTF is simulated for $R = 30\,k\Omega, L = 2kH, C = 0.012\,pF$ *and* $C_0 = 12pF$. The result is shown in Figure 31 presenting the Lorentzian line shape described by Equation (2.31) with the anti-resonance induced by C_0.

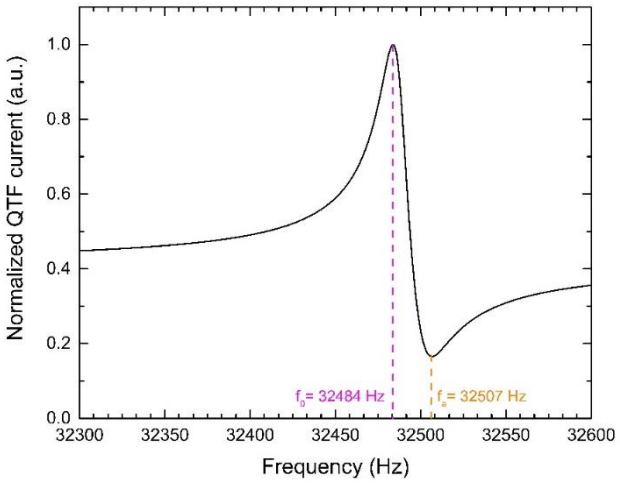

Figure 31: Normalized QTF current function of the excitation frequency. f_0 is the resonance frequency of the QTF and f_a is the anti-resonance.

Using Equation (2.26), f_0 can also be deduced and calculated for the values of L and C used in the simulation.

The anti-resonance induced by the parasitic capacitance occurs close to the resonance frequency and is calculated as [69]:

$$f_{c,a} = \frac{1}{2\pi}\sqrt{\frac{1}{L * \frac{CC_0}{C + C_0}}} = 32503\ Hz \tag{2.32}$$

- **Electrical characterization of the QTF**

The QTF can be characterized by using an electrical stimulation. This technique is very simple and rapid (approximately 10 sec) and can be used in daily experiments to calculate the resonance frequency f_0 and the Q-factor of the QTF (Figure 32a). The response of the latter is recorded under a sinewave excitation, of amplitude V_{exc} and frequency f_{exc} (Figure 32b).

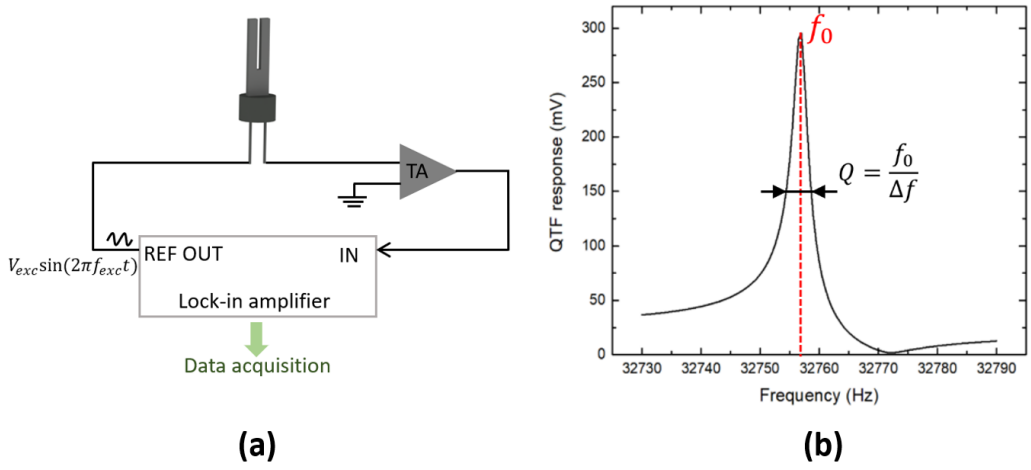

Figure 32: (a) Experimental setup of QTF characterization, (b) Frequency response of the QTF where f_0 is the resonance frequency of the QTF and Q its quality factor.

Usually in such characterization experiments, V_{exc} is taken equal to 1 mV and the frequency is swept over a chosen range of frequencies. The resonance frequency f_0 is used to calculate the Q-factor:

$$Q = \frac{f_0}{FWHM} = \frac{f_0}{\Delta f} \tag{2.33}$$

- **QTF characterization using a resonance tracking technique**

When an external perturbation is brought to an oscillating device, it oscillates according to the frequency imposed by the perturbation. When this perturbation is stopped, the oscillation goes back to the inner frequency of the device: it represents the relaxation phase. In the presented experimental setup (Figure 33) [72], a sinewave of frequency f_{exc} and amplitude V_{exc} is generated using a waveform generator (Tektronix AFG 1022).

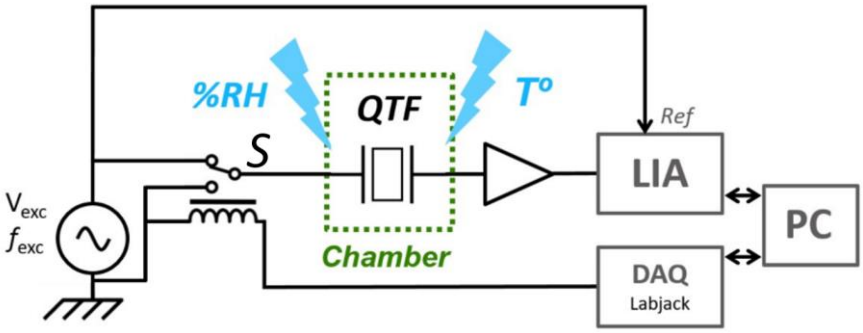

Figure 33: Resonance tracking of the QTF: experimental setup [16].

The measurement is performed following different steps:

- The sinewave is used to electrically excite the QTF (during t_{exc}).
- The excitation is stopped, the switch s is connected to the mass.
- The relaxation signal is recorded on the LIA.

The signal collected from the QTF is amplified with a transimpedance amplifier and demodulated with a Lock-in amplifier (Zurich Instruments MFLI) at the frequency f_{exc}. The collected signal has an exponential decay shape related to the beat frequency $f_0 - f_{exc}$. Its period and envelop are respectively described by Equation (2.34) and (2.35). While the former gives information about the instantaneous frequency of the QTF, the latter gives access to its quality factor.

$$T = \frac{1}{|f_0 - f_{exc}|} \tag{2.34}$$

$$V_{out}(t) = V_{exc} \cdot e^{\frac{-\pi t f_0}{Q}} \tag{2.35}$$

For instance, f_{exc} must be chosen close enough to f_0 to get a good accuracy on the demodulated signal but far enough to avoid $f_0 = f_{exc}$, leading to huge values of T (the period of the signal). In parallel, V_{exc} must be chosen big enough to avoid uncertainty on the demodulated signal but small enough to avoid the saturation of the LIA.

To determine the best experimental conditions, the effect of the sinewave parameters (f_{exc} and V_{exc}) on the QTF parameters (f_0 and Q) can be measured.

For a commercial QTF, the results are reported on Figure 34. For each data point, the demodulated signal is recorded for 60 seconds at a rate of 1 Hz. The mean value and the standard deviation are calculated. The acceptable error intervals for f_0 and Q leading to less than 1% error on the QEPAS signal is calculated (the calculation is detailed in Chapter 4 section 1) and represented by shaded areas. On Figure 34a, $|f_0-f_{exc}| = 20$ Hz and V_{exc} ranges from 3 to 300 mV_{pp}. In Figure 34b V_{exc} is fixed at 0.1 V_{pp} and f_{exc} is chosen to have $|f_0-f_{exc}|$ variation from 5 to 50 Hz.

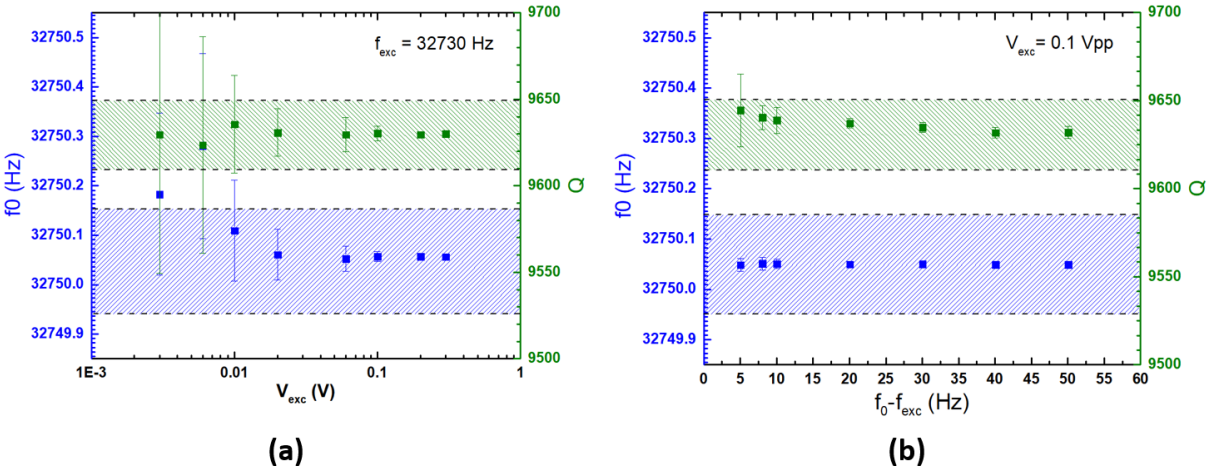

Figure 34: Measured QTF parameters as a function of the excitation amplitude (a) and the frequency (b). The hatched areas correspond to the target accuracy and the error bars to the standard deviation. The excitation time t_{exc} is set to 200 ms to ensure the QTF is at steady state before the onset of the relaxation.

On one hand, for variations of $|f_0-f_{exc}|$ in the range of [5, 50] Hz, f_0 showed a nearly flat response. These observations assure that the measurement is robust and will not be affected by a sudden shift of f_0. On the other hand, for low amplitudes, the large error bars illustrate the random error due to a poor signal-to-noise ratio (SNR). When the excitation amplitude increases, the dispersion decreases and mean values quickly converge. This study is useful to quantify the errors in the characterization set up.

The characterization of the QTF frequency and Q-factor can be done by the mean of the two techniques previously presented. While the former is suitable to stable measurement conditions (temperature, pressure, flow) where the QTF parameters are not affected and do not require to be correct, the latter is adapted to variating conditions as a real time correction of the QTF parameters can be performed.

4- Evaluation of the sensor's performances

4.1- Allan Deviation

An important parameter that was used to describe the sensors in the previous sections is the limit of detection (LOD). It is the lowest concentration of gas that can be detected by the sensor. The LOD is related to the signal-to-noise ratio and the concentration of gas.

Experimentally, the SNR is calculated by recording the measured signal for a known concentration of gas over a period of time. Then, the calculation of the Allan deviation is performed over the total range of data.

The Allan-Werle deviation is a statistical tool used to quantify the stability of the sensor. It has been widely used in spectroscopy and is often considered for 1σ, i.e. when the SNR is equal to 1. The SNR can be improved by increasing the averaging of the signal. Therefore, with a longer time constant a better SNR, thus a better LOD is obtained.

The signal containing N y_i data for a specific concentration of gas C_{gas} is recorded each Δt (Figure 35). A moving average is applied to this signal. The new signal contains $M = \frac{N}{k}$ subgroups originating from the first group. Each new group is separated by $\tau = k\Delta t$. The value of each subgroup m is calculated as the mean of the signal over k data. Therefore, we can write:

$$A_m(\tau) = \frac{1}{k}\sum_{i=1}^{k} y_{(m-1)k+i} \tag{2.36}$$

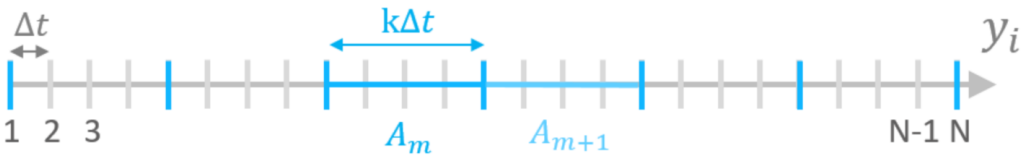

Figure 35: Working principle of the Allan-deviation, with k=4. [16]

The variance of these data can be calculated as:

$$\sigma^2 = \frac{1}{2(M-1)}\sum_{m=1}^{M}[A_m(\tau) - A_{m-1}(\tau)]^2 \tag{2.37}$$

Finally, the SNR is calculated as:

$$SNR(\tau) = \frac{\bar{y}}{\sigma(\tau)} \tag{2.38}$$

With $\bar{y}$ the mean of the variable y_i.

The LOD can be deduced:

$$LOD(\tau) = \frac{C_{gas}}{SNR(\tau)} \tag{2.39}$$

- **Example of Allan deviation measurement:**

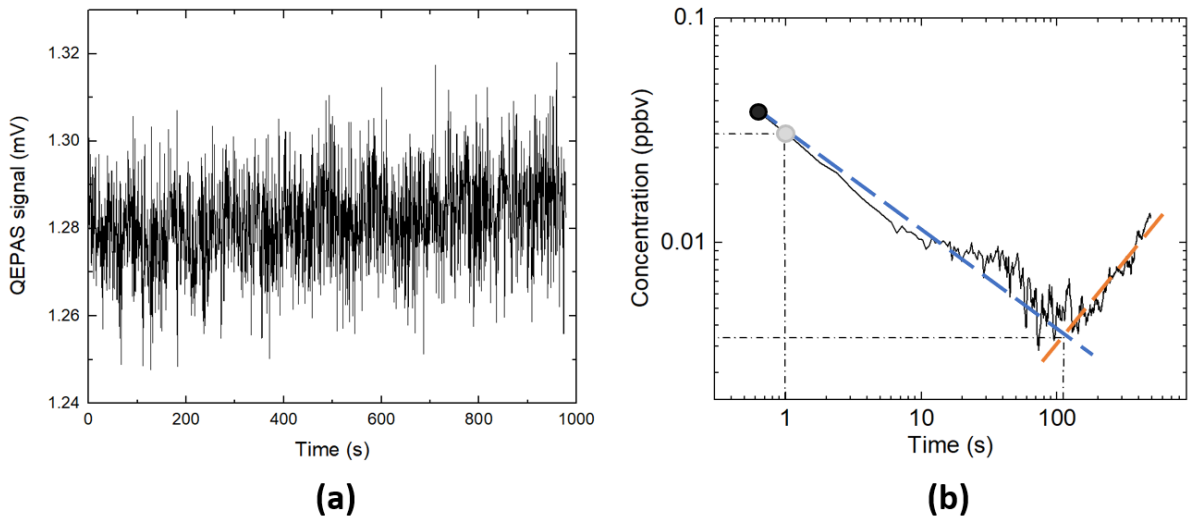

Figure 36: (a) Benzene QEPAS signal recorded over a period of time. (b) Associated Allan plot.

Figure 36a describes a typical signal recorded for Allan deviation calculation. The sensor's output signal is recorded for a certain period of time. The concentration of the gas (benzene, targeted with a laser at 14.8 µm) during that measurement was 5 ppmv. The Δt is here equal to 600 ms. The LOD of the system in this configuration is represented by the first point (black) on the Allan deviation curve (Figure 36b). The grey point at 1 second is often used to described sensors. During time increase, the LOD decreases, showing an amelioration of the detection limits as the averaging time increases. The slope of this first part is correlated to the noise. In QEPAS, this slope (blue curve) is characterized in $\tau^{-1/2}$, referring to the QTF Brownian noise (white noise). The optimum averaging time is obtained around 100 s. Finally, the Allan deviation increases in a linear drift due to low frequencies noises

4.2- NNEA

The Allan deviation is a suitable tool to estimate the stability of the system and quantify the LOD. This LOD can be used to calculate the Normalized Noise Equivalent Absorption (NNEA). The latter is more adapted for comparison between sensors. For example, comparing CO_2 detection between classical photoacoustic and QEPAS. This tool takes into account the power of the laser P (mW), the absorption coefficient at the LOD

concentration α_{LOD} and the integration bandwidth Δf. Most of the time, α_{LOD} is calculated for 1 s, therefore, $\Delta f = 1$. The NNEA is calculated as:

$$NNEA = \frac{\alpha_{LOD} P}{\sqrt{\Delta f}} . \quad (2.40)$$

The NNEA is expressed in $cm^{-1}.W.Hz^{-1/2}$. The lower the NNEA the more sensitive the sensor is.

5- Breath analysis performed with QEPAS.

Table 3 presents a sum up of the breath measurements performed with QEPAS sensors as well as the breath measurement performed with photoacoustic based sensors on SENSIR gases. For each study, the laser type, power and wavelength are reported and the limit of detection compared with the concentration of the target gas in the exhaled breath.

Table 3: QEPAS and PAS for breath analysis

Ref	Techniques	Laser Type WN P	Gas	LOD	Breath sampling	Concentration
[73]	BF-QEPAS On-beam	QCL – 10.359 μm – 48 mW	NH_3	9.5 ppbv (1 s)	On-line 8 volunteers	150-640 ppbv
[74]	QEPAS On beam	DFB Diode laser – 1531.68 nm – 500mW	NH_3	14 ppbv (1 s)	On-line 3 volunteers	170-230 ppbv
[64]	QEPAS Off-beam	FP QCL – 4.7 μm - 100mW	CO	20 ppbv (1 s)	On-line 14 volunteers	0.35-23.2 ppmv
[75]	QEPAS On-beam	DFB-QCL – 10.34 μm – 22 mW	NH_3	6 ppbv (1 s)	On-line	~ 450ppbv
[76]	PAS H-type cavity	CO_2 Laser - 10.59 μm - 36.2 mW	C_3H_6O	11 ppbv	Off-line	Healthy: 200-450 ppbv Cancer patients: 400-720 ppbv
			C_2H_4	6 ppbv		39-201 ppbv
			NH_3	3 ppbv		685-2364 ppbv
[77]	PAS H-type cavity	CO_2 Laser - 10.59 μm – 36.2 mW	C_3H_6O	11 ppbv	Off-line 10 patients 30 volunteers	Healthy: 128-819 ppbv Renal patients: 628-941 ppbv
			C_2H_4	8 ppbv		Healthy: 46-245 ppbv Renal patients: 167-213 ppbv
			NH_3	3 ppbv		Healthy: 452-2420 ppbv Renal patients: 4473-5361ppbv

Conclusion

In order to perform breath measurements and provide the most reliable results, different features were defined. These characteristics also represent the difficulty of performing in vivo measurement. To resume, the main characteristics, if the price and size are excluded, are the selectivity, the sensitivity and the real time measurement. Infrared sensors and more precisely photoacoustic based gas sensors appear as very good candidates as they combine these three points. Amongst the photoacoustic technique, QEPAS was chosen to conduct the measurement presented in this manuscript. The different part composing the QEPAS sensor were described in this chapter. The spectrophone composed of the QTF as an acoustic transducer and an acoustic cavity plays an important role on the sensitivity of the sensor. This block will be studied in the next chapter.

References

[1] A. Chauhan, "GC-MS Technique and its Analytical Applications in Science and Technology," *J. Anal. Bioanal. Tech.*, vol. 5, no. 6, 2014, doi: 10.4172/2155-9872.1000222.

[2] M. R. Ras, F. Borrull, and R. M. Marcé, "Sampling and preconcentration techniques for determination of volatile organic compounds in air samples," *TrAC - Trends Anal. Chem.*, vol. 28, no. 3, pp. 347–361, 2009, doi: 10.1016/j.trac.2008.10.009.

[3] "Yole report on gas sensors. Website accessed on 06-01-2023 : https://www.yolegroup.com/press-release/gas-and-particle-sensors-a-2-2b-market-in-2026/." .

[4] Z. Yunusa, M. N. Hamidon, A. Kaiser, and Z. Awang, "Gas Sensors: A Review," *Sensors & Transducers*, vol. 168, no. 4, pp. 61–75, 2014, [Online]. Available: http://www.sensorsportal.com.

[5] A. T. Güntner, N. J. Pineau, D. Chie, F. Krumeich, and S. E. Pratsinis, "Selective sensing of isoprene by Ti-doped ZnO for breath diagnostics," *J. Mater. Chem. B*, vol. 4, no. 32, pp. 5358–5366, 2016, doi: 10.1039/c6tb01335j.

[6] Eric Bakker and Martin Telting-Diaz, "Electrochemical sensors," *Bioeng. Innov. Solut. Cancer*, vol. 74, no. 12, pp. 47–71, 2019, doi: 10.1016/B978-0-12-813886-1.00004-8.

[7] "Electrochemical sensors, Chapter 2, p 27-35. Website accessed on 06-01-2023 : https://www.yumpu.com/en/document/read/37565118/chapter-2-electrochemical-sensors-international-sensor-technology." .

[8] Emerson Automation Solution, "Electrochemical vs . Semiconductor Gas Detection – a Critical Choice," *Ind. Autom. Asia*, pp. 42–43, 2019.

[9] A. Mirzaei, H. R. Ansari, M. Shahbaz, J. Y. Kim, H. W. Kim, and S. S. Kim, "Metal Oxide Semiconductor Nanostructure Gas Sensors with Different Morphologies," *Chemosensors*, vol. 10, no. 7, 2022, doi: 10.3390/chemosensors10070289.

[10] Y. H. Ochoa-Muñoz, R. Mejía de Gutiérrez, and J. E. Rodríguez-Páez, "Metal Oxide Gas Sensors to Study Acetone Detection Considering Their Potential in the Diagnosis of Diabetes: A Review," *Molecules*, vol. 28, no. 3, 2023, doi: 10.3390/molecules28031150.

[11] G. Li, X. Zhu, J. Liu, S. Li, and X. Liu, "Metal Oxide Semiconductor Gas Sensors for Lung Cancer Diagnosis," *Chemosensors*, vol. 11, no. 4, 2023, doi: 10.3390/chemosensors11040251.

[12] "IRNET-PRO 32MM : https://www.nenvitech.com/products/ndir-sensors/irnet-pro-32/." .

[13] T. L. Cottrell and J. McCoubrey, "Molecular energy transfer in gases," *Educ. Psychol. Meas.*, 1961.

[14] N. S. Prasad, "Optical communications in the mid-wave IR spectral band," *J. Opt. Fiber Commun. Reports*, vol. 2, no. 6, pp. 558–602, 2005, doi: 10.1007/s10297-005-0057-x.

[15] I. E. Gordon *et al.*, "The HITRAN2016 molecular spectroscopic database," *J. Quant. Spectrosc. Radiat. Transf.*, vol. 203, pp. 3–69, 2017, doi: 10.1016/j.jqsrt.2017.06.038.

[16] R. Rousseau, "QEPAS gas sensor for air quality monitoring," 2019.
[17] J. Hodgkinson and R. P. Tatam, "Optical gas sensing: A review," *Meas. Sci. Technol.*, vol. 24, no. 1, 2013, doi: 10.1088/0957-0233/24/1/012004.
[18] R. K. Jha, "Non-Dispersive Infrared Gas Sensing Technology: A Review," *IEEE Sens. J.*, vol. 22, no. 1, pp. 6–15, 2022, doi: 10.1109/JSEN.2021.3130034.
[19] "LI-7500A Open Path CO2/H2O Analyzer. www.licor.com."
[20] "TreyMed CO2 - COMET II and COMET I - sensors : https://www.treymed.com/capno/sensor/sensor.htm."
[21] "ATS/ERS recommendations for standardized procedures for the online and offline measurement of exhaled lower respiratory nitric oxide and nasal nitric oxide, 2005," *Am. J. Respir. Crit. Care Med.*, vol. 171, no. 8, pp. 912–930, 2005, doi: 10.1164/rccm.200406-710ST.
[22] R. O. Crapo, R. L. Jensen, and J. S. Wanger, "Single-breath carbon monoxide diffusing capacity," *Clin. Chest Med.*, vol. 22, no. 4, pp. 637–649, 2001, doi: 10.5339/qmj.2003.1.28.
[23] "'NIOX FENO. Website 09-26-2023: https://www.niox.com/en/niox-vero/niox-technology/.'" .
[24] "'NObreathFENO. Website accessed on 09-26-2023: https://www.nobreathfeno.com/us/nobreath/.'" .
[25] "'FENO medisoft. Website accessed on 09-26-2023: https://mgcdiagnostics.com/fr/produits/feno.'" .
[26] "'Ecomedics. Analyzer CLD 88. Website accessed on 09-26-2023: https://www.ecomedics.com/products/analyzer-cld-88-sp/.'" .
[27] "'Cubic Sensor. Cubic Gasboard-2050. Website accessed on 09-26-2023: https://en.gassensor.com.cn/Spirometer/info_itemid_1019.html.'" .
[28] "'nddMed EasyOne Pro. Website accessed on 09-26-2023: https://nddmed.com/products/complete-pft/easyone-pro.'" .
[29] "'Medisoft Hypair. Website accessed on 09-26-2023: https://mgcdiagnostics.com/fr/produits/hypair-systeme-de-test-de-la-fonction-pulmonaire.'" .
[30] L. Lukasiak and A. Jakubowski, "History of semiconductors.," *J. Telecommun. Inf. Technol.*, doi: 10.2320/materia1962.29.18.
[31] E. Tournié and L. Cerutti, *Mid-infrared Optoelectronics Materials, Devices, and applications*, Elsevier. 2020.
[32] "'Website accessed on 09-26-2023: https://exalos-vision.com/bridge-the-gap-superluminescent-leds/.'" .
[33] "'Website accessed on09-26-2023: https://www.scivax.com/en/application/dfb/.'" pp. 35–50.
[34] A. G. Bell, "On the Production and Peproduction of Sound by Light," 1880.
[35] L. B. Kreuzer, "Ultralow gas concentration infrared absorption spectroscopy," *J. Appl. Phys.*, vol. 42, no. 7, pp. 2934–2943, 1971, doi: 10.1063/1.1660651.
[36] "'SPU0410LR5H-QB. Website accessed on 09-28-2023: https://www.knowles.com/subdepartment/dpt-microphones/subdpt-sisonic-surface-mount-mems.'"
[37] C. Xu, S. Rassel, S. Zhang, A. Aloraynan, and D. Ban, "Single-wavelength water muted photoacoustic system for detecting physiological concentrations of endogenous molecules," *Biomed. Opt. Express*, vol. 12, no. 1, p. 666, 2021, doi:

10.1364/boe.413086.
[38] P. Zbysiński and T. Starecki, "Multichannel Detection of Photoacoustic Signals: Preliminary Results," *Int. J. Thermophys.*, vol. 36, no. 9, pp. 2342–2350, 2015, doi: 10.1007/s10765-015-1929-9.
[39] R. Rousseau, D. Ayache, N. Maurin, W. Trzpil, M. Bahriz, and A. Vicet, "Monolithic Double Resonator for Quartz Enhanced Photoacoustic Spectroscopy," *Appl. Sci.*, vol. 11, no. 5, p. 2094, 2021, doi: 10.3390/app11052094.
[40] A. Aloraynan, S. Rassel, C. Xu, and D. Ban, "A Single Wavelength Mid-Infrared Photoacoustic Spectroscopy for Noninvasive Glucose Detection Using Machine Learning," *Biosensors*, vol. 12, no. 3, pp. 1–19, 2022, doi: 10.3390/bios12030166.
[41] Z. Bozóki, A. Pogány, and G. Szabó, "Photoacoustic instruments for practical applications: Present, potentials, and future challenges," *Appl. Spectrosc. Rev.*, vol. 46, no. 1, pp. 1–37, 2011, doi: 10.1080/05704928.2010.520178.
[42] A. Miklós, P. Hess, and Z. Bozóki, "Application of acoustic resonators in photoacoustic trace gas analysis and metrology," *Review of Scientific Instruments*, vol. 72, no. 4. pp. 1937–1955, 2001, doi: 10.1063/1.1353198.
[43] M. Duquesnoy, "Tuning forks in photoacoustic spectroscopy : Comparative study and new developments," 2021.
[44] V. Zéninari, B. Parvitte, D. Courtois, V. A. Kapitanov, and Y. N. Ponomarev, "Methane detection on the sub-ppm level with a near-infrared diode laser photoacoustic sensor," *Infrared Phys. Technol.*, vol. 44, no. 4, pp. 253–261, 2003, doi: 10.1016/S1350-4495(03)00135-X.
[45] K. Wilcken and J. Kauppinen, "Optimization of a Microphone for Photoacoustic Spectroscopy," *Appl. Spectrosc.*, vol. 57, no. 9, pp. 1087–1092, 2003, doi: 10.1366/00037020360695946.
[46] A. A. Kosterev, Y. A. Bakhirkin, R. F. Curl, and F. K. Tittel, "Quartz-enhanced photoacoustic spectroscopy," *Opt. Lett.*, vol. 27, no. 21, 2002, doi: 10.3969/j.issn.1001-0548.2015.06.025.
[47] K. Chamassi, "Détecteur de gaz multi-espèces par mesure photo-acoustique à effet capacitif," 2018.
[48] W. Trzpil, N. Maurin, R. Rousseau, D. Ayache, A. Vicet, and M. Bahriz, "Analytic optimization of cantilevers for photoacoustic gas sensor with capacitive transduction," *Sensors*, vol. 21, no. 4, pp. 1–22, 2021, doi: 10.3390/s21041489.
[49] T. Seoudi *et al.*, "Highly Sensitive Capacitive MEMS for Photoacoustic Gas Trace Detection," *Sensors*, vol. 23, no. 6, 2023, doi: 10.3390/s23063280.
[50] R. Arndt, "Analytical line shapes for Lorentzian signals broadened by modulation," *J. Appl. Phys.*, vol. 36, no. 8, pp. 2522–2524, 1965, doi: 10.1063/1.1714523.
[51] P. Kluczynski and O. Axner, "Theoretical description based on Fourier analysis of wavelength-modulation spectrometry in terms of analytical and background signals," *Appl. Opt.*, vol. 38, no. 27, p. 5803, 1999, doi: 10.1364/ao.38.005803.
[52] P. Kluczynski, Å. M. Lindberg, and O. Axner, "Background signals in wavelength-modulation spectrometry with frequency-doubled diode-laser light. I. Theory," *Appl. Opt.*, vol. 40, no. 6, pp. 783–793, 2001, doi: 10.1364/AO.40.000783.
[53] S. Schilt, "Mesure de traces de gaz à l'aide de lasers à semi-conducteur," 2002.
[54] S. Schilt, L. Thévenaz, and P. Robert, "Wavelength Modulation Spectroscopy: Combined Frequency and Intensity Laser Modulation," *Appl. Opt.*, vol. 42, no. 33, p. 6728, 2003, doi: 10.1364/ao.42.006728.

[55] A. Vicet, "Etude et réalisation d'un analyseur multigaz à diodes lasers accordables." 2001.
[56] L. Dong, A. A. Kosterev, D. Thomazy, and F. K. Tittel, "QEPAS spectrophones: Design, optimization, and performance," *Appl. Phys. B Lasers Opt.*, vol. 100, no. 3, pp. 627–635, 2010, doi: 10.1007/s00340-010-4072-0.
[57] H. Yi *et al.*, "An acoustic model for microresonator in on-beam quartz-enhanced photoacoustic spectroscopy," *Appl. Phys. B Lasers Opt.*, vol. 108, no. 2, pp. 361–367, 2012, doi: 10.1007/s00340-012-4988-7.
[58] D. A. Diaz Thomas, "Design, fabrication and investigation of Interband Cascade structures for mid-IR VCSELs," 2020.
[59] B. E. A. Saleh and M. C. Teich, *Fundamentals of photonics*. john Wiley & sons, 2019.
[60] G. Wysocki, A. A. Kosterev, and F. K. Tittel, "Influence of molecular relaxation dynamics on quartz-enhanced photoacoustic detection of CO2 at λ =2 μm," *Appl. Phys. B Lasers Opt.*, vol. 85, no. 2–3, pp. 301–306, 2006, doi: 10.1007/s00340-006-2369-9.
[61] J. P. Besson, "Photoacoustic spectroscopy for multi-gas sensing using near infrared lasers," *Lab. nanophotonique métrologie*, vol. Ph.D., no. Thèse No. 3670 (2006), pp. 1–189, 2006.
[62] S. Schilt and L. Thévenaz, "Methane monitoring by near infrared photoacoustic spectroscopy: The importance of relaxation phenomena," no. June, pp. 1–5, 2005, doi: 10.1051/jp4.
[63] J. Hayden, B. Baumgartner, and B. Lendl, "Anomalous humidity dependence in photoacoustic spectroscopy of CO explained by kinetic cooling," *Appl. Sci.*, vol. 10, no. 3, 2020, doi: 10.3390/app10030843.
[64] N. Maurin *et al.*, "First clinical evaluation of a quartz enhanced photo-acoustic CO sensor for human breath analysis," *Sensors Actuators, B Chem.*, vol. 319, no. April, p. 128247, 2020, doi: 10.1016/j.snb.2020.128247.
[65] R. Sarmiento, I. E. Santosa, S. T. Persijn, L. J. J. Laarhoven, and F. J. M. Harren, "Trace nitric oxide detection using CO-laser photoacoustic spectroscopy," *Forum Acusticum Budapest 2005 4th Eur. Congr. Acustics*, no. January, 2005.
[66] H. Wu *et al.*, "Ppb-level nitric oxide photoacoustic sensor based on a mid-IR quantum cascade laser operating at 52 °C," *Sensors Actuators, B Chem.*, vol. 290, no. April, pp. 426–433, 2019, doi: 10.1016/j.snb.2019.04.007.
[67] H. Edwards, L. Taylor, W. Duncan, and A. J. Melmed, "Fast, high-resolution atomic force microscopy using a quartz tuning fork as actuator and sensor," *J. Appl. Phys.*, vol. 82, no. 3, pp. 980–984, 1997, doi: 10.1063/1.365936.
[68] X. Zhou, T. Jiang, J. Zhang, X. Wang, and Z. Zhu, "Humidity sensor based on quartz tuning fork coated with sol-gel-derived nanocrystalline zinc oxide thin film," *Sensors Actuators, B Chem.*, vol. 123, no. 1, pp. 299–305, 2007, doi: 10.1016/j.snb.2006.08.034.
[69] T. N. Ba, "Mesures de traces de gaz par spectroscopie d ' absorption par diodes laser accordables . Application à la surveillance de l ' environnement .," 2014.
[70] M. Christen, "Air and gas damping of quartz tuning forks," *Sensors and Actuators*, vol. 4, no. C, pp. 555–564, 1983, doi: 10.1016/0250-6874(83)85067-7.
[71] S. L. Ahlstrom *et al.*, "Frequency-dependent drag from quantum turbulence produced by quartz tuning forks in superfluid He 4," *Phys. Rev. B - Condens. Matter Mater. Phys.*, vol. 89, no. 1, pp. 22–24, 2014, doi: 10.1103/PhysRevB.89.014515.

[72] R. Rousseau, N. Maurin, W. Trzpil, M. Bahriz, and A. Vicet, "Quartz tuning fork resonance tracking and application in quartz enhanced photoacoustics spectroscopy," *Sensors (Switzerland)*, vol. 19, no. 24, 2019, doi: 10.3390/s19245565.
[73] B. Li, C. Feng, H. Wu, S. Jia, and L. Dong, "Calibration-free mid-infrared exhaled breath sensor based on BF-QEPAS for real-time ammonia measurements at ppb level," *Sensors Actuators B Chem.*, vol. 358, May 2022, doi: 10.1016/j.snb.2022.131510.
[74] Z. Shang *et al.*, "Quartz-enhanced photoacoustic NH3 sensor exploiting a large-prong-spacing quartz tuning fork and an optical fiber amplifier for biomedical applications," *Photoacoustics*, vol. 26, Jun. 2022, doi: 10.1016/j.pacs.2022.100363.
[75] R. Lewicki *et al.*, "Real time ammonia detection in exhaled human breath using a distributed feedback quantum cascade laser based sensor," *Quantum Sens. Nanophotonic Devices VIII*, vol. 7945, p. 79450K, 2011, doi: 10.1117/12.874887.
[76] Mitrayana, D. K. Apriyanto, and M. Satriawan, "CO2 Laser photoacoustic spectrometer for measuring acetone in the breath of lung cancer patients," *Biosensors*, vol. 10, no. 6, May 2020, doi: 10.3390/BIOS10060055.
[77] Mitrayana, J. G. Nikita, M. A. J. Wasono, and M. Satriawan, "CO2 laser photoacoustic spectrometer for measuring ethylene, acetone, and ammonia in the breath of patients with renal disease," *Sens. Bio-Sensing Res.*, vol. 30, Dec. 2020, doi: 10.1016/j.sbsr.2020.100387.

Chapter 3
Towards the optimization of the spectrophone

In the previous chapter, the QEPAS experimental setup was introduced. Basically, this sensor is composed of a light source, in our case, a single mode semiconductor laser, and a spectrophone. The first part of this chapter aims to describe the different configurations of spectrophone that have been adopted in QEPAS experiments over the years and compare their performances. The second part focuses on the off-beam configuration employed to perform the experiments presented in this manuscript. Ultimately, the spectrophone is composed of the QTF (acoustic transducer) and an acoustic cavity, that can be referred to as a microresonator (mR). In this part, an analytical and a numerical model are implemented, and compared, in order to understand the behaviour of the acoustic wave generated inside the cavity and optimize the performances of the sensor.

1- Acoustic cavities used in QEPAS

Since it has been introduced in 2002, different approaches have been investigated for the improvement of the sensor sensitivity. In QEPAS, the amplitude of the output signal depends on the amount of charges generated by piezoelectrical effect by the QTF. The latter depends on the mechanical displacement of the QTF generated by the acoustic force applied by the acoustic wave, which is proportional to the concentration of target gas. To enhance the collected signal, different approaches, aiming to amplify the acoustic wave, have been adopted. In [1], three different configurations are presented by the authors:

- The "bare" configuration: the laser's beam arrives perpendicularly and is directly focused between the prongs of the QTF,
- The "in-plane" configuration: the laser's beam is in plane with the QTF,
- The "on-beam" configuration: the laser's beam is focused inside a designed acoustic cavity, perpendicularly to the QTF's prongs.

Amongst these three configurations, the "on-beam" shows the best results. The acoustic cavity helps confining and amplifying the acoustic wave between the prongs of the QTF, just like it can be done with music instruments. In [1], the mR is made of two tubes placed symmetrically on each side of the QTF and the acoustic wave can be treated as a stationary

wave with an antinode occurring between the tubes. The length L of the tube is calculated with basic equations ($L = \frac{c}{2f}$) giving L = 5.3 mm as half the wavelength of the sound at $f = 32.77\ kHz$. The length L includes the tubes length, the space between the QTF and each tube and the prongs' thickness. The cavity is here designed from a stainless-steel capillary with inner and outer diameter (ID – OD) respectively equal to 0.51 and 1.59 mm. The optimized position of the laser's beam is found at the centre of the prongs and at 0.7 mm from their opening (Figure 1). The NNEA in this configuration is equal to $1.2 \cdot 10^{-7}\ cm^{-1} \cdot W \cdot Hz^{-\frac{1}{2}}$ for CH_4 detection which implies a factor 7.3 of enhancement compared to the bare configuration (NNEA = $8.8 \cdot 10^{-7} cm^{-1} \cdot W \cdot Hz^{-\frac{1}{2}}$).

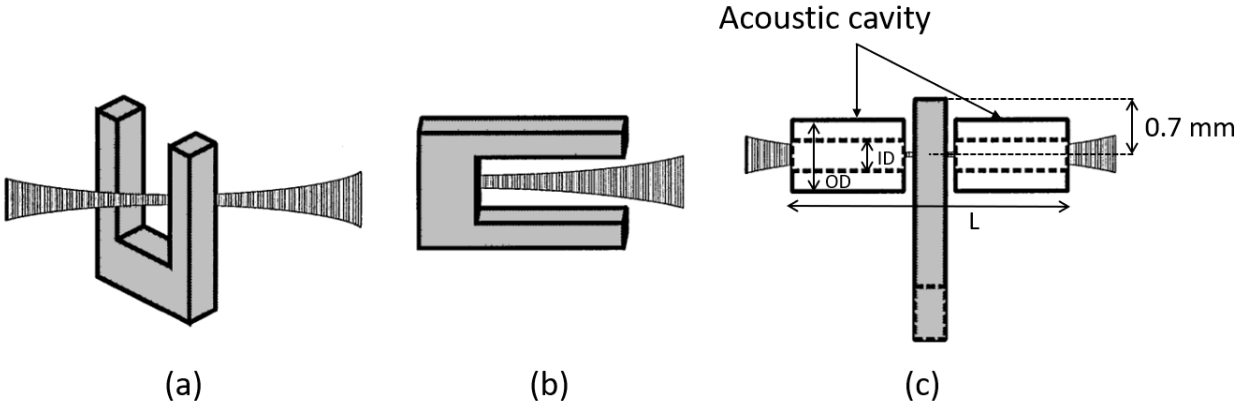

Figure 1: (a) bare, (b) in plane and (c) on-beam configurations presented in [1].

An important part in the optimization of the QEPAS system is placed into the investigation of the mR's geometric parameters (length and diameter) and their relative position to the QTF. Indeed, a better coupling between the two elements composing the spectrophone would necessarily lead to an enhancement of the system's sensitivity. In an ideal case, the maximum of the acoustic pressure should occur between the prongs of the QTF. In 2010, Dong et al [2] have compared the performances of their QEPAS system (detecting C_2H_2) using cavities with different lengths, IDs and ODs values. The first conclusion was that the two tubes cannot be treated as a single tube and that the efficient length of the tube is found between $\lambda/4$ and $\lambda/2$. The optimization of these parameters has resulted in an enhancement of 30 on the signal to noise ratio (SNR) compared to the "bare" configuration.

After this first publication in 2002, QEPAS have raised interest in different research teams as the performances were close to what was achieved with other gas detection techniques. Indeed, the comparison of the on-beam QEPAS and conventional PAS in the detection of C_2H_2 has concluded to very close performances of both sensors ($NNEA_{QEPAS} = 4.1 \cdot 10^{-9}$ and $NNEA_{PAS} = 5.4 \cdot 10^{-9}\ cm^{-1} \cdot W \cdot Hz^{-\frac{1}{2}}$) with a better SNR for the QEPAS. The work has been focused on the optimization of this new detection technique and the proposition of new configurations implying sometimes more than one mR and/or QTF (Table 1).

In 2009, a new configuration is presented by K. Liu et al [3]. This new design is called "off-beam" as the light of the laser is no longer directed between QTF's prongs but inside an acoustic cavity. Here, the acoustic cavity is composed of a tube with a small slit in the middle used to direct the acoustic wave to the QTF. The latter is used as a probe for the generated acoustic wave (Figure 2).

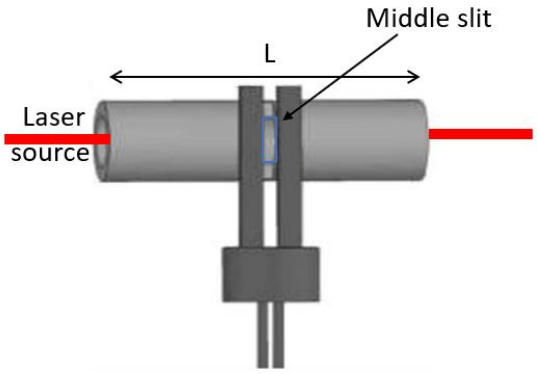

Figure 2: QEPAS spectrophone in off-beam configuration. [3]

The main advantage of this configuration is the decrease of the potential photothermal perturbation induced by the laser hitting the QTF's prongs. The alignment of the laser becomes easier and the technique more adapted to larger laser beams. One drawback of this configuration is the weak coupling between the mR and the QTF and the decrease of the QTF Q-factor induced by viscous losses occurring as air is trapped between the QTF prongs and the surface of the QTF. The optimization of the mR geometry becomes crucial to avoid a complete confinement of the acoustic wave inside the main tube. The experiments conducted reached an $NNEA = 5.9 \cdot 10^{-9}\, cm^{-1} \cdot W \cdot Hz^{-\frac{1}{2}}$close to [2]'s performances. They also investigated the effect of the gap between the mR and the QTF [4]. For instance, a large distance between these two elements lowers their coupling but a very small gap increases viscous damping of the QTF created by very thin air gaps. An amelioration of the mR is proposed to counter these losses [4]. By removing the material from each side of the slit, the distance between the surface of the prongs and the external walls of the mRs is increased, resulting in a reduction of the air trapped between the two surfaces (Figure 3).

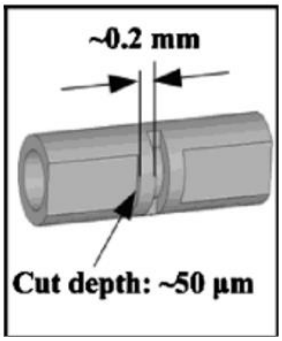

Figure 3: Modified mR proposed by [4]. The surface of the mR is digged in order to increase the space between the QTF and the cavity walls.

H. Yi et al [5] have used acoustic impedances to propose a theoretical approach to determine the mR dimensions in the off-beam configuration. The model is based on the assumption that the mR can be treated as a one-dimensional resonator witnessing longitudinal acoustic resonance as the radius of the mR (ID ~ mm) is much smaller than its length L. The effective lengths are calculated by introducing end-correction taking into account the acoustic radiation outside the tube. In a publication using the same strategy, this research team have presented a T-shaped mR [6], structured exactly as in [3], but replacing the middle slit by a small tube. In contrast with the classic "off-beam" where the slit has to be "digged" at the middle of the main tube, the T-shape can be designed more precisely. The improvement on the signal to noise ratio compared to the "bare" configuration is close to 30, matching the performances of the on-beam configuration [2].

The material used for the design of the mRs has been discussed but the observed improvement in the system's performances could not be exclusively attributed to the use of glass [7], silica, aluminium [8] or stainless-steel tubes. Nevertheless, R. Rousseau [9] have conducted an interesting work on mRs in "T-shaped" configuration investigating different printing techniques and shapes for the small tube. This work has led to the conclusion that micromachined mRs present, indeed, a better quality factor due to the fact that their surfaces are smoother than the 3D printed ones. However, the latter gives more freedom in the choice of the shape. For instance, QEPAS measurements were conducted by the author with different shapes of mR and the best results are presented for an obround-shaped 3D printed mR.

The optimization of the geometric parameters of the mR by performing an empirical work is not always adequate especially when the parameters are interdependent. Firebraugh et al [10] have developed a finite element model using COMSOL Multiphysics to study the on-beam configuration. This work outlines the importance of including the thermal and viscous losses on the inner part of the tube and helps understanding the correlation between each parameter even if the results do not match the experiments conducted by Dong et al [2]. In 2012, Y. Cao et al [11] have used a similar model, including Acoustic Pressure and Piezo Solid modules on COMSOL. This model draws a good agreement with experimental results presented by [2] and [1]:

- The optimum of length is found between $\lambda/4$ and $\lambda/2$.
- The offset on the position of the laser beam regarding the opening of the prongs is found around 0.6 mm.
- An interdependence is found between L and ID: the optimum ID changes when L changes. However, the photoacoustic signal is maximized for thinner tubes.
- The coupling between the mR and the QTF is increased when the gap between each tube and the QTF is reduced. Nevertheless, it is necessary to keep in mind what can exactly be achieved in real life applications, notably, the difficulty of alignment caused by an inadequate, small gaps.

These four configurations: “bare”, “on-beam”, “off-beam” and “T-shape” compose the basic designs of the QEPAS detection technique. However, one can say that research teams do not lack imagination when it comes to improving the performances of their systems. In Table 1, different configurations of the spectrophone are summed up showing the associated NNEA. Some of these designs might be complex to implement but they remain attractive to investigate as the SNR is enhanced by the multiple excitations of the QTF. It is noticed that the NNEA, demonstrating the performances of the sensor, even for more elaborated configuration, still ranges between 10^{-8}-10^{-9}.

Table 1: Different types of QEPAS spectrophones and the performances associated to their implementation

Ref.	Spectrophone configuration	Spectrophone picture	Gaz - wavenumber (cm^{-1})	P (mW)	TC (s)	NNEA ($cm^{-1}W/\sqrt{Hz}$)
[1]	Bare	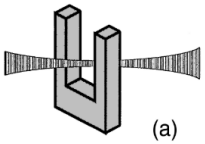	CH_4 5999.5	2	1	$8.8 \cdot 10^{-7}$
[12]	Multi quartz "Bare"	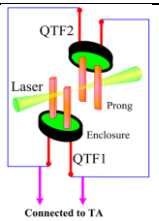	H_2O 7168.4	12.6	1	$5.95 \cdot 10^{-8}$
[1]	On-beam	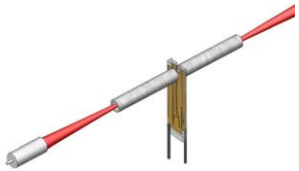	CH_4 5999.5	2	1	$1.2 \cdot 10^{-7}$
[2]			C_2H_2 6529.17	46	1	$3.3 \cdot 10^{-9}$
[13]	Half on-beam		H_2O 7161.41	8	1	$5.3 \cdot 10^{-9}$
[14]	Single tube on-beam	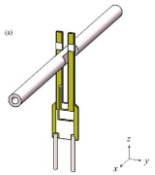	CO_2 6361.25	40	1	$1.21 \cdot 10^{-8}$

[15]	Double on-beam	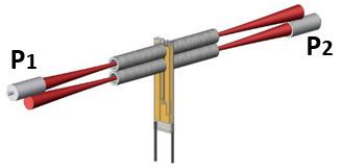	H_2O 7296.65	P1=19 P2=13	0.3	$8.1 \cdot 10^{-9}$ $\sim 4.5 \cdot 10^{-9}$
[16]	Multi quartz on-beam	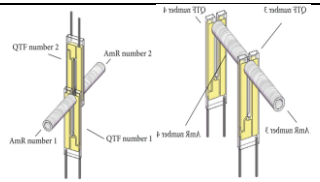	H_2O 7308.82	5.4		$1.24 \cdot 10^{-9}$
[17]	Double on-beam with prism	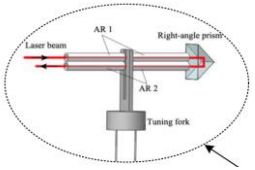	H_2O 7306.79	6.8	0.2	$5.8 \cdot 10^{-8}$
[3]	Off-beam		H_2O 7161.41	8	1	$5.9 \cdot 10^{-9}$
[4]			H_2O 7161.41	8	1	$6.2 \cdot 10^{-9}$
[6]	T- shape	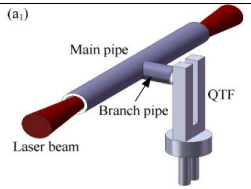	H_2O 7161.41	8	1	$3.9 \cdot 10^{-9}$

[18]	Double pass off-beam	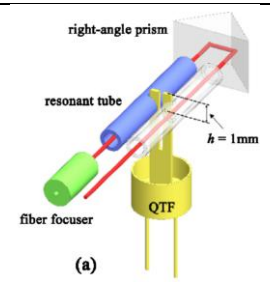	CH_4 6046.95	3.74	0.3	$1.8 \cdot 10^{-8}$
[19]	Double pass off-beam	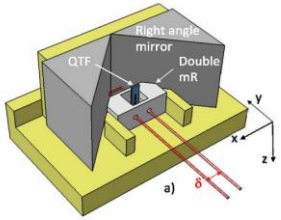	H_2O 7181.18	6	0.5	$1.2 \cdot 10^{-8}$
[20]	Double pass off-beam	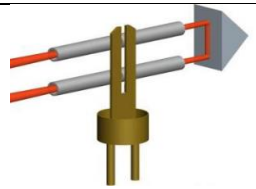	CH_4 6046.95	10		$7.76 \cdot 10^{-8}$
[21]	Four off-beam	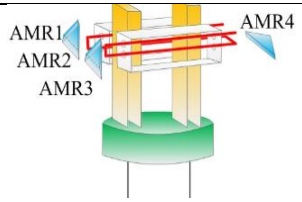	H_2O 7306.75	12		$1.27 \cdot 10^{-9}$
[22]	H-shaped	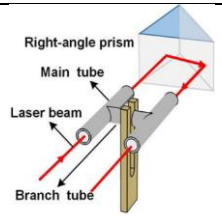	H_2O 7306.7	24	0.2	

In our experimental benchtop, only T-shaped mRs are used. To sum up on what have been presented above, in the T-shaped configuration, the laser beam is not focused between the prongs of the QTF but inside an acoustic cavity, that is parallel to the QTF axis. A small slit located at the middle of the tube directs the stationary acoustic wave formed inside the tube between the prongs of the QTF. This configuration makes the alignment of the laser more comfortable and helps reducing the photothermal perturbations that can be induced by the laser hitting on the surface of the prongs. This effect is even more amplified when using lasers at longer wavelength in the IR, presenting larger beams. Compared to the bare configuration, the SNR of the sensor can be enhanced by a factor 30 counting that the acoustic cavity is well designed and aligned with the QTF.

In the next part, the behaviour of the acoustic wave generated inside the tube and propagating outside the mR walls is studied. For this purpose, we have used COMSOL Multiphysics software to implement the T-shape configuration of the mR. In order to validate this numerical model, an analytical model inspired from the model proposed by H. Yi et al [5] [6] is implemented.

2- Study of the mRs design

The resonance frequency of the commercial QTF employed in QEPAS experiments presented in this study ranges around 32.7 kHz. The resonance frequency of the acoustic cavity should be the closest to the QTF's resonance frequency. The frequency of the stationary acoustic wave that is confined inside the mR is defined by the geometrical parameters of the mR (length and radius). In order to understand the effect of these variables onto the frequency of the acoustic wave, a T-shaped cavity is designed and studied using the Acoustic Pressure (ACPR) module of COMSOL Multiphysics. The results obtained from this numerical model are compared to an analytical model based on the study of the acoustic impedances inside the cavity.

2.1- Global parameters

2.1-1. Constants characterizing the medium

The properties of a wave change according to the medium in which it is propagating. The concentration of gas that is experimentally detected is very low (ppmv or ppbv range). Therefore, the use of air as a propagating material for the acoustic wave is justified. For high concentrations (percentage range), it would have been more suitable to use the constant characterizing the target gas. In addition, experimental measurements are compared to the numerical and analytical model. These measurements are performed for the detection of water in ambient air, which concentration is close to 7750 ppmv. The different constants characterizing the medium are defined in Table 2.

Table 2: Different constants defined for air at atmospheric pressure (1 atm) and ambient temperature (20°C).

Constant	Value	Units	Symbol	Ref.
Bulk viscosity	$1.29 \cdot 10^{-5}$	$\mathrm{Pa.s}$	μ_B	[23] page 315
Dynamic viscosity	$\sim 2 \cdot 10^{-5}$	$\mathrm{Pa.s}$	μ	[23] page 305
Ratio of specific heat	1.4	1	γ	[23] page 314
Heat capacity at constant pressure	1005	$\frac{\mathrm{J}}{\mathrm{kg.K}}$	C_p	[24]
Density	1.292	$\frac{\mathrm{kg}}{\mathrm{m^3}}$	ρ	[24]
Thermal conductivity	0.0234	$\frac{\mathrm{W}}{\mathrm{m.K}}$	κ	[25]
Speed of sound	343	$\frac{\mathrm{m}}{\mathrm{s}}$	c	[23] page 314
Mean molar mass	28	$\frac{\mathrm{g}}{\mathrm{mol}}$	M	[26]
Reference pressure for air	20	$\mu\mathrm{Pa}$	ρ_{air}	COMSOL reference value

2.1-2. Thermal and viscous losses in the system

When considering the propagation of an acoustic wave moving back and forth along a pipe, it is necessary to understand the processes that occur at the surface (rigid walls) of the pipe. If the viscosity in the fluid was negligible, the particles would "slip" along the walls. In reality a velocity gradient can be observed as the value of the particle velocity decreases from the mainstream towards the walls (Figure 4). This phenomenon occurs in a very thin layer called the acoustic boundary layer δ_{tot}.

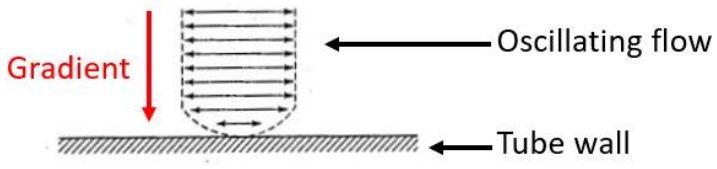

Figure 4: Representation of the effect of the viscous boundary layers on the oscillating flow. Figure adapted from [23].

The effect of the viscosity of the fluid is defined in a viscous boundary layer of thickness [23] (page 305):

$$\delta_{viscous} = \sqrt{\frac{2\,\nu}{\omega}} \tag{3.1}$$

where $\nu = \frac{\mu}{\rho} = 1.55 \cdot 10^{-5}\, m^2.s^{-1}$ is the kinematic viscosity at 20°C in air and $\omega = 2\pi f$ where f is the frequency (Hz).

A thermal boundary layer coexists with the viscous boundary layer. It implies heat transfers from the walls to the fluid. Its thickness is similar to $\delta_{viscous}$ as [23] (page 312),

$$\delta_{thermal} = \frac{\delta_{viscous}}{\sqrt{Pr}} \tag{3.2}$$

where Pr is the Prandtl number, equal to 0.707 for air around 20°C [27].

In the frequency range in which QEPAS using commercial QTFs operates (f ~ 32.7 kHz) the acoustic boundary layer δ_{tot} is about 10 μm. The phenomena that occur in this layer induce losses in the system and can be described through two coefficients, namely, the absorption coefficient for a thermoviscous fluid α_{TV} and the absorption coefficient induced by the walls α_W [23] (page 314, 325):

$$\alpha_{TV} = \frac{\omega^2 \nu}{2c^3}\left[\left(\frac{4}{3} + \frac{\mu_B}{\mu}\right) + \frac{\gamma - 1}{Pr}\right], \tag{3.3}$$

$$\alpha_W = \frac{1}{R}\sqrt{\frac{\omega\mu}{2\rho_0 c^2}}\left(1 + \frac{\gamma - 1}{\sqrt{Pr}}\right). \tag{3.4}$$

In our model, as $\alpha_W \approx 15.36\, nepers.m^{-1} \gg \alpha_{TV} \approx 0.02\, nepers.m^{-1}$, only the walls losses were implemented. The losses values are calculated for $f = 32750\ Hz$ and R=0.36 mm. These losses affect the quality factor of the cavity. They are proportional to $\frac{1}{R}$ thus, they decrease as the radius of the cavity increases.

The mesh is the division of geometry in multiple subdomains of well-defined size and shape (triangular in 2D or tetrahedral in 3D in the presented models), over which the acoustic pressure equations are solved. This naturally involves the discretization of the computation. In the ACPR module of COMSOL Multiphysics, the attenuation in the fluid can be defined by the user. Therefore, it is not necessary to mesh the acoustic boundary layer in order to observe its effect. In software such as COMSOL, working with Finite Element Method (FEM), the meshing process is crucial.

The mesh is adapted regarding the acoustic wavelength. The recommendation to correctly mesh the geometry is to define the bigger element of the mesh as [28]:

$$\frac{\lambda}{10} = \frac{c}{10f} \approx 1\ mm \tag{3.5}$$

Which means that the size of the bigger element composing the mesh must not exceed 1 mm.

The Thermoviscous Acoustic (TA) module of COMSOL Multiphysics could have been employed for this study. However, in this module, the losses cannot be defined manually by the user thus, the acoustic boundary layer needs to be correctly meshed in order to accurately consider the losses in the system. Therefore, the ACPR module was preferred as meshing layers of about $\delta_{tot} = 10\ \mu m$ in the TA module resulted in extremely high computation time.

2.2- Model of a simple pipe: COMSOL design

First, the example of a simple open-open pipe (a tube with two ends open) is studied. This model has been widely described by the acoustic community and the literature did not lack information on the subject. Therefore, it appeared as a straightforward way to validate the COMSOL computations with a well-known analytical model.

The ACPR module of COMSOL solves the Helmholtz equation in the frequency domain for a harmonic excitation:

$$\nabla^2 P + k^2 P = i\omega H C_{gas} \tag{3.6}$$

With ∇^2 the Laplace operator, P is the unknown acoustic pressure (Pa), $k = \frac{\omega}{c}$ is the wave number, $\omega = 2\pi f$ where f is the frequency (Hz), H is related to the heat source and will be described in the next section and C_{gas} a coefficient related to the fluid.

The pressure P and the particle velocity u are calculated in a defined frequency range. The acoustic impedance can be calculated from these two variables as [23] (page 47):

$$Z = \frac{P}{Su} \tag{3.7}$$

2.2-1. The heat source

An acoustic wave is generated in a fluid if the latter is heated and cooled down rapidly. This phenomenon is the consequence of a fast thermal expansion and contraction of the fluid. In order to recreate this acoustic wave, a heat source, representing the modulated laser source involved in QEPAS experiments is defined. The heat source can be defined as [29]:

$$H(x,y,z,t) = \frac{\alpha_{eff}(\omega) \cdot P_{laser}}{\sqrt{1+(\omega\tau)^2}} \cdot g(x,y,z) e^{(i(\omega t - \arctan(\omega\tau))} \quad (3.8)$$

With $g(x,y,z) = \frac{2}{\pi\sigma(x)^2} e^{-\frac{2r^2}{\sigma(x)^2}}$, $\alpha_{eff}(\omega) = \alpha(\omega) \cdot 0.5$ with α the absorption coefficient of the gas and 0.5 related to the first Fourier component in 1f detection method. τ is the relaxation time of the gas in the μs range [30]. Considering a water absorption line at 7181.14 cm^{-1} at a concentration of 7750 ppmv, $\alpha = 0.9\, m^{-1}$ at the maximum of absorption. P_{laser} is the power of the laser, here equal to 6 mW. $\sigma \approx$ 100 µm is the width of the Gaussian beam considered linear in the mR length and r is related to the coordinate position. The amplitude of the heat source is calculated for the defined values and is approximately equal to 10^5.

2.2-2- 2D axisymmetric model

The geometry designed on COMSOL to study the simple pipe is described by Figure 5. Two symmetry plans can be defined by (0, z) and (r, 0) as well as a rotation around the z-axis. Therefore, the 3D representation of a simple pipe of length L and radius R, can be simplified to a 2D axisymmetric model. This simplification offers the advantage of being less time consuming.

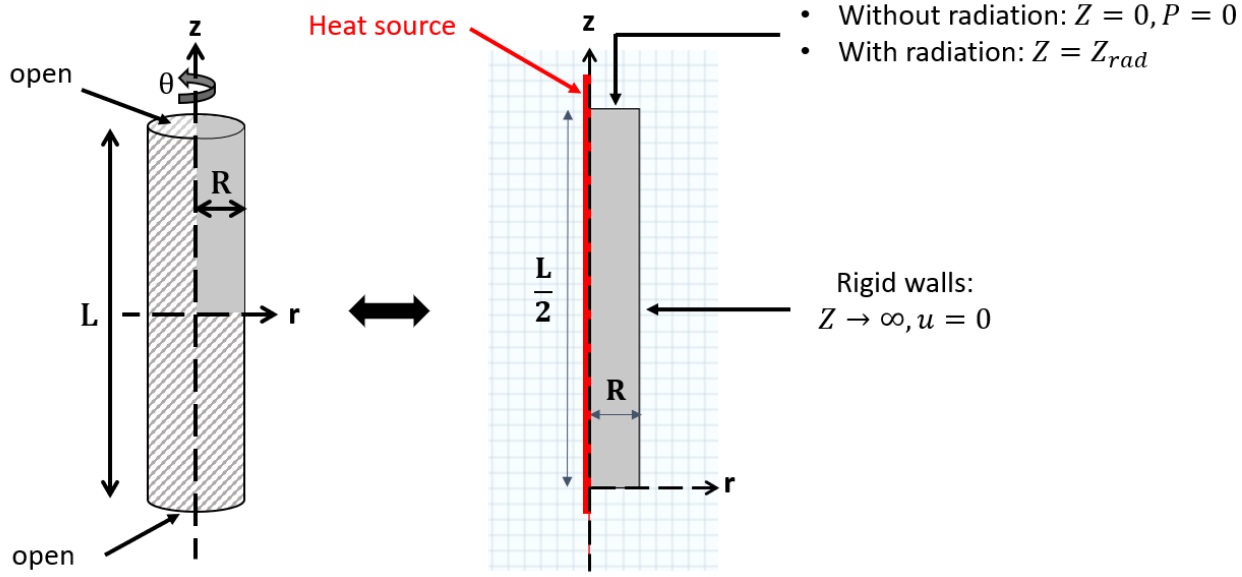

Figure 5: 3D representation of the pipe of length L and radius R and the equivalent 2D model. A symmetry plan is defined in (0, z) as well as in (r, 0) which allows to get rid of the dashed area in the computation. The heat source is defined along the z-axis and the different boundary conditions will be discussed in the text below.

As mentioned above, the tube is filled with air (Table 2). Different conditions, defined by COMSOL, are imposed for the pipe walls and openings:

- Rigid walls: this boundary condition is defined with the linear Euler equation [31] (page 119) and implies that the normal velocity at the walls is zero:

$$-n\left(-\frac{1}{\rho}\nabla P\right)=0 \tag{3.9}$$

For the opening, different conditions are studied:

- **Condition 1:** without radiations: the pressure P and the impedance Z are equal to zero.
- **Condition 2:** with radiations: a radiation impedance Z_{rad} is defined at the openings, implying that one part of the energy radiated outside the tube is reflected back into the pipe. This condition is closer to real-life phenomenon. The velocity particle term in Euler's linear equation is not equal to zero but defined as the total pressure divided by the radiation impedance Z_{rad}:

$$-n\left(-\frac{1}{\rho}\nabla P_t\right)=\frac{P_t i\omega}{Z_{rad}} \tag{3.10}$$

2.3- Model of a simple pipe: analytical model

This analytical model is developed in order to compare and validate the results obtained from the COMSOL simulations. It is based on the estimation of the acoustic impedances inside the tube. Since $R \ll L$ and $R \ll \lambda$ the model of the simple pipe can be treated as a 1D model. Following the dimensions of this model, only the longitudinal acoustic resonance occurs inside the tube [32]. Figure 6 shows the first harmonic of a standing wave materialized in a pipe.

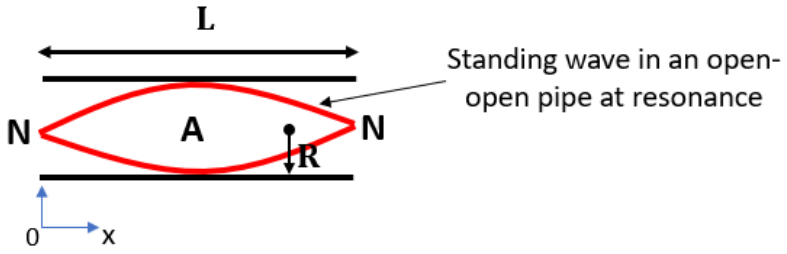

Figure 6: Schematic of a standing wave inside a pipe of length L and radius R. N: nodes occurring at both ends where $Z = 0$. A: antinode.

The acoustic pressure $P(x,t)$ for a standing wave occurring in a pipe can be defined as:

$$P(x,t)=Ae^{i(\omega t-kx)}+Be^{i(\omega t+kx)}. \tag{3.11}$$

where A and B are the amplitude of the acoustic wave, $\omega = 2\pi f$ where f is the frequency (Hz), x is the coordinate position and $k = \frac{\omega}{c} - i\alpha_W$ where c is the sound velocity in air and the imaginary part involves the losses described by α_W defined by Equation (3.4).

The particle velocity is deduced from Newton's second law [31] (page 118) describing a one-dimensional plane wave as:

$$-\rho \frac{\partial u(x,t)}{\partial t} = \frac{\partial P(x,t)}{\partial x} \tag{3.12}$$

where ρ is the density of the gas contained in the medium (air).

By derivation and integration of $P(x,t)$ in Equation (3.12) we obtain:

$$u(x,t) = \frac{1}{\rho c}\left(Ae^{i(\omega t - kx)} - Be^{i(\omega t + kx)}\right). \tag{3.13}$$

By defining the acoustic impedance with Equation (3.7), we can express $Z(x)$ as:

$$Z(x) = \frac{\rho c}{S}\frac{Ae^{-ikx} + Be^{ikx}}{Ae^{-ikx} - Be^{ikx}}. \tag{3.14}$$

In the case of a finite pipe, at the node position ($x = 0$) representing the openings of the pipe, the acoustic impedance can be expressed:

$$Z(0) = Z_0 = \frac{\rho c}{S}\frac{A + B}{A - B} \tag{3.15}$$

Then, by calculating the ratio $\frac{A}{B}$ (see Equation (3.16)) and replacing its expression in Equation (3.14), the acoustic impedance $Z(x)$ at any x position can be expressed as function of the acoustic impedance at the entrance of the tube Z_0:

$$\frac{A}{B} = -\frac{\frac{\rho c}{S} + Z_0}{\frac{\rho c}{S} - Z_0}, \tag{3.16}$$

$$Z(x) = \frac{Z_0 - i\frac{\rho c}{S}\tan(kx)}{\frac{Z_0 S}{i\rho c}\tan(kx) + 1}. \tag{3.17}$$

The different calculation steps are described in Appendix D.

As for the numerical model, different boundary conditions are studied.

Condition 1: without radiation. This first condition is well described by Figure 6. At resonance in an open-open pipe of length L, the condition $Z_0 = Z_L = 0$ is verified since the acoustic pressure at each node tends to 0 and the particle velocity tends to ∞.

Thus, it is possible to write:

$$Z_L = -i\frac{\rho c}{S}\tan(kL) = 0. \tag{3.18}$$

This condition is satisfied if

$$\tan(kL) = 0. \tag{3.19}$$

Which implies that:

$$k = \frac{n\pi}{L}. \tag{3.20}$$

We can deduce, for the first harmonic, n = 1, the length of the pipe as function of the frequency f of the acoustic wave and the sound velocity c :

$$L = \frac{c}{2f}. \tag{3.21}$$

Condition 2: with radiation. In reality, the condition 1 of $Z_0 = Z_L = 0$ can not be satisfied. It can be seen as a mismatch between the 1D model used to define the acoustic impedance and the phenomena occurring in reality (3D). In the case of an open-open pipe, when the acoustic pressure generated inside the tube debouches into the atmosphere the planar wave front occurring inside the cavity becomes spherical. A part of this wave in transmitted and the other part is reflected into the tube from a point located beyond the physical boundaries of the tube [33] (page 493).

The term of radiative impedance has been used by Rayleigh (1894) to describe this phenomenon. Basically, everything happens as if the tube was physically longer. In the case described in Condition 1, the length of the tube, for a given frequency f, is calculated using Equation (3.21). In Condition 2, the radiation phenomenon impose a correction C_L of the length in order to be correctly considered (Figure 7). For a tube open at both ends, the effective length L_{eff} is calculated as:

$$L_{eff} = L + 2 \cdot C_L \cdot R \tag{3.22}$$

The correction is multiplied by 2 in order to consider the correction at each opening. The value of C_L are discussed section 2.4-2. Equation (3.22) implies an interdependence of the length with the radius R.

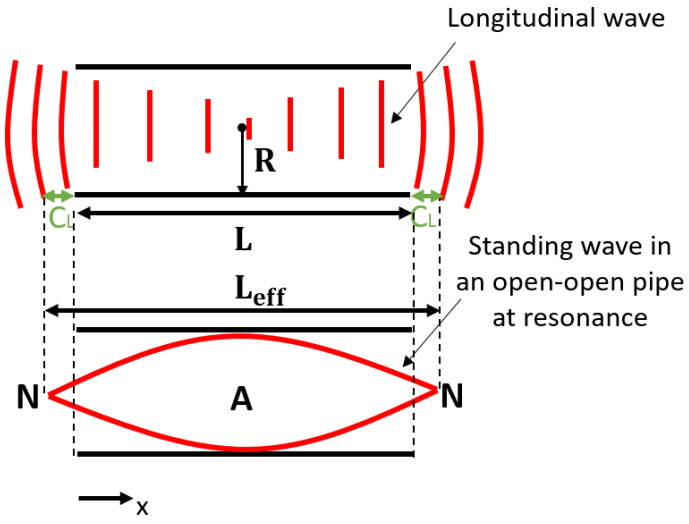

Figure 7: Representation of a longitudinal wave exiting into the atmosphere as a spherical wave. Compared to Figure 3 the nodes are represented beyond the physical length of the pipe. This phenomenon implies a length correction C_L.

2.4- Comparison of the analytical and numerical models

In this section, a comparison between the analytical and numerical model of a simple tube is proposed:

- In the analytical model, the acoustic impedance is calculated at the antinode (Figure 6) where the maximum of the acoustic wave is observed. Using Equation (3.17) with $Z\left(x = \frac{L}{2}\right)$, the acoustic impedance at the middle of the tube as function of the frequency is calculated using a python program. For different pipe lengths L, the frequency corresponding to the maximum of impedance is compared to the numerical model.
- The analytical 1D model supposes that the acoustic impedance at a given section of the tube, i.e. at a certain length x, is constant. COMSOL simulations denote the presence of a gradient of impedance as the pressure and the particle velocity are not constant on one section. Therefore, following Equation (7), the acoustic impedance from COMSOL is calculated by dividing the average acoustic pressure with the average particle velocity at $x = \frac{L}{2}$:

$$Z_{COMSOL}\left(x = \frac{L}{2}\right) = \frac{\int_0^R rP\left(x = \frac{L}{2}\right) dr}{\int_0^R ru\left(x = \frac{L}{2}\right) dr} \tag{3.23}$$

Our model is represented by a 2D axisymmetric model, the section used in the determination of the acoustic impedance is highlighted in blue on Figure 8.

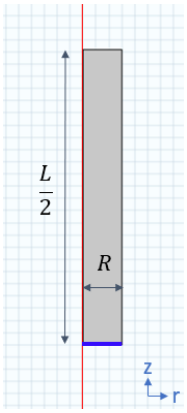

Figure 8: the blue line on the edge of the geometry represents the area over which is integrated the acoustic pressure and particle velocity

2.4-1. Comparison of results obtained for Condition 1: without radiations

In this first study, the acoustic impedance is calculated at $Z\left(x = \frac{L}{2}\right)$ with L defined with Equation (3.21) as $L = \frac{c}{2f}$. For different tube lengths, with a fixed radius of $R = 0.3\ mm$, the frequency corresponding to the maximum of Z is reported (Figure 9).

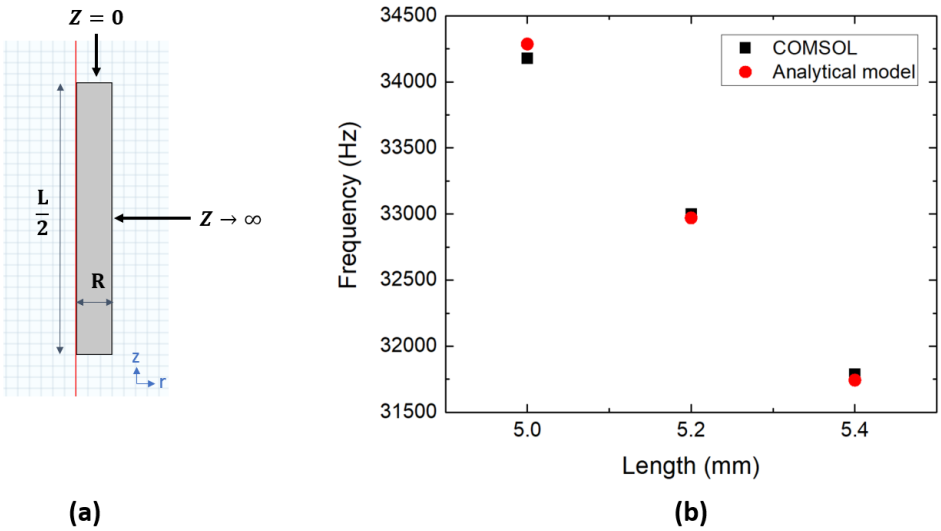

Figure 9: (a) Boundary condition 1 (b) Frequency corresponding to the maximum of acoustic impedance calculated for different pipe lengths obtained with the analytical and numerical model. The radius of the pipe is fixed at R = 0.3 mm.

The error between the two models can be calculated as:

$$Error = \frac{f_{analytic} - f_{COMSOL}}{\frac{f_{analytic} + f_{COMSOL}}{2}} \times 100 \approx 0.2\ \% \qquad (3.24)$$

The numerical and analytical model give comparable results which means that for a simple pipe without radiation, the ACPR module of COMSOL can be used as a reliable prediction tool for the frequency of the generated acoustic wave.

2.4-2. Comparison of results obtained for Condition 2: with radiations

The boundary Condition 2 is closer to the phenomenon that occurs at the openings of a pipe in real-life applications. In this case, a length correction must be considered. The analytical model calculates the impedance $Z\left(x = \frac{L_{eff}}{2}\right)$ in the middle of the tube but the length L_{eff} is calculated from Equation (3.22) as $L_{eff} = L + 2C_L R$. On COMSOL ACPR module, a boundary condition can be defined at the opening in order to consider the radiation Z_{rad} (Figure 5).

The radiation condition as well as the correction coefficient C_L are described in the literature in case the tube is considered flanged or unflanged. While the unflanged describes a tube with extremely thin walls (ID ≈ OD), the flanged describes a tube with extremely large walls (OD ≫ ID). In reality, a tube is described between these two extreme conditions.

- **The unflanged pipe**

The unflanged and flanged conditions that are described can be defined for Z_{rad} presented in Figure 5. However, these conditions affect the propagation of the acoustic wave radiating outside the tube. Even if they are accurately considered in Z_{rad}, it is also necessary to observe their effect for a better comprehension of the phenomena. Thus, the COMSOL geometry is modified: two air buffers are added at each opening in order to assure the continuity of propagation of the acoustic wave outside the tube. (The two geometries: with boundary conditions at the openings or with air buffers to assure the propagation of the wave outside the tube are equivalent).

For an unflanged tube, the air buffers are included as two half circles (Figure 10) in the geometry in order to not modify the thickness of the tube walls. The length of the tube L is equal to 4.8 mm and its radius R equal to 0.3 mm. Figure 10 is observed at ~ 33200 Hz corresponding to the maximum of the acoustic wave intensity.

It is important to note that even if the calculation and the comparison of the numerical and analytical model involves the impedances values, it is the propagation of the acoustic wave that is interesting in the photoacoustic application. In addition, the maximum frequency of the acoustic impedance is retrieved at the maximum of acoustic pressure.

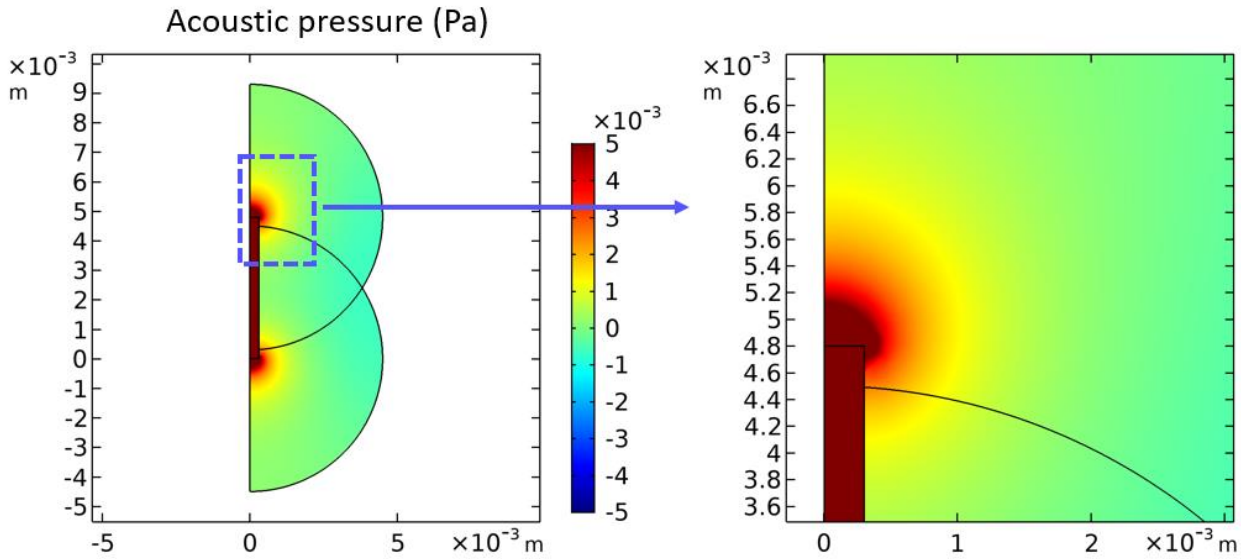

Figure 10: Simulation of an unflanged pipe: half circle air buffers added at the each opening of the simple tube is order to observe the radiation of the acoustic wave outside the tube (Pa). The length of the tube $L = 4.8\,mm$ and its radius $R = 0.3\,mm$. The graph is observed for $f = 33200\,Hz$ corresponding to the maximum amplitude of the acoustic wave.

In the case of an unflanged pipe, the length correction is calculated as [34], [35]:

$$C_{L_{unflanged}} = \frac{0.6133 + 0.027(kR)^2}{1 + 0.19(kR)^2} \tag{3.25}$$

Therefore, the effective length in the analytical model is calculated as:

$$L_{eff} = L + 2 \cdot C_{L_{unflanged}} \cdot R, \tag{3.26}$$

The effect of the length correction in a case of an unflanged pipe is depicted on Figure 11. The length and the radius have an effect on the frequency. Consequently, in Figure 11b, the radius is fixed at $R = 0.3\,mm$ and the values of frequency corresponding to the maximum of impedance are plotted for different lengths. In Figure 11c, it is the length that is fixed at 4.8 mm.

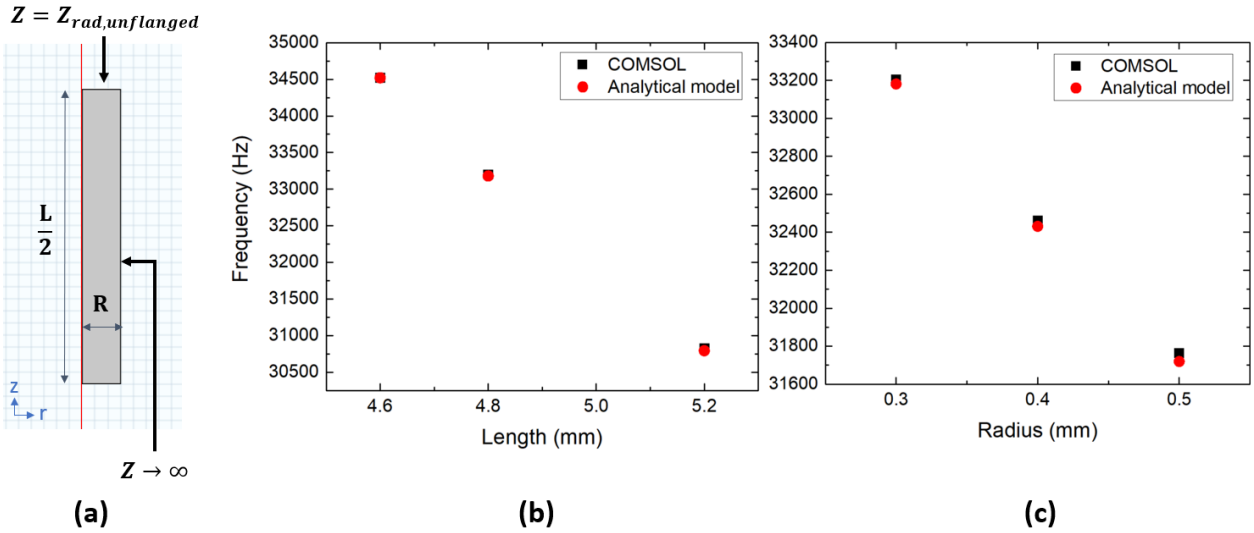

Figure 11: (a) Boundary condition 2: case of an unflanged pipe (b) the frequency obtained for the maximum of acoustic impedance for different pipe length is presented. The radius is fixed at $R = 0.3\ mm$. (c) the effect of the radius onto the frequency depicted, the length is fixed at $L = 4.8\ mm$.

In the case of an unflanged simple pipe, the effect of the length and the radius onto the acoustic impedance also gives very comparable results. Using Equation (3.24), the error is estimated at about 0.2 % calculated on Figure 11c data while the error on the length is neglectable. The frequency decreases when the length and the radius increase and a variation of 100 µm on the geometric parameters leads to a decrease of $\sim$ 1000 Hz on the frequency.

- **The flanged pipe**

The observations that are depicted in Figure 10 for an unflanged tube are performed for a flanged pipe. The air buffers are included as a quarter of circle in the geometry in order to simulate a large wall thickness (Figure 12). The length of the tube L is equal to 4.8 mm and its radius R equal to 0.3 mm. Figure 12 is observed at $\sim$ 32500 Hz corresponding to the maximum of the acoustic wave.

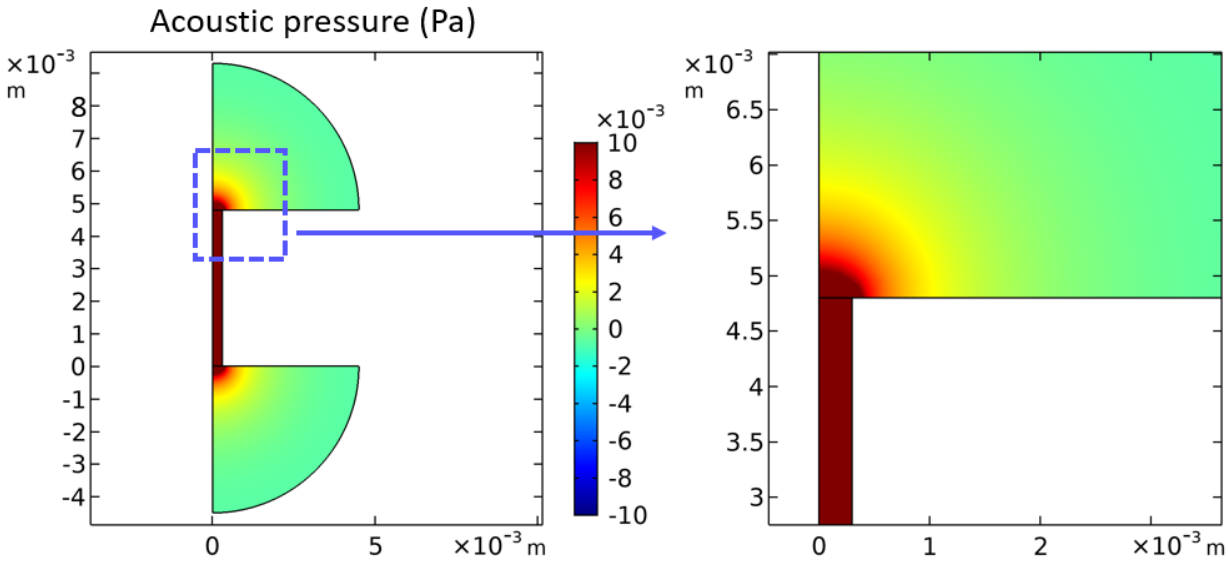

Figure 12: Simulation of a flanged pipe: quarter circle air buffers added at the each opening of the simple tube in order to observe the radiation of the acoustic wave outside the tube. The length of the tube $L = 4.8\ mm$ and its radius $R = 0.3\ mm$. The graph is observed for $f = 32500\ Hz$ corresponding to the maximum amplitude of the acoustic wave.

In the case of a flanged pipe, the length correction is calculated as [34], [35]:

$$C_{L_{flanged}} = \frac{0.82159 - 0.49(kR)^2}{1 - 0.46(kR)^3} \tag{3.27}$$

The effective length is calculated in the analytical model as:

$$L_{eff} = L + 2 \cdot C_{L_{flanged}} \cdot R. \tag{3.28}$$

These approximations are valid for numbers kR ∈]0; 3.8[[34].

The effect of the length correction in a case of a flanged pipe is depicted on Figure 13. The length and the radius have an effect on the frequency. Consequently, in Figure 13b, the radius is fixed at $\mathrm{R} = 0.3\ \mathrm{mm}$ and the values of frequency corresponding to the maximum of impedance are observed for different lengths. In Figure 13c, it is the length that is fixed at 4.8 mm.

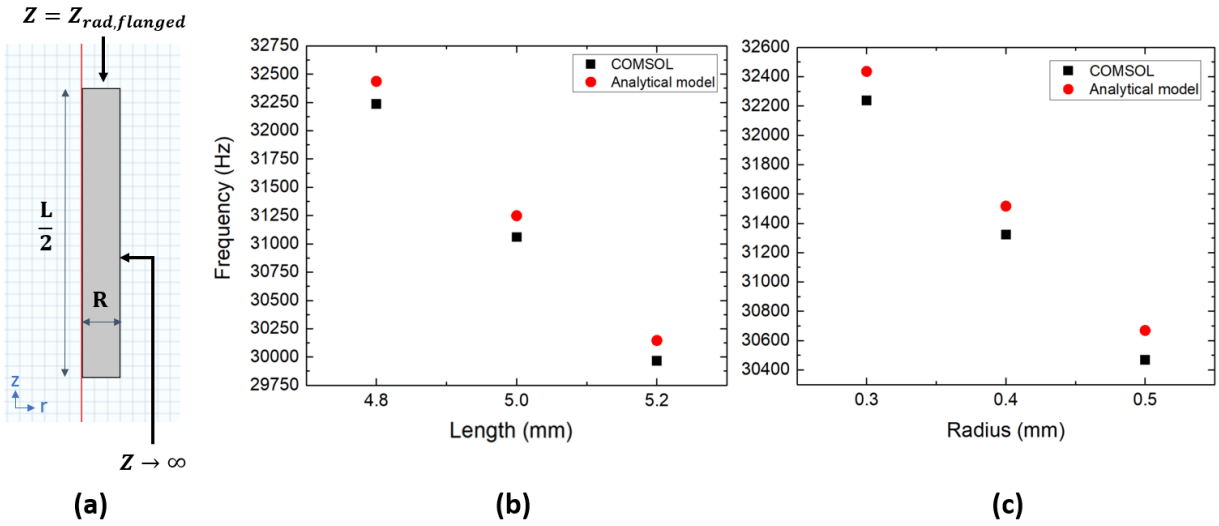

Figure 13: (a) Boundary condition 2: case of a flanged pipe (b) the frequency obtained for the maximum of acoustic impedance for different pipe length is presented. The radius is fixed at $R = 0.3\ mm$. (c) the effect of the radius onto the frequency depicted, the length is fixed at $L = 4.8\ mm$.

In the case of a flanged simple pipe, the effect of the length and the radius onto the acoustic impedance also gives very comparable results, with an acceptable difference of 200 Hz between the analytical and numerical model. This difference leads to an error of 0.6% calculated using Equation (3.24). As observed in the unflanged model, the frequency decreases when the length and the radius increase and a variation of 100 µm on the geometric parameters leads to a decrease of $\sim$ 1000 Hz on the frequency.

Figure 10 is observed for $L = 4.8\ mm$, $R = 0.3\ mm$ and an optimum frequency of 33200 Hz while Figure 12 is observed for the same geometric parameters but for an optimum frequency of 32500 Hz. This difference shows the effect of walls thickness onto the radiation phenomenon as for the same length and radius, the optimum of acoustic impedance is found at frequencies separated by $\sim$ 1000 Hz.

Through this model of a simple pipe, it was possible to confirm that for 3 different configurations, the numerical results obtained from the ACPR module of COMSOL provide results that are comparable to an analytical model that is well referenced in the literature. In the following parts, the T-shaped mR is designed by adding a small tube at the middle of the simple tube. Once again, a numerical and analytical model are adapted to this new configuration and their results are compared.

2.5- T-shaped cavity: COMSOL design

The design of the T-shaped geometry is realized on COMSOL as presented in the Figure 14. In this configuration the symmetry plan in (0, z) and the rotation along z no longer exist. Therefore, the tube cannot be designed in a 2D axisymmetric study and has to be

represented in its 3D shape. The simple pipe, that we are going to call the "main pipe" (or tube), is characterized by its length L and its radius R. A union is formed with another tube, called the "small tube". This tube is positioned perpendicularly at the middle of the main tube and is characterized by its length l and its radius r. As for the previous model, the tube is filled with air and the constant characterizing the medium are presented in Table 2. A schematic representation of the 3D T-shaped model is also presented in Figure 14. The propagation axis of the heat source as well as the boundary conditions are depicted.

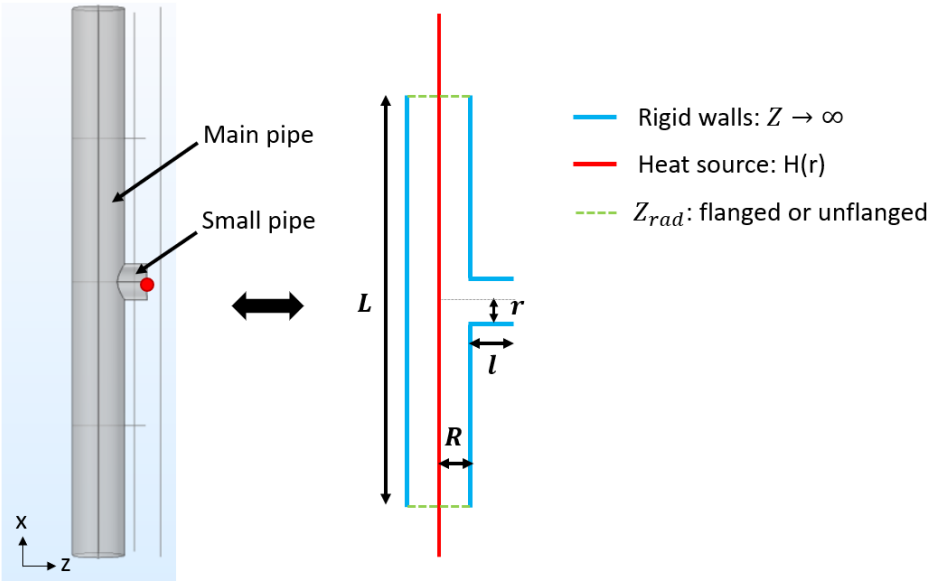

Figure 14: COMSOL geometry designed for the T-shaped mR and its schematic representation showing the geometric dimensions, boundary conditions and heat source propagation axis. The amplitude of the acoustic pressure is measured in the following part at the exit of the small tube represented by the red dot on the 3D pattern.

The boundary condition 1 (presented section 2.2) is far from reality thus, not relevant to be studied in the present configuration. Only the radiation condition is studied in this section, for a flanged or an unflanged tube.

2.6- T-shaped cavity: analytical model

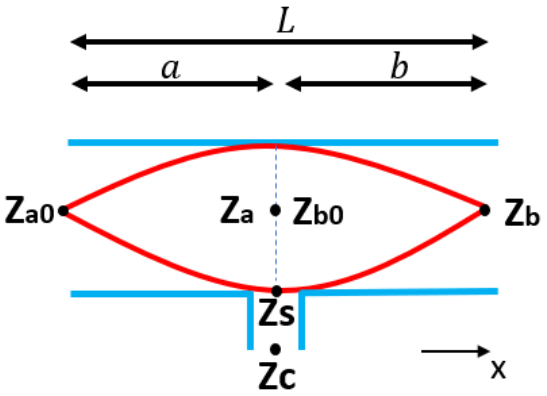

Figure 15: Schematic representation of the T-shaped mR used in the analytical model.

A standing acoustic wave generated in an open-open pipe with a small tube at its middle is now considered (Figure 15). The model that is described in the following part is based on H. Yi et al [5], [6] model proposed for the T-shaped mR used in QEPAS experiments.

To begin, the main pipe, of length L, can be separated in two tubes with the same length $a = b = \frac{L}{2}$ (Figure 15). The first step consists of defining the acoustic impedances at four different points inside the main tube. In the first part of length a, the acoustic impedances Z_{a0} and Z_a are calculated respectively at $x_a = 0$ and $x_a = a$. In the second part of length b, the acoustic impedances calculated at $x_b = 0$ (also corresponding to $x_a = a$) and $x_b = b$ are defined respectively as Z_{b0} and Z_b.

The acoustic impedances Z_a and Z_b can be calculated from Equation (3.17):

$$Z_a = \frac{Z_{a_0} - i\frac{\rho c}{S}\tan(ka)}{\frac{Z_{a_0}S}{i\rho c}\tan(ka) + 1} \tag{3.29}$$

and

$$Z_b = \frac{Z_{b_0} - i\frac{\rho c}{S}\tan(kb)}{\frac{Z_{b_0}S}{i\rho c}\tan(kb) + 1} \tag{3.30}$$

Now that the acoustic impedances in the middle of the tube are defined, let's retrieve the acoustic impedance in the small tube.

As defined in the previous model of a simple pipe, at resonance the acoustic impedance at the nodes is equal to zero. Then,

$$Z_{a_0} = Z_b = 0. \tag{3.31}$$

The acoustic impedance at the node formed by the three impedances $Z_a - Z_{b_0} - Z_s$ can be written as in an electrical circuit (Figure 16) [33] (page 487).

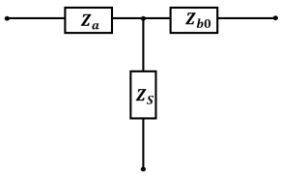

Figure 16: Electric representation of three impedances in parallel.

Thus, we can write:

$$\frac{1}{Z_a} = \frac{1}{Z_{b_0}} + \frac{1}{Z_s} \tag{3.32}$$

Using Equation (3.31), it is possible to deduce the Z_a and Z_{b0} values from Equation (3.29) and (3.30). By replacing their expression in Equation (3.32), we obtain:

$$-\frac{i\rho c}{SZ_s} = \frac{2}{\tan\left(\frac{kL_{eff}}{2}\right)}. \tag{3.33}$$

In order to calculate the length L_{eff} from Equation (3.33), Z_s needs to be defined as function of the acoustic impedance at the output of the small tube. From Equation (3.17), it is possible to deduce:

$$Z_c = \frac{Z_s - i\frac{\rho c}{s}\tan(kl_{eff})}{\frac{Z_s s}{i\rho c}\tan(kl_{eff})+1}. \tag{3.34}$$

l_{eff} represents the effective length of the small tube and s its cross-section area.

Once again, at resonance the acoustic impedance at the output of the small tube is equal to zero.

$$Z_c = 0. \tag{3.35}$$

Z_s can be written as:

$$Z_s = \frac{i\rho c}{s}\tan(kl_{eff}). \tag{3.36}$$

As l_{eff} is very small, Taylor series expansion of first order can be used to calculate:

$$\tan(kl_{eff}) = kl_{eff} \tag{3.37}$$

Thus, Equation (3.36) becomes:

$$Z_s = \frac{i\rho c}{s}kl_{eff} \tag{3.38}$$

The acoustic conductivity σ_s is introduced:

$$\sigma_s = \frac{s}{l_{eff}} \tag{3.39}$$

Equation (3.38) can be written as function of σ_s:

$$Z_s = \frac{i\rho ck}{\sigma_s} \tag{3.40}$$

Finally, by replacing expression (3.40) in Equation (3.33), we can deduce:

$$\tan\left(\frac{kL_{eff}}{2}\right) = -\frac{2kS}{\sigma_s} \tag{3.41}$$

As L_{eff} designates the geometric value it can only be attributed positive values. Therefore,

$$\frac{kL_{eff}}{2} = \pi - \arctan\left(\frac{2kS}{\sigma_s}\right) \tag{3.42}$$

And L_{eff} is deduced from Equation (3.42) as:

$$L_{eff} = \frac{c}{f}\left(1 - \frac{1}{\pi}\arctan\left(\frac{4\pi fS}{\sigma_s c}\right)\right) \tag{3.43}$$

By adding the length correction, we can calculate the real length of the main tube L:

$$L = L_{eff} - 2 \cdot C_L \cdot R = \frac{c}{f}\left(1 - \frac{1}{\pi}\arctan\left(\frac{4\pi fS}{\sigma_s c}\right)\right) - 2 \cdot C_L \cdot R, \tag{3.44}$$

where C_L is the correction coefficient defined for flanged and unflanged pipes respectively in Equation (3.27) and (3.25). The Equation (3.44) shows that the length of the main pipe involved in the calculation of the acoustic impedance relies on the geometric dimensions of this small tube.

2.7- Comparison of the analytical and numerical models

With the analytical model, it is possible to calculate, for a given frequency, the length L of the tube. Therefore, on COMSOL (numeric), the frequency corresponding to the maximum of the acoustic impedance is calculated for different tube lengths. Then, for the same frequency, the length L is calculated using a python script (analytical). The different length values are compared in the case where the T-shaped tube is flanged or unflanged.

Note that σ_s takes into account the length of the small tube l. As a radiation is occurring from this exit, the length needs to be correct as it is done for the main pipe length L. The correction coefficient is the same C_L coefficient defined for the flanged and unflanged pipe.

The results of the analytical and numerical model are presented in Figure 17. This study is conducted for different values of L, in case the geometry is flanged or unflanged. The other geometric parameters are fixed: $l = 0.3\ mm$, $R = 0.36\ mm$ and $r = 0.25\ mm$.

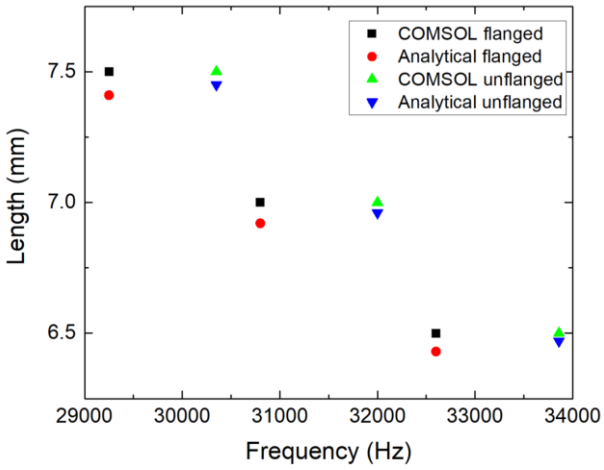

Figure 17: Comparison of the numerical model of a flanged and unflanged pipe with the analytical model of a flanged and unflanged pipe. For a given value of frequency corresponding to the maximum of acoustic impedance, the length L is reported.

The results presented in Figure 17 are promising. A difference of approximately 0.1 mm is found between the analytical model and the COMSOL simulations leading to a difference of approximately 250 Hz on the frequency. Considering this difference, it is possible to use the proposed COMSOL model in order to understand the effect of the different geometric dimensions onto the generated acoustic wave.

The effect of R, l and r onto the resonance frequency of the acoustic impedance is investigated for an unflanged and a flanged tube (Table 3).

Table 3: Evolution of the frequency of the acoustic impedance with the variation of each geometric dimensions: L, R, l and r

Dimensions (mm)	**Frequency (Hz)**
$L \uparrow$	$\downarrow$
$R \uparrow$	$\downarrow$
$l \uparrow$	$\downarrow$
$r \uparrow$	$\uparrow$

While the frequency appears to shift to lower values when the main tube length and radius as well as the small tube's length (L, R and l) increase, the contrary is observed when the radius of the small tube (r) increases. This must be considered when designing a new resonator.

2.8- Comparison of COMSOL results with experimental results

In this section, the COMSOL simulations are compared to experimental values. For this purpose, cavities of different lengths are printed using a 3D printing machine.

One of the most widespread technique used in 3D printing is the Stereolithography (SLA) [36]. The working principle is simple: a UV laser is focused onto a photosensitive resin. The selective exposition to the laser light induces the polymerization and solidification of the resin. Movable mirrors direct the light of the laser into the resin in order to draw the 2D pattern. This process is repeated as the 3D pattern is constructed layer by layer (Figure 18).

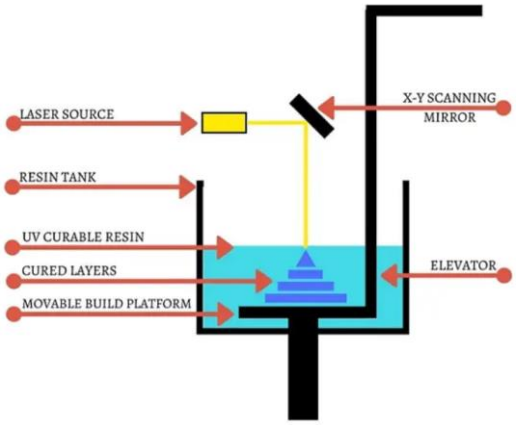

Figure 18: Schematic representation of the working principle of Stereolithography (SLA). [37]

The Institute of Electronics and Systems (IES) of the University of Montpellier is equipped with a Form3 3D printer from formlabs. The xy resolution of this machine as well as its minimum layer thickness ranges around 25 µm. Different cavities are designed using CATIA v5 software (Dassault system) and printed using our laboratory facilities.

The characterization of the cavities is performed through photoacoustic (PA) measurements. A DFB QCL laser targeting a water absorption line around 1906 cm^{-1} is focused inside each cavity and a typical microphone used in PAS [38] is positioned in front of the small tube to probe the PA signal. The measurement is performed on ambient air (Figure 19)

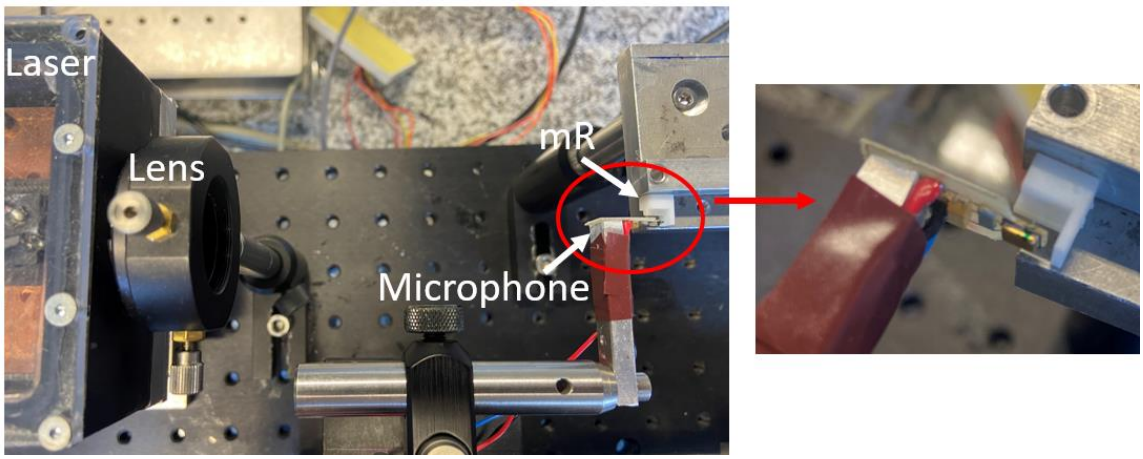

Figure 19: Characterization setup of the mR. The PA signal measured with a microphone [9] is retrieved by exciting water molecules in ambient air around 5.2 µm.

During the measurement, the position of the cavity is fixed and the microphone is positioned on a xyz stage. The microphone is mounted on a PCB where a hole is drilled to have access to the membrane that will be centred in front of the opening of the small tube. In order to not perturbate the propagation of the acoustic wave, an optimum position of 0.75 mm is set between the cavity and the microphone [9]. The response of the microphone is retrieved from the PA signal normalized by the response of the microphone.

Seven cavities with three different lengths of the main pipe are characterized. $L = 6, 5$ and $4.5\ mm$. The radius of the main pipe $R = 0.36\ mm$, the length of the small pipe $l = 0.3\ mm$ and its radius $r = 0.25\ mm$ (Figure 20). The results are compared to COMSOL values and presented in (Figure 21).

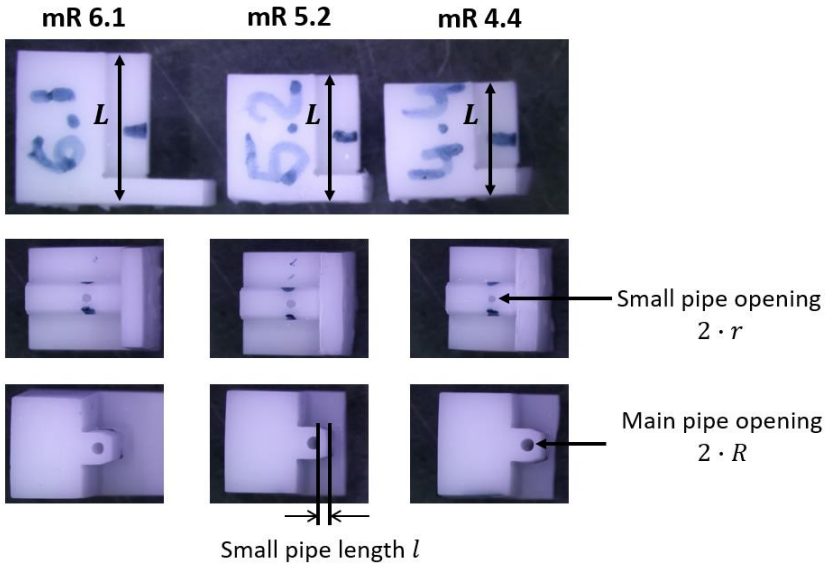

Figure 20: 3D printed cavities with expected $R = 0.36\ mm, l = 0.3\ mm$ and $r = 0.25\ mm$. The length L is equal to 6, 5 and 4.5 mm respectively for mR 6.1, 5.2 and 4.4.

The PA signal obtained from the characterization of the different cavities is reported on Figure 21 (black squares). The COMSOL results obtained for a flanged (green dot) and unflanged (magenta triangle) tube with the expected dimensions are also presented. A mismatch of more than 5000 Hz is observed between the experimental and the COMSOL model (flanged and unflanged). Different reasons could be at the origin of this error. First of all, the roughness of the surface induced by the deposition of the multiple layers during the manufacturing of the cavities which can interfere with, or disturb the generation of the acoustic wave. Another source of error is also the shape of the openings that are not strictly round as expected. A study has shown the effect of different slit shapes onto the measured frequency of the acoustic wave characterized with a similar setup [9]. Finally, one major source of error that can be studied in this comparison is the size of the small tube radius. Indeed, an important error has been observed on the size of this parameters. Therefore, for different cavities observed with a microscope, the size of the smallest radii observed was around 0.17 mm. Therefore, the COMSOL results that could be obtained for such a radius, by keeping the other parameters fixed, are presented for the unflanged (blue triangle) and flanged model (red dot) (Figure 21).

The results show that the frequency switches to smaller frequencies when the radius decreases. By taking into account this source of error, the experimental frequency values lay between the unflanged and flanged prediction of COMSOL.

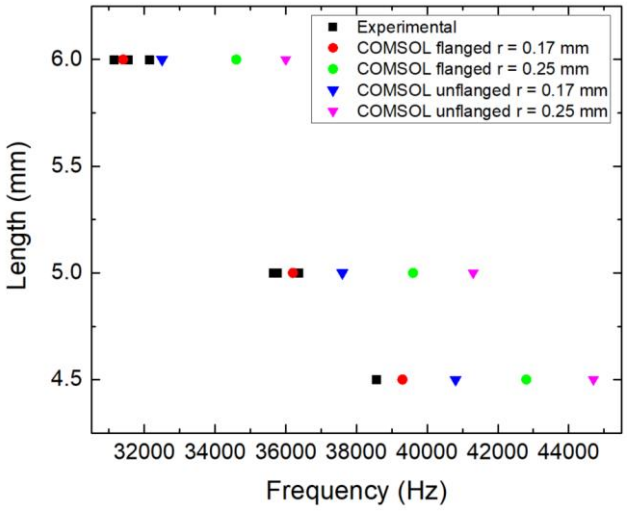

Figure 21: Comparison of experimental values of frequency obtained from the T-shape measurement of the acoustic signal generated in cavities of different lengths with COMSOL predictions for a flanged and unflanged model. The radius of the small tube is adapted in order to consider potential error sources on the measured frequency.

The different mRs tested are printed at the same time. For the measurement, three different mRs of $L = 6\ mm$ and $L = 5\ mm$ and two mR of length $L = 4\ mm$ (black squares) were measured. Except for the last group, the other lengths of mRs do not present the same resonance frequency which illustrates the error caused by the manufacturing. By

considering these errors on r into the COMSOL simulations, the experimental results are closer to the flanged model which is expected as the mR is built in a block (resine) and cannot be considered as totally unflanged.

In the next section, we will see that the frequency of the measured acoustic wave generated inside the tube as well as its amplitude can be modified when the QTF (acoustic transducer used in QEPAS experiments) is placed in front of the mR opening.

3- Multiphysics study of the spectrophone

Relying on the designed model, the propagation of the acoustic wave occurs in the z-axis. The QTF used in QEPAS experiments as a signal transducer is introduced to the model as a quartz material. The QTF is positioned at the output of the small tube, where the acoustic wave exits. The crystallographic orientations of the QTF are defined as presented in the Chapter 2. The propagation of the acoustic wave along the z-axis is investigated as well as the effect of the position of the QTF onto the frequency of the generated acoustic wave. By using the Solid mechanics interface of COMSOL, it is possible to observe the mechanical deformations of the quartz element. In order to assure the continuity of the acoustic wave outside the walls of the mR, the impedance conditions are replaced by a large air buffer. This buffer is built big enough to not perturbate the propagation of the acoustic wave and avoid reflection toward the mR. In this configuration, the mR is considered as unflanged as the OD = ID. The dimensions of the acoustic cavity are $L = 7\ mm$, $R = 0.36\ mm$, $l = 0.3\ mm$ and $r = 0.25\ mm$ and the resonance frequency is observed around 32 kHz as it is depicted in Figure 17. The surface of this buffer is coarsely meshed to avoid long computation time (Figure 22). Additionally, the phenomenon arising far from the mR and QTF are not relevant in this study.

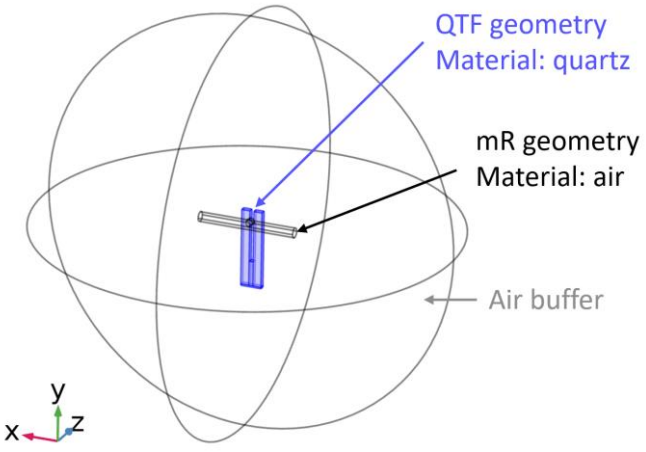

Figure 22: COMSOL geometry defined for Multiphysics study.

3.1- Propagation of the acoustic wave along the output of the small tube

The acoustic pressure retrieved from COMSOL simulations and directly involved in the mechanical displacement of the QTF is studied. On Figure 23, the red line describes the direction is which the acoustic wave exits the cavity and propagates towards the QTF. The amplitude of the acoustic wave is studied along this red line, from the middle of the main tube to a distance located after the QTF.

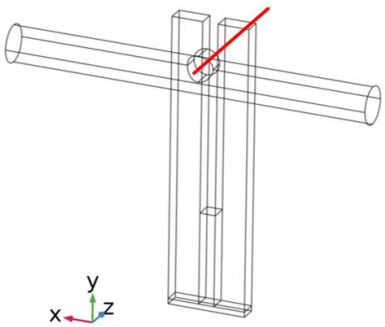

Figure 23: COMSOL simulations: the propagation of the acoustic wave is investigated along the z-axis represented with the red line.

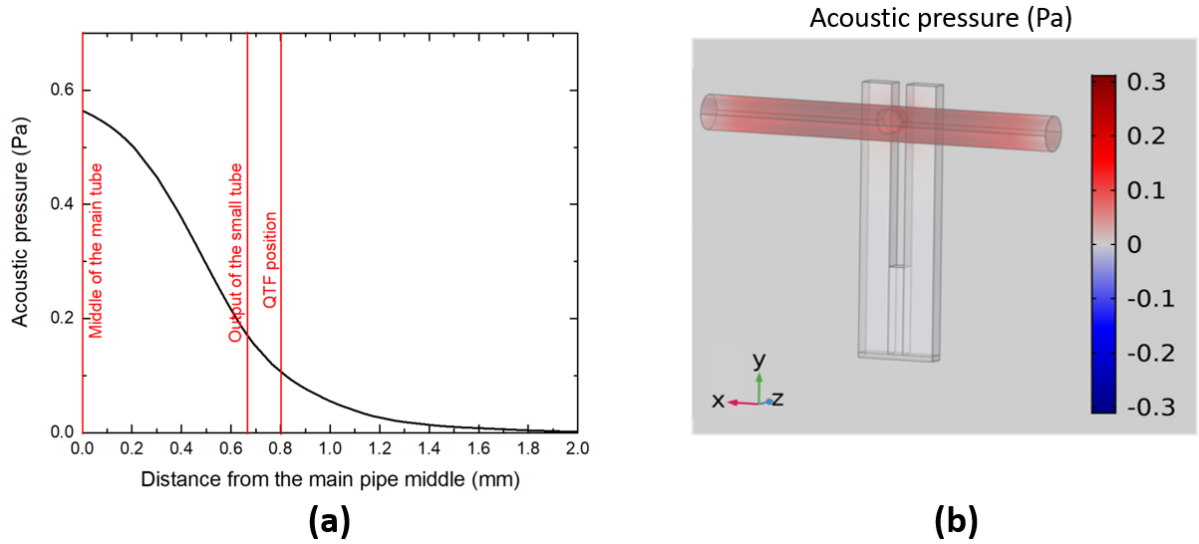

Figure 24: (a) COMSOL simulations of the propagation of the acoustic wave along the z-axis. (b) Corresponding acoustic pressure amplitude (Pa) inside the mR.

The investigation of the propagation of the acoustic wave along the z-axis shows that less than half the amplitude of the acoustic wave generated in the middle of the pipe is measured at the output of the small tube and at the QTF position (Figure 24). For the same amplitude of heat source $(5 \cdot 10^5\ W/m^3)$ the propagation of the acoustic wave in the bare configuration was investigated. In this case, the acoustic wave is measured from the middle of the QTF toward one of its prongs (along the x-axis). The amplitude of the acoustic wave reaching the prongs of the QTF is close to 0.002 Pa. This value shows the amplifying effect of the acoustic cavity with approximately a factor 100 between the two configurations.

Using COMSOL as a tool, by changing the shape of the resonator, its dimensions and by adapting the position of the two elements composing the spectrophone, it is possible to observe the variations of the acoustic pressure along this axis and maximize its amplitude. In [9] instead of using a cylindric small tube, the shape has been experimentally modified and, for the same geometrical dimensions of the main tube, different frequencies were observed as well as an enhancement of the acoustic wave measured with a microphone.

3.2- QTF prongs displacements and charges generation

The displacements of the QTF generated by the acoustic wave can be observed when combining the ACPR and the Solid mechanics interface. For two different frequencies, 29 kHz and 32.1 kHz, the generated displacement of the QTF and the acoustic pressure are observed on Figure 25.

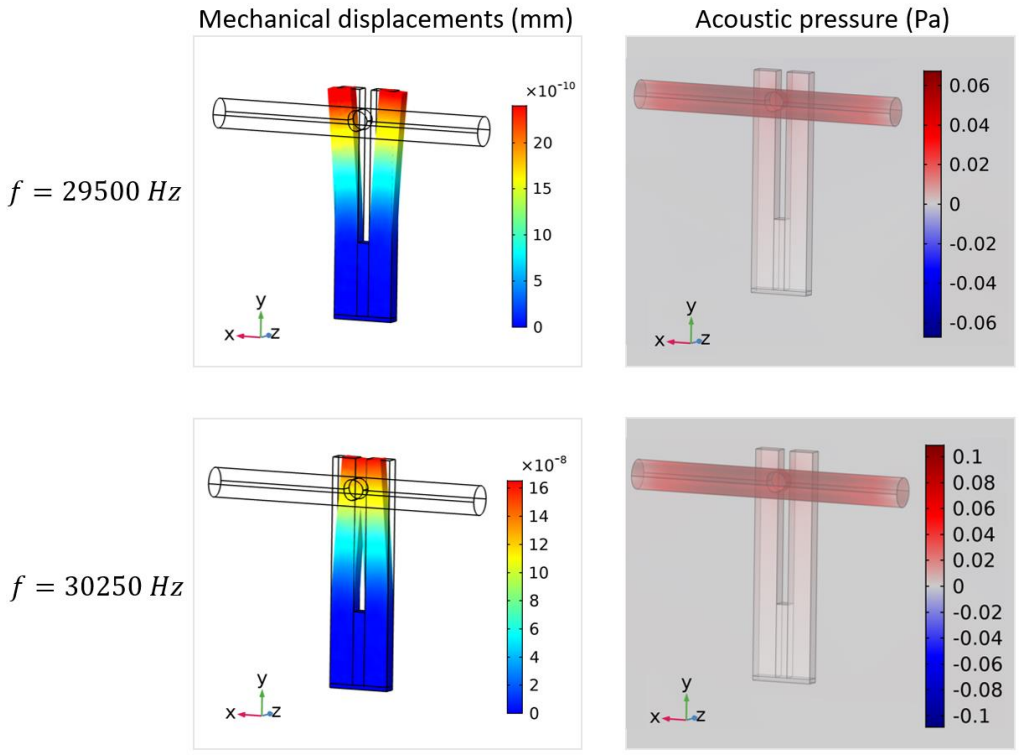

Figure 25: COMSOL simulations: mechanical displacement of the QTF generated by the acoustic wave for different frequencies. The QTF is located around 50 µm from the opening of the small tube along the z-axis. Along the y-axis, the top of the prongs are located at 0.3 mm from the centre of the small tube and centered along the x-axis.

A zero displacement condition is imposed to the base domain of the QTF. A higher amplitude of the acoustic wave is observed around 32 kHz. These values are not presented in this graph as it was meant to observe the in-plane displacement of the QTF. The current QTF that is represented in these simulations is built in different blocks assembled with an union condition. It is necessary to redesign this QTF in order to observe the resonance

frequency at 32 kHz (as for commercial QTFs) because, in the current configuration, the defined boundary conditions do not reflect the real physical constraints of the QTF.

The electrical charges generated by the displacement of the QTF prongs can be calculated using the following equation [39]:

$$\frac{I}{x_L} = 3.42 \times f \times \frac{tw}{y}, \tag{3.45}$$

where I is the generated electrical charges (A) per displacement unit (m). f is the frequency in Hz, t, w and y are respectively the thickness, the width and the length of the prongs (m). The generated electrical charges are calculated in Figure 26.

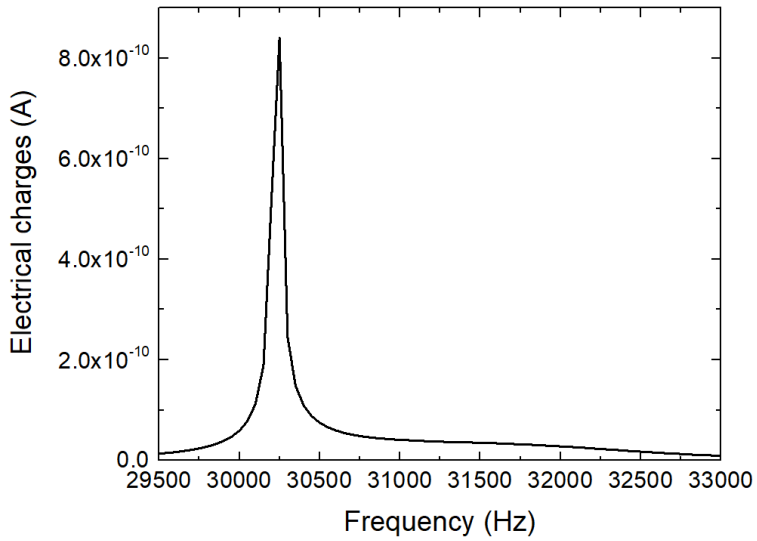

Figure 26: Electrical charges generated by the displacement of the QTF prongs. The values of the displacement is measured at the top the QTF and calculated with Equation (3.45).

The electrical charges were calculated with Equation (3.45), however, further improvement of the model implies the introduction of the Piezoelectric module of COMSOL into this Multiphysics model to correctly observe the generated charges.

3.3- Optimum QTF position

The effect of the position of the QTF on the resonance frequency and the amplitude of the acoustic wave is investigated in this section. The acoustic wave is measured at the output of the small tube, at the distance separating the opening of the tube from the QTF prongs. Mathematically, positioning the QTF in front of the small tube induces a change of the acoustic conductivity of the tube which induces a different length correction [6]. The investigation of the Q-factor and the resonance frequency of the QTF has been performed when moving the QTF in the x-y-z directions [9].

The objective being to optimize the acoustic wave amplitude, this study can be performed in order to find a compromise between the amplitude of the acoustic wave collected between the prongs of the QTF and the optimum position of the QTF that does not affect the generation and the propagation of this wave at the frequency that is defined by the dimensions of the cavity.

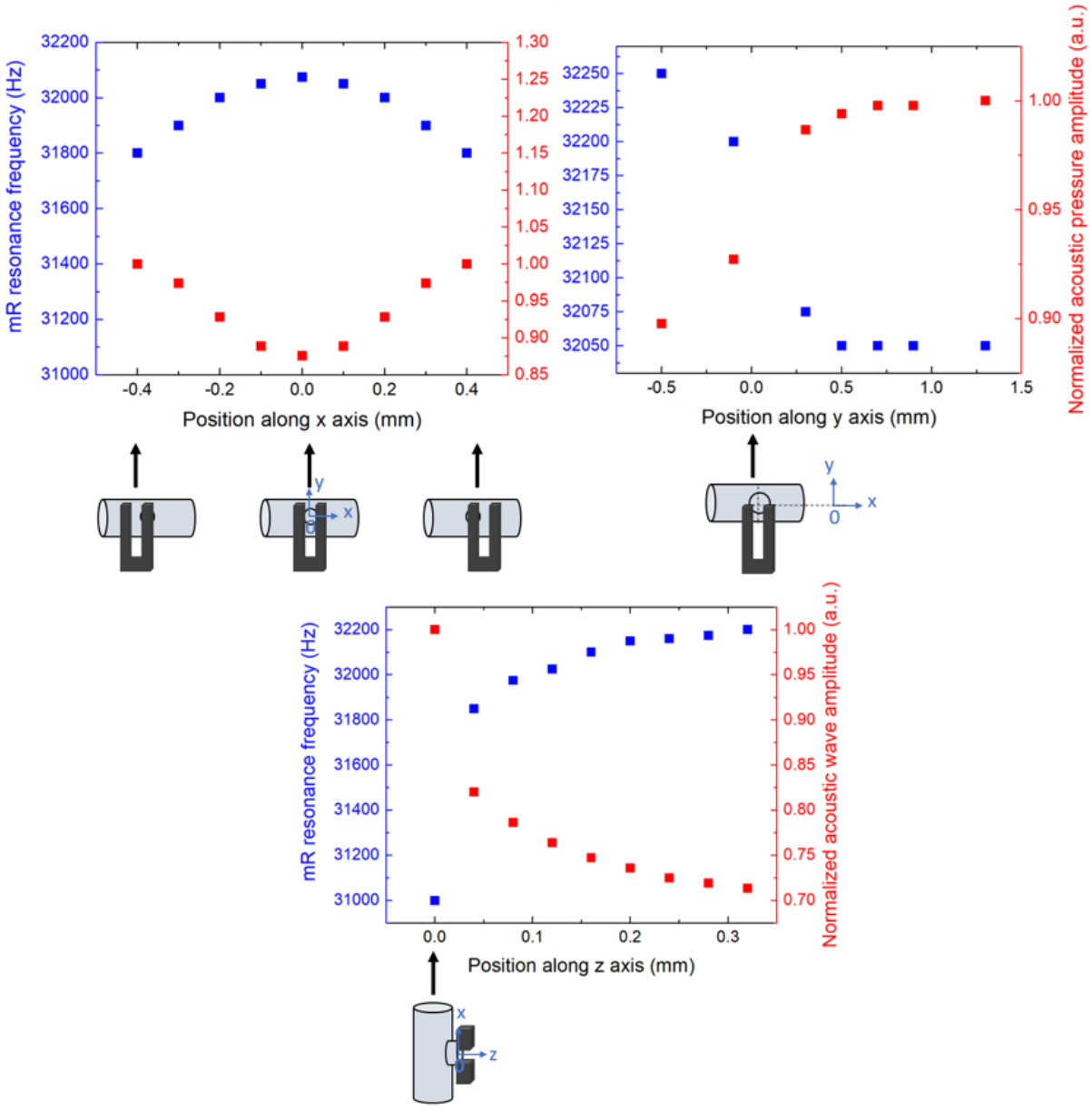

Figure 27: COMSOL simulations: frequency and amplitude of the acoustic wave measured at the output of the small tube when moving the QTF along (a) the x-axis: the position on z-axis = 0.14 mm and on y-axis = 0.3 mm above the centre of the small tube, (b) the y-axis: the QTF is centred along the x-axis and the position along z-axis = 0.14 mm) and (c) the z-axis: the QTF is centred along the x-axis and the position along y-axis = 0.3 mm above the centre of the small tube.

The amplitude of the acoustic wave as well as its frequency is measured:

- When the QTF is moving along the y axis: the amplitude of the acoustic wave increases as long as the QTF's prong appears in front of the small tube. The frequency follows the opposite trend. However, a stabilization of both values is observed around y=0.5 mm where the prongs of the QTF are above the top of the small tube.
- When the QTF is moving along the x axis: again, in this study, the frequency and the amplitude of the acoustic wave follow two opposite trends. While the QTF's prongs are moving along the x axis, the frequency shift to lower values when the opening is obstructed with the surface of the prongs. Simultaneously, the amplitude of the acoustic wave reaches a maximum value.
- When the QTF is moving along the z axis: when the prongs of the QTF are in contact with the surface of the small tube, the amplitude of the acoustic wave as well as its frequency shows outlier values. When the QTF is moving far from the mR, the amplitude of the acoustic wave decreases.

Finally, these observations show that the QTF interferes with the generation of the acoustic wave at the predicted frequency. The optimum of the photoacoustic signal should be obtained for the maximum of acoustic pressure amplitude. Along the x-axis, the QTF must be positioned at x=0 in order to symmetrically excite the two prongs. The optimization of the position of the QTF can be observed from the y and z-axis. Finally, these observations follow what has been observed experimentally for the photoacoustic signal [9]. The acoustic pressure is maximized when the QTF is the closest in the z-axis to the mR and when the latter is positioned around 0.7 mm from its top part.

Conclusion

This chapter constitutes a comprehensive study of the acoustic cavity used to enhance the sensitivity of the QEPAS sensor. The development of the analytical model helped in the validation of the COMSOL (numerical) model. The Multiphysics model can be used as a tool to optimize the acoustic wave generation and observe the behaviour of different geometries comparable, for example, to what is used in musical instruments to amplify the sound. In order to use COMSOL as a prediction tool, the current model has to be more representative of the real-life design and further development must be performed in the fabrication of the mR. The off-beam configuration with 3D printed mRs presenting a resonance frequency that is closest to the QTF's are used to perform the measurements conducted in the next chapter.

References

[1] A. A. Kosterev, Y. A. Bakhirkin, R. F. Curl, and F. K. Tittel, "Quartz-enhanced photoacoustic spectroscopy," *Opt. Lett.*, vol. 27, no. 21, 2002, doi: 10.3969/j.issn.1001-0548.2015.06.025.

[2] L. Dong, A. A. Kosterev, D. Thomazy, and F. K. Tittel, "QEPAS spectrophones: Design, optimization, and performance," *Appl. Phys. B Lasers Opt.*, vol. 100, no. 3, pp. 627–635, 2010, doi: 10.1007/s00340-010-4072-0.

[3] K. Liu, X. Guo, H. Yi, W. Chen, W. Zhang, and X. Gao, "Off-beam quartz-enhanced photoacoustic spectroscopy," *Opt. Lett.*, vol. 34, no. 10, p. 1594, 2009, doi: 10.1364/ol.34.001594.

[4] K. Liu *et al.*, "Trace gas detection based on off-beam quartz enhanced photoacoustic spectroscopy: Optimization and performance evaluation," *Rev. Sci. Instrum.*, vol. 81, no. 10, 2010, doi: 10.1063/1.3480553.

[5] H. Yi, K. Liu, S. Sun, W. Zhang, and X. Gao, "Theoretical analysis of off beam quartz-enhanced photoacoustic spectroscopy sensor," *Opt. Commun.*, vol. 285, no. 24, pp. 5306–5312, 2012, doi: 10.1016/j.optcom.2012.07.056.

[6] H. Yi, W. Chen, S. Sun, K. Liu, T. Tan, and X. Gao, "T-shape microresonator-based high sensitivity quartz-enhanced photoacoustic spectroscopy sensor," *Opt. Express*, vol. 20, no. 8, p. 9187, 2012, doi: 10.1364/oe.20.009187.

[7] A. A. Kosterev and F. K. Tittel, "Ammonia detection by use of quartz-enhanced photoacoustic spectroscopy with a near-IR telecommunication diode laser," *Appl. Opt.*, vol. 43, no. 33, pp. 6213–6217, 2004, doi: 10.1364/AO.43.006213.

[8] A. A. Kosterev, F. K. Tittel, D. V. Serebryakov, A. L. Malinovsky, and I. V. Morozov, "Applications of quartz tuning forks in spectroscopic gas sensing," *Rev. Sci. Instrum.*, vol. 76, no. 4, 2005, doi: 10.1063/1.1884196.

[9] R. Rousseau, "QEPAS gas sensor for air quality monitoring," 2019.

[10] S. L. Firebaugh, E. A. Terray, and L. Dong, "Optimization of resonator radial dimensions for quartz enhanced photoacoustic spectroscopy systems," *Laser Reson. Microresonators, Beam Control XV*, vol. 8600, no. February 2013, p. 86001S, 2013, doi: 10.1117/12.2004581.

[11] Y. Cao, W. Jin, and H. L. Ho, "Optimization of spectrophone performance for quartz-enhanced photoacoustic spectroscopy," *Sensors Actuators, B Chem.*, vol. 174, pp. 24–30, 2012, doi: 10.1016/j.snb.2012.08.014.

[12] Y. Ma *et al.*, "Multi-quartz-enhanced photoacoustic spectroscopy," *Appl. Phys. Lett.*, vol. 107, no. 2, pp. 1–4, 2015, doi: 10.1063/1.4927057.

[13] H. Yi *et al.*, "An acoustic model for microresonator in on-beam quartz-enhanced photoacoustic spectroscopy," *Appl. Phys. B Lasers Opt.*, vol. 108, no. 2, pp. 361–367, 2012, doi: 10.1007/s00340-012-4988-7.

[14] H. Zheng *et al.*, "Single-tube on-beam quartz-enhanced photoacoustic spectroscopy," *Opt. Lett.*, vol. 41, no. 5, p. 978, 2016, doi: 10.1364/ol.41.000978.

[15] L. Dong *et al.*, "Double acoustic microresonator quartz-enhanced photoacoustic spectroscopy," *Opt. Lett.*, vol. 39, no. 8, p. 2479, 2014, doi: 10.1364/ol.39.002479.

[16] H. Zheng *et al.*, "Multi-Quartz Enhanced Photoacoustic Spectroscopy with Different Acoustic Microresonator Configurations," *J. Spectrosc.*, vol. 2015, pp. 1–7,

2015, doi: 10.1155/2015/218413.
[17] Y. Liu, J. Chang, J. Lian, Z. Liu, Q. Wang, and Z. Qin, "Quartz-enhanced photoacoustic spectroscopy with right-angle prism," *Sensors (Switzerland)*, vol. 16, no. 2, pp. 1–7, 2016, doi: 10.3390/s16020214.
[18] L. Hu *et al.*, "Quartz-enhanced photoacoustic spectroscopic methane sensor system using a quartz tuning fork-embedded, double-pass and off-beam configuration," *Photoacoustics*, vol. 18, no. March, p. 100174, 2020, doi: 10.1016/j.pacs.2020.100174.
[19] R. Rousseau, D. Ayache, N. Maurin, W. Trzpil, M. Bahriz, and A. Vicet, "Monolithic Double Resonator for Quartz Enhanced Photoacoustic Spectroscopy," *Appl. Sci.*, vol. 11, no. 5, p. 2094, 2021, doi: 10.3390/app11052094.
[20] C. Lin, X. Yan, and Y. Huang, "An all-optical off-beam quartz-enhanced photoacoustic spectroscopy employing double-pass acoustic microresonators," *Opt. Commun.*, vol. 503, p. 127447, 2022, doi: 10.1016/j.optcom.2021.127447.
[21] Z. Wang *et al.*, "Quartz-Enhanced Photoacoustic Spectroscopy Based on the Four-Off-Beam Acoustic Micro-Resonator," *J. Light. Technol.*, vol. 38, no. 18, pp. 5212–5218, 2020, doi: 10.1109/JLT.2020.2998848.
[22] Y. Ma, Y. Hong, S. Qiao, Z. Lang, and X. Liu, "H-shaped acoustic micro-resonator-based quartz-enhanced photoacoustic spectroscopy," *Opt. Lett.*, vol. 47, no. 3, pp. 0–3, 2022.
[23] D. T. Blackstock, "Fundamentals of Physical Acoustics." p. 541, 2000.
[24] S. El-Busaidy, B. Baumann, M. Wolff, L. Duggen, and H. Bruhns, "Experimental and numerical investigation of a photoacoustic resonator for solid samples," *Sensors (Switzerland)*, vol. 19, no. 13, 2019, doi: 10.3390/s19132889.
[25] K. Stephan and A. Laesecke, "The Thermal Conductivity of Fluid Air," *J. Phys. Chem. Ref. Data*, vol. 14, no. 1, pp. 227–234, 1985, doi: 10.1063/1.555749.
[26] G. Badino, "The legend of carbon dioxide heaviness," *J. Cave Karst Stud.*, vol. 71, no. 1, pp. 100–107, 2009.
[27] ""The Engineering ToolBox (2018). Air - Prandtl Number. Website accessed on 09-27-2023: https://www.engineeringtoolbox.com/air-prandtl-number-viscosity-heat-capacity-thermal-conductivity-d_2009.html."" .
[28] F. Moser, L. J. Jacobs, and J. Qu, "Modeling elastic wave propagation in waveguides with the finite element method," *NDT E Int.*, vol. 32, no. 4, pp. 225–234, 1999, doi: 10.1016/S0963-8695(98)00045-0.
[29] W. Trzpil, N. Maurin, R. Rousseau, D. Ayache, A. Vicet, and M. Bahriz, "Analytic optimization of cantilevers for photoacoustic gas sensor with capacitive transduction," *Sensors*, vol. 21, no. 4, pp. 1–22, 2021, doi: 10.3390/s21041489.
[30] M. Duquesnoy, "Tuning forks in photoacoustic spectroscopy : Comparative study and new developments," 2021.
[31] L. E. Kinsler, A. R. Frey, A. B. Coppens, and J. V. Sanders, "Fundamentals of Acoustics," *The Journal of the Acoustical Society of America*, vol. 72, no. 3. p. 1090, 1982, [Online]. Available: http://scitation.aip.org/content/asa/journal/jasa/72/3/10.1121/1.388211.
[32] G. Mayer and J. Gigon, "Mesure par ultrasons des constantes élastiques des solides," *J. Phys. le Radium*, vol. 16, no. 8–9, pp. 704–706, 1955, doi: 10.1051/jphysrad:01955001608-9070400.
[33] E. G. Richardson, *Technical Aspects of Sound: Vol. 1*. 1953.
[34] A. N. Norris and I. C. Sheng, "Acoustic radiation from a circular pipe with an

infinite flange," *J. Sound Vib.*, vol. 135, no. 1, pp. 85–93, 1989, doi: 10.1016/0022-460X(89)90756-6.
[35] S. Yong, "Comparing Theory and Measurements of Woodwind-Like Instrument Acoustic Radiation," *Technology*, no. January, 2009.
[36] A. Jadhav and V. S. Jadhav, "A review on 3D printing: An additive manufacturing technology," *Mater. Today Proc.*, vol. 62, pp. 2094–2099, 2022, doi: 10.1016/j.matpr.2022.02.558.
[37] "'SLA schematic. Website accessed on 09-28-2023: https://www.nouvelleecole.fr/blog/techniques-dimpression-3d-fdm-sla-sls.'" .
[38] "'SPU0410LR5H-QB. Website accessed on 09-28-2023: https://www.knowles.com/subdepartment/dpt-microphones/subdpt-sisonic-surface-mount-mems.'"
[39] D. Courjon and C. Bainier, *Le champ proche optique: Théorie et applications*. 2001.

Chapter 4
Quartz enhanced photoacoustic spectroscopy for breath analysis

The first part of this chapter is dedicated to the adaptation of the QEPAS setup to breath analysis and the implementation of a breath sampling system to ensure repeatable measurement conditions.

In the second part of this chapter, calibrated measurements of CO, NO, isoprene and acetone as well as breath measurements using the previously presented sampling system are proposed.

Finally, the QEPAS setup is combined with the Medisoft Ergocard apparatus used at Montpellier Hospital (Clinical Physiology department) in order to perform real-time breath measurements associated with capnography and flow assessment.

1- Humidity effect on QEPAS stability

QEPAS has been used as a detection technique in many applications such as environmental gas detection [1], exhaled breath analysis [2] or for food-industry (detection of ethylene). Measurements performed in laboratory conditions, under standardized procedures, with calibrated gas bottles and controlled humidity and temperature are very simple to perform: the light of the laser is focused inside the gas cell containing an already known concentration of the target gas and, from the data acquisition system, the user receives a magnitude (voltage) corresponding to this concentration. However, on-field measurements can be more challenging. The previously cited parameters, often characterizing the working environment, can act in a non-neglectable way on the stability of the sensor. In real-life application, the variation of the humidity, temperature, flow and their effect on the measurement cannot be controlled or predicted.

The QEPAS signal is usually defined as proportional to the power of the laser source, the absorption coefficient of the gas and Q-factor of the QTF and inversely proportional to its resonance frequency. The very high quality factor of the QTF makes QEPAS almost immune to background noises but at the same time very sensitive to frequency drifts. Nevertheless, if environmental conditions cannot be controlled or predicted, the frequency

and the Q-factor are, alternatively, two experimental values that can be taken into account. Different teams working on QEPAS measurements have faced these issues by developing techniques relying on the measurement of the frequency and the Q-factor in order to correct their variations [3]–[5].

In a previous project conducted in our laboratory, R. Rousseau has developed a technique to measure the QTF's parameters and perform a correction in order to stabilize the QEPAS signal. Indeed, before any QEPAS measurement, the resonance frequency of the QTF is measured by the mean of an electrical excitation as presented in Chapter 2 section 3.3. This value is used simultaneously by the LIA as a reference frequency for the demodulation of the measured signal and for the modulation the laser. During QEPAS measurement, if the frequency of the QTF is affected by any outside variations, it is possible to lose information related to the amplitude of the signal as the reference of the LIA and the resonance frequency of the QTF are no longer matching. It is sometimes not possible to perform an electrical characterization of the QTF during the analysis of a gas sample, especially if the application is targeting real-time measurement, as this method can take up to 10 seconds to be completed. Therefore, by using the method presented in Chapter 2 section 3.3, it is possible, in about one second, to measure the frequency and the Q-factor of the QTF and perform a correction of the LIA parameters in case of variation [6].

1.1- Effect of humidity on the QTF frequency and Q-factor

1.1-1. Experimental setup

As the exhaled breath is saturated in terms of relative humidity, the resonance tracking method presented in Chapter 2 is implemented in order to understand the effect of this parameter onto the resonance frequency and Q-factor of the QTF and the stability of the QEPAS signal. In this part, three different QTFs are compared: commercial QTF and two types of custom QTFs especially designed for QEPAS experiments. These QTFs have been provided as part of a collaboration between our laboratory and the Polysense team from the University of Bari (Italy).

These QTFs are characterized by larger prongs spacing ($\sim 1\ mm$) which makes the alignment of the laser more comfortable and helps avoiding the photothermal perturbations especially with long wavelength laser presenting larger beams. Moreover, these QTFs are also more adapted to the detection of slow relaxing molecule as they present lower resonance frequencies that are closer to the relaxation frequency of some gases such as CO or NO.

The custom QTFs used in this study are presented in Figure 1 and their dimension are compared to the commercial QTFs in Table 1.

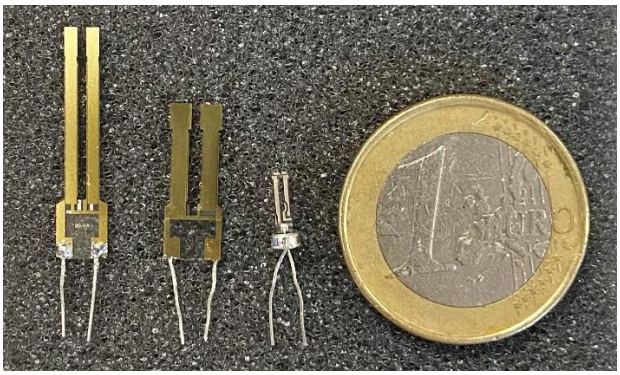

Figure 1: From left to right, the QTFs are referenced as: AV-08, T1-08 and commercial (NC38LF by Fox Electronics).

Table 1: Comparison of the dimensions of each category of QTF.

Ref QTF	Prong length (mm)	Prong width (mm)	Prong spacing (mm)
AV-08	16.0	1.2	0.8
T1-08	Base: 7.0 Head: 2.4	Base: 1.4 Head: 2.0	0.8
Commercial	~3.8	0.6	0.3

The effect of the temperature on the frequency of the QTF is well known and specified by manufacturers. The frequency evolves in a parabolic shape when the temperature increases. The effect of the humidity on the different parameters characterizing the QTF, meaning the resonance frequency and the quality factor was questioned as soon as the QTF was diverted from its intended use in vacuum. In this section the effect of humidity on different QTFs is compared. In the chapter 2, the characterization setup that is used to perform this study has been detailed.

As a reminder, the measurement is based on the investigation of the beat frequency recorded from the QTF in response to an external sinewave excitation of amplitude V_{exc} and frequency f_{exc}. The period of the beat frequency informs on the frequency of the QTF f_0 and its envelop describes the Q-factor Q (Equation (2.34), (2.35) Chapter 2).

The optimum excitation parameters for the commercial QTF were assessed in the chapter 2. The same experiment has been conducted for the two categories of custom QTFs. The first step consists of fixing V_{exc} and measure the beat signal for a certain value of f_{exc}. The second step is the measurement of different excitation amplitudes V_{exc} at a fixed f_{exc}. These experiments are conducted for 1 minute at a rate of 1 Hz, each. The results are presented in Figure 2 and summed up in Table 2.

The optimum is chosen for values presenting the smaller deviations. f_{exc} is chosen small enough as long as $f_{exc} \neq f_0$ and V_{exc} is chosen big enough to avoid errors on the measurement but small enough in order to not saturate the input of the LIA.

Table 2: Resonance frequency, Q-factor and optimum values characterizing the sinewave excitation: f_{exc} (Hz) and V_{exc} (mVpp), for each QTF.

Ref QTF	f_0 (Hz)	Q	$\lvert f_{exc} - f_0 \rvert$ (Hz)	V_{exc} (mVpp)
AV-08	3800	7500	2	100
T1-08	12450	15000	3	100
Commercial	32750	8000	20	100

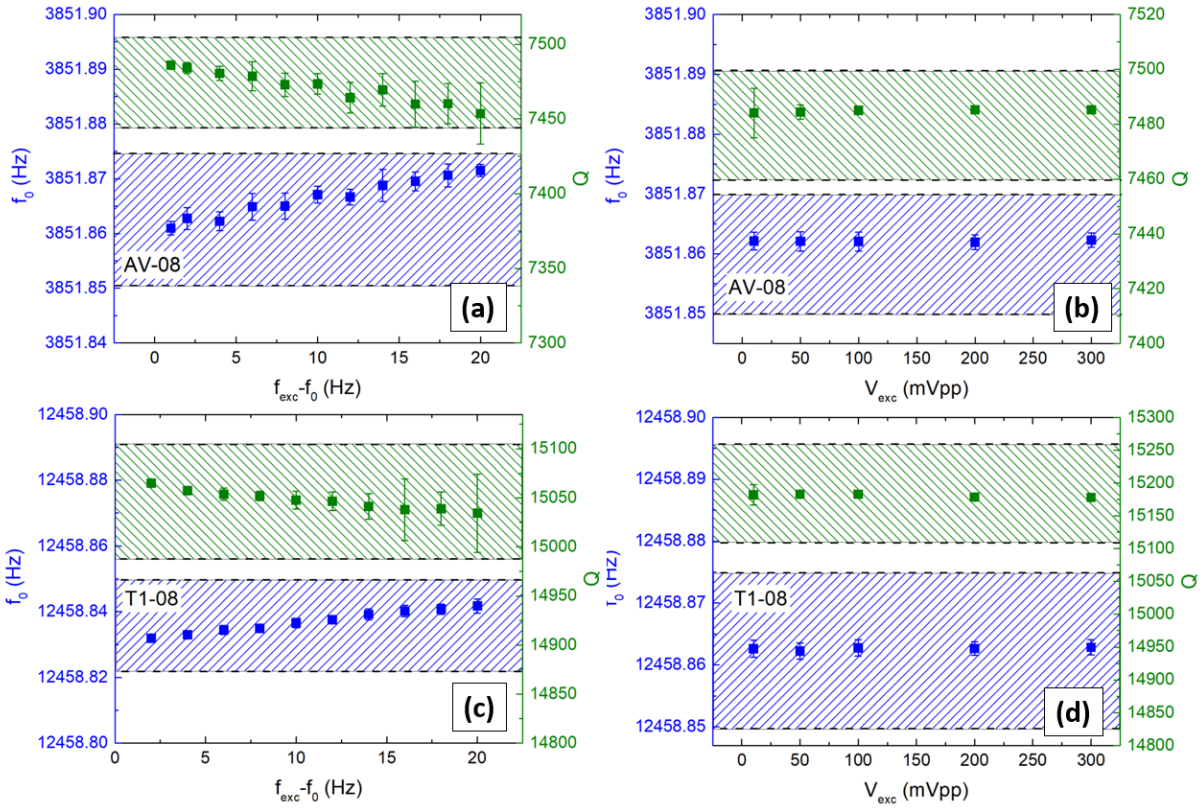

Figure 2: Investigation of the optimum excitation frequency and amplitude of the sinewave (f_{exc}, V_{exc}) for each QTF. (a-b) respectively corresponds to $\lvert f_{exc} - f_0 \rvert$ and V_{exc} for the AV-08 group and (c-d) to $\lvert f_{exc} - f_0 \rvert$ and V_{exc}, respectively, for T1-08 group. The measurement conducted for the commercial QTF are presented in Chapter 2 section 3.3.

In order to ensure a stabilized and controlled humidity, the measurements were performed in a humidity chamber (ESPEC SH-242). Different humidity steps are generated, from 30 to 90% of relative humidity (%RH) with an increasing step of 10%. Each humidity step lasts 20 minutes to make sure that the humidity in the chamber is completely stabilized. At

the end, two steps of 50 and 30 %RH are added to assure the repeatability of the measurement. The temperature in the chamber is kept constant at 22 °C.

1.1-2. Required accuracy on the QTF parameters during QEPAS

An important specification to have for industrial sensors is the accuracy on the displayed values (concentrations, signal amplitude). Most gas sensors assure an accuracy of a few percent, therefore, this criterion has been followed in the subsequent definitions. The QEPAS signal is the final value displayed by the sensor. Thus, an acceptable relative error of 1% is established. The accuracy that needs to be reached on f_0 and Q to not exceed this 1% error is calculated as follows:

$$\frac{\Delta S}{S(f_0)} < 0.01 \tag{4.1}$$

The QEPAS signal is represented by a Lorentzian lineshape, centered at f_0, the resonance frequency of the QTF. The response of the QTF is electrically represented with the well-known Butterworth-Von Dyke (BVD) model. This model has already been introduced in Chapter 2 section 3.3 showing that the QEPAS signal is proportional to the squared admittance of the QTF, representing a Lorentzian function:

$$S^2(f, Q) = \frac{CQ^2}{1 + \left(\frac{2Q(f - f_0)}{f_0}\right)^2} \tag{4.2}$$

In this equation, C is a constant that is related to the transimpedance gain (10^7) and the BVD model parameters which are included in f_0 and Q as well.

The defined 1% amplitude error can be associated to an error on the measured frequency Δf_0.

By isolating f in Equation (4.2), we obtain:

$$f(S) = \pm \frac{f_0}{2Q} \sqrt{\frac{CQ^2}{S^2} - 1} + f_0 \tag{4.3}$$

The frequency error Δf_0 for a commercial QTF with a $f_0 = 32$ kHz and a Q = 8000 in atmospheric conditions is found noting that:

$$S^2(f_0) = CQ^2, \tag{4.4}$$

Thus,

$$\Delta f_0 = |f_0 - f(S - \Delta S)| = \frac{f_0}{2Q}\sqrt{\frac{1}{\left(1 - \frac{S(f_0)}{\Delta S}\right)^2} - 1} \tag{4.5}$$

$$\Delta f_0 = \frac{32 \times 10^3}{2 \times 8000}\sqrt{\frac{1}{(1 - 0.01)^2} - 1} = 0.28\ Hz. \tag{4.6}$$

As the QEPAS signal at resonance ($f = f_0$) is linearly related to the Q-factor, the error on the latter is easily estimated as:

$$\frac{\Delta Q}{Q} = \frac{\Delta S}{S(f_0)} \leftrightarrow \Delta Q = 0.01Q = 80. \tag{4.7}$$

Figure 3 represents the variation of the frequency in green corresponding to a 0.28 Hz shift and the variation of 80 on the Q-factor in blue both leading to a relative error of 1% on the QEPAS signal, shift free, represented in black.

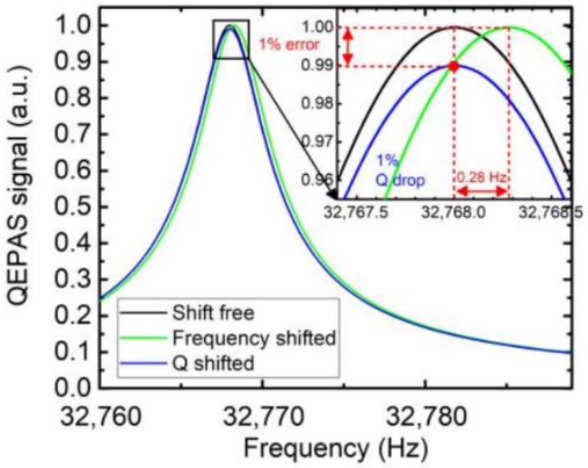

Figure 3: The QEPAS signal is associated to a Lorentzian curve centered at 32.768 kHz with a Q-factor of 8000. The frequency response of the shift-free QEPAS signal is represented in black and present a maximum value at $f = f_0$. The frequency response is represented for a frequency shift of 0.28 Hz (green) and a Q-factor reduction of 80 (blue). The intersection of the two curves at $f = f_0$ corresponds to the 1% error calculated on the QEPAS signal [4].

For both types of custom QTFs, the same 1% error is estimated on f_0 and Q according to their values. The results are described in Table 3.

Table 3: Variations of f_0 and Q, respectively, Δf_0 and ΔQ, leading to 1% error on the QEPAS signal, reported for each group of QTF. The calculation is performed on the fundamental mode.

Ref QTF	f_0 (Hz)	Q	Δf_0 (mHz)	ΔQ
AV-08	3800	7500	36	75
T1-08	12450	15000	60	150
Commercial	32750	8000	280	80

1.1-3. Experimental results

The study of the variation of the QTF parameters was made following two steps:

- Investigating the **deviation of f_0 and Q during a stabilized value of humidity** (arbitrary measured for 70 %RH) as it could be the case in a QEPAS experiment with controlled humidity (for example breath sensing with controlled humidity).
- **The difference of mean values of f_0 and Q between 30% and 90 %RH** is investigated considering the case of a real-life measurement where the humidity would increase rapidly (for example breath sensing with no control of the humidity).

The presented results are interpreted on the basis of an acceptable error of 1% on the QEPAS signal. The calculated variation of *f0* leading this 1% error were equal to 0.28, 0.036 and 0.06 Hz respectively for commercial, AV-08 and T1-08 group.

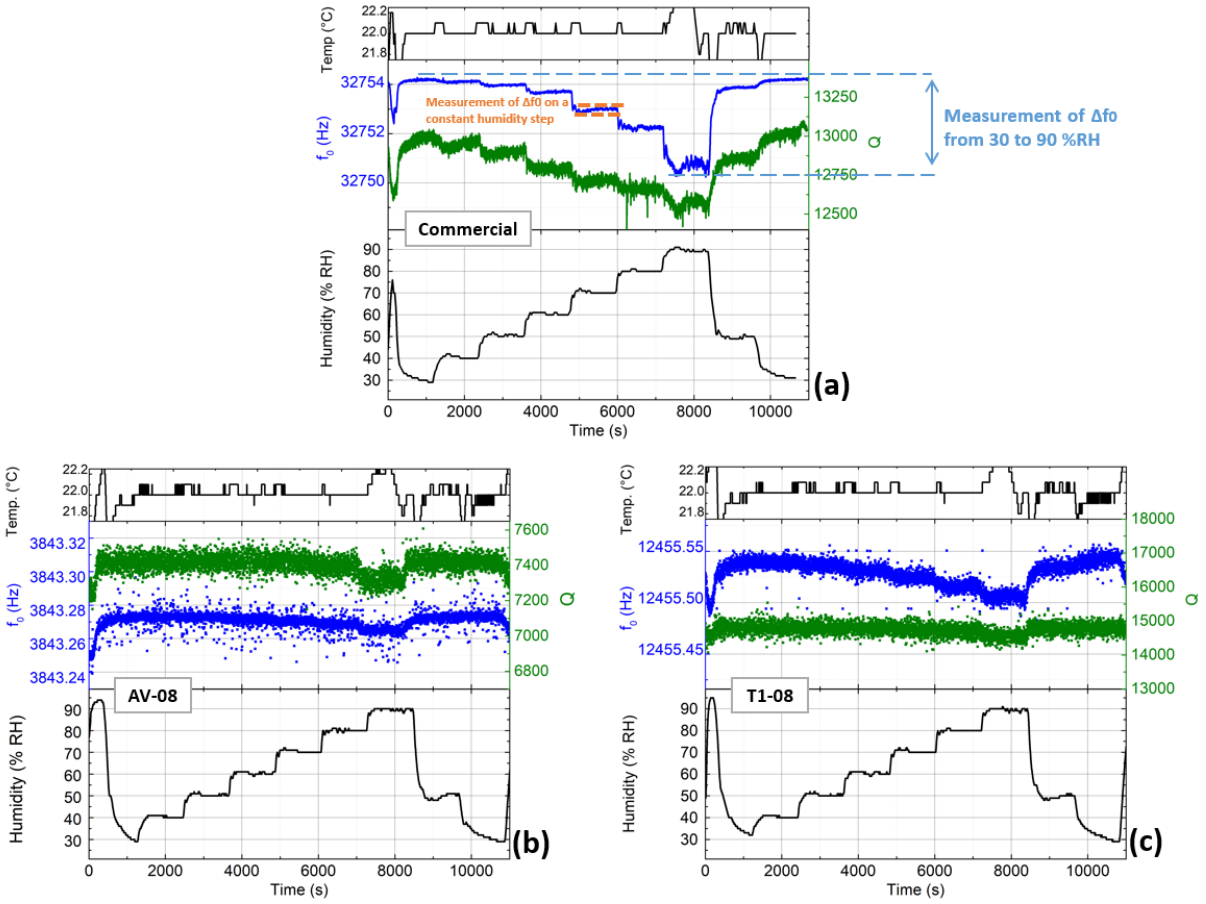

Figure 4: Frequency and quality factor measurement for different humidity steps with a fixed temperature of 22°C. Humidity and temperature data were collected from the humidity chamber software. Variation of f_0 and Q were measured with a LabVIEW program. a) commercial QTF, b) AV-08 and c) T1-08. The time constant of the LIA was set to 1 ms for proper BF demodulation. The study of f_0 and Q variation for different steps of humidity was performed in two conditions described in blue and orange dashed lines (a).

Figure 4a describes the variation of the **commercial QTF** parameters. It shows a shift of approximately 2 Hz when varying the humidity from 30 to 80 %RH and about 1.5 Hz between 80 and 90 %RH which represents a maximum shift of about 3.5 Hz between the lowest and the highest value of humidity. On a constant value of humidity, f_0 variations were very small: ~0.025 Hz. The same investigations were realized for the custom QTFs and the results are summarized in Table 4. **For each QTF**, the largest shift of f_0 is occurring at 90 %RH. The variation of f_0 when moving from 80 to 90 %RH was approximately equal to the shift occurring when the humidity was increased from 30 to 80 %RH. It is also at 90 %RH that the largest error on the temperature was observed. It could be estimated that this error, approximately equal to ±0.2 °C, occurred due to the difficulties to keep this humidity value stable.

On a constant value of humidity, i.e. by keeping the humidity level stable during the experiment, both commercial and custom QTFs presented non-significative variations of

their resonance frequency showing that the characterization setup is stable and accurate. In fact, there was approximately a factor of 0.1 between measured variations of f_0 and calculated values leading to 1% of error for each group of QTFs.

The comparison of frequency variations between 30 and 90 %RH showed a difference in behavior between custom QTFs and commercial ones. Several commercial QTFs were tested, the dispersion of the data shows unpredictable variations in high humidity conditions (80-90 %RH) whereas, both groups of custom QTF presented sustainable variation in the same conditions. For commercial QTFs the variations of f_0, ranging between 0.5 and 3 Hz, was above the acceptable defined values. In this comparison, the AV-08 group (Figure 4b) presented more stable results than the T1-08 (Figure 4c). The measured values for AV-08 (resp., for T1-08) were about 0.0055 (resp., 0.05) and were 5 times (resp., 1.2 times) smaller than the calculated values.

Table 4: Comparison of measured variation of f_0 and Q to the related calculated variation leading to 1% error on the measured QEPAS signal. The measured variation of f_0 and Q are obtained by varying the humidity between 30% and 90 %RH.

	Variations of f_0 (Hz)			**Variations of Q**		
	Target	**Experimental**		**Target**	**Experimental**	
	Calculated for 1% error	**Inter-step 30-90 %RH**	**Intra-step 70 %RH**	**Calculated for 1% error**	**Inter-step 30-90%RH**	**Intra-step 70 %RH**
Commercial (presented)	0.280	3.5	0.025	80	391.5	22.7
Statistics on commercials	0.280	1.105±1.612	0.01±0.01	80	365.7±393.1	19.1±2.8
AV-08 A	0.036	0.0055	0.0035	75	10	100
AV-08 B	0.036	0.0087	0.0058	75	86	60
T1-08 A	0.06	0.052	0.0064	150	40	300
T1-08 B	0.06	0.041	0.0042	150	381.7	250

In Table 4, the results are presented for a commercial QTF and for each group of custom QTFs. Several measurements were performed on commercial QTFs and mean values were extracted from these experiments including 6 QTFs.

While we are still uncertain about the origin of the high dispersion observed on commercial QTF, one must consider the necessity to perform additional measurements on each group of QTF in order to build a statistic and potentially observe a trend. Further measurements for a better understanding of the humidity effect may imply the development of custom QTFs with dimensions that are closer to the commercial ones.

The irregular variation of f_0 leads us to focus our concern on this crucial parameter that is taken into consideration at different stages in the experiments. However, the inconsistent variations of the quality factor are more complex to describe. For commercial QTFs, the variation of Q from 30 to 90 %RH might be a cause of instability in the system while they are acceptable on a constant humidity value. For custom QTFs, the observation of the variations of Q could not lead to the definition of a trend.

Different observations that need to be investigated, can be proposed to explain f_0 and Q variations:

- During measurements presented in Figure 4, the QTF was connected to a metallic support and that support was in mechanical contact with the metallic surface of the humidity chamber. The mechanical vibrations of the support as well as the air flow generated by the fan present inside the chamber can possibly be the cause of this "degradation" observed on Q. It was even more pronounced for custom QTF due to their higher length and thinner thickness. Measurements presented in Figure 2 were performed on constant humidity level. These measurements were performed before launching the machine, i.e. with the machine's door open, thus the condition of temperature and humidity inside the chamber are equal to the ambient ones. The dispersion observed in this figure, for the chosen parameters ($|f_0\text{-}f_{exc}| = 20$ Hz and $V_{exc} = 100\ mV_{pp}$), is less significant than what was reported during the measurement performed with humidity variations.
- QTFs have been exposed to high levels of humidity. Experiments presented in this paper were conducted at least two times. The surface of the QTFs was observed with a microscope. However, with a magnification down to 100x, no physical degradations of the QTFs was noticed. Consequently, these observations cannot explain the variation of Q, neither f_0.
- In the literature, the effect of humidity on the resonance frequency was investigated when using QTFs as humidity sensors as they can be very sensitive to mass changes [7]. Hygroscopic coating was added on the QTFs prongs and the effect of different coating thickness investigated. The variations were measured with an oscillating circuit: the shift of the frequency is negative when humidity increases and more pronounced for a thicker coating as the surface for water deposition is increased. In

the investigation of QTF as humidity sensor [7], the presence of small water droplets settling on the surface of the prongs due to their roughness was considered . This added non-uniform mass can be a cause of the observed damping.

Even if they were not especially designed for photoacoustic sensing, commercial QTFs present very comparable QEPAS performances to custom QTFs as long as the humidity is stabilized during the measurement. In that case, commercial QTFs remain a cheaper, smaller and efficient option for gas sensing. Nevertheless, in some applications such as breath analysis, the relative humidity can reach 90 % at the end of the exhalation, implying a large increase of the humidity in the sensor usually operating at room humidity. The results obtained through these measurements showed more reliable performances of custom QTFs in that case while commercial QTFs' behavior can be unpredictable.

Although custom QTFs are especially designed to resonate at lower frequencies, adapted to match the relaxation frequency of some slow relaxing gas detected in photoacoustic applications and even though they seem to be more stable to drastic humidity changes, we decided to keep working with commercial QTFs. Indeed, commercial QTFs are widely available and cheaper. Their small size opens up the way to the miniaturization of the gas cell thus, the sensor. Moreover, the previously presented results shows a very good stability of these devices if the humidity is maintained stable. Regarding humidity, as presented in chapter 2, this parameter has a significant impact in the process leading to the generation of the acoustic wave. The direct consequence of that phenomenon is that for a fixed concentration of gas (if its relaxation path through water relaxation is prevailed), different magnitudes can be measured for different humidity levels. In the chapter 2, this effect was demonstrated on some molecules such as CO and NO, leading to an enhancement of the PA signal by a factor of 10 (in the case of CO). Therefore, it is crucial to be able to control the humidity and avoid working in highly variable environment if we are not able to compensate its effect.

The humidity in the breath is not stable and its level can be different from one subject to the other. In the 1st chapter, we mentioned the importance of working in standardized conditions is order to avoid false measurements. Therefore, the humidity must be stabilized and the use of the commercial QTFs seems justified.

The following part of the chapter are dedicated to the development of a bubbling bath used to stabilize the humidity.

1.2- Stabilization of the humidity: homemade bubble bath

In this manuscript, two techniques used to stabilize the humidity in a gas mixture are described. In this section, the bubbler humidifier is presented. In the last part of this chapter, membranes designed with Nafion material are described.

The humidifier which function is to stabilize the humidity coming from the exhaled breath constitutes the first stage of the breath sampling system. Bubbler humidifiers are one of the most common way to humidify and stabilize the humidity in a gas mixture. In the rest of the chapter we are going to call it a bubble bath or bubbler. The principle is as simple as its fabrication: the gas is humidified in a water container. The gas arrives in a tube immersed in the water where multiple small holes are drilled (Figure 5). Bubbles are formed and charged in humidity by rising to the surface where they can exit from the container by a tube kept outside of the water. By implementing this bubble bath, the objective is to stabilize and decrease the humidity during the breath measurement.

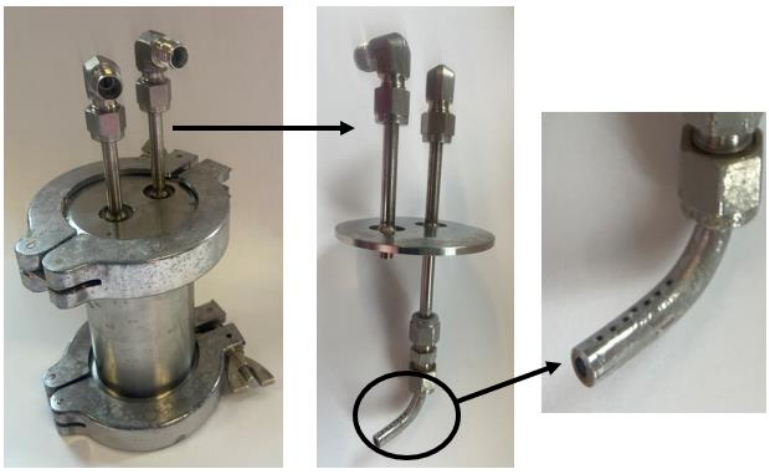

Figure 5: Bubble bath used in breath measurement and immerse tube with small drilled holes conducting to the generation of air bubbles.

The exhaled breath temperature ranges around 33 °C and is basically saturated in relative humidity (95 %RH). Despite the fact that the humidity is variable between each subject, if the exhaled breath is directed directly to the gas cell, condensation will certainly occur on the "metallic" walls of the cell and windows as they are close to room temperature. Figure 6 describes this phenomenon.

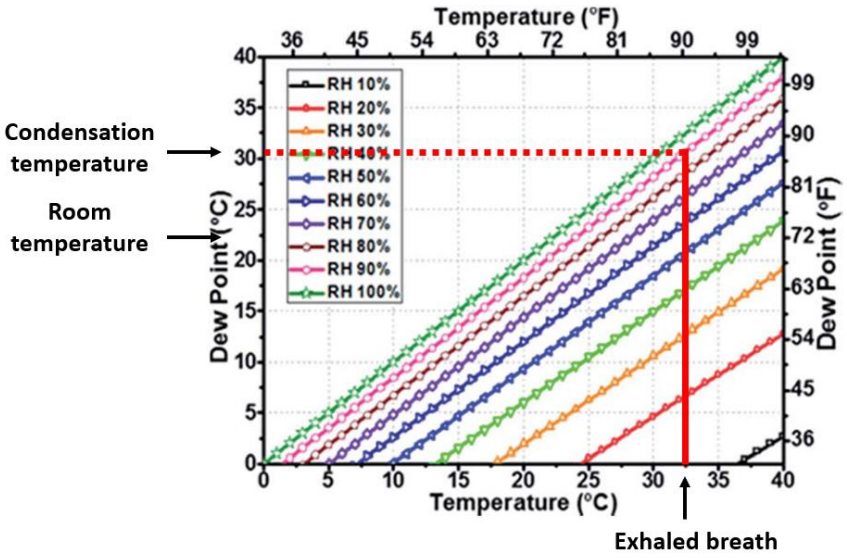

Figure 6: Dew point as function of the temperature, for different relative humidity. The exhaled breath condensates around 30 °C meaning that inside the gas cell, that is close to 22 °C, condensation may occur. [8]

As long as the bubble bath helps to stabilize the humidity in order to not disturb the frequency of the QTF and allows it to reach a low level to prevent this condensation phenomenon, the final value of the relative humidity at the exit of the bubble bath is not important to define.

In addition, in this sampling system, the measurement is carried out through the complete expiration of the physiological volume. Consequently, the bubble bath has to be "passive" and not act as a resistance for the subjects during exhalation.

On a more technical level, the response time of the sensor must be affected as little as possible. For that purpose, the volume of the bubble bath was reduced as much as possible and its characteristics as function of the temperature and its effect on the QEPAS signal are investigated in the next sections through an empirical study.

1.2.1- Temperature effect on humidity level

The aim of this experiment is to assess the effect of the bubble bath temperature onto the relative humidity of the gas arriving to the QEPAS gas cell after passing through the bubbling water system.

The humidity level in the gas cell is measured by the mean of a humidity sensor (HIH-4000 Series) and the data are recorded from an Arduino board on a LabVIEW program. The accuracy of the sensor ± 3.5 %RH and its response time close to 5 seconds.

The experimental setup is simple: dry N_2 is flushed through the bubble bath with a flow of about 1 L/min and the humidity level is measured after humidification of the dry gas in water at ambient temperature (tap water temperature close to 19 °C) and close to 6 °C. In order to decrease the temperature of the bubble bath a water coil, in which water close to 3°C circulates, is soldered onto the bubble bath. Thermal paste is added in order to facilitate the conduction and the system is enclosed into a foam sheath.

On Figure 7 the result of this first experiment is presented. The dry N_2 is humidified through the bubbler and the humidity is stabilized at a certain value for each water temperature. Indeed, when the bubble bath is kept at room temperature, the measured humidity level in the gas cell is close to 90 %RH. When the bubble bath is close to 6 °C, the level of humidity is stabilized at around 40 %RH.

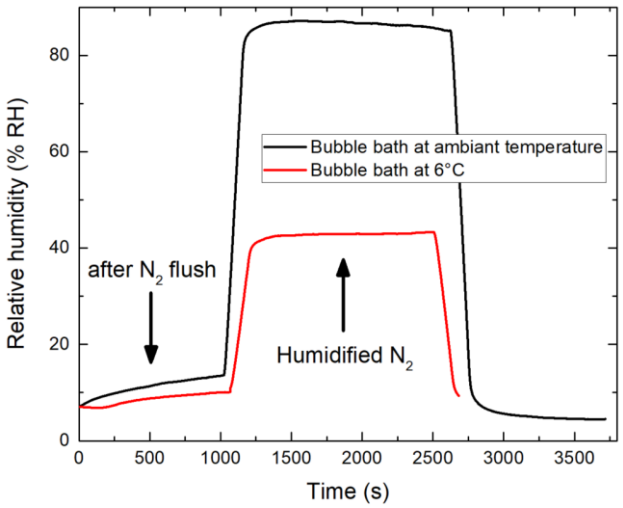

Figure 7: Relative humidity measured inside the QEPAS gas cell after flushing dry N_2 through the bubble bath maintained at room temperature (black) and close to 6°C (red). The N_2 flush is maintained at 1 L/min.

The capacity of a gas to hold water decreases as its temperature decreases. This value is expressed in kg of water vapor per kg of air and depends of the temperature of the gas. Therefore, the bubble bath is efficiently working, if the gas at the output of the bubbler is saturated (100 %RH) in water vapor. In that case, the humidity ratio ranges close to 0.014 kg/kg and 0.006 kg/kg respectively at room temperature and at 6°C. Which is in line with the fact that the air holds less water at lower temperatures. When the gas exits the bubble bath, the tubes and the gas cell are closer to 20-22°C. The humidity ratio remains the same but the relative humidity changes from 100 %RH to ~ 40 %RH and $80-90$ %RH respectively for the gas humidified at 6 °C and at room temperature. This phenomenon can be explained by Figure 8.

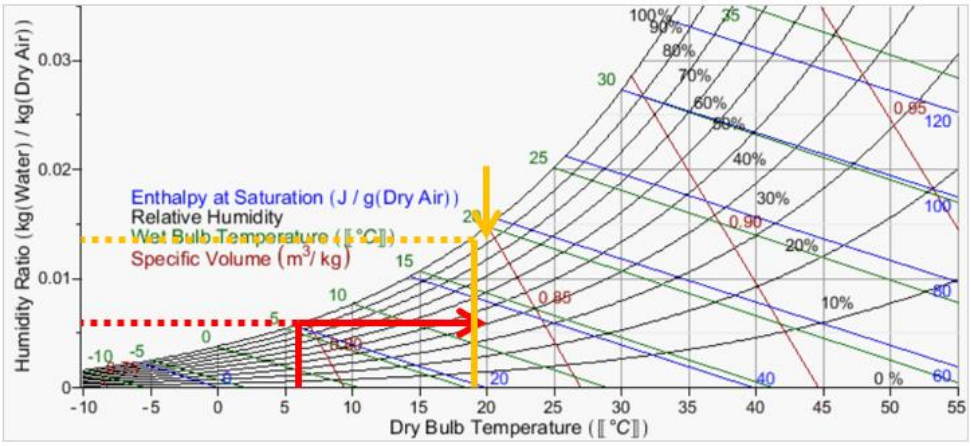

Figure 8: For different relative humidity and temperature, the humidity ratio is calculated. The red lines describe the gas humidified at 6 °C and arriving to the gas cell around 20°C and the yellow lines describe the gas humidified around 19°C.

The efficiency of the bubble bath depends on different parameters including the flow rate of the gas, its residence inside the water, the length of the immersed tube and the size of the holes. These parameters were not investigated in this manuscript. However, when humidifying the air through water around 6°C, the relative humidity will be close to 40 %RH at 20°C and lead to a dew point around 7.5 °C, which helps preventing condensation on the cell's walls and windows.

The effect of the cold bubble bath is then observed on the exhaled breath. The humidity inside the gas cell is measured with the humidity sensor presented above. First the subject is exhaling into the cold bubble bath and the output gas is directed to the gas cell (left Figure 9). Then, the subject is exhaling directly into the gas cell (right Figure 9).

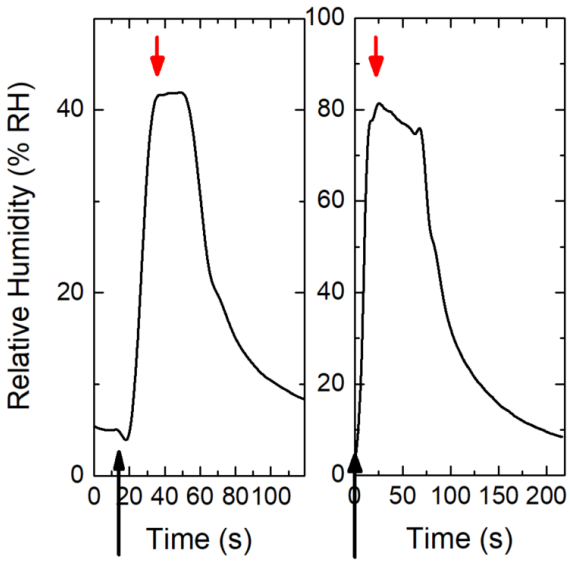

Figure 9: Left: the effect of the cold bubble bath (6°C) is measured on the exhaled breath. Right: the exhaled breath is directly sent to the gas cell. The black arrow shows the beginning of the exhalation and the red arrow shows the end of the exhalation.

The conducted experiments show that it is possible to stabilize the humidity coming from the breath by the mean of a bubble bath while reducing its level by changing the temperature of the bath to lower values. Thus, it is possible to keep the humidity close to 40 %RH in order to avoid working in extreme conditions that are more severe for the transducer as predicted in section 1 of this chapter.

1.2-2. The effect of temperature on the shape of the signal

During the first trials experimenting the measure of exhaled breath gases with a QEPAS sensor, one major issue was the shape of the signal. Basically, the concentration of gas, here carbon monoxide from the breath, rises to a certain value but starts to decrease even if the subject is still exhaling, which is not correct according to the expirogram of CO where an end tidal plateau should be observed [9]. This abnormal peak is mostly due to a frequency perturbation, as shown by the result of the section 1 of this chapter, caused by the high amount of humidity introduced into the gas cell. In fact, during these first trials, the gas cell was flushed (rinced) with dry N_2 and the breath measurement were conducted through the bubble bath. The humidity inside the cell increases from 0 to around 90 %RH which could cause a high drift of the frequency and a loss of signal. Therefore, in the following measurements, the effect of different humidity levels is assessed.

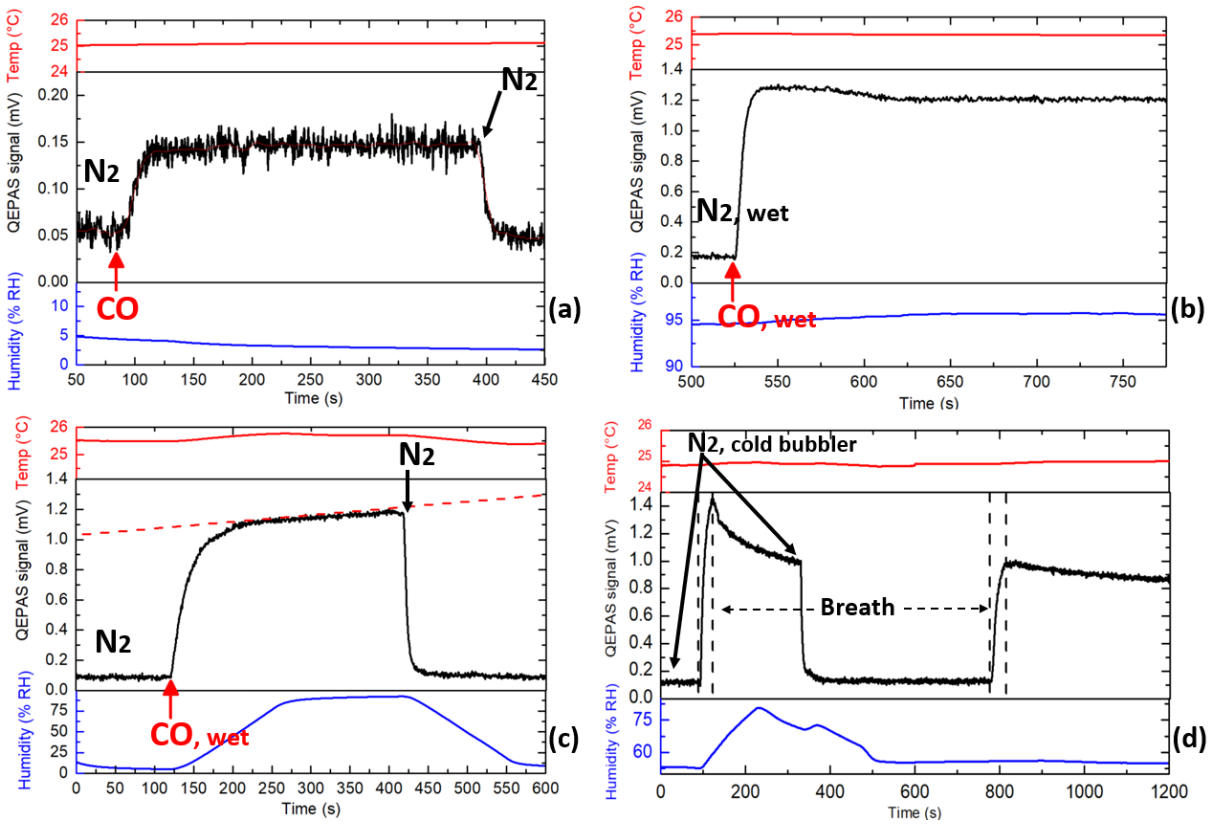

Figure 10: (a-c) Photoacoustic signal measured for 1 ppmv of CO in different experimental conditions. The humidity and the temperature (thermistor) are measured inside the gas cell. (a) QEPAS signal measured on dry CO. (b) QEPAS signal measured on wet CO: the humidification is done with the bubbler at ambient temperature. During (a) and (b) the humidity is kept constant in the gas cell. (c) The gas cell is flushed with dry N2 and the QEPAS signal measured on wet CO, humidified with the bubbler at ambient temperature. (d) QEPAS signal from breath CO: by exhaling directly into the gas cell (first part) and by exhaling through the cold bubbler (6°C) (second part).

The measurements are conducted on a CO absorption line around $\lambda = 4.6$ µm. A calibrated concentration of dry carbon monoxide (1 ppmv) in N_2 is used. During these measurements the temperature and the current of the laser are fixed. The first measurement is conducted on a dry sample of CO (Figure 10a). The signal increases when the gas is introduced to the gas cell and reaches a plateau around 0.15 mV. The humidity is stabilized close to zero during the experiment (blue curve). In the second experiment (Figure 10b), the humidity of the cell is stabilized at around 95 %RH (blue curve). First, dry N_2 is flushed through the bubble bath at room temperature ($N_{2,\,wet}$). When the humidity in the gas cell is stabilized, CO is flushed through the bubble bath into the gas cell ($CO_{,\,wet}$), the signal increases, marking a little inflection before completely stabilizing at around a magnitude of 1.2 mV. If the measurement at a settled value of humidity seems to reach a plateau, it is not the case if the humidity varies drastically when the gas is introduced to the gas cell. Indeed, Figure 10c shows that the signal, when passing from 0 to 90 %RH (reached respectively with dry N_2 flush and wet CO), is not reaching a plateau even after a long period of time (dashed red line).

With the purpose of understanding the consequence of these last observations upon the breath humidity and analysis, we conducted two different experiments (Figure 10d). In these experiments the humidity of 50 %RH is reached by humidifying the gas through the bubble bath around (6°C-8°C). For the first expiration (delimited with the black dashed lines) the subject is asked to exhale directly into the gas cell without passing by the humidifier which results in an increase of the humidity and the signal of CO. However, it is possible to observe that the signal starts to decrease even if the subject is still expiring through the gas cell. For the second expiration, the subject is exhaling through the cold bubbler. The results show a stabilization of the signal during the whole exhalation procedure and a plateau reached for end tidal part.

To sum up on the previously presented work, the stabilization of the humidity level is crucial in order to provide a reliable measurement and correct concentration of the gas. According to our last observations, an acceptable and stable level of humidity, i.e. 40 %RH, is achievable by reducing the temperature of the bubble bath (around 6°C). In addition, it appears more consistent to keep the humidity level in the gas cell always constant to avoid high changes of humidity leading to frequency shifts.

1.3- Measurement of the flow

Different mass flow meters were available in our laboratory. The possibility to build a numeric interface and record the shape of the flow curve is valuable in the measurement of the breath to estimate the beginning of the exhalation. However, a mass flow meter needs a high pressure (1 bar at least) at its entrance which is physiologically impossible to execute. The aim of this work being the standardization of the breath measurement, we have used rotameters using their visual appearance to define a range of flow to not exceed. Due to that, before any measurement, we asked the subjects to perform several breathing procedures to get acclimated to the device and be able to respect the flow ranges ($\pm$ 1.5 L/min). The measurement of the flow can only be described from a qualitative perspective as no data can be extracted from the rotameters. For some subject it felt like they were holding back their breath and for others it felt like they needed to force the expiration. In both cases, asking the subject to control their flow, even with a visual sign represented on the flowmeter, was not natural. Therefore, this variability needs to be considered as a bias in the measurements.

1.4- Design of a new gas cell: time response reduction

Regarding the reduction of the response time of the sensor, the first intuition led to the reduction of the gas cell volume. Indeed, QEPAS technique offers a high potential of miniaturization as the phenomenon leading to the generation of a PA signal is measured at a very localized scale, at the neighborhood of the QTF. Therefore, it is possible to reduce the volume of the gas cell in order to reduce the gas volume that needs to be "recycled" (chased out) of the gas cell at the beginning of the experiment. The volume of the big gas cell (in which the measurement presented in the previous sections were performed) is close to 60 mL. The design of the reduced gas cell was performed on CATIA v5 software and manufactured in our laboratory. The volume of the reduced cell is close to 2 mL. Figure 11 presents the two gas cells and their dimensions. The volume calculated above considers the support of the spectrophone, this support occupies an important volume that is subtracted from the air volume to recycle. Figure 12 shows the response time of the QEPAS sensor using the normal cell and the reduced one when 1ppmv of CO is flushed through the bubble bath to the gas cell with a constant flow of 1 L/min.

The effect of the volume reduction is summed up in Table 5. The rise time is the time between 10 % and 90 % of the maximum value and the response time is the time to reach $\pm$ 5% of the maximum value.

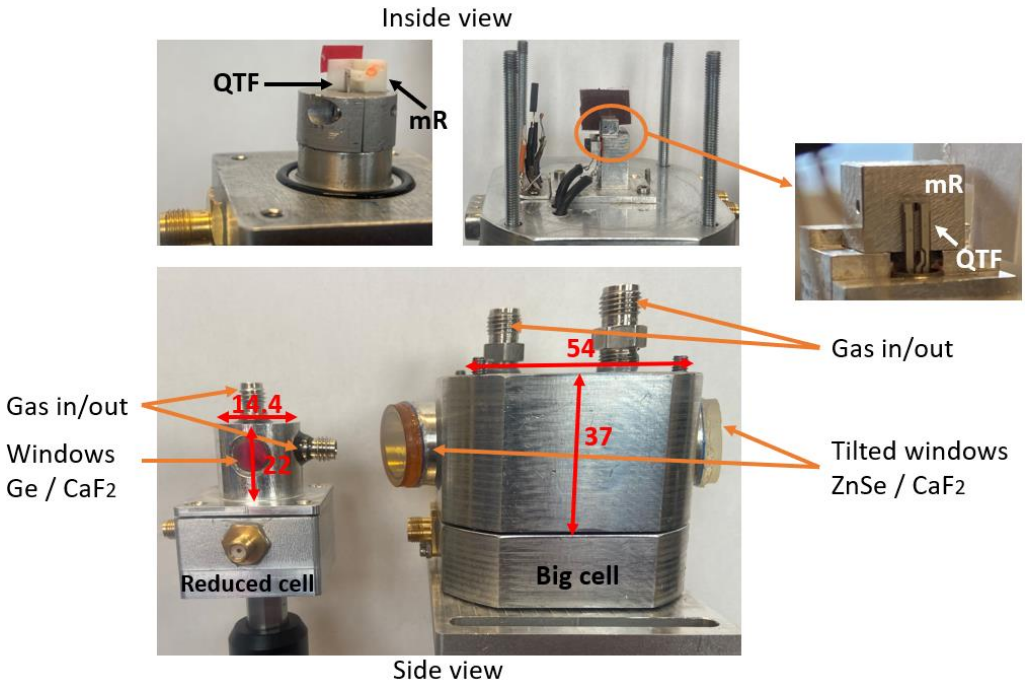

Figure 11: Big and reduced gas cell: inside view presenting the spectrophone (mR + QTF) and side view presenting the windows and gas in/outlet. The dimensions of the cells are given in mm.

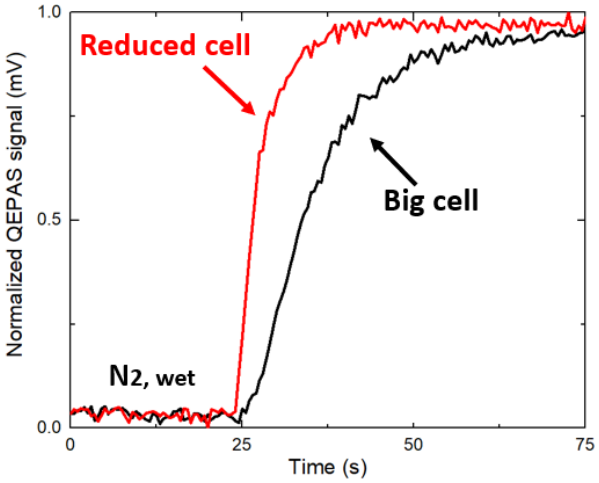

Figure 12: Effect of the gas cell volume reduction onto the response time of the sensor. The measurement is conducted on wet CO (with bubbler at ambient temperature) (1 ppmv) with a flow rate of 1 L/min.

Table 5: Rise time and response time of the sensor conducted with the big and the reduced gas cell when 1 ppmv of CO is flushed through the bubble bath at ambient temperature before entering the gas cell at a flow rate of 1 L/min.

	Big cell	**Reduced cell**
Rise time (s)	20	10
Response time (s)	40	25

In the last part of this chapter, the QEPAS sensor is combined with the Medisoft apparatus. The Medisoft apparatus measures the expiration and inspiration flow rate and the exhaled concentration of CO_2. The provided physiological information that must be combined with the exhaled concentration measured with the QEPAS sensor only hold meaning if they are acquired at the same time. The Medisoft measurements are performed in less than one second, therefore it is crucial to reduce the response time of the QEPAS. The response time presented in Table 5 includes the bubble bath. When this element is taken off the experimental setup, the response time of the sensor ranges between 1 and 2 seconds. These measurements are presented in the last part of this chapter.

To sum up on this first part, the effect of the humidity onto the frequency of the QTF that is considered at different stage of the experiment setup was assessed. The results showed the necessity to conduct the measurement in a constant and reduced level of humidity compared to what can be found in the exhaled breath. A breath sampling system has been implemented. It involves a bubble bath that is capable of providing a stable and reduced humidity, a flowmeter and a gas cell with a reduced volume helps reaching response time close to 1 s for an efficient breath investigation.

In the next part, the experimental setup for the detection of CO, NO, isoprene and acetone is presented.

2- SENSIR gases detection using QEPAS

As presented in the first chapter, this project aims to detect four different gases that were defined according to their implication in cardiovascular diseases: carbon monoxide, nitric oxide, isoprene and acetone.

The detection of any gas begins with the definition of the laser source and the wavelength working range. The choice is made according to:

- the intensity of the absorption line as the QEPAS signal is proportional this value,
- the interferences with water and CO_2 that are present in high amount in the exhaled breath
- the availability of the light sources.

Once the working wavelength is defined, different steps are necessary for the calibration of the sensor and will be detailed in the next sections.

2.1- Carbon monoxide detection at $\lambda = 4.6$ µm

2.1.1- Wavelength working range and laser source

The targeted absorption line of each compound is recovered from HITRAN database. In this case, the absorption path is defined at 1 cm. The concentration of CO is 1 ppmv and the atmospheric concentration for H_2O and CO_2 are defined respectively at 7750 ppmv and 340 ppmv. The V-R spectrum of CO shows, among other, two different regions in the near and mid-IR. However, the intensity of the absorption lines at 4.6 µm are about 140 times higher than those present at 2.3 µm (Figure 13).

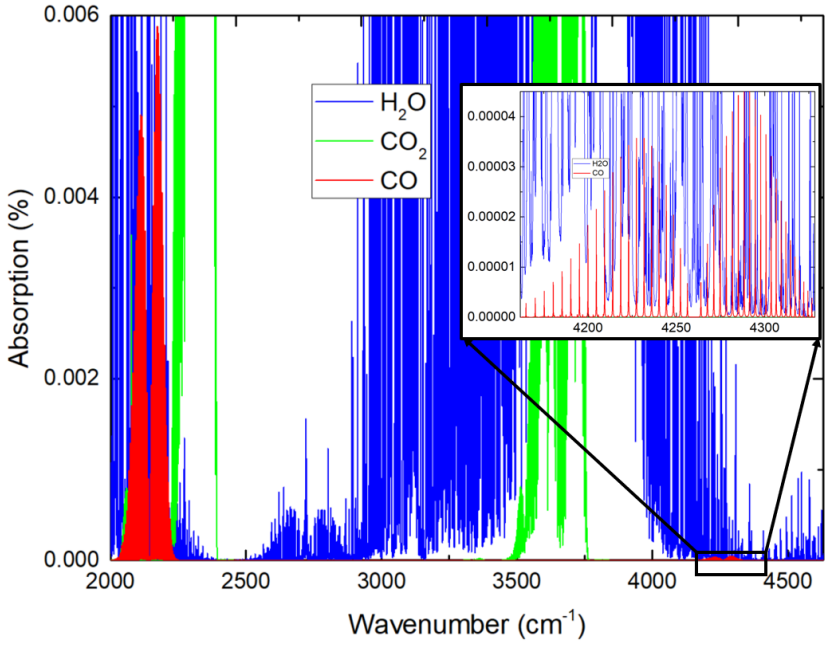

Figure 13: V-R spectrum of CO around 2100 and 4250 cm^{-1} with the H_2O and CO_2 interferents. The data were retrieved from HITRAN database. The concentrations were equal to 1, 7750 and 340 ppmv respectively for CO, H_2O and CO_2. The pathlength was equal to 1 cm.

The employed laser source is a commercial DFB-QCL operated in continuous wave regime (Adtech Photonics). The specification of the laser is given in Figure 14a. The absorption line of CO, located exactly at 2172.7 cm^{-1} is targeted between 20 and 25 °C. The CO is simulated for 1 ppmv and the H_2O for 7750 ppmv. At 20°C, in the absorption region, the optical power of the laser is close to 50 mW (Figure 14b).

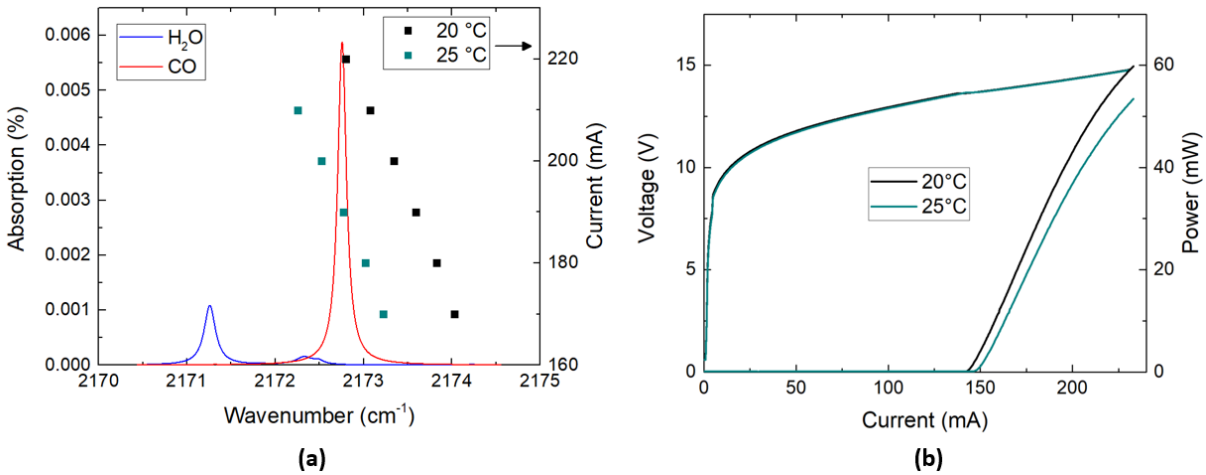

Figure 14: (a) Targeted CO absorption line at 2172.7 cm^{-1} and tuning range of the laser between 20 and 25 °C. (b) Power and Voltage as function of the injection current (PIV) at 20 and 25 °C.

2.1.2- CO QEPAS signal: optimization

Figure 15a shows a typical 2f QEPAS signal obtained for 20 ppmv of CO (generated with a calibrated gas cylinder). As presented in the experimental setup in Chapter 2 section 3, the light of the laser is focused inside the gas cell using a black diamond aspherical lens (Thorlabs C028TME-E) coated between 3-5 µm. The laser is modulated at $\frac{f_0}{2}$ $\sim 16.378\ kHz$ with an optimum modulation amplitude calculated from the experimental results presented in Figure 15b. The QEPAS setup is used in an off-beam configuration. The QEPAS signal is obtained by performing a current sweep of the injection current of the laser. The signal recorded from the QTF and amplified with the transimpedance amplifier is sent to the LIA (EG&G 7260) for 2f demodulation with a time constant of 100 ms.

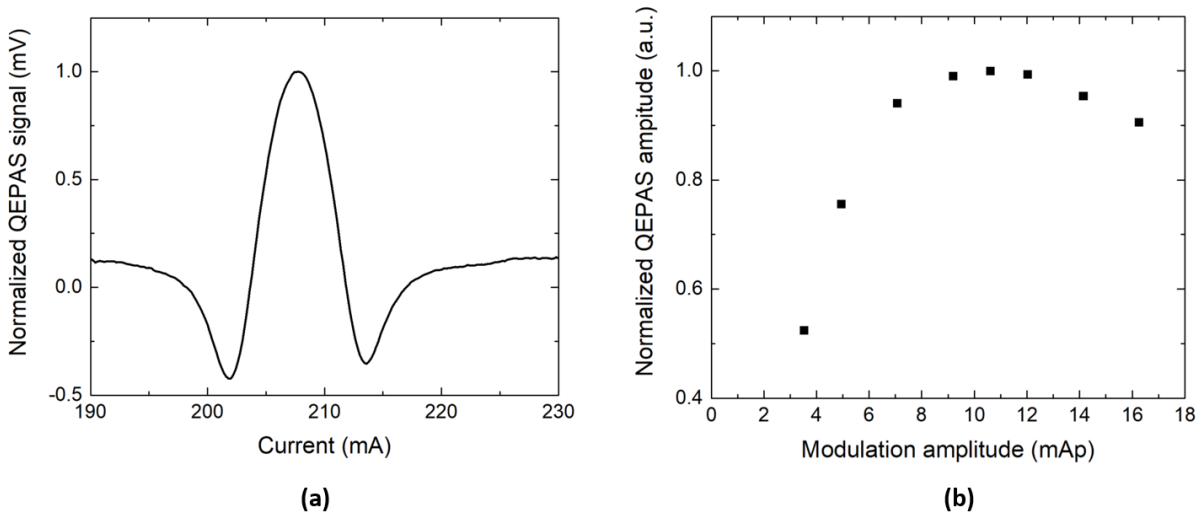

Figure 15: (a) 2f-signal obtained for 20 ppmv of dry CO. The laser's temperature was stabilized around 22°C and the modulation amplitude set at 10.6 mA peak. (b) Amplitude of QEPAS 2f-signal according to the modulation amplitude. The optimum is found at 10.6 mAp.

2.1.3- Sensor calibrations

The calibration of the sensor takes place once the sensors parameters are optimized, i.e, the modulation amplitude and frequency. The laser injected current is fixed at 207.5 mA and the signal is recorded over a period of time. The calibration of the sensor consists of recording its response to different concentrations of the target gas. In the following experiments, a gas mixing system (GasMix-2 Aiolos) is used to generate different controlled concentrations of CO from a 20 ppmv calibrated cylinder (the vector gas is N_2). Four different concentrations of CO are generated: 0.5, 1, 5 and 10 ppmv. The output voltage of the sensor is measured in 3 different conditions (Figure 16):

- The gas is directly sent to the gas cell (dry: black squares),
- The gas passes through the bubble bath at ambient temperature before entering the gas cell (wet: red squares),
- The gas passes through the cold bubble bath (6°C), before entering the gas cell (cold bubbler: blue squares).

The error on the amplitude is measured around 0.01 mV. The error bars are reported on Figure 16.

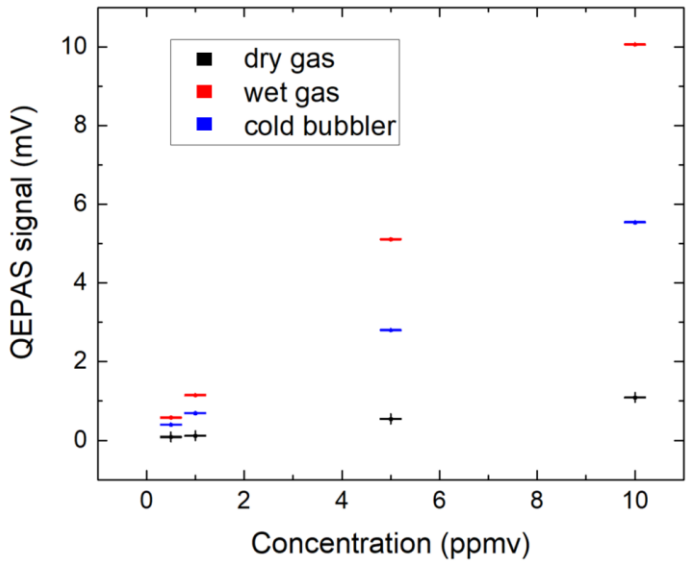

Figure 16: QEPAS signal obtained for 0.5, 1, 5 and 10 ppmv of CO: dry, wet and cold bubbler, i.e. the gas is humidified with the bubbler at ambient temperature and a 6°C, respectively.

In the three different cases, the sensor achieves linear responses with R^2 = 0.999, 0.99982 and 0.998 respectively for dry, wet and cold bubbler data. Water has a significant effect on the amplitude of the QEPAS signal as we can calculate that the signal of CO humidified at room temperature is 10 times higher than the dry CO signal as observed in Chapter 2 (section 3.2-3)

2.1.4- Allan deviation and NNEA

In the Chapter 2 section 4.1, the Allan deviation and the NNEA have been presented as tools to evaluate the performances of the sensor.

Allan deviation is conducted to determine the limit of detection of the sensor as function of the integration time. 1 ppmv of CO humidified with the cold bubbler (6°C) is introduced

into the gas cell and the 2f-signal is recorded for 10 minutes. The Allan deviation is calculated.

The limit of detection at 1 s in 2f is equal to 17 ppbv giving $NNEA = 3.5 \cdot 10^{-8}\, W \cdot cm^{-1} \cdot Hz^{-0.5}$. The optimum averaging time is obtained for 100 seconds.

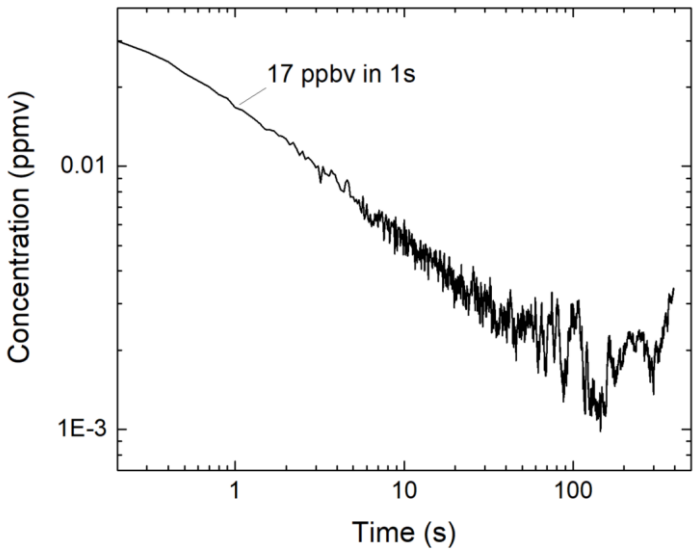

Figure 17: Allan deviation showing the limits of detection (LOD in ppmv) as function of the integration time (s). The signal is recorded for 1 ppmv of wet (bubble bath at ambient temperature) CO. The LOD is equal to 17 ppbv at 1s and the optimum averaging time obtained for 100 s.

2.2- Nitric oxide detection at 5.2 µm

2.2.1- Wavelength working range and laser source

The V-R spectra of NO depicts strong absorption line (ν_1) around 5.2 µm (1900 cm^{-1}) approximately 67 times stronger than the ν_2 group (inset around 3700 cm^{-1}). The absorption of NO and its interferents is given in Figure 18 for 1 ppmv of NO, 7750 ppmv of water and 340 ppmv of CO_2. The absorption pathlength is fixed at 1 cm.

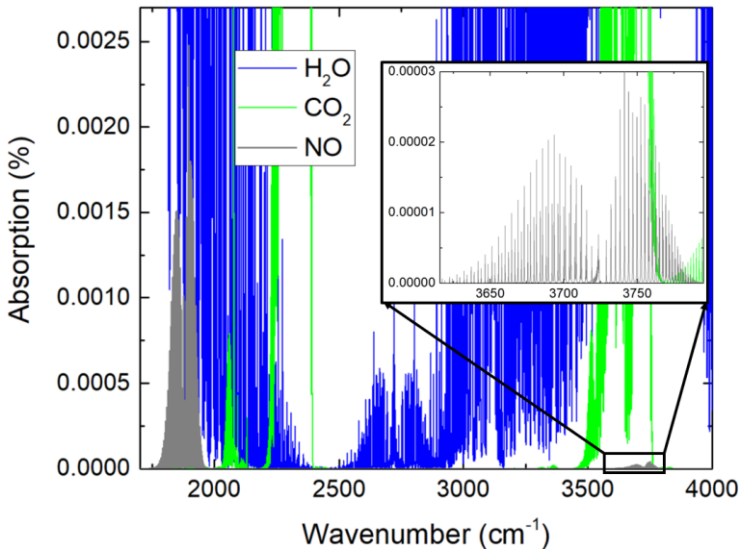

Figure 18: V-R spectrum of NO around 1900 and 3700 cm^{-1} with the H_2O and CO_2 interferents. The data were retrieved from HITRAN database. The concentrations were equal to 1 ppmv, 7750 ppmv and 340 ppmv respectively for CO, H_2O and CO_2. The pathlength was equal to 1 cm.

The laser used for NO detection is a MirSense DFB – QCL operating at 20 °C in continuous wave regime. The spectrum of the laser is presented in Figure 19a. In the absorption region, around 750 mA, the optical power of the laser is close to 20 mW (Figure 19b). A water absorption line as well as a smaller absorption line of NO are reachable in the tuning range of the laser at 20 °C

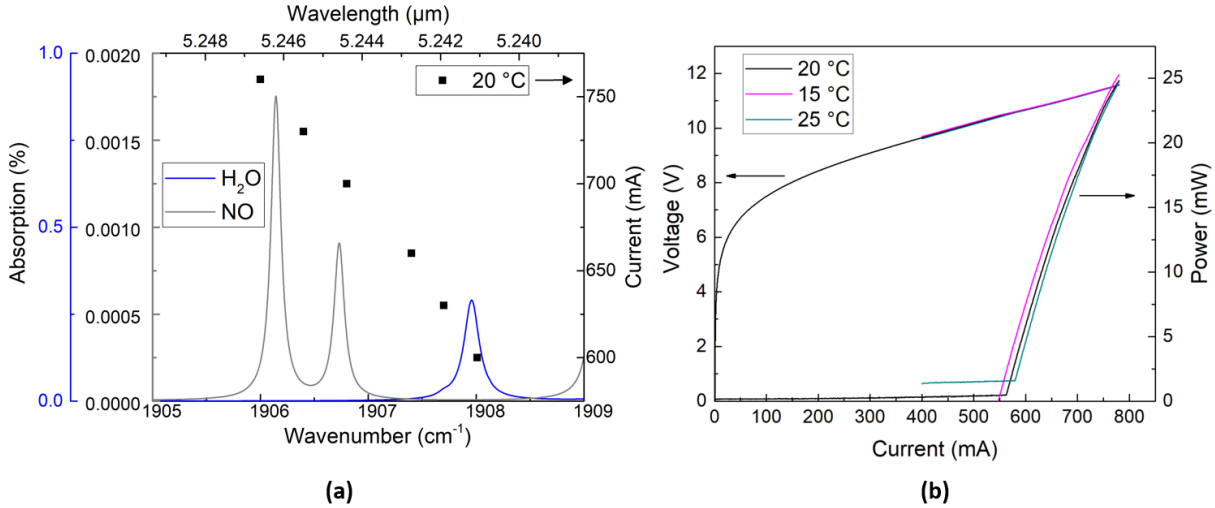

Figure 19: (a) Targeted CO absorption line at 1906.1 cm^{-1} and tuning range of the laser at 20°C. (b) Power and voltage as function of the injection current (PIV) at 15, 20 and 25 °C. The offset observed before the threshold current at 25 °C is due to ambient light measured by the powermeter.

2.2.2- NO QEPAS signal: optimization

Figure 20a shows the second harmonic of the QEPAS signal obtained for 50 ppmv of NO. The light of the laser is modulated around 16.378 kHz and the optimum modulation amplitude is evaluated from Figure 20b. The signal is recovered with a time constant of 200 ms.

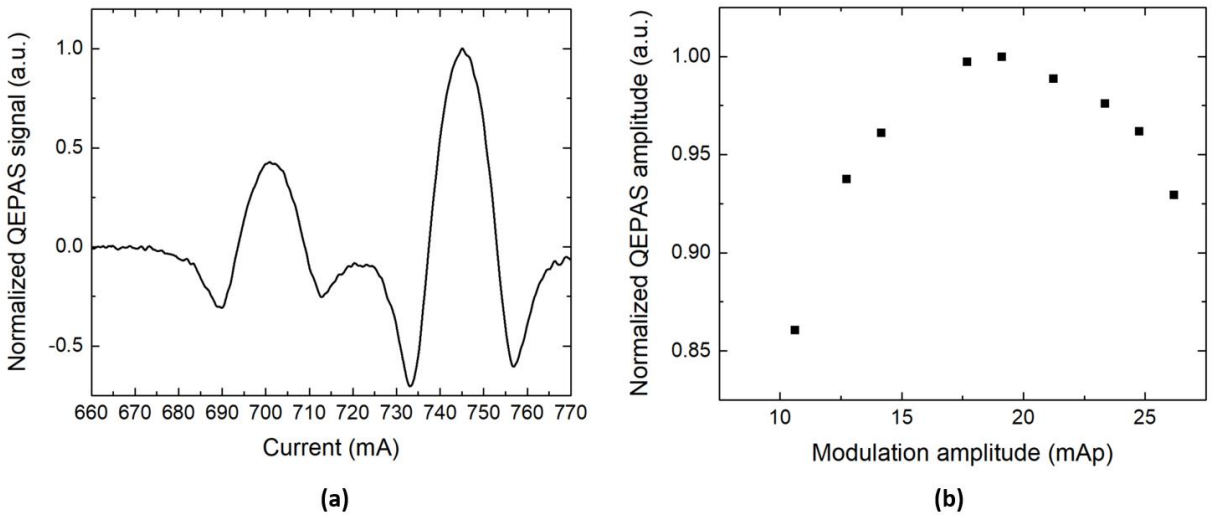

Figure 20: (a) 2f-signal obtained for 50 ppmv of dry NO showing the two reachable absorption lines. The laser's temperature was stabilized at 20°C and the modulation amplitude set at 18 mAp. (b) Amplitude of QEPAS 2f-signal according to the modulation amplitude. The optimum is found at 18 mA peak.

2.2.3- Sensor calibrations

Using the same gas mixing unit as presented for CO detection but with a 50 ppmv calibrated bottle of NO (in dry N_2), different concentrations of NO are observed in different conditions: dry and with humidified with the cold bubbler (6°C). The magnitude of QEPAS signal is retrieved for concentrations equal to 0.1, 0.5, 1 and 5 ppmv. By flushing the NO into cold bubble bath (cold bubbler, blue squares), the signal can be enhanced approximately by a factor 8 as calculated in Chapter 2 section 3.2-3 (Figure 21). The standard deviation calculated for the dry and cold bubbler measurement respectively ranges around 0.008 and 0.01 mV. The error bars are reported on the graph. The sensor is characterized by linear response with R^2=0.99998 and 0.99615 respectively for cold bubbler and dry measurements.

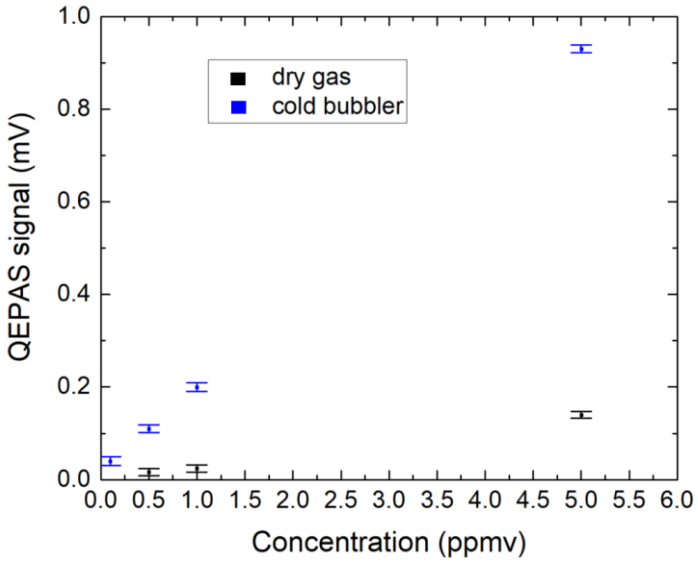

Figure 21: 2f-QEPAS signal obtained for 0.1, 0.5, 1 and 5 ppmv of NO: dry, humidified through the bubbler at 6°C. These measurements were conducted with a time constant of 200 ms.

2.2.4- Allan deviation and NNEA

To measure the Allan deviation, the gas cell is filled with 50 ppmv of NO humidified through the bubble bath at ambient temperature. The 2f-signal is recorded for about 10 minutes.

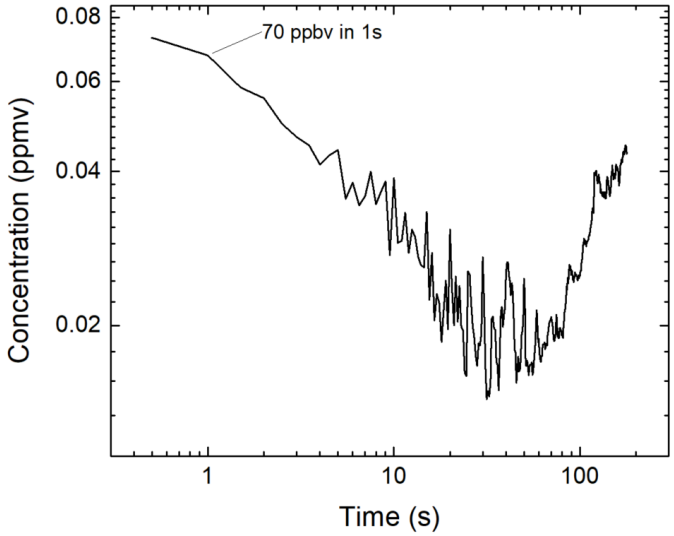

Figure 22: Allan deviation showing the limits of detection (LOD in ppmv) as function of the integration time (s). The signal is recorded for 50 ppmv of wet (bubble bath at ambient temperature) NO. The LOD is equal to 70 ppbv at 1s and the optimum averaging time obtained for 40 s.

The limit of detection at 1s in 2f is equal to 70 ppbv giving $NNEA = 1.22 \cdot 10^{-8}\, W \cdot cm^{-1} \cdot Hz^{-0.5}$. The optimum averaging time is obtained for 40 seconds.

2.3- Acetone detection at 8.2 µm

2.3.1- Wavelength working range and laser source

Acetone absorption lines are somehow particular. As a matter of fact, most absorption lines in the infrared domain present a classical Lorentzian line shape at atmospheric pressure. However, other types of line shapes can be observed for complex molecules such as acetone. Figure 23 shows the absorption of acetone obtained from Cross Section data available in HITRAN database. The graph is plotted for 7750 ppmv of water, 340 ppmv of CO_2 and 1 ppmv of acetone with a pathlength of 1 cm. In the near and mid-infrared, the acetone spectrum presents different absorptions near 3000, 1740, 1380 and 1220 cm^{-1}. The last three zones are at least 3 times more intense than the absorption around 3000 cm^{-1}. A focus on each line is proposed in Figure 24 as well as a comparison with interfering water lines for a concentration of 1 ppmv for each compound. Therefore, we will focus our concern on the study of these three different zones. A laser source tuned around 1740 cm^{-1} is available in our laboratory. Nevertheless, considering the breath analysis during which is not possible to dry completely the exhaled air, this zone is not suitable as the absorption lines of water are in the same range as the acetone absorption. The lines in the 1380 and 1220 cm^{-1} ranges remain the most interesting. The intensity of absorption in both regions are nearly the same. Regardless of that, water absorption lines are observed on each side of the acetone present at 1380 cm^{-1} and they have a significative contribution at higher concentrations. Let us consider an exhaled breath application during which the concentration of water is close to 40 %RH ~ 12000 ppmv and a high concentration of acetone of about 1 ppmv measured in a healthy and fasting subject. Figure 25 shows, for these concentrations, that the acetone at 1380 cm^{-1} is not distinguished from water anymore while it is still the case for the 1220 cm^{-1} absorption line.

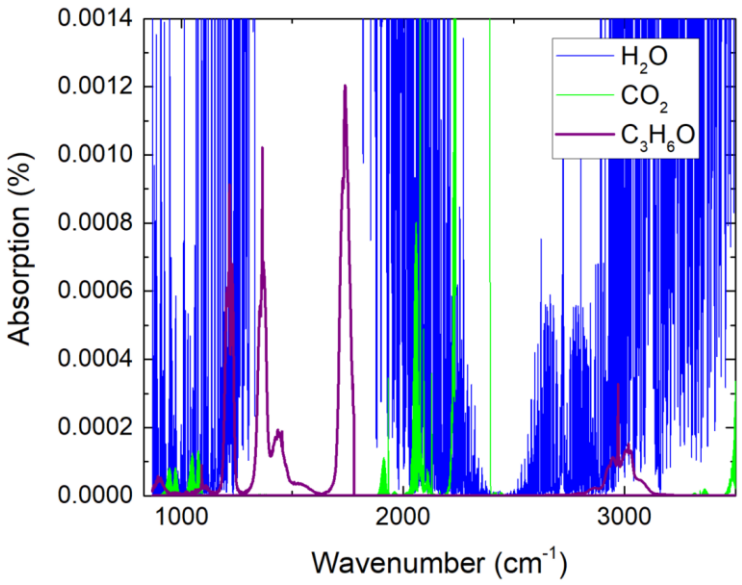

Figure 23: Acetone (C_3H_6O) absorption lines plotted from the HITRAN cross section database. The concentration of acetone is 1 ppmv. Different absorption lines are observed around 3000, 1740, 1380 and 1220 cm^{-1}. The interference with water (7750 ppmv) and CO_2 (340 ppmv) is presented.

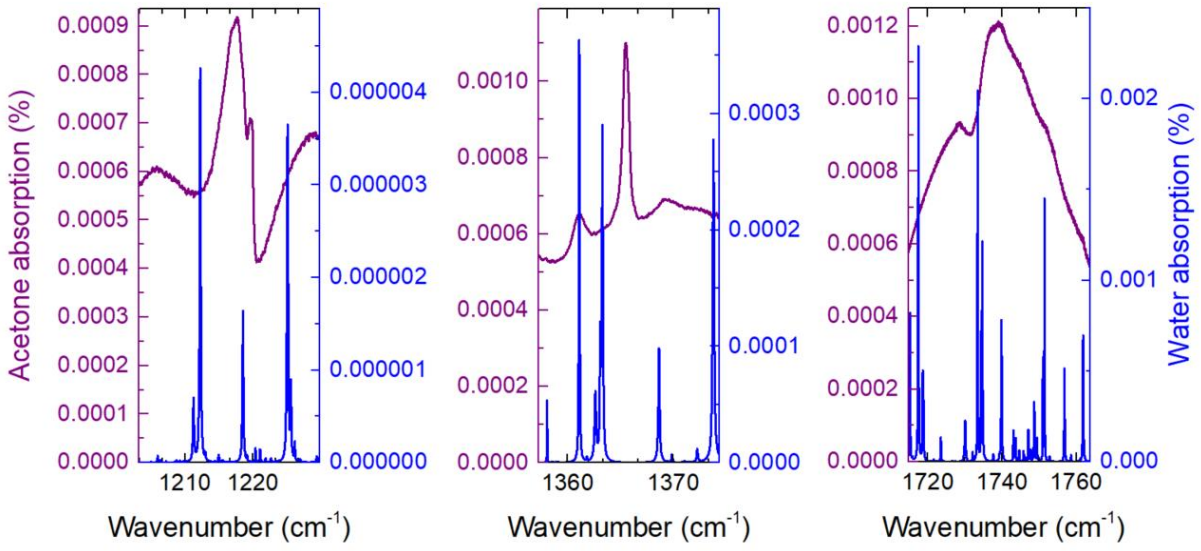

Figure 24: Focus on the acetone absorption lines around 1220, 1380 and 1740 cm^{-1}. The concentration of acetone is set to 1 ppmv and the concentration of water is 1 ppmv. The pathlength is 1 cm.

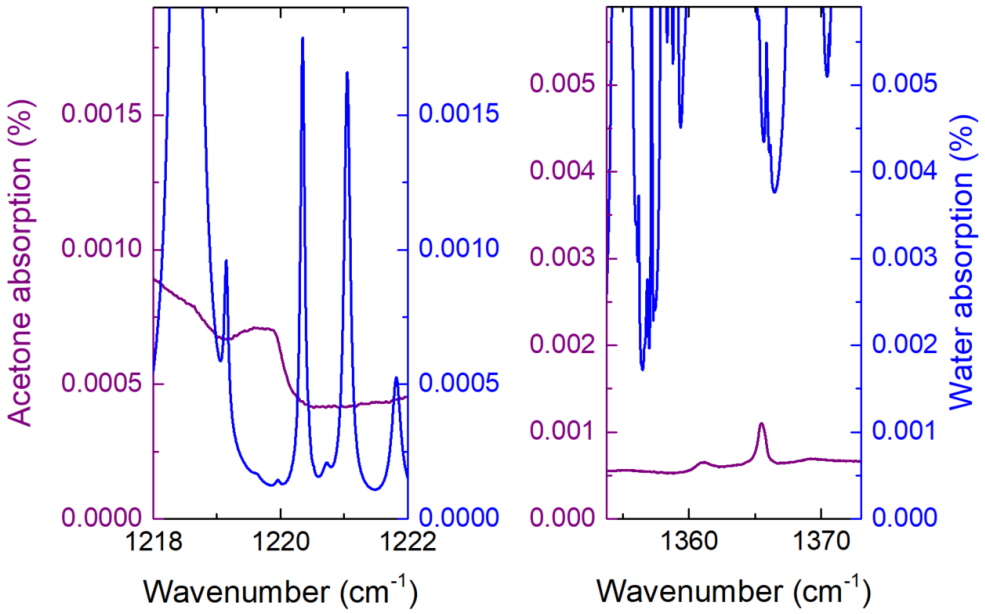

Figure 25: Comparison of acetone (1 ppmv) absorption lines at 1380 and 1220 cm^{-1}. The concentration of water is set to 12000 ppmv corresponding the concentration of water reachable with the bubbler at 6°C.

A commercial DFB-QCL (Alpes lasers) tuned across 1220 cm^{-1} is acquired for the detection of acetone. The spectra of this laser source are exhibited in Figure 26a. Figure 26b shows the power of the laser as a function of the injected current. At 10 °C, the laser source targets a little inflection in the acetone line shape, thinner than the rest of the line, around 500 mA. In this case, the optical power of the laser is close to 16 mW.

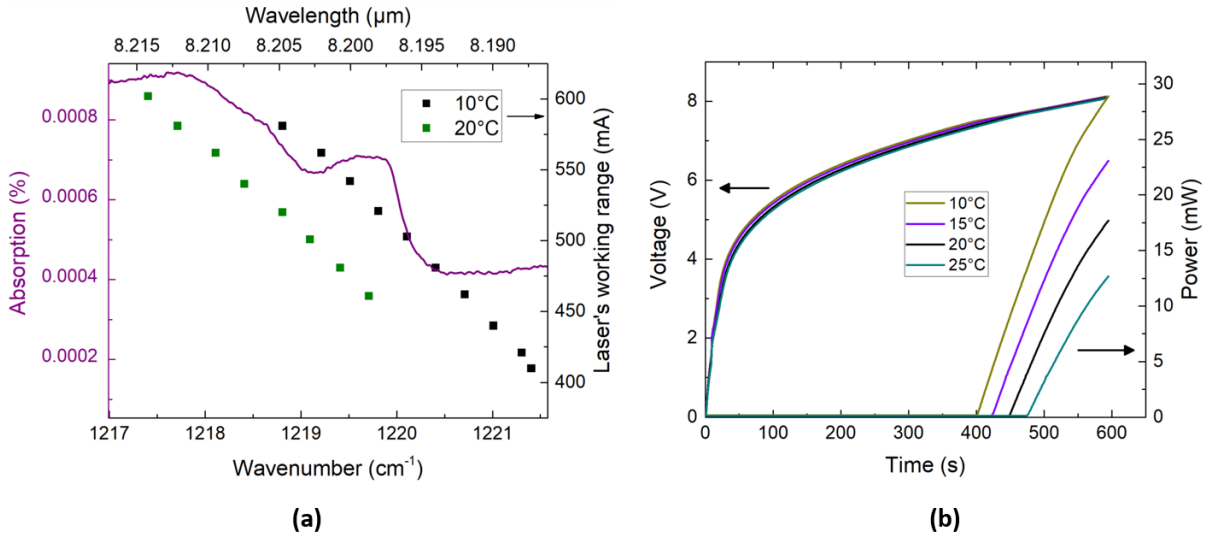

Figure 26: (a) Targeted acetone absorption line at 1220 cm^{-1} and tuning range of the laser between 10 and 20 °C. (b) Power and voltage as function of the injection current (PIV) at 10, 15, 20 and 25 °C.

2.3.2- acetone QEPAS signal: optimization

As described in the previous paragraph, the absorption lines of the acetone are not classical Lorentzian, but, they are broader therefore, the theory of WMS described in Chapter 2 section 2.3 does not exactly apply in this case. Thus, it is necessary to perform amplitude modulation in which the laser is electrically set on and off, as if it was operated in pulsed regime. Consequently, the current of the laser is fixed and a sinewave is used to modulate the amplitude, the maximum of the sine is leading to around 500 mA while the minimum of the sine is leading below the current threshold. The frequency of the sinewave is around 32.758 kHz adapted for 1f detection. Normally, a square signal is used for amplitude modulation instead of a sinewave, however, the observation of the electrical signal at the output of the current drive (Thorlabs (ITC4005QCL)) showed that the square is distorted implying a cutoff frequency. The use of a sinewave was prevailed in this case.

As the injecting current of the laser is scanned across the absorption line, the shape of the latter is drawn. The research of an optimum of modulation amplitude is performed (Figure 27a) but the shape obtained for CO or NO and presented in Figure 15b and Figure 20b can not be expected in this case. Figure 27b presents the 1f signal obtained for a modulation amplitude of 85 mAp compared to the absorption line shape.

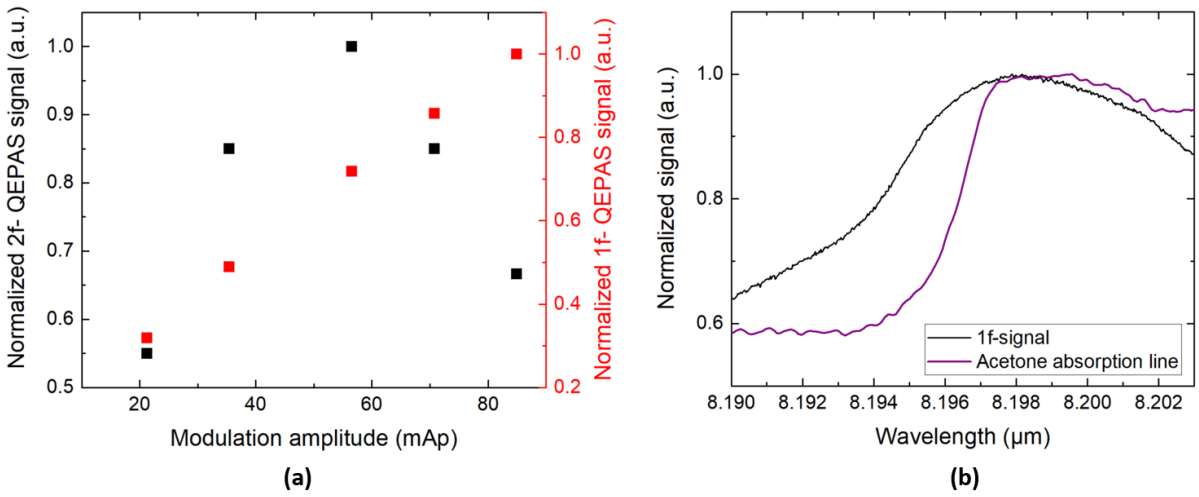

Figure 27: (a) Amplitude of QEPAS signal according to the modulation amplitude. The optimum is found at 60 mAp for the 2f-signal as the distorted signal is combined with the laser threshold, no optimum can be found for 1f-signal. (b) 1f-signal obtained for 100 ppmv of dry acetone with a modulation amplitude of 85 mAp. The experimental signal is normalized and compared to the normalized absorption line of 1 ppmv of acetone.

2.3.3- Sensor calibrations

A calibrated bottle of 100 ppmv of acetone in dry N_2 is used to generate smaller concentration of acetone in order to calibrate the sensor. The results obtained for 0.5, 1, 2 and 5 ppmv of acetone are presented in Figure 28. A high background is observed during these measurements. The response of the sensor is normalized according to this background. The standard deviation is approximately equal to 0.008 mV. The error bars are presented on the graph. The sensor shows a linear response characterized with R^2=0.9997. The background observed on the 1f signal due to the broad absorption line and the noise generated by the cell walls even more amplified at high modulation amplitude.

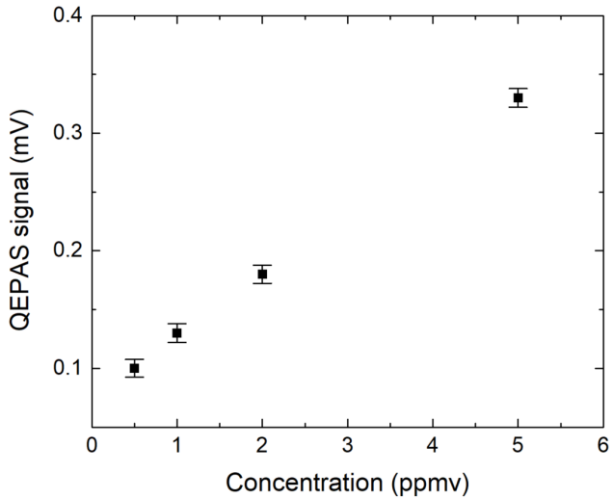

Figure 28: 1f-QEPAS signal obtained for 0.5, 1, 2 and 5 ppmv of dry acetone. The measurements were performed with a time constant of 200 ms.

2.3.4- Allan deviation and NNEA

To measure the Allan deviation, the gas cell is filled with 2 ppmv of dry acetone. The 1f-signal is recorded for about 10 minutes.

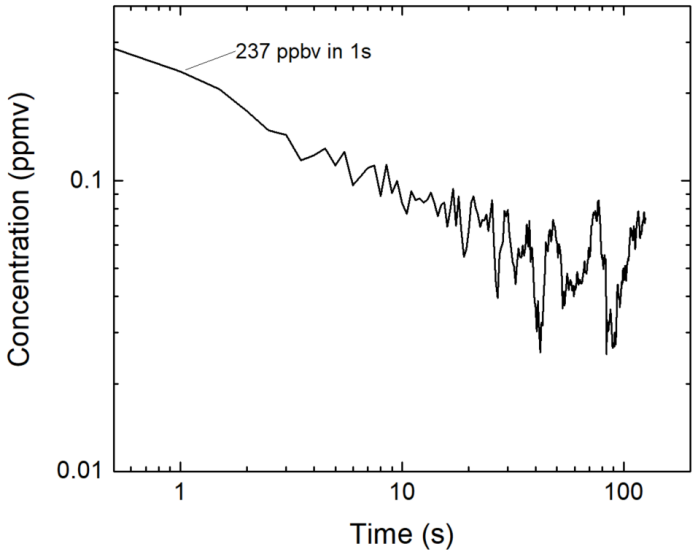

Figure 29: Allan deviation showing the limits of detection (LOD in ppmv) as function of the integration time (s). The signal is recorded for 2 ppmv of dry acetone. The LOD is equal to 237 ppbv at 1s and the optimum averaging time obtained for 100 s.

The limit of detection at 1s in 1f is equal to 237 ppbv giving $NNEA = 1.84 \cdot 10^{-8}\, W \cdot cm^{-1} \cdot Hz^{-0.5}$. The optimum averaging time is obtained for 100 seconds.

The results presented for the acetone detection module are performed on dry acetone. Indeed, no signal showing the signature of acetone was measured when the acetone was flushed into the bubble bath as if the gas condensates instead of being humidified in the bubbler. For now, we are not able to provide a calibration curve of humidified acetone representative of the breath. Although the sensor present performances in terms of limits of detection that are enough for breath investigations, it cannot operate with humidified gas samples.

In the investigation of breath acetone, Mitrayana et al. [10] have used CaCl2 scrubber to remove the water from breath sample collected in Teddlar bags. This method was tested with our experimental setup. However, after long expirations, the scrubber that traps the humidity becomes wet and sticky. In order to quickly remove the humidity, one idea is to heat the scrubber. No stable results were obtained and this idea was abandoned as it is not adapted for on-line and real-time measurements. Maiti et al [11] have proposed to use a water condenser allowing to selectively remove water from a gas mixture, keeping acetone in the gas phase. Their measurement using a Fourier Transform Infrared spectroscopy (FTIR) have permitted the measurement of about 1.1 ppmv of breath acetone from healthy volunteer.

2.4- Isoprene detection at 11 µm

2.4.1- Wavelength working range and laser source

Isoprene demonstrates two intense absorption lines close to 900 cm^{-1} (11 µm). These absorption lines are thinner than the acetone ones but remain broader than those observed for NO or CO and cannot be defined as Lorentzian. The interfering water and CO_2 line are presented in Figure 30. An InAs/AlSb DFB -QCL manufactured in our laboratory targeting an isoprene line at 906.3 cm^{-1} (11.03 µm) and operating in CW regime is used for the detection. The spectrum of this laser at 5 °C around the targeted absorption line is presented in Figure 31a. The optical power around the absorption line, at 340 mA, reaches about 2 mW (Figure 31b).

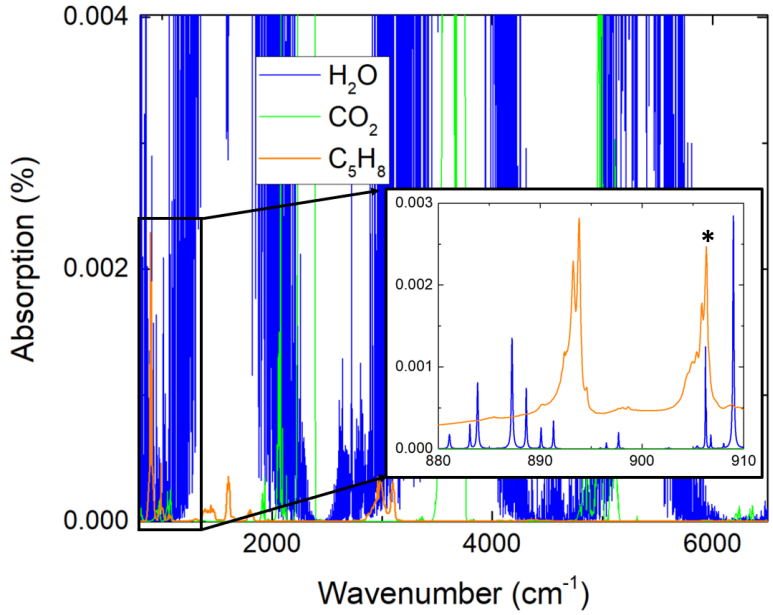

Figure 30: Isoprene (C_5H_8) absorption lines obtained from the HITRAN cross sections. The concentration of isoprene is 1 ppmv. Inset shows two strong absorption lines around 900 cm^{-1}. The interference with water (7750 ppmv) and CO_2 (340 ppmv) is presented. The asterisk represents the targeted absorption line.

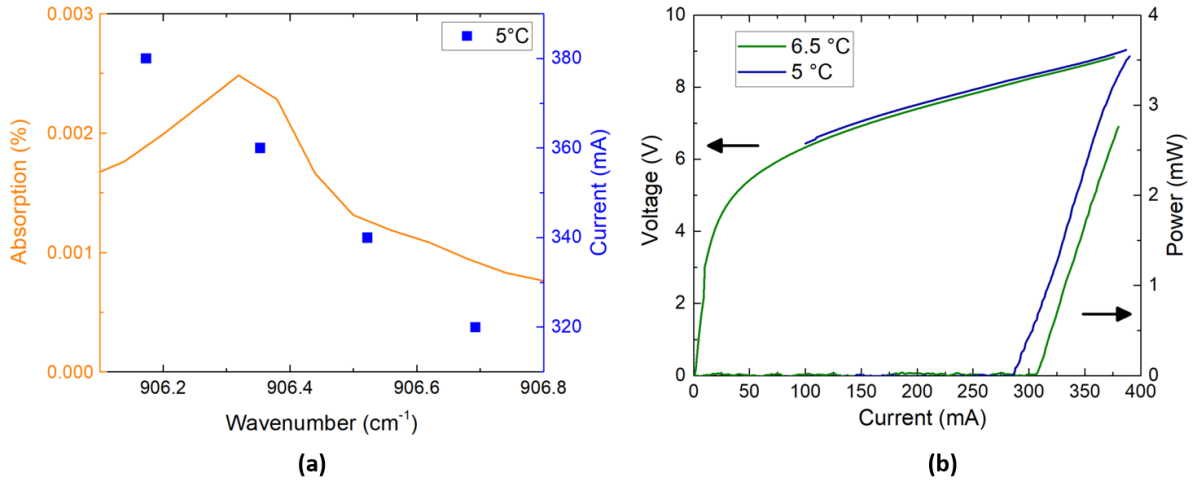

Figure 31: (a) Targeted isoprene absorption line at 906.3 cm^{-1} and tuning range of the laser at 5 °C. (b) Power and voltage as function of the injection current (PIV) at 5 and 6.5 °C.

2.4.2- Isoprene QEPAS signal: optimization

On a similar note to the experiments conducted on acetone, it is not expected that the modulation amplitude reaches an optimum. However, the maximum value of amplitude that preserves the laser from operating in its current limits is used as amplitude of modulation. (Figure 32b). This value is different for 1f and 2f measurements. The QEPAS signal is presented in Figure 32a. The 1f and 2f signal are represented in comparison to the targeted absorption line of isoprene. The shape of both 1f and 2f signal is broader than what is usually observed, however, one can easily recognize the beginning of a 1f and 2f signal. In Figure 32a dashed lines have been manually added to ease the understanding of the reader as the current limitations of the laser do not allow a complete reconstitution of the photoacoustic signal. The dotted lines show that the maximum of the 2f corresponds to the maximum of absorption and the maximum of 1f corresponds to the position where the slope of the absorption line is higher. These characteristics are also retrieved in classical WMS.

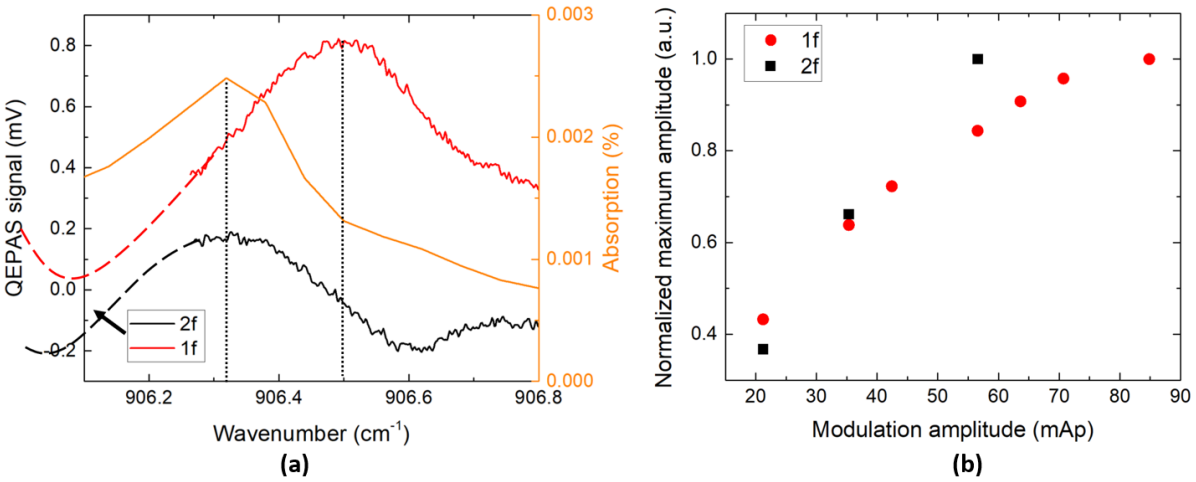

Figure 32: (a) 1f and 2f photoacoustic signal compared to the targeted isoprene absorption line. The signal was obtained for 10 ppmv of isoprene and a modulation amplitude of 50 mAp. The dashed lines are added manually to show the reconstitution of the 1f and 2f signal as the current limitations of the laser does not allow the complete reconstitution of the PA signal. The dotted lines show the correspondence between the maximum of the PA signal and the absorption line. (b) Amplitude of QEPAS signal according to the modulation amplitude.

2.4.3- Sensor calibrations

Different concentrations of isoprene are generated from a calibrated bottle of 50 ppmv of isoprene. The results obtained for the 1st and 2nd harmonic of the signal are presented for 0.25, 0.5, 1, 5 and 10 ppmv of isoprene (Figure 33). No calibration was performed on humidified isoprene as no significant effect of water was found on the isoprene PA signal (Chapter 2 section 3.2-3).

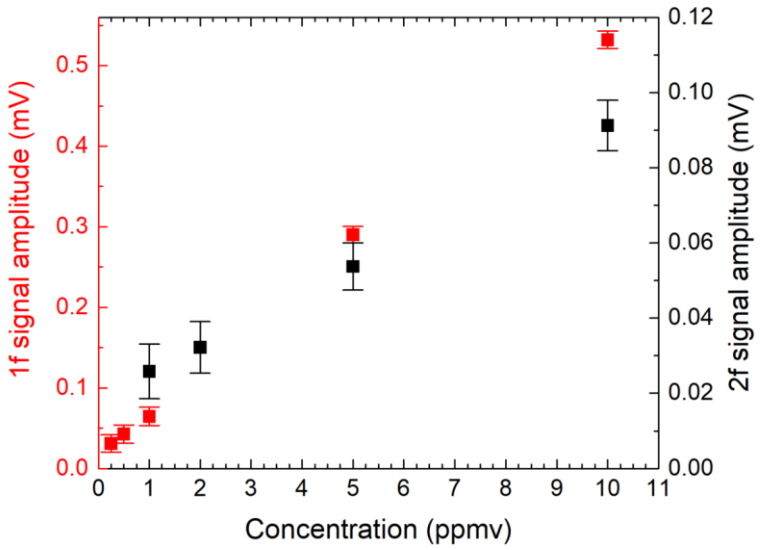

Figure 33: 1f-2f-QEPAS signal obtained for 0.25, 0.5 1, 5 and 10 ppmv of dry isoprene. The measurements were performed with a time constant of 500 ms.

The sensor presents linear response respectively in 1f and 2f with R^2=0.998 and 0.9994. The standard deviation calculated for the 1f and 2f-signal ranges around 0.01 mV

2.4.4- Allan deviation and NNEA

To measure the Allan deviation, the gas cell is filled with 2 ppmv of dry isoprene. The 2f-signal is recorded for about 10 minutes.

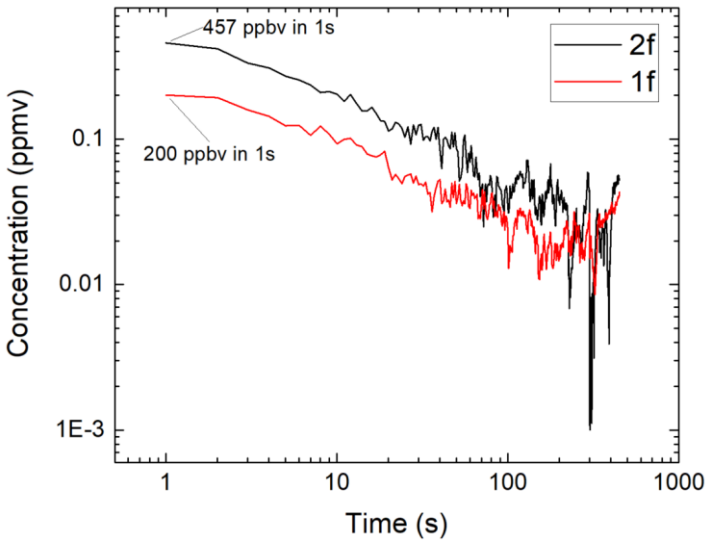

Figure 34: Allan deviation showing the limits of detection (LOD in ppmv) as function of the integration time (s). The signal is recorded for 2 ppmv of dry isoprene. The LOD for 1f and 2f signal is respectively 200 ppb and 457 ppbv in 1s. The optimum averaging time obtained for 200 s.

The limit of detection at 1s in 1f is equal to 200 ppbv giving $NNEA = 9.92 \cdot 10^{-9}\, W \cdot cm^{-1} \cdot Hz^{-0.5}$. The optimum averaging time is obtained for 200 seconds.

The concentration of isoprene in healthy subjects at rest are around 100 ppbv. Unfortunately, the detection module developed for the investigation of isoprene cannot be used for breath investigation for healthy subjects at rest. However, the concentration of isoprene can reach 800 ppbv at the beginning of a physical exercise [12] which would be detectable by our QEPAS detection module.

2.5- Conclusion

Four different sensors have been developed for the detection of four different gases involved in cardiovascular diseases. During the period of time covering the SENSIR project, for administrative reasons, it was not possible to have access to a cohort of patients at the hospital to perform breath measurement using our QEPAS detection module in parallel to their medical routine. Therefore, the exhaled breath measurements that are presented in this thesis were conducted in our laboratory on volunteers (colleagues).

The exhaled concentration of these gases in the breath of patients are different (higher) from what can be measured in the breath of healthy subjects. It is necessary to compare the minimum detectable concentrations reached by our sensor to the required working ranges for detection in healthy subjects. Table 6 presents the limits of detection of the different detection modules in comparison to the required working range for breath investigation of healthy volunteers.

Table 6: QEPAS detection module limits of detection and required working for healthy adult breath investigation.

Gas	Sensor detection limits (ppbv in 1s)	Required working ranges (ppbv)	Patients concentrations (ppbv)	
CO	17	> 1000	> 4000	[13]
NO	70	< 25	> 25	
C_3H_6O	237	< 400	> 496	[14]
C_5H_8	200	> 80	285 ± 30	[15]

To sum up:

- The CO sensor is able to perform measurement on healthy subjects.
- The NO sensor presents interesting limits of detections however the concentrations of NO in the breath of healthy volunteers cannot be detected in the present configuration. Different options involving a more powerful laser source are considered to reach lower limits of detection.
- The acetone sensor presents limits of detection that are enough for breath measurements but the sampling system and humidity management needs to be adapted to this species.
- The isoprene sensor could be used to investigate breath isoprene in healthy persons during physical exercise.

The performances achieved by our QEPAS sensor make the measurement of exhaled carbon monoxide possible. In the next section, measurements of carbon monoxide performed in the breath of volunteers using the sampling system described in the section 1.2 of this chapter are presented.

3- Exhaled carbon monoxide

The measurements presented in this section are performed on two different groups of volunteers, smokers and non-smokers. Therefore, it is possible to use the QEPAS sensor to discriminate each group of persons.

The presented measurements are performed with the CO sensor presented in section 2.1 using one of the "big cell" which explains the response time of the sensor.

Before any measurement, objectives of the measurements and the working principle of the sensor are explained to the volunteers. They complete a form available in Appendix E. The measurement is totally non-invasive.

During the measurements, the volunteer is sitting on a chair in a natural position. Anti-bacterial mouthpieces are used for each person. This mouthpiece is connected to the bubble bath, controlled in temperature (8°C), by the mean of a Silicone tube of 4 mm of diameter. A flow meter is connected at the output of the bubble bath and its output is directed to the gas cell where the gas is analysed (Figure 35).

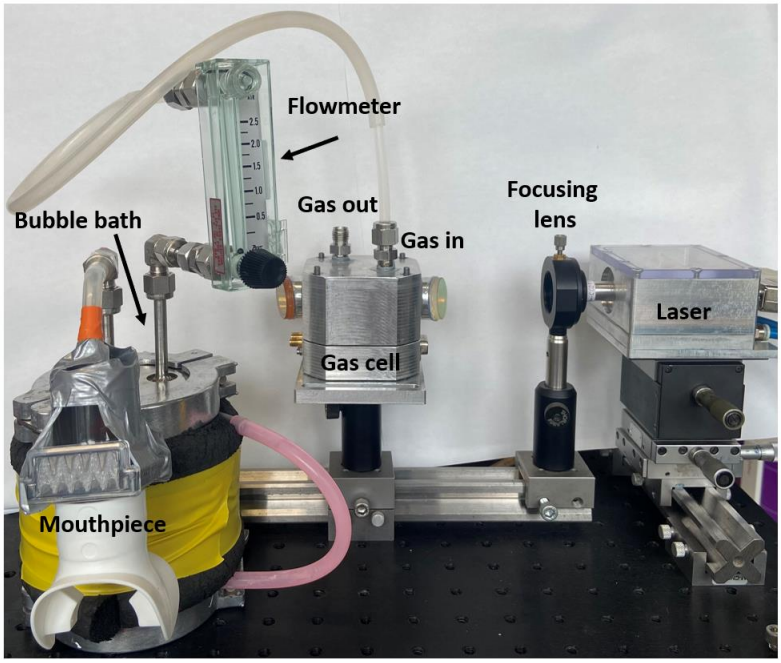

Figure 35: Typical experimental setup used for breath investigation composed of an anti-bacterial mouthpiece, a temperature-controlled bubble bath, a flowmeter and the gas detection module compose of the laser focused inside the gas cell by the mean of a focusing lens.

To perform these measurements, the subject is asked to take a deep inspiration, put on a nose clip in order to prevent air from escaping through the nose, and expire as much as possible (total lung volume) at a flow of $\pm$ 1.5 L/min observed on the flowmeter. At the end of the expiration, N_2 is flushed through the bubble bath into the gas cell in order to remove the expired air.

The optimum parameters of the laser presented in section 2.1 are fixed and the signal is recorded over a period of time covering the whole expiration to which is added a period of time to observe the behaviour of the signal. Before the measurements, the gas cell is flushed

with N_2 passing through the cold bubble bath (here 8°C) to maintain a stabilized humidity during the measures.

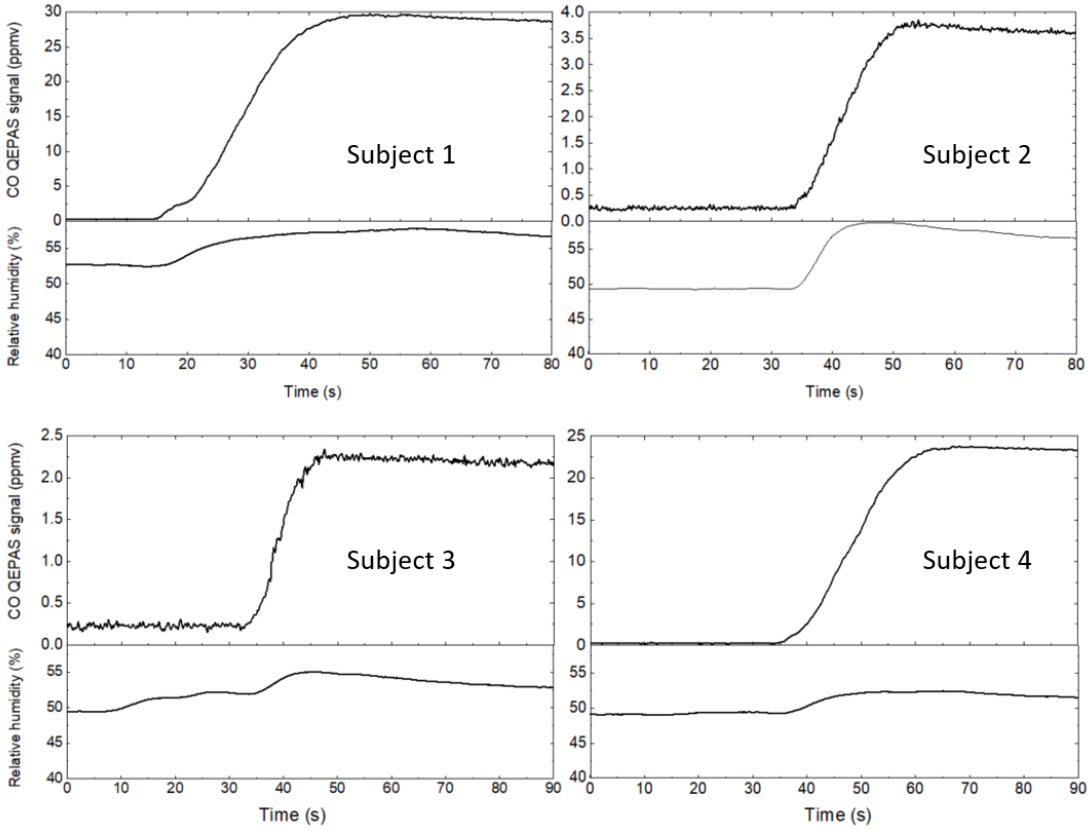

Figure 36: Breath CO concentration (ppmv) measured with QEPAS setup described in section 2.1. The measurement is performed on four volunteers: 1 and 2 are male and smokers, 3- is a male non-smoker and 4- is a female smoker.

Measurements conducted on 4 volunteers are presented in Figure 36. The volunteers presented different demographic situations:

- Subject 1 is a male, smoker
- Subject 2 is a male, occasional smoker
- Subject 3 is a male, non-smoker
- Subject 4 is a female, smoker

The concentrations of carbon monoxide are higher in the breath of smokers (30, 3.75 and 24 ppmv, respectively, for the subject 1, 2 and 4) than in the breath of non-smokers (2.25 ppmv). In the literature, a limit of 10 ppmv [16] has been defined to separate smokers from non-smokers. However, another limit of 6 ppmv [17] has been established as the concentration of CO for abstinent smokers are lower.

During the measurement, one can observe that the humidity increases at the beginning of the exhalation due to errors in maintaining the temperature of the bubble bath at the correct value. Calibration of the sensor at 55 %RH (reach at the end of the expiration) was used in order to convert the voltage (PA signal) into CO concentration (ppmv).

4- Combination of QEPAS and Medisoft sensor

Medisoft has been a partner on the SENSIR project. One of the main objectives of this project is to develop a sensor that is able to communicate with sensors that are already used at the hospital. Moreover, being able to connect our sensor with the apparatus that are already used in medical routine is somehow interesting as an additional measurement would be performed during a single consultation and tests. The words "connect" and "communicate" employed when talking about the two sensors involve electrical communication but also breath sampling.

The QEPAS sensor gives information on the exhaled concentration of a gas related to a certain disease. Combining these values to the real-time measurement of CO_2 proposed by Medisoft as well as the flow would lead to the re-composition of the entire expirogram of the target gas as the CO_2 level is used to discriminate the respiratory compartments.

The next sections will focus, on a technical level, on the Ergocard sensor, acquired in august 2022 and the modifications that occurred on the previously presented setup in order to establish the communication between the two different sensors.

4.1- Ergocard sensor

In its original configuration, the Ergocard sensor is constituted with a NDIR CO_2 sensor [18], an electrochemical O_2 sensor and a flow measurement performed with a Pitot tube. The apparatus has been modified to match our specifications and to be flexible to our needs. Thus, the O_2 sensor has been removed. Indeed, only four analog inputs are available on the apparatus and O_2 occupies one of them. By removing the O_2 sensor, enough inputs are available for the CO, NO, isoprene and acetone sensors. The breath sampling system is adapted to tests performed during physical efforts. Basically, the subject breathes normally (inhale/exhaled) into a single use anti-bacterial mouthpiece. The measurement of the flow is performed with a Pitot tube connected to this mouthpiece. A pump, located at the last part of the sampling system is extracting the air from the output of the mouthpiece. First of all, the air passes through a Nafion tube, that lowers and stabilizes the humidity in the extracted breath. Then, the breath is directed to the CO_2 sensor and exhausted into the

room. On the Medisoft software, called Expair II, the flow as well as the concentration of CO_2 are displayed simultaneously (Figure 37).

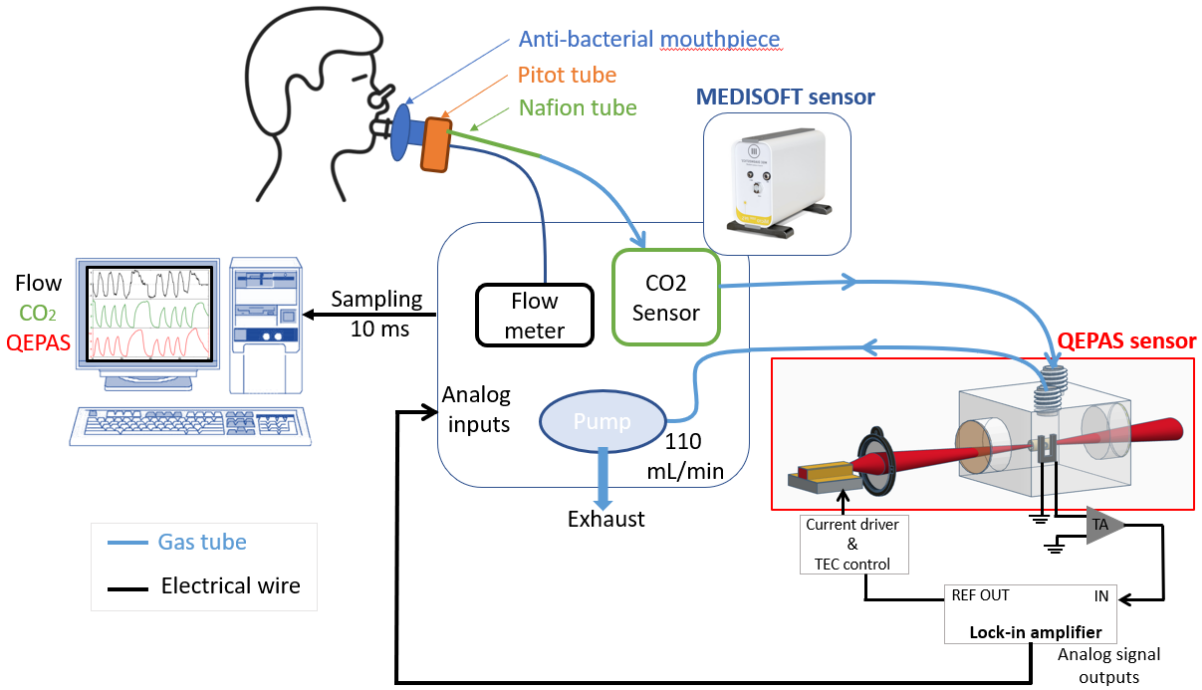

Figure 37: Schematic representation of the breath sampling system and Medisoft sensor to which the QEPAS sensor is connected. The CO_2, Flow and QEPAS measurement are sampled at the same rate (10 ms).

4.1.1- Pressure measurement using Pitot tube

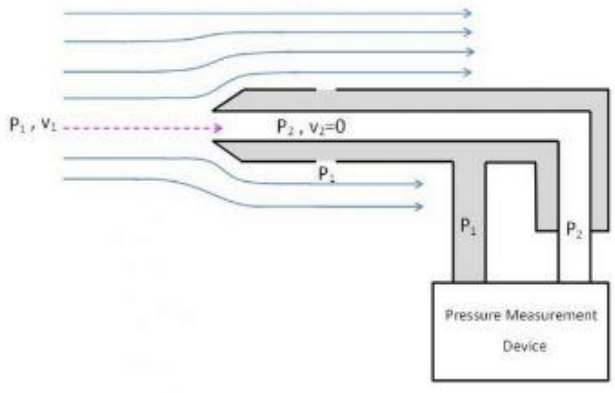

Figure 38: Schematic description of a Pitot tube.

The working principles of Pitot tubes is simple. Basically, it consists of two tubes (Figure 38): one is measuring the dynamic pressure P_2 (in our case induced by the inhaled or exhaled air) and the other one is measuring the atmospheric pressure P_1. The total pressure P_{tot} measurement by the pressure transducer is given by the addition of the two pressures and can be calculated with Bernoulli's equations:

$$P_{tot} = P_1 + P_2, \tag{4.8}$$

$$P_{tot} = P_1 + \frac{\rho \mathrm{v}^2}{2}. \tag{4.9}$$

In this equation, ρ is the density of the air and v its velocity. The velocity can be deduced to estimate the flow as:

$$\mathrm{v} = \sqrt{\frac{2(P_{tot} - P_1)}{\rho}}, \tag{4.10}$$

$$Flow = \mathrm{v}\rho^2 \tag{4.11}$$

The pitot tube furnished by Medisoft is connected to the Prevent Flow Sensor (PFS). This flow meter is bidirectional, it allows the measurement of the inhalation and expiration in the range of $\pm$ 18 L/s with an accuracy of $\pm$ 3%.

The calibration of the Pitot tube is performed through a 3 Litre syringe connected at the mouthpiece location. Two sets of measurement are performed: "low flow" and "high flow" describing a slow and rapid breathing manoeuvre. A colour indication displayed on the software informs the user if the test has been well performed.

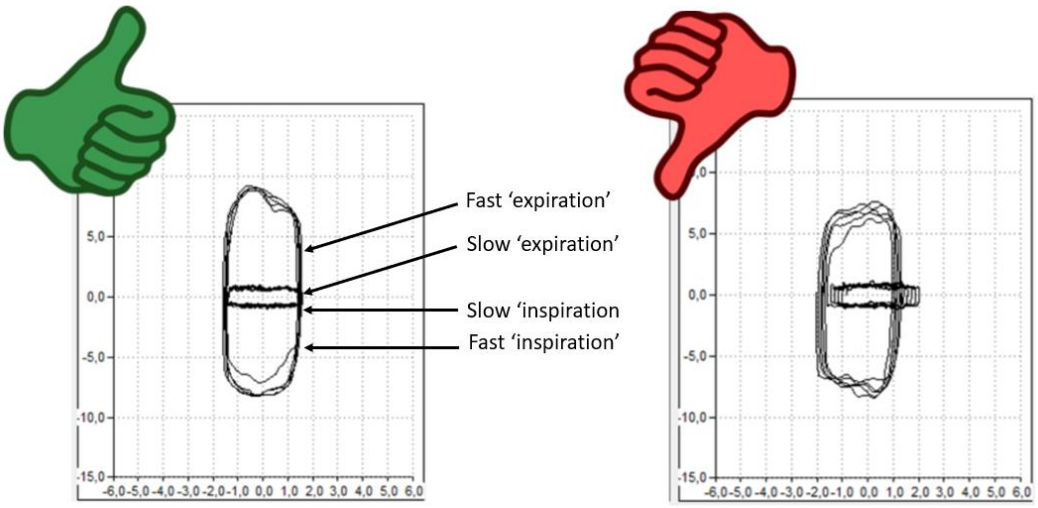

Figure 39: Volume-flow calibration (respectively represented on x and y axis) of the Medisoft sensor PreVent Pitot tube. The terms 'expiration' and 'inspiration' represents in this calibration the air inspired in and chased out of the syringe.

4.1.2- The Nafion technology

The Permapure company have developed different tubes made of Nafion membranes that are capable of decreasing the humidity in a mixture. Nafion is a polymer of Teflon with a fluocarbon and sulfonic acid side chains. The performances of the tube are related to the gas flow and the input humidity. When a humidified air flows through the Permapure tube, the water is absorbed by the sulfonic group. Then, the water diffuses to the environment creating an equilibrium between the mixture and the ambient level of humidity.

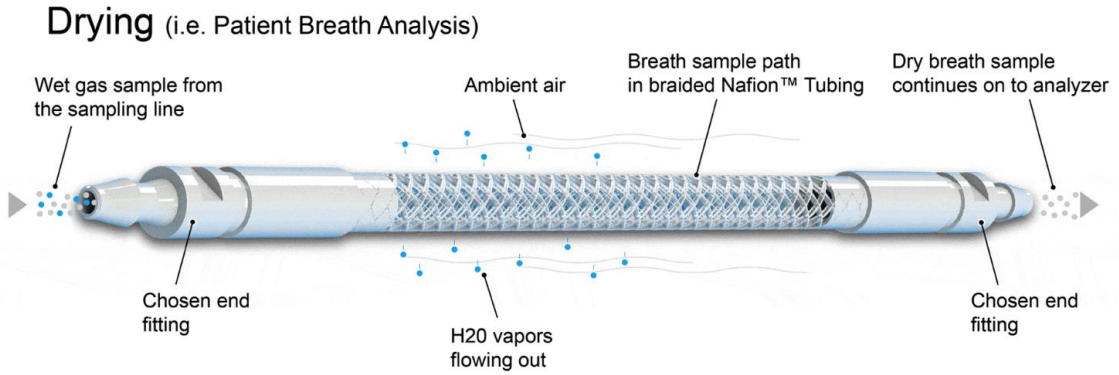

Figure 40: Schematic of the working principle of Nafion tubes (BE™ series Moisture Echangers).

Nafion is impermeable to oxides such as CO and NO and simple forms of hydrocarbons such as isoprene which makes it a good candidate to integrate in the sampling system dedicated to the detection of these gases. Nevertheless, it is permeable to ketones including acetone. Therefore, the humidity needs to be managed in a different manner when performing acetone measurement in a wet sample.

4.1.3-Capnography: CO_2 sensor

The CO_2 sensor implemented in the Ergocard is a NDIR sensor developed by TreyMed [18]. This sensor is capable of measuring concentration of CO_2 ranging between 0 and 13% and offers a response time of about 30 ms. Before any measurement, the sensor is calibrated with a calibrated mixture of gas containing O_2 (16 %)/CO_2 (4 %) in N_2. A colour indication displayed on the software informs the user if the measured value of CO_2 by the sensor is comparable to the defined value of the apparatus.

4.2- Connecting both sensors

The communication between both sensors has been established as presented in Figure 37. Concerning the gas tubing: the systems (CO_2 sensor and QEPAS sensor) are connected in serie. The subject is breathing into the mouthpiece, the flow is calculated and displayed for inhaling and exhaling processes. The pump located at the end of the circuit samples the breath gas at a rate of 0.11 L/min. First the gas circulates through the Nafion tube before being analysed by the CO_2, then the QEPAS sensor and exhausted in the room.

The amplitude of the demodulated signal can be sent to one of the four analog inputs available on the Ergocard. Indeed, the LIA has different analog outputs that can be defined as the magnitude of the demodulated signal. Therefore, the QEPAS signal, the CO_2 and the flow are displayed and sampled at the same rate, 10 ms.

4.2.1- The effect of the pump on the QTF's frequency

At the beginning of each measurement involving both sensors, a sudden loss of the signal was observed. This problematic was each time corrected by manually adjusting the resonance frequency which was suddenly changed. Therefore, it appeared necessary to understand what kind of degradation is caused whenever the pump was activated.

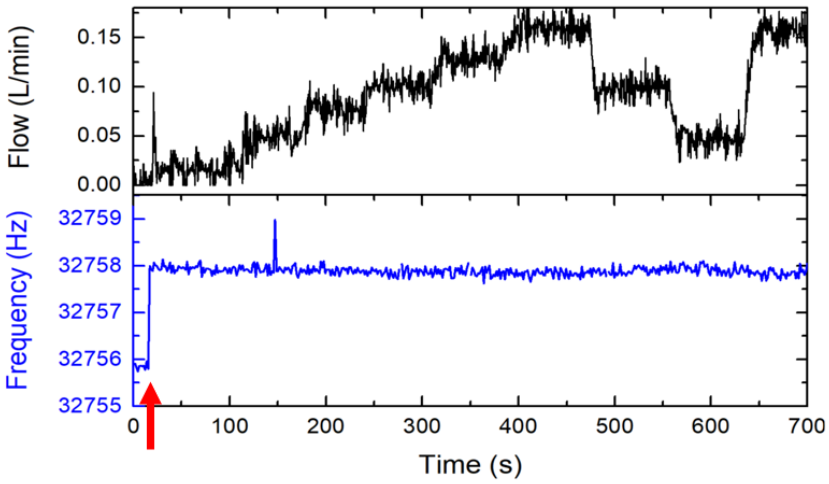

Figure 41: Variation of the resonance frequency of the QTF when the pump of the Medisoft apparatus is turned on (red arrow). The frequency is measured with the resonance tracking technique presented in Chapter 2. The flow is measured with (Bronkhorst MASS-VIEW 302).

The resonance tracking technique presented in Chapter 2 section 3.3 was used to retrieve the resonance frequency of the QTF for different flow rates ranging between 0 to 0.15 L/min. For each tested QTF an important shift of approximately 2 Hz was observed at the exact moment when the pump was turned on (red arrow on Figure 41). During the rest of the measurement the frequency did not seem to be affected by the variation of the flow. Consequently, the frequency of the QTF is checked manually at the beginning of each tests.

4.2.2- Breath measurements

Breath investigation was performed with the CO sensor combined with the Medisoft sensor. The presented measurement is performed on a smoker and a non-smoker. In the breath samples presented section 3, only the forced expiratory procedure could be performed as the subject cannot inspire through the bubble bath. With the Medisoft's breath sampling system, the subject can breathe normally (inspiration and expiration) but the nose clip remains necessary. During the expiration a sample of the expired air is extracted by the pump and circulates towards the gas sensors. During the inspiration, it is the ambient air that is analyzed by the gas sensors.

For this test, different procedures are performed:

- The subject is asked to breath (inspire and expire) normally.
- The subject is asked to take a deep inspiration and expire its total lung volume.

This last procedure gives information on the alveolar concentration of CO.

As expected, the concentration of CO is higher for the smoker (~15 ppmv) than for the non-smoker (< 2 ppmv). The measurement of the flow indicates the moment at which the subject started to exhale, but can also be a good indicator of abnormal ventilatory rates. The hypoventilation (breathing too slow) or hyperventilation (breathing too fast) can also be indicated with the value of CO_2, that would respectively increase or decrease. The value of CO_2 reports on the airway management (Chapter 1). By combining the CO_2 value to the CO value, it is possible to define the complete expirogram of the measured molecule (Figure 42).

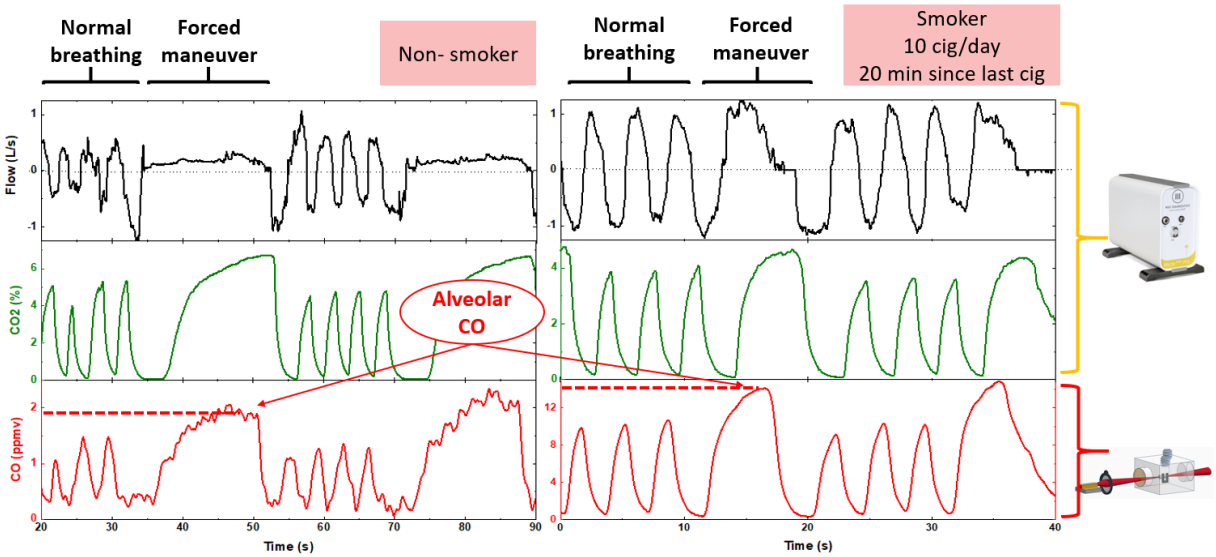

Figure 42: CO, CO_2 and flow measurement performed by combining the QEPAS and Medisoft apparatus. The measurement is performed on smoker and non-smoker during a normal breath and forced maneuver.

During these measurements, the schematic presented in Figure 37 was modified, the gas circulates first through the QEPAS sensor before going to the CO_2 (Medisoft sensor). This modification implies an additional tube length that implies a time delay between the CO and CO_2 measurements.

The time response of the CO sensor, meaning the time to reach ± 5 % of its maximum value is about 2 seconds allowing almost real time measurements. We believe the response time of the sensor can be reduced by reducing the length of tube that separates both sensors.

Conclusion

In this chapter, we have demonstrated the establishment of an exhaled air sampling system capable of addressing issues related to humidity stabilization and reduction. This system allowed us to conduct measurements of CO in the exhaled air of both smoker and non-smoker volunteers using the QEPAS sensor that was implemented. The Medisoft device, routinely used in medical practice, was electrically connected and, through its air sampling system, interfaced with various QEPAS sensors (CO, NO, acetone, and isoprene). The measurement of CO in exhaled air, combined with CO_2 and flow measurements (performed by the Medisoft), enables us to demonstrate almost real-time monitoring and propose a reconstruction of the complete CO expirogram. The measurements performed on CO are encouraging, however, NO, isoprene and acetone detection module has to be implemented with the CO's in order to clinically validate the measurements.

References

[1] D. Ayache *et al.*, "Benzene sensing by Quartz Enhanced Photoacoustic Spectroscopy at 14.85 μm," *Opt. Express*, vol. 30, no. 4, p. 5531, 2022, doi: 10.1364/oe.447197.

[2] N. Maurin *et al.*, "First clinical evaluation of a quartz enhanced photo-acoustic CO sensor for human breath analysis," *Sensors Actuators, B Chem.*, vol. 319, no. April, p. 128247, 2020, doi: 10.1016/j.snb.2020.128247.

[3] H. Wu *et al.*, "Beat frequency quartz-enhanced photoacoustic spectroscopy for fast and calibration-free continuous trace-gas monitoring," *Nat. Commun.*, vol. 8, no. May, pp. 1–8, 2017, doi: 10.1038/ncomms15331.

[4] R. Rousseau, "QEPAS gas sensor for air quality monitoring," 2019.

[5] M. Duquesnoy, "Tuning forks in photoacoustic spectroscopy : Comparative study and new developments," 2021.

[6] R. Rousseau, N. Maurin, W. Trzpil, M. Bahriz, and A. Vicet, "Quartz tuning fork resonance tracking and application in quartz enhanced photoacoustics spectroscopy," *Sensors (Switzerland)*, vol. 19, no. 24, 2019, doi: 10.3390/s19245565.

[7] A. Carullo, A. Vallan, A. S. Afify, and J. M. Tulliani, "Development of a fast humidity sensor based on quartz tuning fork," in *Conference Record - IEEE Instrumentation and Measurement Technology Conference*, 2016, vol. 2016-July, doi: 10.1109/I2MTC.2016.7520375.

[8] Y. Ko, C. Lee, Y. Kim, Y. Kim, Y. J. Yun, and Y. Jun, "Dew point temperature as an invariant replacement for relative humidity for advanced perovskite solar cell fabrication systems," *J. Mater. Chem. A*, vol. 6, no. 42, pp. 20695–20701, 2018, doi: 10.1039/C8TA06689B.

[9] R. Ghorbani and F. M. Schmidt, "ICL-based TDLAS sensor for real-time breath gas analysis of carbon monoxide isotopes," *Opt. Express*, vol. 25, no. 11, p. 12743, 2017, doi: 10.1364/oe.25.012743.

[10] Mitrayana, D. K. Apriyanto, and M. Satriawan, "CO2 Laser photoacoustic spectrometer for measuring acetone in the breath of lung cancer patients," *Biosensors*, vol. 10, no. 6, May 2020, doi: 10.3390/BIOS10060055.

[11] K. S. Maiti, M. Lewton, E. Fill, and A. Apolonski, "Sensitive spectroscopic breath analysis by water condensation," *J. Breath Res.*, vol. 12, no. 4, 2018, doi: 10.1088/1752-7163/aad207.

[12] J. van den Broek *et al.*, "Selective monitoring of breath isoprene by a portable detector during exercise and at rest," *Sensors Actuators B Chem.*, vol. 357, Apr. 2022, doi: 10.1016/j.snb.2022.131444.

[13] S. Cheng *et al.*, "Association of exhaled carbon monoxide with subclinical cardiovascular disease and their conjoint impact on the incidence of cardiovascular

outcomes," *Eur. Heart J.*, vol. 35, no. 42, pp. 2980–2987, 2014, doi: 10.1093/eurheartj/ehu052.

[14] F. G. Marcondes-Braga *et al.*, "Exhaled acetone as a new biomarker of heart failure severity," *Chest*, vol. 142, no. 2, pp. 457–466, 2012, doi: 10.1378/chest.11-2892.

[15] S. Mendis, P. A. Sobotka, and D. E. Euler, "Expired hydrocarbons in patients with acute myocardial infarction," *Free Radic. Res.*, vol. 23, no. 2, pp. 117–122, 1995, doi: 10.3109/10715769509064026.

[16] A. O. Goldstein, S. P. Gans, C. Ripley-Moffitt, C. Kotsen, and M. Bars, "Use of Expired Air Carbon Monoxide Testing in Clinical Tobacco Treatment Settings," *Chest*, vol. 153, no. 2, pp. 554–562, 2018, doi: https://doi.org/10.1016/j.chest.2017.11.002.

[17] M. Underner and G. Peiffer, "Interprétation des valeurs du CO expiré en tabacologie," *Rev. Mal. Respir.*, vol. 27, no. 4, pp. 293–300, 2010, doi: https://doi.org/10.1016/j.rmr.2009.09.004.

[18] "TreyMed CO2 - COMET II and COMET I - sensors : https://www.treymed.com/capno/sensor/sensor.htm."

Conclusion

Different specifications were defined at the beggining of this project for the develoment of the gas sensors applied to the breath analysis: high sensitivity, high selectivity and real time analysis. First, the sensor must be sensitive enough in order to detect the smallest concentrations of gas found in the exhaled breath. Second, the sensor needs to be selective enough in order to accurately discriminate between all species present in a complex gas matrix. Finally, the real time analysis is a key point as the objective was not only to measure a certain concentration of gas during the expiration but monitor the variation of the target gas concentration in each airways compartment.

Chapter 1 is presented as an introduction to the medical application with the definition of different physiological concepts. Indeed, this chapter introduced the respiratory system as well as the mechanics of respiration and perfusion. Altogether, these concepts help understanding the composition and the variability factors of the expired air. Then, the second part of the chapter presents the endogenous production of CO, NO, acetone and isoprene as well as their link with the cardiovascular diseases (or condition). In order to be able to define a pathological concentration threshold, a systematic review and meta-analysis was performed for breath acetone concentrations. The rigorous metodology of this research work was presented as well as the conclusion that shed light on the importance of the standardisation of the measurements conditions to overcome the inter and intra-induvidual bias on the detected concentration.

Chapter 2 presents the different categories of gas sensors that dominate the market. Amongst them, electrochemical and NDIR sensors are respectively implemented in medical devices for the measurement of exhaled NO (asthma diagnosis) and CO (pulmonary diffusion after inhalation of CO) at the hospital. The electrochemical sensors are not suitable for real time measurement and the availability of NDIR sensor is limited by their optical filters bandwidth. Finally, QEPAS matches the specifications needed for the breath sensor, with an excellent selectivity and sensitivity and an almost real-time measurements. The different blocks composing the QEPAS sensors are studied, inclucling WMS, QTF characterization techniques and water effect through molecular relaxation principles. These measurements have shown the necessity to control the humidity variations as the sensor performances can be enhanced with a factor 10 in presence of water.

Chapter 3 presents a numerical model built with COMSOL Multiphysics for the study of the off-beam spectrophone. This model was validated in a first place by the mean of an analytical model based on the definition of the acoustic impendances inside the cavity. Both

model present comparable results which means that the numerical model can be employed to study and optimise the generation of the acoustic wave inside the acoustic cavity instead of performing an experimental empirical work. The comparison of the frequency of the acoustic wave calculated with the numerical model and measured experimental have shown some discrepancy. Indeed, the different tests performed with the numerical model have shown that for a difference of 0.1 mm on the geometric dimensions, a frequency shift higher than 1 kHz can be observed. The errors between the numeric simulations and the experiments can be attributed to the errors observed on the dimensions of the 3D-printed cavities. Future work will focus on the design of micromachined acoustic cavities. Even if the production time is longer, the dimensions and the smoothness of the internal surfaces can be better controlled.

Chapter 4 presents the experimental work conducted during this project.

The first part of this chapter shows that if the humidity is under certain conditions necessary for the enhancement of the PA signal, it can also be a cause of instability as its variations affect the resonance frequency of the QTF therefore it has to be stabilized.

The second part of this chapter presents the implementation of a homemade breath sampling system including a bubble bath capable of managing the humidity issues as long as it is well stabilised in temperature.

Four different QEPAS setups were implemented for NO, CO, acetone and isoprene and achieved performances corresponding to the state of the art for QEPAS sensors. Measurements of CO in healthy subjects were performed with the homemade breath sample.

The NO and isoprene sensors showed correct performances however not enough to perform measurement on healthy subjects presenting lower breath concentrations of each gas. Different techniques may be implemented to optically (optical cavity) or mechanically (for example, multiple acoustic cavities) enhance the performances of these sensors. By conserving the simple off-beam configuration, the limit of detection of the sensors can be enhanced with a using laser source exhibiting higher optical power as the PA signal is proportional to this parameter.

The calibrated and dry measurements performed on the detection of acetone have shown limits of detection that are enough for the breath investigation. However, no measurements were performed in presence of humidity as no signature of acetone could be distinguished in the PA signal after humidifying the gas in the bubble bath. We are working on a different setup for the acetone measurements including the heating of the gas cell in order to be able to exhale directly into it and avoid the condensation of water or acetone.

The last part of the chapter 4 details the different electrical connections and adaptation of the breath sampling system between the QEPAS sensors and the Medisoft Ergocard apparatus. This work has conducted to the reconstruction of the expirogram of CO for

healthy subjects. The reduction of the gas cell volume led to a response time close to 1 second making the monitoring of CO concentration during the complete expiration possible. In addition to the measurement of CO performed with QEPAS, the flow rate measurement and the capnography provide crucial information on the airway management and for the diagnosis. Indeed, the chapter 1 have shown that the different mechanisms involved in the respiration affect the composition of the exhaled breath but also that the concentration of CO_2 informs on the origin of the breath in the respiratory system. Therefore, an interesting monitoring/ diagnosis tool is obtained from the combination of these three measurements.

This thesis constitutes a first step in this project aiming to the implementation of QEPAS as a breath sensor. The different issues related to the management of the humidity, the very low detectable concentrations and variations highlight the differences between working in calibrated laboratory, conditions and working "on field". A special attention must be attributed to measurements performed on humans. Indeed, the sensor needs to match the requirements in terms of performances (sensitivity, selectivity and response time) and consider the variability factors (such as humidity) in order to provide a measurement that is the most accurate and standardised possible as the challenge is related to a medical diagnosis. The successful reconstruction of the expirogram of CO constitutes an encouraging step in the development of QEPAS as a breath sensor. Nevertheless, it is not possible to conclude on a diagnosis by measuring a single molecule. Therefore, a different alternative has to be studied for the isoprene and NO setups and for the management of the interference of water with acetone measurements.

Further work will be dedicated to the combination of the four sensors for simultaneous and real-time measurements. This system will be studied and validated in a clinical study carried out in 2024 in the Clinical Physiology department of Montpellier Hospital, involving patients admitted with cardiovascular pathologies.

One of the objectives of this clinical study will be the clinical validation of the QEPAS sensor and measurement of the four different gases in the exhaled breath of patients and volunteers. During this study, complete expirograms will be generated for the four different gases in the two groups composing the cohort in order to enrich a database dedicated to the training of an artificial intelligence used for diagnosic purpose. This database currently includes CO expirogram data measured in smokers and non-smokers volunteers, and is being developed in collaboration with the IDESP laboratory in Montpellier.

Publications

Papers

Rousseau, R., Ayache, D., Trzpil, W., Bahriz, M., & Vicet, A. (2021). Passive Electrical Damping of a Quartz Tuning Fork as a Path to Fast Resonance Tracking in QEPAS. *Sensors*, *21*(15), 5056.

Ayache, D., Trzpil, W., Rousseau, R., Kinjalk, K., Teissier, R., Baranov, A. N., ... & Vicet, A. (2022). Benzene sensing by Quartz Enhanced Photoacoustic Spectroscopy at 14.85 µm. *Optics Express*, *30*(4), 5531-5539.

Trzpil, W., Maurin, N., Rousseau, R., Ayache, D., Vicet, A., & Bahriz, M. (2021). Analytic Optimization of Cantilevers for Photoacoustic Gas Sensor with Capacitive Transduction. *Sensors*, *21*(4), 1489.

Rousseau, R., Ayache, D., Maurin, N., Trzpil, W., Bahriz, M., & Vicet, A. (2021). Monolithic Double Resonator for Quartz Enhanced Photoacoustic Spectroscopy. *Applied Sciences*, *11*(5), 2094.

Gouzi, F., Ayache, D., Hédon, C., Molinari, N., & Vicet, A. (2021). Breath acetone concentration: too heterogeneous to constitute a diagnosis or prognosis biomarker in heart failure? A systematic review and meta-analysis. *Journal of Breath Research*.

Trzpil, W., Charensol, J., Ayache, D., Maurin, N., Rousseau, R., Vicet, A., & Bahriz, M. (2022). A silicon micromechanical resonator with capacitive transduction for enhanced photoacoustic spectroscopy. *Sensors and Actuators B: Chemical*, *353*, 131070.

Ayache, D., Rousseau, R., Kniazeva, E., Charensol, J., Seoudi, T., Bahriz, M., ... & Vicet, A. (2023). Commercial and Custom Quartz Tuning Forks for Quartz Enhanced Photoacoustic Spectroscopy: Stability under Humidity Variation. *Sensors*, *23*(6), 3135.

Seoudi, T., Charensol, J., Trzpil, W., Pages, F., Ayache, D., Rousseau, R., ... & Bahriz, M. (2023). Highly Sensitive Capacitive MEMS for Photoacoustic Gas Trace Detection. *Sensors*, *23*(6), 3280.

Conferences- Oral presentations

Proc. SPIE 11871, Optical Design and Engineering VIII, 118710T (12 Sep 2021), Wioletta Trzpil, Roman Rousseau, Diba Ayache, Nicolas Maurin, Aurore Vicet, Michael Bahriz, An analytic model for cantilever optimization for photoacoustic gas sensing with capacitive transduction

Proc. SPIE 11868, Emerging Imaging and Sensing Technologies for Security and Defence VI, 118680D (12 Sep 2021); Wioletta Trzpil, Nicolas Maurin, Diba Ayache, Roman Rousseau, Aurore Vicet, Michael Bahriz, Silicon micro-electromechanical resonator for enhanced photoacoustic gas detection

Proc. SPIE PC12013, MOEMS and Miniaturized Systems XXI, PC1201308 (09 Mar 2022); Wioletta Trzpil, Roman Rousseau, Diba Ayache, Julien Charensol, Aurore Vicet, Michael Bahriz, A capacitive resonant MOEMS on silicon for photoacoustic spectroscopy

Proc. SPIE PC12009, Quantum Sensing and Nano Electronics and Photonics XVIII, PC120090K (05 Mar 2022) ; Wioletta Trzpil, Diba Ayache, Roman Rousseau, Julien Charensol, Aurore Vicet, Michael Bahriz ; A silicon micromechanical resonator with capacitive transduction for laser-based photoacoustic spectroscopy

Proc. SPIE PC12009, Quantum Sensing and Nano Electronics and Photonics XVIII, PC1200913 (05 Mar 2022); Diba Ayache, Wioletta Trzpil, Julien Charensol, Nicolas Maurin, Roman Rousseau, Fares Gouzi, Michael Bahriz, Aurore Vicet ; Infrared spectroscopy for exhaled breath diagnosis

15th MIOMD, University of Surrey, Guildford, UK, 1 – 3 September 2021 (Online), Infrared spectroscopy for exhaled breath diagnosis. D. Ayache, W. Trzpil, J. Charensol, R. Rousseau, N. Maurin, F. Gouzi, M. Bahriz, A. Vicet.

15th MIOMD, University of Surrey, Guildford, UK, 1 – 3 September 2021 (Online); Silicon micro-electromechanical resonator for enhanced photoacoustic gas detection; W. Trzpil, J. Charensol, D. Ayache, N. Maurin, R. Rousseau, A. Vicet and M. Bahriz

Design, Test, Integration and Packaging of MEMS/MOEMS (DTIP'2022); A new silicon based microelectromechanical resonator for photoacoustic gas sensing; Tarek SEOUDI, Wioletta TRZPIL, Julien CHARENSOL, Diba AYACHE, Roman ROUSSEAU, Elena KNIAZEVA, aurore VICET, Michael BAHRIZ

A new silicon based microelectrochemical resonator for photoacoustic gas sensing. Charensol Julien, Seoudi Tarek, Trzpil Wioletta, Ayache Diba, Vicet Aurore, Bahriz Michael. Field Laser Applications in Industry and Research (FLAIR), Sept. 2022

Novel near-IR DFB laser-diodes for gas spectroscopy; E. Kniazeva, D. Diaz-Thomas, D, Ayache, G. Boissier, M. Bahriz, P. Patimisco, V. Spagnolo, A. Vicet; Mir5ens conference, 4-6 July 2022 in Wrocław

A. Vicet, D. Ayache, J. Charensol, T. Seoudi, E. Kniazeva, E. Rosenkrantz F. Gouzi, M.Bahriz Photoacoustic infrared gas sensors based on mechanical resonators for environmental to diagnosis applications, OPTICA sensing congress 30 july-3 august 2023 Munich (invite)

A. Vicet, D. Ayache, J. Charensol, T. Seoudi, E. Kniazeva, E. Rosenkrantz, F. Gouzi, M. Bahriz Laser sensing based on photoacoustic techniques: resonators studies and applications, PIERS 2023, 3-6 July 2023 Prague (invite)

D. Ayache, J. Charensol, T. Seoudi, N. Molinari, F. Gouzi, M. Bahriz, and A. Vicet exhaled breath analysis by quartz enhanced photoacoustic spectroscopy, PIERS 2023, 3-6 July 2023 Prague

T. Seoudi, J. Charensol, W. Trzpil, F. Pages, D. Ayache, R. Rousseau, A. Vicet, and M. Bahriz, Highly Sensitive Silicon Based Micro-Electromechanical Resonator for Photoacoustic Gas Sensing, PIERS 2023, 3-6 July 2023 Prague

T. Seoudi, J. Charensol, W. Trzpil, F. Pages, D. Ayache, R. Rousseau, A. Vicet, and M. Bahriz, Highly Sensitive Silicon Based Micro-Electromechanical Resonator for Photoacoustic Gas Sensing, DTIP 2023, 28-31 May 2023 Malta

T. Seoudi, J. Charensol, W. Trzpil, F. Pages, D. Ayache, R. Rousseau, A. Vicet, and M. Bahriz. Highly sensitive MEMS for photoacoustic gas sensing, OPTICA sensing congress 30 july-3 august 2023 Munich

Conferences- Posters

Infrared spectroscopy for exhaled breath diagnosis
Diba Ayache, Wioletta Trzpil, Julien Charensol, Nicolas Maurin, Roman Rousseau, Fares Gouzi, Michael Bahriz, Aurore Vicet, SPIE photonics west

W. Trzpil, N. Maurin, D. Ayache, R. Rousseau, A. Vicet and M. Bahriz « Analytic optimization of cantilever for photoacoustic gas sensor with capacitive transduction » Semiconductor and Integrated, OptoElectronics (SIOE) Online conference 1-2 April 2021

Breath analysis and diagnosis by quartz enhanced photoacoustic spectroscopy (QEPAS), Diba Ayache, Daniel Andres Diaz Thomas, Julien Charensol, Elena Kniazeva, Alexei Baranov, Michael Bahriz, Fares Gouzi, Aurore Vicet. Field Laser Applications in Industry and Research (FLAIR), Sept. 2022

QEPAS sensors based on novel laser-diodes for on-drone detection, E. Kniazeva, D. Diaz Thomas, D. Ayache, G. Boissier, M. Bahriz, P. Patimisco, V. Spagnolo, A. Vicet. Field Laser Applications in Industry and Research (FLAIR), Sept. 2022.

Appendix A

PICOS (population, interventions, comparators, outcomes and study designs) criteria.

P	• Humans, adults (at least 18 years old), male and female • Healthy subjects: without any chronic diseases or treatment that could modify the concentration of acetone in the body. • Heart failure patients: any kind of heart failure, FEVG < 50%, patients recruited with a medical exam.
I	N/A
C	N/A
O	• Any studies mentioning a measured concentration of acetone in the exhaled breath (not buccal air). • Any kind of analytical method and sampling (on-line/ off-line).
S	• Studies including more than 15 subjects. • All types of reviews are excluded. • Comparative studies: heart failure or other diseases vs. control group

Appendix B

Study data items for extraction

About the study	About the HF
• References (team, title, date) • Control (0) or HF subjects (1) • Pathology associated • Study population (number) • Number of male and female • Age: mean, SD • IMC: mean +- SD • Smoking habits • Diet (1/0)	• Class NYHA • % FEVG • BNP • HF: stable (1) or decompensated (0)
About the sampling	**Acetone concentration**
• Sampling: online (1) or offline (0) • Method of sampling • Analytical method • Type of sampling • Alveolar washout (1/0) • Expiratory flow control (1/0)	• Concentration: mean, SD • Concentration: median, IQR or range

Some of these data are conditions: 1 is used in case the condition is filled and 0 if not. "Pathology associated": some studies involve control in comparison to other pathologies it is important to know for which purpose the controls have been recruited. "Type of sampling": the sampling can be alveolar or full exhaled air or bronchial.

Appendix C

Reasons for exclusion of 55 full-texts studies

Reason of exclusion	Number	Reference
Measurement of acetone in the exhaled breath is not the aim of the study	10	Chen Q et al (2020), Sukul et al (2017), Sukul et al (2017), Prabhakar et al (2015), Sukul et al (2014), Worall et al (2013), Dummer et al (2011), Boshier et al (2010), Thekedar et al (2009), Gonzalez et al (2008)
Population recruited at the hospital	3	Adam et al (2019), Hanouneh et al (2014), Dolch (2008).
Population <15	19	Bovey et al (2018), Righettoni et al (2014), Grabowska et al (2013), White et al (2013), Ma V et al (2010), Bloor et al (2006), Anderson et al (2006), Senthlinohan et al (2001), Senthlinohan et al (2001), Kumagai et al (1999), Diskin et al (2003), Mitrayana et al (2020), Galasetti et al (2005), Mieksch et al (2008), O'Hara et al (2009), Boshier et al (2011), Tanda et al (2014), Bayrakil et al (2016), Grabowska et al (2017).
Fake controls	4	Andrews et al (2018), Chien PJ (2017), Ueta I (2014), Gilchrist (2013).
Measurements performed on kids (less than 18 years old)	1	Dryahina (2017)
No control and no HF patients	1	Qiao (2014).
Reviews	2	Crofford et al (1997), Smith et al (2007).
Measures performed on buccal air or not from exhaled breath	4	Angerer (1991), Tanda (2007), Velde (2009), Ross (2009)
No acetone measurement	2	Mizumuma (1993), Wysocki (1997)
Does not match PICOS criteria	9	Fenske (1999), Grote (1997), Stoner (2017), Huzier (2012), Fan GT (2014), Giannoukos (2014), King (2012), Satoh (1996), Righettoni (2012).

Appendix D

The purpose of this appendix is to detail the different calculation steps leading to the expression of the acoustic impedance Z in a simple pipe and a T-shaped pipe.

1- Acoustic pressure

The model of a simple pipe can be treated as a one-dimensional model as the radius of the pipe R is much smaller than its length L ($R \ll L$) and the acoustic wavelength λ ($R \gg \lambda$) (Figure 43).

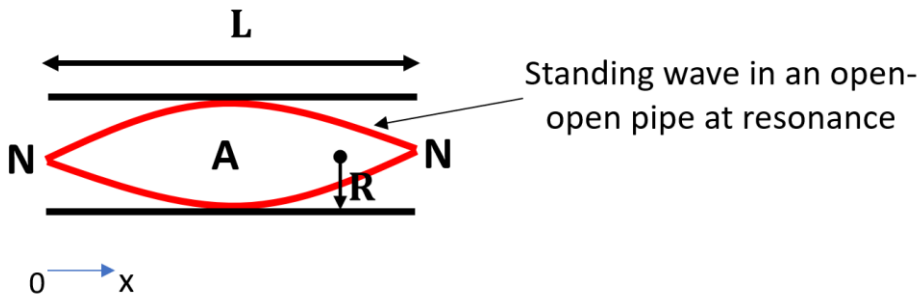

Figure 43 : standing wave inside a pipe of length L and radius R. N: nodes occurring at both ends where Z = 0. A: antinode

The acoustic pressure inside the pipe can be expressed as a one-dimensional standing wave as:

$$P(x,t) = A\, e^{i(\omega t - kx)} + Be^{i(\omega t + kx)} \quad (1)$$

Where x is related to the coordinate position and $k = \frac{\omega}{c} = \frac{2\pi f}{c}$ with c the sound velocity ($m.s^{-1}$) and f, the frequency (Hz)

2- Particle velocity

In order to express the particle velocity inside the tube, let us take the example of a very small section of an enclosed fluid with pressure variation along its length:

Newton's second law applied to a one-dimensional plane wave gives:

$$F = ma \tag{2}$$

With F the force (N), $a = \frac{du}{dt}$ the acceleration (m.s^{-2}) with u the particle velocity (m.s^{-1}) and $m = \rho S dx$, the mass (kg) with ρ the density (kg.m^{-3})

$$F = S\left(P - P + \left(\frac{\partial P}{\partial x}\right)dx\right) = -Sdx\frac{\partial P}{\partial x} \tag{3}$$

With S, the cross section of the pipe.

From (2) and (3) we can write:

$$\rho S\frac{du}{dt}dx = -Sdx\frac{\partial P}{\partial x} \tag{4}$$

This equation represents linear Euler equation describe in [1] (page 119, equation 5.4.10)

The particle velocity can be deduced from (4):

$$\frac{du}{dt} = -\frac{1}{\rho}\frac{\partial P}{\partial x}$$

$$u(x,t) = -\frac{1}{\rho}\int \frac{\partial P}{\partial x}\, dt$$

$$u(x,t) = -\frac{1}{\rho}\int \frac{\left(A\, e^{i(\omega t - kx)} + Be^{i(\omega t + kx)}\right)}{\partial x}dt$$

$$u(x,t) = -\frac{1}{\rho}\left(-A\frac{ik}{i\omega}e^{i(\omega t-kx)} + B\frac{ik}{i\omega}e^{i(\omega t+kx)}\right)$$

Knowing that $\frac{k}{\omega} = c$,

$$u(x,t) = \frac{1}{\rho c}\left(Ae^{i(\omega t-kx)} - Be^{i(\omega t+kx)}\right) \quad (5)$$

3- Acoustic impedance

The acoustic impedance for a stationary wave inside the pipe is not expressed in the time domain and can be defined as [2] (page 47, equation E-10):

$$Z(x) = \frac{P(x)}{Su(x)} = \frac{\rho c}{S}\frac{Ae^{-ikx} + Be^{ikx}}{Ae^{-ikx} - Be^{ikx}} \quad (6)$$

For x=0, $Z(0)$ is expressed as:

$$Z(0) = \frac{\rho c}{S}\frac{A+B}{A-B} \quad (7)$$

Let us express the ratio $\frac{A}{B}$ with $Z(0) = Z_0$:

$$Z_0(A-B) = \frac{\rho c}{S}(A+B)$$

$$Z_0\frac{A}{B} - Z_0\frac{B}{B} = \frac{A}{B}\frac{\rho c}{S} + \frac{\rho c}{S}\frac{B}{B}$$

$$\frac{A}{B} = -\frac{\frac{\rho c}{S} + Z_0}{\frac{\rho c}{S} - Z_0} \quad (8)$$

Therefore, we can express $Z(x)$ in (6) as function of Z_0 using (8):

$$Z(x) = \frac{\frac{A}{B}e^{-ikx} + e^{ikx}}{\frac{A}{B}e^{-ikx} - e^{ikx}}$$

$$Z(x) = \frac{\rho c}{S}\frac{-\frac{\frac{\rho c}{S} + Z_0}{\frac{\rho c}{S} - Z_0}e^{-ikx} + e^{ikx}}{-\frac{\frac{\rho c}{S} + Z_0}{\frac{\rho c}{S} - Z_0}e^{-ikx} - e^{ikx}}$$

$$Z(x) = \frac{\rho c}{S}\frac{\left(\frac{\rho c}{S} + Z_0\right)e^{-ikx} - \left(\frac{\rho c}{S} - Z_0\right)e^{ikx}}{\left(\frac{\rho c}{S} + Z_0\right)e^{-ikx} + \left(\frac{\rho c}{S} - Z_0\right)e^{ikx}}$$

$$Z(x) = \frac{\rho c}{S}\frac{Z_0(e^{-ikx} + e^{ikx}) + \frac{\rho c}{S}(e^{-ikx} - e^{ikx})}{Z_0(e^{-ikx} - e^{ikx}) + \frac{\rho c}{S}(e^{-ikx} + e^{ikx})}$$

Knowing that $\tan x = \frac{\sin x}{\cos x} = \frac{e^{ix} - e^{-ix}}{i(e^{ix} + e^{-ix})}$,

$$Z(x) = \frac{\rho c}{S}\frac{Z_0 + i\frac{\rho c}{S}\frac{e^{-ikx} - e^{ikx}}{i(e^{-ikx} + e^{ikx})}}{\frac{\rho c}{S} + iZ_0\frac{e^{-ikx} - e^{ikx}}{i(e^{-ikx} + e^{ikx})}}$$

$$Z(x) = \frac{\rho c}{S}\frac{Z_0 - i\frac{\rho c}{S}\tan(kx)}{\frac{\rho c}{S} - iZ_0\tan(kx)}$$

$$Z(x) = \frac{\rho c}{S} \frac{Z_0 - i\frac{\rho c}{S}\tan(kx)}{\frac{\rho c}{S}\left(\frac{Z_0\, S}{i\rho c}\tan(kx) + 1\right)}$$

$$Z(x) = \frac{Z_0 - i\frac{\rho c}{S}\tan(kx)}{\frac{Z_0\, S}{i\rho c}\tan(kx) + 1} \tag{9}$$

At resonance and anti-resonance in an open-open pipe of length L, the acoustic impedance at the nodes is equal to zero. Therefore,

$$Z_0 = Z_L = 0 \tag{10}$$

Then, the length of the pipe can be calculated from nine as:

$$Z_L = 0 = -i\frac{\rho c}{S}\tan(kL)$$

This equation is true for $\tan(kL) = 0$ therefore,

$$k = \frac{\pi}{L}n$$

We can deduce L as:

$$L = \frac{n\pi}{k} = \frac{n\pi c}{2\pi f} = \frac{nc}{2f}$$

For n=1 (first harmonic):

$$L = \frac{c}{2f} = \frac{\lambda}{2} \tag{11}$$

The acoustic impedance is calculated in the middle of the pipe as $Z\left(x = \frac{L}{2}\right)$.

4- Acoustic impedance in a T-shaped pipe

The definition of the acoustic impedance inside a T-shaped pipe is inspired from Hi et al [3].

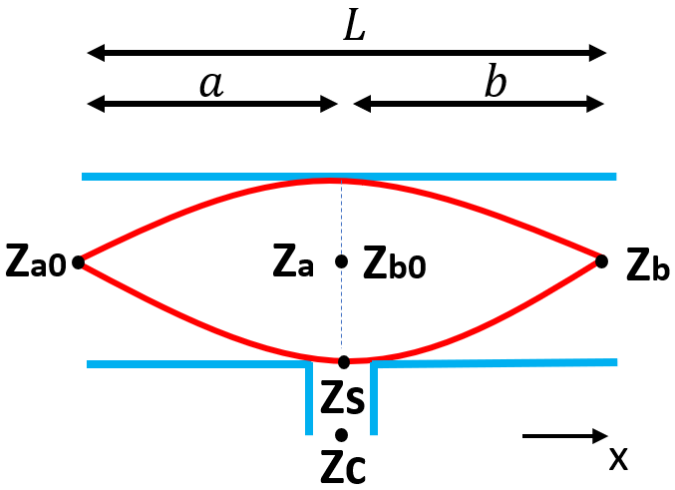

Figure 44 : Schematic representation of the T-shaped mR used in the analytical model

In the case of a T-shaped pipe (Figure 44), a small tube is added at the middle of the presented in the previous part. The main tube can be separated in two part $a = b$.

From (9) we can express the acoustic impedance Z_a and Z_b in each part as:

$$Z_a = \frac{Z_{a0} - i\frac{\rho c}{S}\tan(ka)}{\frac{Z_{a0}\,S}{i\rho c}\tan(ka) + 1} \tag{12}$$

$$Z_b = \frac{Z_{b0} - i\frac{\rho c}{S}\tan(kb)}{\frac{Z_{b0}\,S}{i\rho c}\tan(kb) + 1} \tag{13}$$

At resonance, the acoustic impedance at the nodes is zero. Therefore, $Z_{a0} = Z_b = 0$ leads to:

$$Z_a = -i\frac{\rho c}{S}\tan(ka) \tag{14}$$

$$Z_{b0} = i\frac{\rho c}{S}\tan(kb) \tag{15}$$

The impedance at the node is defined as in an electrical circuit:

$$\frac{1}{Z_a} = \frac{1}{Z_{b0}} + \frac{1}{Z_s} \tag{16}$$

Replacing (14) and (15) in (16), we can express Z_s:

$$\frac{1}{Z_s} = \frac{1}{-i\frac{\rho c}{S}\tan(ka)} - \frac{1}{i\frac{\rho c}{S}\tan(kb)}$$

$$-i\frac{\rho c}{SZ_s} = \frac{1}{\tan(ka)} + \frac{1}{\tan(kb)}$$

As $a = b = \frac{L_{eff}}{2}$, we have:

$$-i\frac{\rho c}{SZ_s} = \frac{2}{\tan\left(k\frac{L_{eff}}{2}\right)} \tag{17}$$

4.1- Acoustic impedance in the small tube

Let's now express Z_s function of Z_c , expressing the impedance in the small tube. From (9), we have:

$$Z_c = \frac{Z_s - i\frac{\rho c}{s_2}\tan\left(kl_{eff}\right)}{\frac{Z_s\, s_2}{i\rho c}\tan\left(kl_{eff}\right) + 1} \tag{18}$$

Where s_2 is cross the section of the small tube and l_{eff} is the effective length of the small tube.

At resonance $Z_c = 0$, therefore,

$$Z_s = i\frac{\rho c}{s_2}\tan(kl_{eff}) \tag{19}$$

As l_{eff} is very small, from the Taylor series expansion of first order, we can write $\tan(kt_0) \approx kt_0$

Thus, (19) becomes:

$$Z_s = i\frac{\rho c}{s_2}kl_{eff} \tag{20}$$

The acoustic conductivity σ_s for the small tube can be introduced as:

$$\sigma_s = \frac{s_2}{l_{eff}} \tag{21}$$

By replacing with (21), (20) can be written as:

$$Z_s = i\frac{\rho c}{\sigma_s}k \tag{22}$$

4.2- Effect of the small tube on the length of the main pipe

By replacing (22) in (17), we retrieve

$$-i\frac{\rho c\sigma_s}{iS\rho ck} = \frac{2}{\tan\left(k\frac{L_{eff}}{2}\right)}$$

$$\frac{2}{\tan\left(k\frac{L_{eff}}{2}\right)} = -\frac{\sigma_s}{Sk}$$

$$\tan\left(k\frac{L_{eff}}{2}\right) = -\frac{2kS}{\sigma_s} \tag{23}$$

L_{eff} can only be attributed positive values. Then, we can write:

$$\tan\left(k\frac{L_{eff}}{2} \pm \pi\right) = -\frac{2kS}{\sigma_s}$$

$$k\frac{L_{eff}}{2} = \pi - arctan\left(\frac{2kS}{\sigma_s}\right)$$

$$L_{eff} = \frac{c}{f}\left(1 - \frac{1}{\pi}\arctan\frac{4\pi fS}{\sigma_s c}\right) \tag{24}$$

The real length of the tube is calculated adding the correction:

$$L = \frac{c}{f}\left(1 - \frac{1}{\pi}\arctan\frac{4\pi f S}{\sigma_s c}\right) - 2C_L R \tag{25}$$

C_L is the correction coefficient calculated for a flanged or unflanged pipe given by [4][5].

References

[1] L. E. Kinsler, A. R. Frey, A. B. Coppens, and J. V. Sanders, "Fundamentals of Acoustics," *The Journal of the Acoustical Society of America*, vol. 72, no. 3. p. 1090, 1982, [Online]. Available: http://scitation.aip.org/content/asa/journal/jasa/72/3/10.1121/1.388211.

[2] D. T. Blackstock, "Fundamentals of Physical Acoustics." p. 541, 2000.

[3] H. Yi, K. Liu, S. Sun, W. Zhang, and X. Gao, "Theoretical analysis of off beam quartz-enhanced photoacoustic spectroscopy sensor," *Opt. Commun.*, vol. 285, no. 24, pp. 5306–5312, 2012, doi: 10.1016/j.optcom.2012.07.056.

[4] S. Yong, "Comparing Theory and Measurements of Woodwind-Like Instrument Acoustic Radiation," *Technology*, no. January, 2009.

[5] A. N. Norris and I. C. Sheng, "Acoustic radiation from a circular pipe with an infinite flange," *J. Sound Vib.*, vol. 135, no. 1, pp. 85–93, 1989.

Appendix E

FORMULAIRE FOR CARBON MONOXIDE MEASUREMENT IN THE EXHALED BREATH

NAME	AGE	WEIGTH	SIZE

SMOKER YES NO

NUMBER OF CIG/DAY

DO YOU STAY NEAR SMOKERS?

TYPE OF CIGARETTES

DO YOU OCCASIONALLY SMOKE?

TIME SINCE LAST CIGARETTE ?

PHYSICAL EXCERCISES YES NO

HOW OFTEN ?

PUBLIC TRANSPORT ? WALK ?

ALCOHOL CONSUMPTION

EVERYDAY 2-3x /WEEK OCASIONALLY

RARELY NEVER

FOOD CONSUMPTION

FASTING TIME SINCE LAST MEAL

ASTHMA

YES, TREATED YES, NOT TREATED NO